Planetary dynamics and high precision optical and near-IR spectroscopy

Testing the planetary hypothesis around evolved K-giants

Trifon Trifonov
Landessternwarte, Zentrum für Astronomie (ZAH) of Heidelberg University

Heidelberg 2014

Dissertation in Astronomy
submitted to the
Combined Faculties of the Natural Sciences and Mathematics
of the Ruperto-Carola-University of Heidelberg, Germany,
for the degree of
Doctor of Natural Sciences

M.Sc. ***Trifon Trifonov***
born in: Blagoevgrad, Bulgaria

Oral examination: 04.02.2014

Planetary dynamics and high precision optical and near-IR spectroscopy

Testing the planetary hypothesis around evolved K-giants

Trifon Trifonov
Landessternwarte, Zentrum für Astronomie (ZAH) of Heidelberg University

Referees: **Prof. Dr. Andreas Quirenbach**
Priv.-Doz. Dr. Christoph Mordasini

Zusammenfassung

Das Ziel meiner Dissertation ist der Nachweis und die Charakterisierung von extrasolaren Planeten um entwickelte Sterne mit Hilfe präziser Radialgeschwindigkeitsmessungen. Ich habe mit einer Stichprobe von G und K Riesen gearbeitet, die seit 1999 am Lick Observatorium beobachtet wurden. Planeten um entwickelte Sterne zu detektieren ist allerdings eine anspruchsvolle Aufgabe. Riesensterne können intrinsische, langzeitperiodische Radialgeschwindigkeitsvariationen aufweisen, die zum Beispiel von großen Sternflecken oder nicht-radialen $g-$Moden Pulsationen verursacht werden und die als Planetensignale missgedeutet werden können. Auf Grund der Tatsache, dass die Spektren des Hamilton Spektrographen für eine Linienprofilanalyse nur eine relativ niedrige Auflösung ($R = 60\,000$) besitzen, können diese Phänomene nicht eindeutig ausgeschlossen werden. Meine Arbeit konzentriert sich darauf nachzuweisen, dass die genau untersuchte Radialgeschwindigkeitsvariationen unserer Objekte, die konsistent mit einem oder mehreren sub-stellaren Begleitern ist, tatsächlich planetaren Ursprungs ist. Um dieser Frage nachzugehen, habe ich zwei quantitative Tests eingesetzt:

Als Erstes habe ich eine Datenreduktionssoftware für CRIRES, den Nahinfrarotspektrographen ($R = 100\,000$) der ESO, entwickelt. Hiermit habe ich präzise Radialgeschwindigkeiten im Nahinfraroten erhalten und diese auf Konsistenz mit den optischen Daten des Lick Observatoriums geprüft. Intrinsische Variationen der sterne haben Unterschiede in Phase und Amplitude zwischen optischen und nahinfraroten Radialgeschwindigkeiten zur Folge. Dagegen erwartet man, dass die beiden Datensätze im Falle eines Planeten konsistent sind. Zum Zweiten habe ich detaillierte $\chi^2_{\rm red}$ Gitter erstellt, um die dynamischen Eigenschaften der Systeme in der Umgebung der wahrscheinlichsten Parameter zu erforschen. Jede orbitale Konfiguration des $\chi^2_{\rm red}$ Gitters wurde mit dem "Mercury N-body simulator" getestet. Beide Methoden haben sich als sehr erfolgreich herausgestellt und sind als separate Teile in meine Dissertation eingebunden. Die erreichte Präzision im Nahinfraroten ist in der Größenordnung von $30-40$ m s^{-1}, genau genug, um die Phase und Amplitude der Radialgeschwindigkeit und damit den planetaren Ursprung der beobachteten Radialgeschwindigkeitsvariationen zu bestätigen. Das dynamische Modell zeigt bessere $\chi^2_{\rm red}$ − Werte als ein die überlagerung mehreren Keplermodelle. Dies ist ein Nachweis dafür, dass in der Tat wechselwirkende Planeten für die Dopplerverschiebungen verantwortlich sind. Der Langzeitstabilitätstest zeigt, dass einige der Systeme stabile Parameter besitzen, während der Rest breite, langzeitstabile Regionen im orbitalen Parameterraum einnimmt, die sich innerhalb des 1 oder 2 σ Bereichs der am besten angepassten Parameter befinden.

Abstract

The aim of my PhD dissertation is the detection and characterization of extrasolar planets around evolved intermediate stars using precise Doppler spectroscopy. I worked with a sample of G and K giants, which have been observed since 1999 at Lick Observatory. Finding planets around evolved stars, however, is an ambitious task. Giants can exhibit intrinsic long-period RV variations that can effectively mimic a planet, such as large surface spots or even non-radial $g-$mode pulsations. Given the fact that Hamilton spectra have relatively low resolution ($R = 60\,000$) for line profile analysis, those phenomena cannot be excluded. My research focuses on proving the planetary hypothesis for those objects in our science sample that show well-defined RV signature consistent with one or more sub-stellar companion(s). Thus, I have applied two quantitative tests that can finally close the case for our planetary candidates:

First, I have developed a data reduction pipeline for the ESO near infrared spectrograph CRIRES ($R = 100\,000$). I have obtained precise RV from the near-IR, and I searched for consistency with the Lick optical data. Intrinsic stellar RV variations will lead to differences in RV phase and amplitude between the optical and near-IR, while, in case of a planet, both data sets are expected to be consistent. Second, I have constructed detailed $\chi^2_{\rm red}$ grids in order to explore the dynamical properties of the fits around the best fit. Each orbital configuration from the $\chi^2_{\rm red}$ grids have been tested with the *Mercury* N-body simulator. Both methods turned out to be very successful and are included as separate parts of my PhD thesis. The near-IR velocity precision is in the order of $30-40$ m s^{-1} , enough to confirm the RV phase and amplitude, and thus, the planetary nature of most of our candidates. The dynamical fitting shows better $\chi^2_{\rm red}$ values than the multiple Keplerian model. This is a prove that indeed interacting planets are responsible for the Doppler shift. The long term stability test shows that some systems have a stable best fit, while the rest have broad and confident long term-stable regions in orbital parameter space within 1 or 2σ from the best fit.

“New ideas pass through three periods:

- *It can’t be done.*
- *It probably can be done, but it’s not worth doing.*
- *I knew it was a good idea all along !”*

Arthur C. Clarke

CONTENTS

LIST OF FIGURES

LIST OF TABLES

CHAPTER 1

INTRODUCTION

It has long been speculated that our solar system is not unique, and the universe must harbor endless examples of planetary systems orbiting around the stars in our galaxy and beyond. Perhaps the first evidence supporting this hypothesis comes from the ancient Greek philosopher Democritus (460 − 370 BC). He believed that the universe was made of microscopic unbreakable atoms that form everything known to man, and moreover our world is just one among many others in the universe. According to Democritus, some of those different worlds might have even more than one sun − something that has been confirmed recently. This concept of the universe, however, was not accepted, until Nicolaus Copernicus work *De revolutionibus orbium coelestium* − 'On the Revolutions of the Celestial Spheres', published in 1543, almost two thousand years later. The Copernican model argued with the Ptolemaic understanding of the universe, and finally placed the Earth and the planets in orbit around the Sun. Nevertheless, the science revolution in astronomy had to wait almost one more century until the development of telescope optical system by Italian astronomer Galileo Galilei (1564−1642). With his very primitive telescope (in our understandings) he discovered the moons of Jupiter, and showed that there are other hierarchical systems and thus more or less confirmed the Copernican model. At that time the German astronomer Johannes Kepler (1571−1630) first defined the laws of planetary motion and further helped the acceptance of the heliocentric model. We shall also not forget the most epic pioneer in astronomy of all − the Italian astronomer Giordano Bruno (1548 − 1600), who went even beyond the Copernican heliocentrism: he proposed that the Sun was essentially a star, similar of those that we see at the night sky, and that the universe must contains an infinite number of inhabited worlds populated by other intelligent beings[1]. Giordano Bruno eventually was bound, gagged and publicly burned alive near Vatican by the Roman inquisition, because of his believes.

Now in the early twenty first century we already know that extrasolar planetary systems do exist and with the fast technological and scientific progress we are already finding potentially habitable planets. Techniques such as the high-precision radial velocity, transiting method, grav-

[1] cited from: http://www.theharbinger.org/xvi/971111/birx.html

itational micro-lensing and more recently the great success on the direct imaging of extrasolar planets, have become in studying the planetary occurrence, evolution and formation scenarios.

The first confirmed extrasolar planet was discovered in 1992 by the radio astronomers Alexander Wolszczan and Dale Frail, (Wolszczan & Frail 1992), who noticed regular variations in the rapidly pulsed radio pulsar PSR 1257+12. In fact this variations are caused by the gravitational effects of two planets orbiting the dead star, and thus is valid to claim that Wolszczan & Frail (1992) discovered also the first discovery multiple planetary system a part of our solar system. A few years later, the detection of an extrasolar planet orbiting the main sequence star 51 Peg, by Mayor & Queloz (1995), triggered a whole new era in the modern astronomy – the exoplanet quest that became one of the most important flows in the modern science. 51 Peg b was found using the high-precision Doppler technique, which by now is the most successful method for extrasolar planet discoveries.

Now almost twenty years after the discovery of 51 Peg b, by September 2013, a total of 927 extra solar planets have been confirmed using a different observational techniques and their number is constantly growing[2]. These planets are found in 715 planetary systems, including 144 multiple planetary systems. Some remarkable examples of multiple planetary systems are known in the literature: The five planet system around 55 Cnc (Fischer et al. 2008), the six planets around Kepler−11, the possible habitable planets from the six planet system around Gl 581 (Vogt et al. 2010), or even the possible nine dense but still well-separated low-mass planets around the solar-type star HD 10180 (Tuomi 2012).

Even with the large number of extrasolar planets that have been discovered in the past twenty years, finding a planet is a very challenging task. First of all, the planets do not emit any light in the optical, and they can only reflect light from their host star. At visible wavelengths, this reflection is estimated to be a billion times dimmer than the parents star brightness, and thus often is almost impossible to image a planet directly. Direct imaging, however, turns out to be very successful recently. This technique is effective only in the infrared, where the detection of very distant young and hot planets is in principle possible.

Detection methods like the high precision radial velocity technique and the transiting method have proven to be very successful. Indeed, the vast majority of known extrasolar planets have been detected through one of these methods. However, those are indirect techniques and they have their strengths and weaknesses. The radial velocity method is not sensitive to the orbital orientation and thus we can only measure the minimum planetary mass, but we can effectively determine the rest of the orbital elements. On the other side, the transit method reveals the radius of a planet and its inclination allowing to constrain the mass, but suffers from many false positives and usually requires independent confirmation from another detection technique such as the radial velocity method. Another successful indirect technique is the gravitational micro-lensing (Wambsganss 2011), however, this method cannot reproduce the planetary detection event.

The focus of this Thesis will be on the detection and characterization of planetary companions around stars that already had evolved from the main sequence (MS). This research study has used the precise Doppler technique in two wavelength domains: the optical and in the near

[2]for up to date reference – www.exoplanet.eu

infrared (near-IR).

I will introduce our precise Lick observatory radial velocity survey, which started more than thirteen years ago with the goal to discover planetary companions and to understand the planet formation and evolution around intermediate-mass stars. Later, a sub-sample of twenty stars from this study was observed in the near-IR with the ESO high resolution ($R = 100\,000$) infrared (IR) spectrograph CRIRES. My contribution was to develop a pipeline that can extract precise near-IR radial velocities that can be comparable with those from Lick. I have spent most of my research on the stability analysis of the targets in our sample where the Doppler signal is consistent with more than one companion in the system.

In this Thesis some chapters are based on refereed papers that have been published, submitted or are under preparation and will be submitted to peer-review magazines in the very near future. If a figure or a table have been used from outside source, the reference will be given and explicitly will be noted if it has been have modified from the original.

The content of this Thesis is as follows:

This Introductory chapter is meant to be a starting point for the reader. Here I will reveal the basic knowledge needed for the rest of this Thesis. Mostly because this work explicitly follows the results from a Doppler survey, a short description of the radial velocity technique will be introduced. I will briefly compare the evolutionary stages between low and intermediate-mass stars, which will both eventually end up as red giants. Later I will summarize the planetary occurrence around giant stars and finally, in this Introduction chapter I will show how to distinguish the giant stars intrinsic radial velocity variations from a planetary signal.

In Chapter §2, I will introduce our observational set up when using the Coudé Auxiliary Telescope (CAT) and the Hamilton spectrograph at Lick observatory. After the technical description I will give an overview of the initial goal of our Lick study based on Frink et al. (2001). Recently, the final results of our sample have been submitted for publication Reffert et al. (2014), and I will reveal the most important conclusions from our long term survey.

In Chapter §3, an overview of the observations with the ESO CRIRES spectrograph will be given. I will describe the methods of how we obtained a precise radial velocities from the near-IR and the final results will be discussed. This Chapter follows Trifonov et al. 2014b (in prep.).

Chapter §4 will be focused on the dynamical stability of the η Cet planetary system. This chapter is an overview of Trifonov et al. (2014), announcing the discovery of unique planetary system consistent with two massive planets orbiting the K giant η Cet. I have presented a deep dynamical simulations that show with a high probability that the system must be observed near edge-on, and must be involved in a 2:1 mean motion resonance (MMR). This system appears to be the only one truly planetary system around giant star who's stability has been proven.

In Chapters §5, §6 and §7 I will introduce some of the most spectacular planetary systems found from the Lick survey. We have found mostly single planetary companions but some of them have minimum masses that can be classified as brown dwarfs. In the Lick sample, we have found multiple hierarchical systems including a MMR planetary pairs or even planets orbiting around a giant in a binary system. The planets discussed in these Chapters have passed the near-IR test with CRIRES. With small exceptions (ι Dra §5.3 - never been observed with CRIRES)

all are showing phase and amplitude variations that very adequately are following the model prediction from the optical data. In addition, for all the multiple planets systems, a long-term dynamical test has been done.

Finally, I will finish this Thesis with a Summary overview and discussion about my future plans and science prospects based on the work I have done.

1.1 THE RADIAL VELOCITY TECHNIQUE

Due to its movement in space, a star will have a relative velocity towards or away from an observer on Earth. The radial component of the star's velocity can be determined by measuring the displacement of the stellar spectral lines from the laboratory references using Doppler spectroscopy. In general, a star's radial velocity usually does not change sufficiently during a set of observations, so it can be assumed as constant (absolute radial velocity). However, when a star has an unseen companion in a non face-on orbit with respect to the observer, periodic variations on the star's radial velocity will occur. This is due to the star's movement around the common mass center (the system's barycenter), and it is caused by the companion's gravity pull. The star's spectrum will be blue-shifted when the star moves towards the observer and it will be red-shifted when it moves away (see Fig. 1.1).

With the Doppler method only five orbital elements can be obtained: the orbital period P, the time of passage through periastron T, the orbital eccentricity e, the longitude of periastron and the star's radial velocity amplitude $K_\star$, which is function of the companion mass. The line of nodes Ω and the orbital inclination i, on the other hand, cannot be determined from spectroscopic observations alone (for details on the orbital parameters see Murray & Dermott (1999)). Several further transformations can be done. The semi-major axis $a_\star$ of the primary around the center of mass is related to $K_\star$ by:

$$a_\star \sin i = \frac{P}{2\pi} \sqrt{(1 - e^2)}\, K_\star \tag{1.1}$$

Where i is not known but, according to Kepler's Third Law:

$$a^3 = \frac{P^2}{4\pi^2} G(m_\star + m_p) \tag{1.2}$$

where $a \equiv a_\star + a_p$ is the semi-major axis of the relative orbit of the two components. G is the universal gravitational constant, $m_\star$ and m_p the mass of the primary and the mass of the companion respectively.

Doppler spectroscopy is sensitive only to orbits that are not face-on respect to the observer, and the shift amplitude around the absolute radial velocity depends on the mass of the companion and its orbital inclination, thus only the minimum mass of the companion can be determined. By using $a_\star m_\star = a_p m_p$ and the above equations, this can be seen from the following relation:

$$\frac{(m_p sin\ i)^3}{(M_\star + m_p)^2} = \frac{P}{2\pi G} K_\star^3 \sqrt{(1-e^2)^3} \tag{1.3}$$

The left-hand side of this equation is the so-called *mass function* of a star-planet system. If the mass of the star $M_\star$ is known and m_p is the planet mass, we can approximate $M_\star + m_p \approx M_\star$, and this gives:

$$m_p sin\ i \approx \left(\frac{P}{2\pi G}\right)^{1/3} K_\star M_\star^{2/3} \sqrt{(1-e^2)} \tag{1.4}$$

It is easy to see that we indeed observe only the minimum planet mass and if we take $\sin i \neq 1$ ($i \neq 90°$), the mass of the planet must rise to satisfy the right side equation[3]. In more convenient units one can write:

$$m_p \sin i\ [M_{\rm Jup}] \approx 3.5\text{x}10^{-2} K_\star\ [m\,s^{-1}]\ P^{1/3}\ [yr] \tag{1.5}$$

In each individual case the actual mass of the planet may be considerably larger than this lower limit inferred from the radial-velocity technique ($m_p \sin i$). In a statistical sense, however, it is more likely to observe an object nearly equator-on than nearly pole-on. It turns out that in 87% of all known planetary systems $\sin i \geq 0.5$, and that in only 0.5% of all cases $\sin i \leq 0.1$. Therefore, distributions of $m_p \sin i$ from radial velocity surveys are fairly representative of the true distribution of planetary masses (for more details see Quirrenbach (2006)).

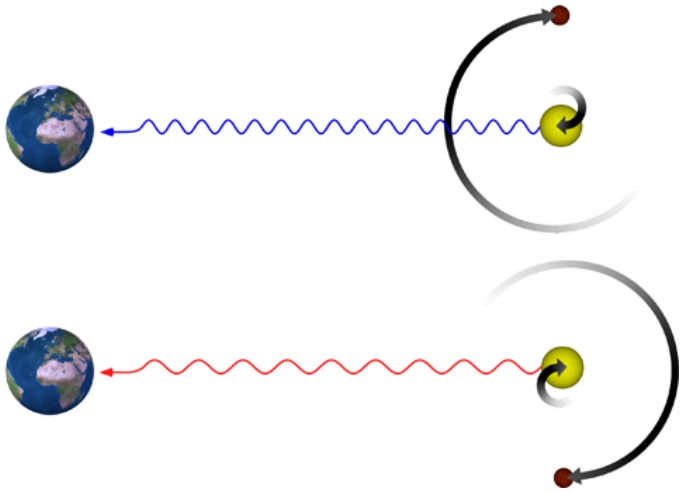

Figure 1.1: The radial velocity technique using a Doppler spectroscopy to detect extrasolar planets. While the star is orbiting around the system's barycenter, we can measure periodic spectral shift and obtain information about the system's configuration. *Credit*: taken from http://www.sciencedaily.com/releases/2012/05/120531101903.htm – made by Th. Udem, MPQ

[3]This is valid valid only for the simple case of one substellar/planetary companion orbiting a star. Orbital parameters in high order hierarchical systems are better described in Jacobi coordinates (Lee & Peale 2002)

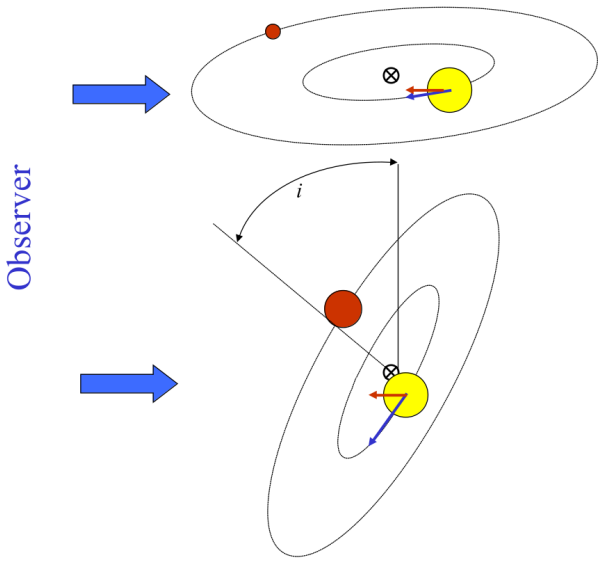

Figure 1.2: We measure only the radial component (*red velocity vector*), so we cannot be confident whether we are detecting a planetary mass object with orbital plane almost edge-on or a high mass object viewed perpendicular to the orbital plane. We can only detect the minimum mass ($m_p \sin i$) of the object. *Credit*: Artie Hatzes's lecture notes.

In cases where the companion has a stellar nature these periodic Doppler shifts are on the order of km s^{-1}, and are thus relatively easy to detect. When the companion is a planet, the radial velocity is on the order of tens of m s^{-1} and requires state of the art spectrographs that are able to go down to such precision.

The key to reach this kind of precision is the usage of high resolution Échelle spectrographs that can cover practically the whole optical wavelength range in a single spectrum. Such instruments are HARPS (High Accuracy Radial Velocity Planet Searcher), installed at the La Silla Observatory in Chile (Mayor et al. 2003), HIRES (The High Resolution Echelle Spectrometer) on the Keck Telescope (Vogt & Keane 1993), Hamilton Échelle spectrograph at Lick observatory (Vogt 1987) and more. Each spectral line gives a measurement of the Doppler shift, so when using an Échelle spectrographs we can measure a maximum set of stellar lines needed to achieve maximum accuracy. The next crucial step is to obtain a very accurate wavelength calibration on the science spectra. Two very different but perhaps equally successful techniques have been developed to precisely track radial velocity variations down to 1 m s^{-1} or in some cases even below.

The first technique is using a Iodine gas absorption cell placed at the entrance of the spectrograph's slit as is shown in Fig. 1.3, and thus the stellar and the Iodine gas spectra are superimposed on the CCD detector (Marcy & Butler 1992; Valenti et al. 1995; Butler et al. 1996). The iodine spectra is very well studied, and the deep and sharp Iodine lines are used as a wavelength references. This method measures only the relative radial velocity to a stellar template - stellar spectra which is usually obtained earlier without iodine cell. The absolute radial velocity cannot be determined with the Iodine cell method, but it is also not required as we are interested only in the velocity variations around the absolute radial velocity. The stellar and Iodine spectra are

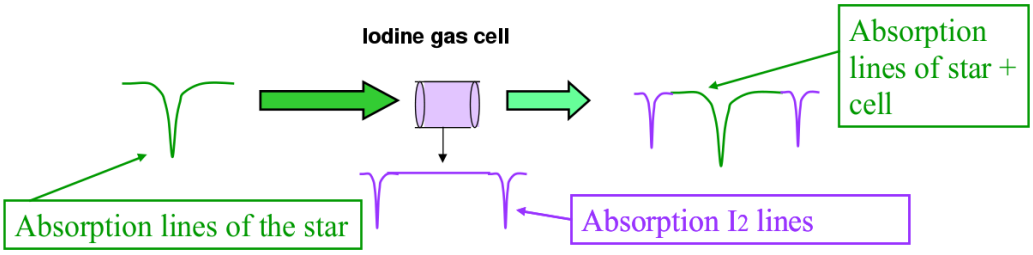

Figure 1.3: Basic description of the I_2 cell method. Stellar spectrum is taken simultaneously with a well studied I_2 spectra used as reference. *Credit*: Artie Hatzes's lecture notes.

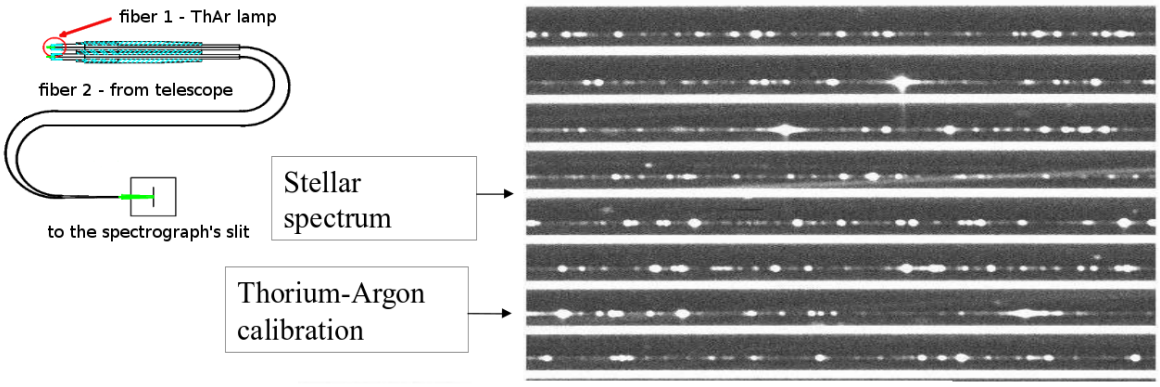

Figure 1.4: Spectrograph equipped with ThAr lamp calibration source. The stellar and ThAr calibration spectra are taken at the same time. *Credit*: Artie Hatzes's lecture notes modified by the author.

always taken simultaneously, so any spectrograph instabilities do not influence on the measured radial velocity, and thus it is a relatively inexpensive and very efficient solution.

The second method uses simultaneous wavelength calibration by obtaining a spectrum with a ThAr lamp with well defined spectral lines. This technique requires a high level of temperature stability, and construction costs for this kind of instruments are very high. Nevertheless, this technique appears to be the most accurate at our time. For example, HARPS, with an accuracy of $\sigma_{RV} = 0.3\ \mathrm{m\,s^{-1}}$, can locate many rocky, Earth-like planets. This technique derives an absolute radial velocity obtained by the cross-correlation method (Baranne et al. 1996) between the science spectra and a weighted stellar linelist mask (Pepe et al. 2002).

One of the disadvantages of the Doppler technique is that it is sensitive only to late type stars. Main Sequence (MS) stars of spectral type earlier than F5 are hot stars, which due to their fast rotation have broadened their spectral lines. In addition, the stellar photosphere must be sufficiently stable which eliminates faint and active M dwarf stars[4]. Evolved giant stars are the most suitable objects for RV monitoring because they are cool stars, that have lots of sharp lines and rotate slowly. A Schematic of the obtained RV precision versus the star's spectral type is shown in Fig. 1.5.

[4]However, in the near future M dwarfs will be studied under the CARMENES project by obtaining precise radial velocities from the optical and the near-IR simultaneously (Quirrenbach et al. 2013)

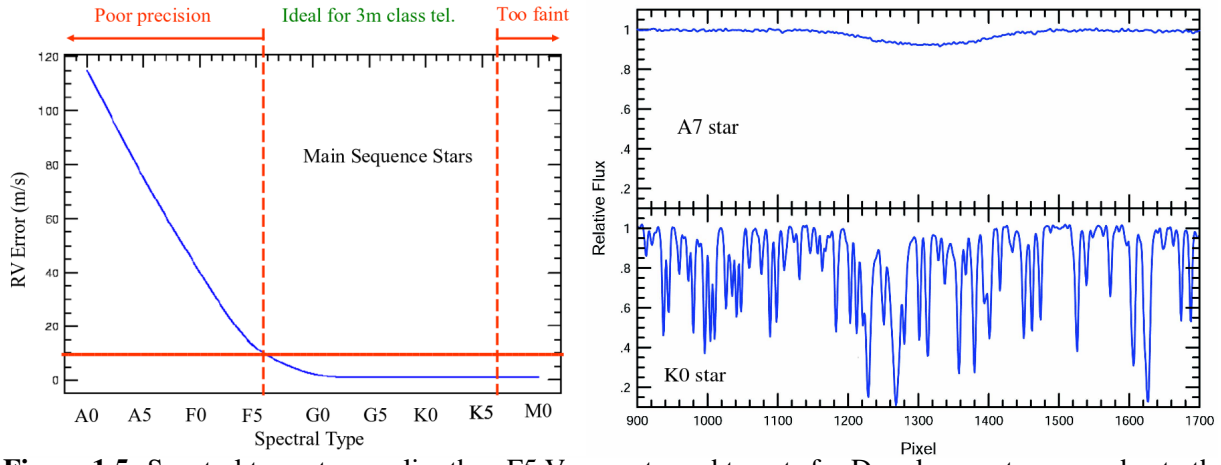

Figure 1.5: Spectral type stars earlier than F5 V are not good targets for Doppler spectroscopy due to the luck of stellar lines. *Credit*: Artie Hatzes's lecture notes modified by the author.

1.2 PLANETS AROUND EVOLVED GIANT STARS

As already mentioned, over 50 planets have been discovered around red giant stars and their number is fast increasing. Thus, to understand better the giant stars from spectral class G and K, in §1.2.1 I will briefly introduce the physical properties and the evolutionary phases of low and intermediate mass stars, which are the progenitors of the red giants. In §1.2.2 I will introduce the most widely-accepted core accretion theory of planet formation, and I will reveal its strengths and weaknesses. Finally, in §1.2.3 a summary of the discoveries of extrasolar planets around giant stars will be introduced, and I will summarize their orbital parameter distributions.

This sub-chapter is based on the book of Carroll & Ostlie (2006) and the most recent publications in the literature about the planet formation theories and the planetary occurrence around giant stars.

1.2.1 EVOLUTIONARY STAGES OF LOW AND INTERMEDIATE-MASS STARS

All stars form in large gravitationally collapsing molecular clouds in the interstellar medium. The composition of these clumps is mostly gas and dust consistent with hydrogen (H), a substantial fraction of helium (He) and small amounts of heavier elements such as oxygen (O), carbon (C), silicon (Si) and iron (Fe), which in astronomy jargon are called *"metals"*. This process of star formation usually takes millions of years before the condensed star embryos (or so-called *"protostars"*) reach a sufficiently high temperature and density, necessary to ignite the hydrogen fusion. With the establishment of a stable energy source by burning the hydrogen into helium in the core of the star, the gravitational energy term becomes insignificant and the star finally settles onto the main sequence (Carroll & Ostlie 2006). The lifetime on the MS strongly depends on the initial mass of the formed star, as more massive stars exhaust their H much more rapidly than the low mass members of the MS. It will take only a few million years for the most massive stars with $M > 20 M_{\odot}$, but up to hundreds of billions of years for the red dwarf MS stars.

Although, on different time scales, stars with masses in the range from about 0.5 to around 8 $M_{\odot}$ will all end up as inflated and very luminous red giants of spectral class K and M. In the case of a solar mass star ($0.5 \leq M/M_{\odot} \leq 2.5$), when the hydrogen burning ceases in the core of the star the core begins to contract while a thick hydrogen-burning shell continues to consume the available fuel. With the rising temperature in the shell due to core contraction, the shell actually produces more energy than the core did on the main sequence, causing the luminosity to increase, the envelope to expand slightly, and the effective temperature to decrease (Carroll & Ostlie 2006).

However, the evolution off the MS for an intermediate mass star with $2.5 \leq M/M_{\odot} \leq 8$ is somehow different. Detailed depictions of the evolutionary tracks for low and intermediate mass stars in the H-R diagram are illustrated in Fig. 1.6.

The contraction phase in the intermediate mass stars is associated with the release of gravitational potential energy. This phase causes the luminosity to increase slightly, the radius of the star to decrease, and the effective temperature to increase. Eventually the temperature outside the helium core increases sufficiently to cause a thick shell of hydrogen to burn. Because the ignition of the shell is quite rapid, the overlying envelope is forced to expand slightly, absorbing some of the energy released by the shell. As a result, the luminosity decreases momentarily and the effective temperature drops. Later, the evolution for the low and intermediate mass stars follows a complicated sequence of evolutionary stages:

For both low and intermediate-mass stars, while the shell continues to consume the hydrogen the helium core steadily increases in mass and becomes nearly isothermal. This causes the envelope of the star to expand and the effective temperature to decrease, moving to the redder side of the H-R diagram. This phase of the stars evolution is known as the sub-giant branch (SGB). For the intermediate mass stars, the expanding envelope for a short time absorbs enough energy to cause the luminosity to decrease slightly before entering the Red Giant Branch (RGB).

During the RGB phase, due to the increased opacity in the stellar interior, both low and intermediate-mass stars develop a convection zone near the surface that carries away the energy evolved from fusion. As the star climbs the RGB, its convection zone deepens until the base reaches down into regions where the chemical composition has been modified by nuclear processes, an event called 'first dredge-up'.

The evolutionary path along the red-giant branch depends on the mass of the star, but also on its initial chemical composition (i.e. metallicity).

During the RGB phase the core of a low mass stars will continue its gravitational collapse until it reaches an equilibrium with the electron degeneracy pressure. Then the core will stop collapsing further but it will continue to rise in temperature. When the temperature is roughly 10^8 K, it will begin fusing helium to carbon via the 3α process (cite). This so-called 'helium flash' process is extremely fast, lasting only few seconds, but releases enormous amount of energy. The luminosity generated by the helium burning core reaches 10^{11} $L_{\odot}$, (Carroll & Ostlie 2006) comparable to that of an entire galaxy! However, this luminosity is absorbed by the overlying layers of the envelope, and never reaches the surface, but can cause some stellar mass loss. After the helium burning phase the low mass stars leave the RGB and move through the Asymp-

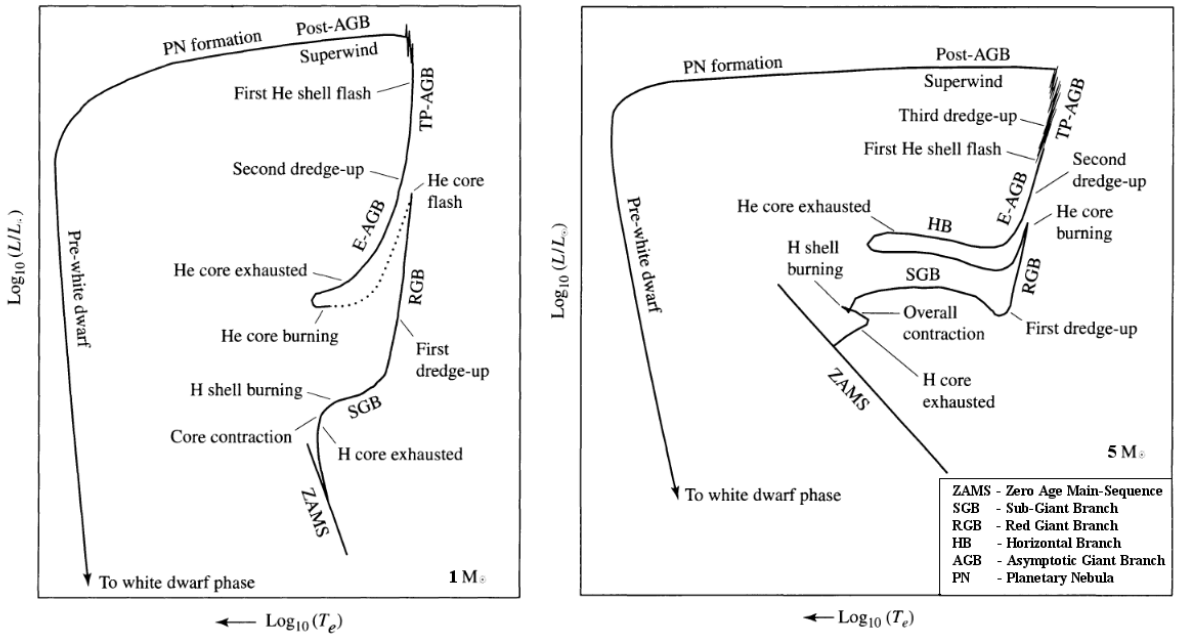

Figure 1.6: A schematic diagram of the evolution of solar type and an intermediate-mass star of 5 $M_{\odot}$ from the zero-age main sequence (ZAMS) through the giant phases and the formation of a white dwarf star. Both stars reach the RGB phase, but following different evolutionary tracks. The 5 $M_{\odot}$ has an additional turning point before the SBG and an additional HB phase(s). *Credit*: Carroll & Ostlie (2006) modified by the author.

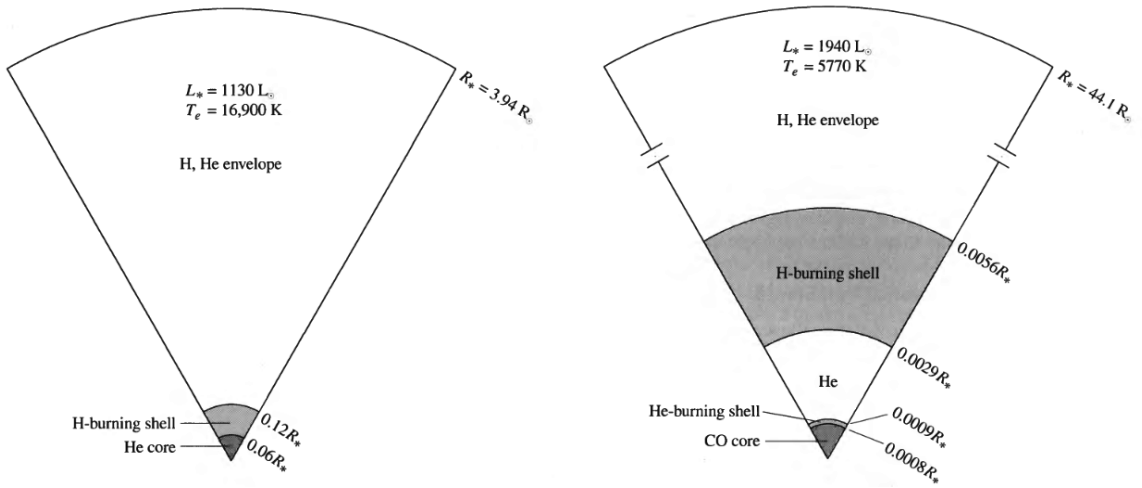

Figure 1.7: *Left*: Intermediate-mass star with a helium core and a hydrogen-burning shell shortly after the shell ignition. *Right*: the same star on the early asymptotic giant branch with a carbon-oxygen core and hydrogen and helium-burning shells. *Credit*: Carroll & Ostlie (2006)

totic Giant Branch (AGB) phase a second red-giant slope in the HR diagram. There the star is extremely inflated and loses most of its mass. The final product is a planetary nebula (PN) with the core of the star exposed, ultimately becoming a white dwarf.

In intermediate mass stars no helium flash is produced. The collapsing core will reach 10^8 K before it is dense enough to be degenerate, so helium fusion will begin much more smoothly. The further evolution of intermediate mass stars depends on their metallicity. The core helium burning phase of a star's life is called the horizontal branch (HB) in metal-poor stars, while Metal-rich helium-burning stars instead lie on the so-called red clump in the HR diagram.

When the helium is exhausted in the core of more massive stars the star collapses once again, causing helium in an outer shell to begin fusing. At the same time hydrogen may begin fusion in a shell just outside the burning helium shell. The helium fusion results in the build up of a carbon-oxygen (CO) core. A star below the intermediate-mass limit of 8 $M_\odot$ will never start further fusion in its degenerate CO core (see Fig. 1.7). Instead, it will continue on the AGB phase, eject its outer layers by forming a PN and again, as in the low mass star population, will become a white dwarf.

1.2.2 Planet formation

The large number of extrasolar planets discovered in the past twenty years triggered enormous theoretical efforts to explain planet formation and evolution. The observations show a large contrast between our local example − the solar system and the broad range of extrasolar planers orbital characteristics, such as mass, distance to the host star and their eccentricity (see Fig. 1.9).

Current theory of planet formation states that planets are made from a core accretion of the gas and dust remnants after star birth. Shortly explained, the best accepted planetary formation scenario is the following: While the protostar's clump is getting denser, the conversion of angular momentum leads to the rotation speed of the debris disk to increase, while the nebula radius decreases. As result the clump flattens taking a form of a disk around the proto-star (Nakamoto & Nakagawa 1994). The proto-planetary disk feeds the central star with matter for a few tens of millions of years, causing the inner section of the disk to reach high temperatures, enough to evaporate most of the water and organic molecules. The remaining material left is some of the silicates and heavy elements such as iron (Kessler-Silacci et al. 2006). These ingredients are the building blocks of the terrestrial planets.

According to the Solar Nebular Disk Model of core accretion (Woolfson 1993), the water poor dust in the inner part of the debris disk is initially microscopic, but due to collisions and aggregation, the matter is condensed in centimeter-sized grains. These grains are supposed to grow by further sticking together into planetesimals, which then assemble into planets with solid cores (Montmerle et al. 2006).

The core accretion model states that the giant planets must be formed beyond the so-called "snow line" in the outer part of the disk consisting mainly of ice (see Fig. 1.8 b). Giant planets are the product of accretion of ice rich planetesimals until the core reaches approximately 10 Earth masses. Then, the core is massive enough to start accumulating gas from the protoplanetary

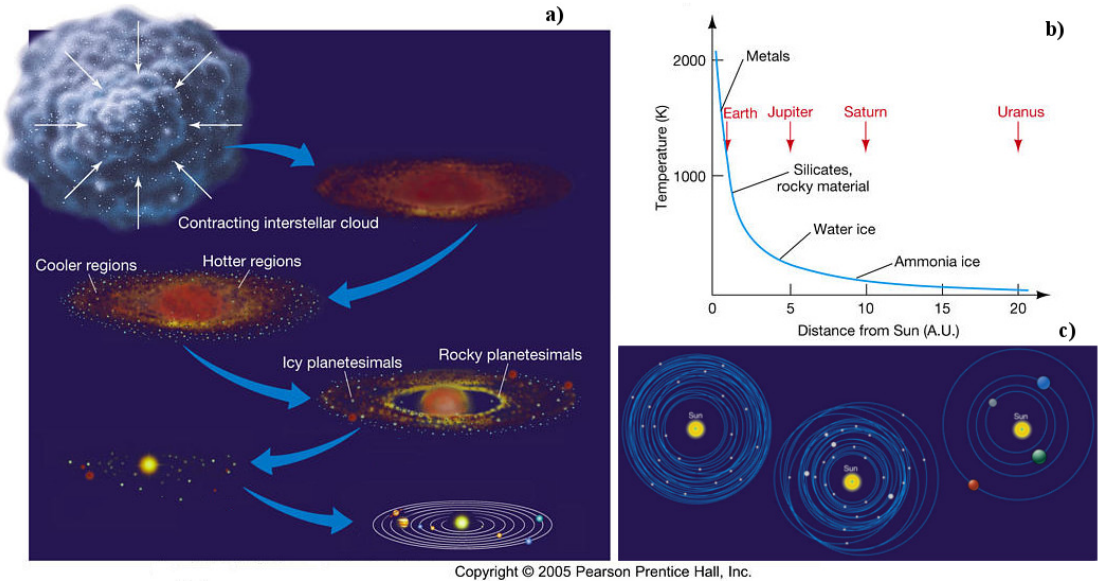

Figure 1.8: Solar Nebular Disk Model of core accretion planet formation scenario. A dusty a proto-planetary disk during it's initial evolution form small millimeter size planetesimals. With time this particles must be involved in another accumulation processes forming the inner terrestrial planets and the cores of the giant planets behind the snow line. *Credit*: The University Of Oregon, modified by the author.

disk by migrating inwards through the star. The migration stops when the disk gas and dust it is exhausted, leaving the planets on their final orbits.

This model gives a good explanation of the existence of inner terrestrial "rocky" planets and the outer gas and ice giants in the Solar system. More over, observations of protoplanetary accretion disks around very young T Tauri stars seem to provide good arguments in favor of core accretion theory. However, this theory also has problems. For example, so far the core accretion model cannot fully reproduce the evolutionary path from grains to kilometer size planetesimals. Simulations shows that planetesimal formation is ineffective as dust particles grow larger than 1 meter (Youdin & Shu 2002).

Another partly unsolved problem is the distribution of the discovered extrasolar planets semi-major axis and orbital eccentricity. For instance, if we assume that proto-planetary disks around other stars must generate planetary configurations similar to the Solar system, then the observed extrasolar planetary systems must be nearly circular and consistent with low-mass rocky planets in the interior, with giants further out from the star. In reality we know of the existence of many Peg 51 b like hot giants orbiting their parent star in an orbit much closer than Mercury in the Solar system, and thus presents a problem for planetary formation and evolution. One can criticize that this is only selection bias, because those objects are more easily found by Doppler and Transiting techniques, and in future we will be able to find Solar system analogues. Furthermore, hot Jupiters might indeed form by core accretion in massive disks and during Type I migration to accumulate dust and gas all the way to the parent star.

We also see that most of the discovered planets have moderate and high eccentricities or

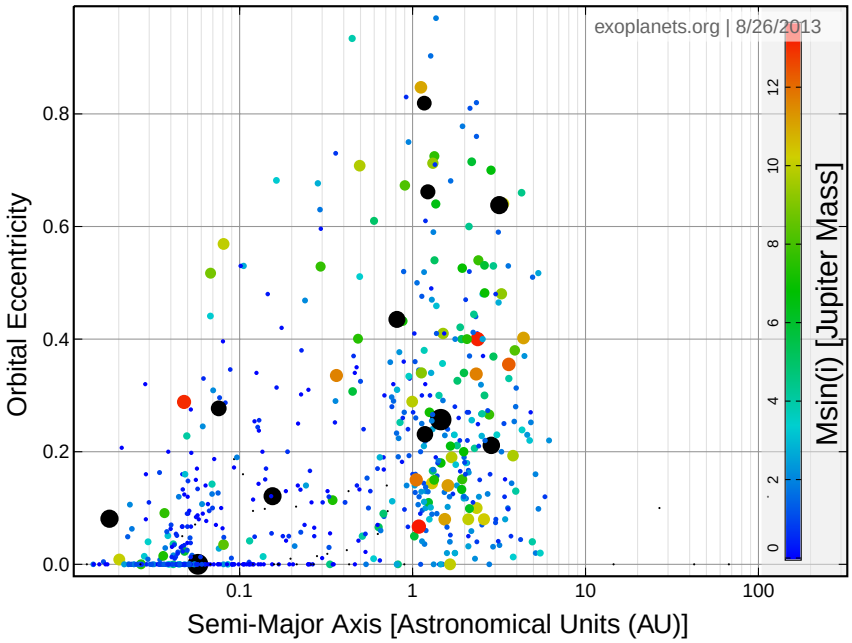

Figure 1.9: There are many low mass planets in close and circular orbits, but most of the known extrasolar planets are eccentric. Black circles notate companions with minimum masses that are already over 13 M_{Jup} thus, a Brown dwarf objects. *Credit*: www.exoplanets.org.

even sometimes star-gazing orbits. This phenomenon, however, somehow contradicts with the Type I migration scenario, because the planets must circularize their orbits by accumulating dust and gas during this stage of their formation. One possible explanation can be planetary system instabilities that might occur during the system's evolution. Ejections or collisions between planets might force the eccentricities to become large and to differ sufficiently from the initial architecture. Kozai effects from an external massive disturber might be one more reason for the observed eccentricity distribution and non-planar orbits. The planetary interactions during the evolution are probably one of the important factors for the seen planetary configurations.

It is also very likely the observed diversity of extrasolar planets properties to be a natural consequence of the different properties of proto-planetary disks (Mordasini et al. 2009). Only combination of observations and theory will reveal the final answer.

1.2.3 Planet occurrence around G and K giant stars

Although the total number of discovered planets around MS stars is continuously increasing, the total number of known substellar companions around giant stars is still relatively low. By November 2013, 56 sub-stellar companions orbiting in 53 giant stars have been announced. Most of the discoveries come from precise Doppler surveys including our own using the Hamilton Spectrograph at Lick Observatory (Frink et al. 2001) and on which this work is based. Table 1.1

gives a full list of planets around giants available in the literature[5].

We have poor statistics for the planet population of early intermediate-mass stars as they have spectral classes earlier than F and as was discussed in §1.1, a precise radial velocity search around such targets is not possible. On the other hand, intermediate-mass stars are in most cases the progenitors of the evolved red giants, whose properties are ideal for a planet search with the precise radial velocity technique. The fact that the number of planets around evolved giants is relatively low is somehow odd. It opens some questions about the planet formation and evolution around red giants and intermediate-mass stars in general. The low planet rate could be a selection effect, as most of the planet search studies are focused on MS solar type stars, but can also be correlated with the stellar evolution and the planetary systems that they may potentially harbor.

Fig. 1.10 shows some interesting dependencies when looking at the known extrasolar planets around evolved giants (see Table 1.1). One can see that the vast majority of the planets found around intermediate-mass evolved stars have well-separated orbits with semi-major axis larger than 0.6 AU (e.g. Sato et al. 2008a).

This observational fact can be a result of several scenarios:

1. It is possible that at least low mass and relatively close planets do exist, but they have not been detected yet most possibly due to the high intrinsic stellar jitter seen in some giants from later spectral type.

2. As reaching the red giant branch the star entails some mass loss, the star's gravitational pull becomes weaker and the close planets migrate outwards, so no short period companions are present.

3. The higher accretion rates in massive proto-planetary disks might lead to fast disks dissipating before planets are able to migrate close to the central stars, and no close orbit planets ever have been formed.

4. Given the fact that red giants are very inflated stars, even if they had a very close-by or hot Jupiters in the earlier epochs, now they are swallowed by the parent star.

5. In case the star harbored a planetary system in the past, with the stellar evolution and more general with the mass loss of the central star the stability might be broken due to collisions or ejections and eventually there might be no planets in close orbits.

[5] http://www.lsw.uni-heidelberg.de/users/sreffert/giantplanets.html

Table 1.1: All planets known to orbit a giant star and published in refereed journals*

Star	HIP	Sp. type	[Fe/H]	$M_\star$ [$M_\odot$]	$m_p sini$ [M_{Jup}]	Period [days]	Reference
ι Dra	75458	K2 III	0.11	1.05 ± 0.36	8.8	511 ± 0.1	Frink et al. (2002)
Pollux	37826	K0 IIIb	0.07	1.86	2.9 ± 0.3	589.7 ± 3.5	Reffert et al. (2006)
HD 11977	8928	G5 III	−0.21 ± 0.1	1.91	6.54	711	Setiawan et al. (2005)
HD 47536	31688	K1 III	−0.68	0.94	5	430	Setiawan et al. (2003)
HD 13189	10085	K2 II	−0.39 ± 0.19	2−7	8−20	471.6 ± 6.0	Hatzes et al. (2005)
ϵ Tau	20889	K0 III	0.17 ± 0.04	2.7 ± 0.1	7.6 ± 0.2	594.9 ± 5.3	Sato et al. (2007)
HD 104985	58952	G9 III	−0.35	2.3	8.3	199.505 ± 0.085	Sato et al. (2003)
NGC2423 No.3			0.14 ± 0.09	2.4 ± 0.2	10.6	714	Lovis & Mayor (2007)
NGC4349 No.127			−0.12 ± 0.04	3.9 ± 0.3	19.8	678	Lovis & Mayor (2007)
4 UMa	42527	K1 III	−0.25 ± 0.04	1.23 ± 0.15	7.1 ± 1.6	269.3	Döllinger et al. (2007)
HD 17092		K0 III	0.22	2.3 ± 0.3	4.6 ± 0.3	359.9 ± 2.4	Niedzielski et al. (2007)
11 Com	60202	G8 III	−0.35 ± 0.09	2.7 ± 0.3	19.4 ± 1.5	326.03 ± 0.32	Liu et al. (2008)
18 Del	103527	G6 III	−0.052 ± 0.023	2.3	10.3	993.3 ± 3.2	Sato et al. (2008a)
ξ Aql	97938	K0 III	−0.205 ± 0.039	2.2	2.8	136.75 ± 0.25	Sato et al. (2008a)
HD 81688	46471	K0 III−IV	−0.359 ± 0.020	2.1	2.7	184.02 ± 0.18	Sato et al. (2008a)
14 And	116076	K0 III	−0.24 ± 0.03	2.2	4.8	185.84 ± 0.23	Sato et al. (2008b)
81 Cet	12247	G5 III	−0.06 ± 0.03	2.4	5.3	952.7 ± 8.8	Sato et al. (2008b)
HD 102272 b	57428	K0 III	−0.26 ± 0.08	1.9	5.9 ± 0.2	127.58 ± 0.30	Niedzielski et al. (2009a)
HD 102272 c	57428	K0 III	−0.26 ± 0.08	1.9	2.6 ± 0.4	520. ± 26	Niedzielski et al. (2009a)
HD 240210		K3 III	−0.18 ± 0.12	0.82 ± 0.15	5.21	501.75 ± 2.33	Niedzielski et al. (2009b)
BD +20 2457 b		K2 III	−1.00 ± 0.07	2.8 ± 1.5	21.42	379.63 ± 2.01	Niedzielski et al. (2009b)
BD +20 2457 c		K2 III	−1.00 ± 0.07	2.8 ± 1.5	12.47	621.99 ± 10.20	Niedzielski et al. (2009b)
HD 173416	91852	G8 III	−0.220 ± 0.09	2.0 ± 0.3	2.7 ± 0.3	323.6 ± 2.2	Liu et al. (2009)
42 Dra	90344	K1.5 III	−0.46 ± 0.05	0.98 ± 0.05	3.88 ± 0.85	479.1 ± 6.2	Döllinger et al. (2009b)
HD 139357	76311	K4 III	−0.13 ± 0.05	1.35 ± 0.24	9.76 ± 2.15	1125.7 ± 9.0	Döllinger et al. (2009b)
11 UMi	74793	K4 III	0.04 ± 0.04	1.80 ± 0.25	11.20 ± 2.47	516.22 ± 3.25	Döllinger et al. (2009a)
HD 32518	24003	K1 III	−0.15 ± 0.04	1.13 ± 0.18	3.04 ± 0.68	157.54 ± 0.38	Döllinger et al. (2009a)
HD 110014	61740	K2 III	0.19 ± 0.05	2.17 ± 0.26	11.09	835.48 ± 6.04	de Medeiros et al. (2009)
HD 119445	66892	G6 III	0.04 ± 0.18	3.9 ± 0.4	37.6 ± 2.6	410.2 ± 0.6	Omiya et al. (2009)
HD 145457	79219	K0 III	−0.14 ± 0.09	1.9 ± 0.3	2.9	176.30 ± 0.39	Sato et al. (2010)
HD 180314	94576	K0 III	0.20 ± 0.09	2.6 ± 0.3	22	396.03 ± 0.62	Sato et al. (2010)
γ Leo	50583	K0 − K4 III	−0.51 ± 0.05	1.23 ± 0.21	8.78 ± 1.0	428.5 ± 1.25	Han et al. (2010)
ν Oph b	88048	K0 III	0.06 ± 0.1	2.72 ± 0.15	22.3	529.9 ± 0.1	Quirrenbach et al. (2011)
ν Oph c	88048	K0 III	0.06 ± 0.1	2.72 ± 0.15	24.5	3184 ± 7	Quirrenbach et al. (2011)
HD 175679	92968	G8 III	−0.14	2.7 ± 0.3	37.3	1366.8 ± 5.7	Wang et al. (2012)
HD 240237	114840	K2 III	−0.26 ± 0.07	1.69 ± 0.42	5.3	745.7 ± 13.8	Gettel et al. (2012b)
BD +48 738		K0 III	−0.20 ± 0.07	0.74 ± 0.39	0.91	392.6 ± 5.5	Gettel et al. (2012b)
HD 96127	54232	K2 III	−0.24 ± 0.10	0.91 ± 0.25	4.0	647.3 ± 16.8	Gettel et al. (2012b)
BD +20 274		K5 III	−0.46 ± 0.07	0.8 ± 0.2	4.2	578.2 ± 5.4	Gettel et al. (2012a)
HD 219415		K0 III	−0.04 ± 0.09	1.0 ± 0.1	1.0	2093.3 ± 32.7	Gettel et al. (2012a)
ϵ CrB	78159	K2 III	−0.32 ±0.001	1.7 ± 0.1	6.7 ± 0.3	417.9 ± 0.5	Lee et al. (2012a)
HD 66141	39311	K2 III	−0.323 ± 0.034	1.1 ± 0.1	6.0 ± 0.3	480.5 ± 0.5	Lee et al. (2012b)
75 Cet	11791	G3 III:	0.00 ± 0.04	2.49	3.0	691.9 ± 3.6	Sato et al. (2012)
o UMa	41704	G4 II−III	−0.09 ± 0.02	3.09 ± 0.07	4.1	1630 ± 35	Sato et al. (2012)
o CrB	75049	K0 III	−0.29 ± 0.03	2.13	1.5	187.83 ± 0.54	Sato et al. (2012)
κ CrB	77655	K0 III−IV	0.10 ± 0.04	1.51 ± 0.19	1.6	1251 ± 15	Sato et al. (2012)
HD 208527	108296	M1 III	−0.09 ± 0.16	1.6 ± 0.4	9.9 ± 1.7	875.5 ± 5.8	Lee et al. (2013)
HD 220074	115218	M2 III	−0.25 ± 0.25	1.2 ± 0.3	11.1 ± 1.8	672.1 ± 3.7	Lee et al. (2013)
BD +15 2940	78407	K0	0.28 ± 0.07	1.1 ± 0.2	1.1	137.48 ± 0.34	Nowak et al. (2013)
HD 233604		K5	−0.36 ± 0.04	1.5 ± 0.3	6.6	192.00 ± 0.22	Nowak et al. (2013)
τ Gem	34693	K2 III	0.14 ± 0.1	2.3 ± 0.3	20.6	305.5 ± 0.1	Mitchell et al. (2013)
91 Aqr	114855	K0 III	−0.03 ± 0.1	1.4 ± 0.1	3.2	181.4 ± 0.1	Mitchell et al. (2013)
HD 112410	63242	G8 III	−0.31 ± 0.09	1.54 ± 0.05	9.18	124.6	Jones et al. (2013)
HD 2952	2611	K0 III	0.00 ± 0.04	2.54	1.6	311.6	Sato et al. (2013)
HD 120084	66903	G7 III	0.09 ± 0.05	2.39	4.5	2082	Sato et al. (2013)
om Ser	77578	G8 III	−0.24 ± 0.02	2.17	1.7	277.02	Sato et al. (2013)

*the planets discussed in this Thesis are not included in the table

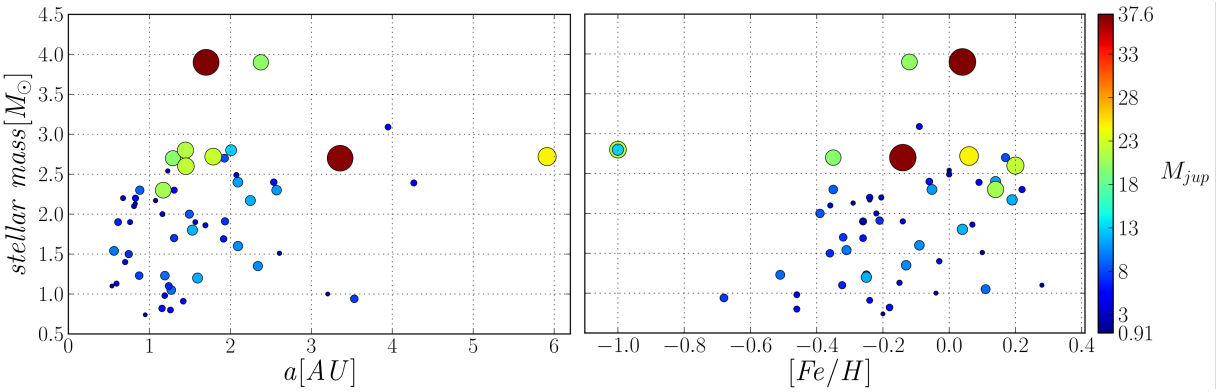

Figure 1.10: The semi-major axis distribution of planets around giant stars as a function of the stellar mass. *Left* shows that most of the planets are usually well-separated from their host. All planets with a different color than blue are basically brown dwarf candidates as their minimum mass is larger than the 13 M_{Jup} limit. Those objects clearly orbit more massive stars showing signs of correlation between the stellar mass and the mass of the companions. The planetary occurrence and the metallicity distribution of the host stars function of their mass (*right*) is still unclear.

Another interesting conclusion from the most recent planetary statistics around giants is that, in general more massive stars tend to have a more massive planets and at a higher frequency. At larger stellar masses ($\sim 2.5 M_\odot$) the companion occurrence is entirely dominated by brown-dwarf objects. Perhaps, these results are natural having in mind that intermediate mass stars have initially more massive disks from which proto-planetary objects can accumulate enough mass to reach brown dwarfs masses. A multiple system of two brown dwarfs is know to orbit the giant ν Oph (Quirrenbach et al. 2011; Sato et al. 2012) in 6:1 MMR (see §6.3). This is very strong evidence that even brown dwarf mass objects can form in a circumstellar disks.

The correlation between the planet occurrence and metallicity is well studied for MS stars (Fischer & Valenti 2005; Udry & Santos 2007; Mordasini et al. 2012). The statistics for MS stars show that the probability for a star to host a planet is increasing with the star's metallicity. A similar trend is observed for subgiants (Johnson et al. 2010), although their planetary occurrence also increases with the stellar mass. Johnson et al. (2010) show that more massive and metal rich stars have a higher probability of hosting a planet.

Fig. 1.10 (*right*) shows that planets around giants are likely to be around stars with lower metallicity than Solar. The results can be also very biased from the large uncertainty, in determining the stellar masses and their metallicity. Thus, large samples of evolved stars must be monitored to give meaningful statistical interpretations. Pasquini et al. (2007) and Takeda et al. (2008) studied such a planet-metallicity correlation for evolved stars, and they did not find evidence supporting metallicity as a factor for planet occurrence. After all, results the from Fig. 1.10 show that intermediate-mass stars with low metallicity have even formed brown dwarfs objects from their massive proto-planetary disks. The main factor defining the planetary occurrence might be the initial mass of the star/proto-planetary disk (Ida & Lin 2005) rather than the chemical abundance. However, metal rich stars must have more dusty disks from which solid cores

form and we should expect a positive planet correlation with metallicity.

Based on our Lick survey we have found that the planet-metallicity correlations agreed with the positive dependency derived for main-sequence stars (Fischer & Valenti 2005; Udry & Santos 2007). We also have found that giant planet occurrence rate and stellar mass are strongly correlated. Results from our survey are submitted for publishing in Reffert et al. (2014) and will be discussed more detailed in Chapter §2 and in the following Chapters in this work.

1.3 Giant stars additional radial velocity variations

In addition to planets, two more phenomena intrinsic to the late type stars might cause radial velocity shift similar to that of substellar companions. Large rotating dark (or light) stellar spots will affect the line shape during the different observational epochs and can be easily confused as a radial velocity shift from planet (§1.3.3). Long term non-radial gravitational $g-$mode pulsations (§1.3.2) can be another source of confusion, when one searches for planets around giants. Finally, a $p-$mode solar-like pulsations in giants usually have periods of several days, and thus are seen as stellar jitter in a regular radial velocity sample (§1.3.1).

1.3.1 Intrinsic stellar scatter (p-mode pulsations)

All evolved stars are intrinsic RV variables at some level. The most prominent RV variable phenomena are the rapid solar-like $p-$mode oscillations. This acoustic or pressure $p-$mode oscillation, is excited by convection pressure fluctuations within the star. The typical periods of these oscillations are on the order of few days. This is usually much more frequent than the typical RV observing sampling, and thus this type of RV variations appear as stellar scatter on the observed RV curve. Such variations have been reported for late G giants (Frandsen et al. 2002; De Ridder et al. 2006; Zechmeister et al. 2008) and K giants (Barban et al. 2004). Our K giant survey (see §2), however, shows that many of these stars have fairly stable radial velocities (Frink et al. 2001; Reffert et al. 2014). In fact, about 2/3 of the stars observed are drawn from a distribution with a mean radial velocity scatter of ≈ 20 m s^{-1}. There is also a correlation with the star's bolometric color, in the sense that redder stars of later spectral class have larger scatter amplitudes (see Fig. 4.2). Typical values for late K giants is up to 50 m s^{-1}, or even more for early M giants. However, this RV bias cannot be confused with a planetary signal, even if the observed amplitudes are very large. G and K giants are very inflated stars and RV periods of few days would simply mean that the proposed planets orbit very close or within the stellar atmosphere, which seems to be not physical.

1.3.2 NON-RADIAL *g*-MODE PULSATIONS

Another powerful source of radial velocity variations might be the non-radial gravity mode ($g-$mode) pulsations. The $g-$mode pulsations in principle can have periods of several hundred days and semi-amplitudes with several hundred m s^{-1}, and can be easily mistaken with planetary Doppler signal.

Oscillation modes are described in terms of three quantum numbers: n – order or overtone, number of radial number, l – degree, number of surface nodes, m – azimuthal order, number of surface nodes running through the pole .

Those types of pulsations can make some of the star's surface to sink towards the star center and other to move towards the observer. The star changes its shape while keeping its volume essentially constant. This kind of non-radial pulsation in principle can cause a sufficient spectral profile changes that might be wrongly interpreted as companion-driven Doppler shift. Depending on which surface area is dominating for a given epoch, one can observe a positive or negative radial velocity shift due to the stellar lines asymmetry (Fig. 1.11).

However, it is not yet known theoretically whether such long period non-radial g-mode pulsations can be excited in G or K giants. The problem comes from the extremely expanded convective zone in this stars. Theoretically, g-mode pulsations in giant stars should be concentrated only in the radiative zone of the star and not in the outer convective envelope. In the convection, zone buoyancy is a destabilizing force, so gravity is unable to act as a restoring force.

Mechanisms that could excite a high-order non-radial pulsation mode should also excite many other similar modes. There is no plausible mechanism that could selectively excite one single mode, and thus mimic a planetary signal (Quirrenbach 2006).

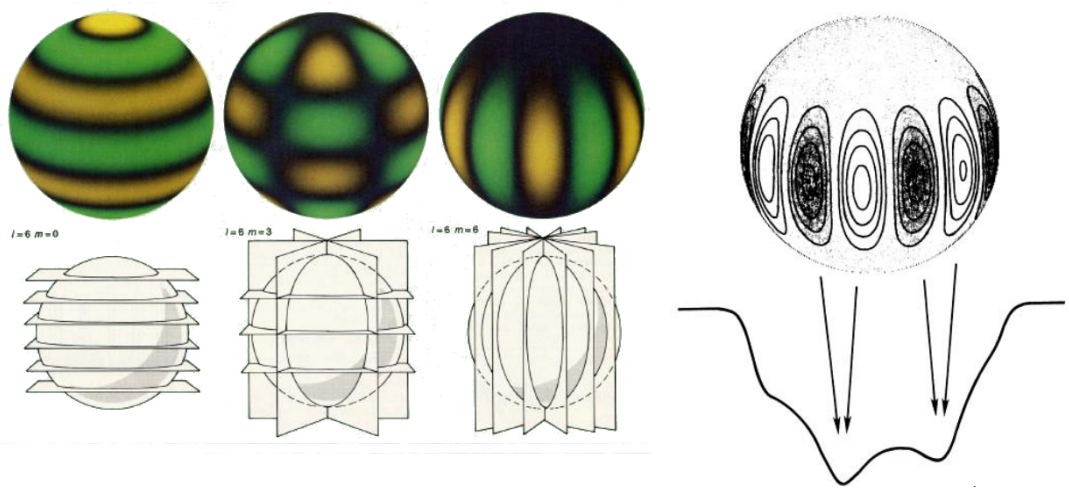

Figure 1.11: Illustration of non-radial modes – l = 6, m = 0; l = 6, m = 3; l = 6, m = 6. If exist, non-radial $g-$mode pulsations in giants can also distort the line profile. Depending on how the modes are aligned towards the observer, the lines profiles can be deformed in such way that can mimic blue or red Doppler shift *Credit*: Artie Hatzes's lecture notes.

Recently, a study of hundreds of relatively nearby red giants from the Kepler mission (Bedding et al. 2011), reveals interesting results. It turns out that evolved giants indeed show signs of $g-$mode pulsations, but with periods of only 50 seconds for hydrogen-shell-burning stars, and between 100 to 300 seconds for helium burning stars – in any case, irrelevant to be mixed up with substellar companions.

It is somehow unlikely that this phenomenon can produce a surface pulsation that might be detectable even if such excitation is possible. Moreover, this kind of pulsation must be related with additional photometric variability, and thus is easy to exclude by this criteria. So far there is no conclusive theory supporting the $g-$mode pulsations as a possible creator of long-term and large amplitude radial velocity.

However, I have to leave this question open, as previously Hekker (2007) showed that K giants that do not have a photometric variations exhibit line bisector variations that in fact can be explained with non-radial pulsations with nodes.

1.3.3 Stellar spots

In the case of a surface stellar spot(s) rotating together with the star, the spectral lines can be distorted. Depending on the position of the spot, while the star is rotating the overall line distortion might lead to either blue or red shift. Due to the finite spectral resolution of our days *state of the art* spectrographs, this distortion cannot be fully resolved, and the change of the line profile can be easily interpreted as radial velocity shift caused by a sub-stellar companion. Spots, however, will also lead to photometric variations with the same rotational period as the star and they can be detected using high precision photometry observations. Another diagnostic tool can be modeling the line bisector shape (Gray 1982), but this diagnostic technique requires very high resolution spectra ($R = 100\,000$), for the line profile to be well modeled. Fig. 1.12 shows the radial velocity variation function of the bisector variations on ξ Bootis A. The model from Toner & Gray (1988) clearly shows that a rotating spot can distort the line profile in such a manner as to cause periodic Doppler drift.

1.4 Confirming the planetary hypothesis

To distinguish the intrinsic to the star radial velocity variability, discussed in §1.3, from those caused by a sub-stellar companions, one needs precise diagnostic tools. In particular, long before the first discoveries of extra solar planets, it had been known that some K giants exhibit radial velocity variations with periods of several hundred days and semi-amplitudes of several hundred $\mathrm{m\,s^{-1}}$, but the interpretation was not clear. Walker et al. (1989) found that RV variations are common among K giant stars and it was thought that it is more likely for the K giants to be a new type of RV variables and thus the planetary hypothesis was dismissed. In our days, astronomers are more convinced of the presence of substellar companions around evolved giant stars giving the large number of discovered planets around main-sequence stars. However, pulsations or rotational modulation of surface features around these objects cannot be excluded (e.g. Hatzes &

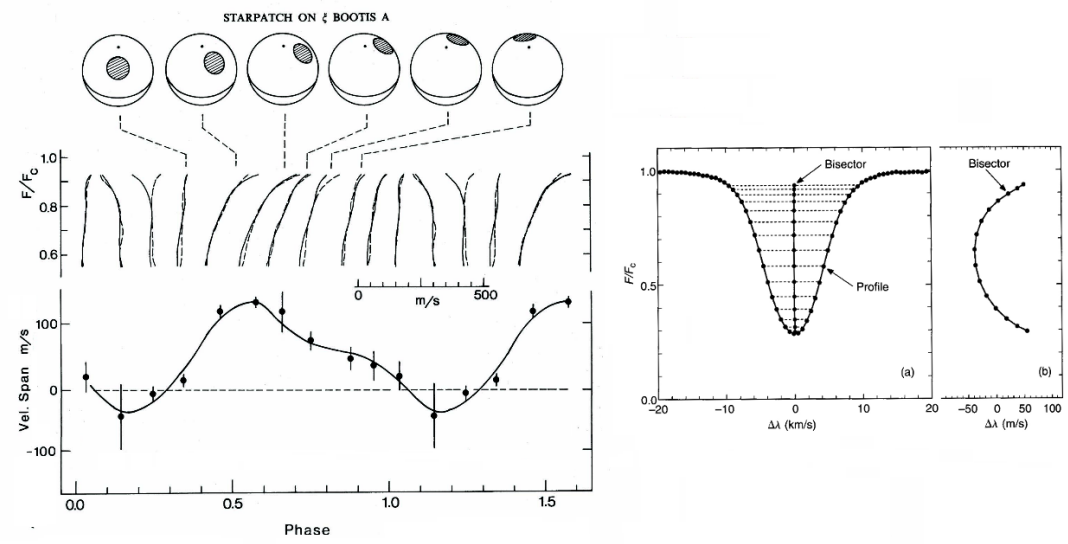

Figure 1.12: Stellar spots cause changes in the line bisectors and hence cause a fake radial velocity periodicity. *Left* panel shows the phase period of a rotating spot on the surface of ξ Bootis A Toner & Gray (1988). Line shape change is expected during the rotation of the spot, and thus cause a periodic RV shift. *Right* panel shows in more details the line bisector, which is line made up from the midpoints on the line profile at different levels. A zoom on the line bisector can reveal the persistence of an asymmetric line profile. *Credit*: Artie Hatzes's lecture notes and ξ Bootis A plot from Toner & Gray (1988), modified by the Author.

Cochran 1999). As discussed in §1.3.3 and §1.3.2 intrinsic features can deform the line profiles, so measuring the spectral line bisectors can be good diagnostic tool. Nevertheless, the absence of any spectral line variations is just a necessary condition, but not sufficient to undoubtedly prove the existence of a sub-stellar companion. Spots, for example, can still mimic as planets without any line bisector variations in the optical (Setiawan et al. 2008; Huélamo et al. 2008). In this work line bisector measurements have not been obtained and will not be discussed in details. Such an extensive analysis over our Lick sample have already been done by Hekker (2007).

In this Thesis I introduce two other independent methods of planetary confirmation. The first tests the optical Doppler data with that from the near-IR regime, searching for consistency between both data sets (§1.4.1). The second is the dynamical stability and only concerns planetary systems with more than one companion (§1.4.2).

1.4.1 RADIAL VELOCITY TEST IN THE NEAR INFRARED

Using the Doppler technique a planet orbiting a star should be detectable with a very similar RV amplitude and orbital period at all wavelength ranges. If a cold spot is responsible for the RV pattern observed in the optical, the obtained near-IR radial velocities are expected to be of smaller amplitude. Fig. 1.13 explains this effect by illustrating the intensity of black bodies with T_{eff} = 4500 K and 3800 K. The hotter one represents the stellar disk temperature of a K giant

and the cooler one the intensity of a surface spot. The contract between the two in the optical is obviously much larger than this in the $H-$band. In case of spots the line deformation will be much lower in the near-IR, and thus we could expect lower or almost flat RV amplitude in the $H-$band (Huélamo et al. 2008; Bean et al. 2010). Similarly, one would expect non-radial $g-$mode pulsations to result in a different velocity amplitude at visible and infrared wavelengths (Percy et al. 2001).

An upcoming survey of M dwarfs simultaneously using an optical and near-IR high-resolution échelle spectrographs ($R \sim 80\,000$) is planned under the CARMENES project[6], at the 3.5-m telescope on Calar Alto, Spain. The aim of this project is to detect low-mass planets in their habitable zones, around low mass stars later than M4-M5 with mass $M < 0.2\ M_{\odot}$ with precision of $\sim 1\ \mathrm{m\,s^{-1}}$. Observing at the same time in the optical and in the near-IR will reveal the true nature of the radial velocity periodicities, and will provide an important statistics on the planetary distribution around M dwarfs.

An infrared test in combination with the line bisector variations and precision photometry (if such are available) can effectively prove or exclude the sub-stellar nature of the velocity signal.

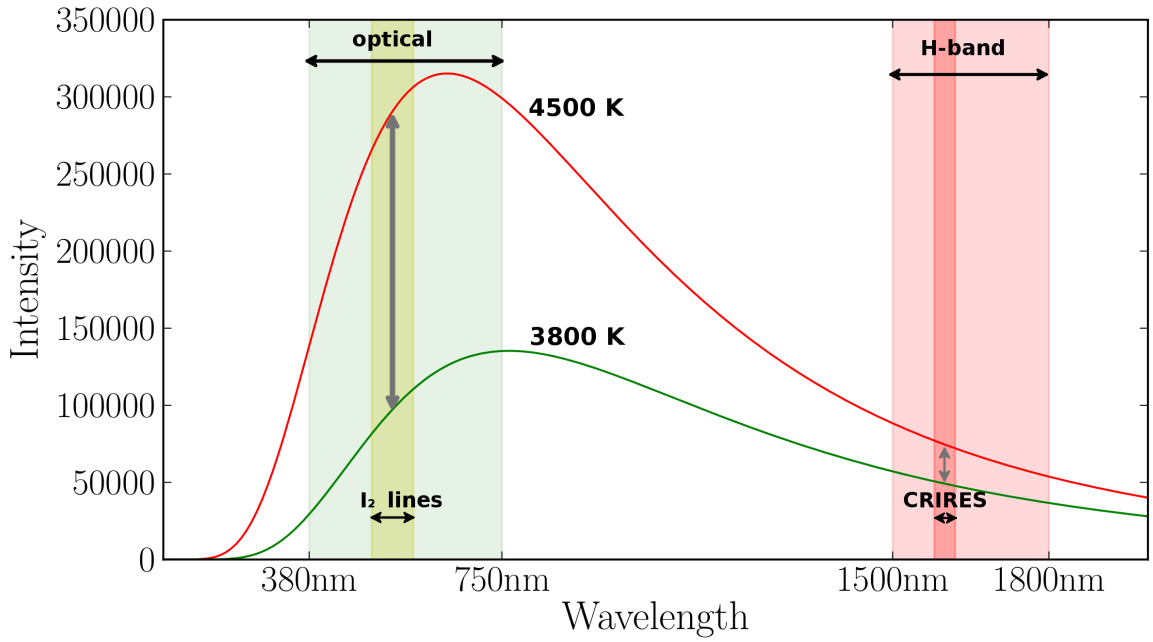

Figure 1.13: Intensity of black bodies with T_{eff} = 4500 K and 3800 K. The contrast between the two is much larger in the optical than in the $H-$band. Thus, in case of intrinsic to the star radial velocity variations, the overall line deformation will be more noticeable in the optical. Comparing optical and near-infrared Doppler velocities can be the key test for the planetary hypothesis.

[6]Calar Alto high-Resolution search for M dwarfs with Exo-earths with Near- infrared and optical Echelle Spectrographs (Quirrenbach et al. 2013)

1.4.2 STABILITY ANALYSIS

In the most trivial case when only one planet is orbiting a star, the system should be long term stable in any kind of orbital configuration. However, adding a third body in the system, makes the picture much more complicated. Then, due to the planetary gravitational interactions, the system's evolution gets extremely complex to be solved analytically even in this low order hierarchical case. In order just to see whether a three body system can be initially stable one can use the Hill stability approximation given in Gladman (1993) :

$$\Delta = (a_2 - a_1)/a_1 > 2\sqrt[6]{3}(\mu_1 + \mu_2)^{1/3} \approx 2.4(\mu_1 + \mu_2)^{1/3} \tag{1.6}$$

where μ_1 and μ_2 are the ratios of the planetary masses with respect to the mass of the central star, and a_1 and a_2 the orbital radii, which means that two initially co-planar planets cannot have an orbital separation less than Δ (they cannot enter each others Hill spheres), otherwise close approaches might disrupt the system.

The Hill criteria can give an initial guess of the systems stability, but cannot give any detailed information on the orbital evolution. To solve this problem very sophisticated N-body dynamical simulators like, SWIFT (Duncan et al. 1998) or MERCURY (Chambers 1999) must be used. Those packages are developed to calculate the orbital evolution of the Solar system, but can be effectively used for extrasolar planetary systems.

Although when the radial velocity signal is consistent with one planet there is no need for a stability test when the radial velocity data shows signs of more than one companion it is more or less obligatory to be performed. Even if the derived orbits are well separated and *Hill stable*, the system can be still unstable if the planetary eccentricities are higher and long term orbital evolution can be a very important diagnostic tool. This is valid especially when the derived orbits are close enough to perturb each other significantly.

The dynamical test, however, often must be detailed and complete testing of various configurations must be done. In some cases, the uncertainties of the orbital parameters passed to the integrator might prevent clear statements on the dynamical state of a given system. The best fit solution might turn out to be unstable, but in the order of orbital uncertainties a stable solution(s) might exist.

There are many of such examples in the literature, where the nominal best-fit Keplerian orbits represent an unstable system, which should self-destruct quickly, but a small adjustment of the orbital parameters lead to a stable system.

Long Doppler surveys can observe a given planetary system for many periods. In case the planetary system is consistent with multiple companions the mutual gravitational interactions between the bodies are expected to significantly influence their orbital configuration and the resulted RV curve. This is especially valid for resonant and/or dense planetary systems, where the gravitational perturbations are strong. Therefore, it is very important to perform a self-consistent dynamical analysis for the RV data. In these systems the obtained dynamical fit must reproduce the RV signal much better than a simple multiple Keplerian model, which simply adds the projected signatures of single planets and ignores planet-planet interactions.

1.4.3 Stability analysis strategy in this work

In this Thesis for all the fitting needs, I have used the freely-available *Systemic Console* package (Meschiari et al. 2009). This software combines all the useful routines needed for the characterization of planetary systems. Fitting the RV data with the *Console* is relatively easy and is done by adopting either a Keplerian model (used in this work only for data consistent with one substellar companion) or more sophisticated Newtonian dynamical fits, such as the Gragg-Bulirsch-Stoer integration method (B-SM: Press et al. 1992) used in this work for fitting RV curves consistent with multiple planetary systems. *SYSTEMIC* uses parameter minimization of the reduced chi-square statistic:

$$\chi^2_{red} = \frac{1}{\nu} \sum_{i=1}^{N_i} \frac{(O_i - C_i)^2}{\sigma^2_{RV_i}} \tag{1.7}$$

where ν represents the degree of freedom (DOF) left in the fitting algorithm as the difference between the numbers of the observational points and the number of the fitted parameters in the model ($N_{rv} - M_{fit}$). The observed radial velocity in each epoch is O_i, and $C_i = f(M_{fit})$ is the calculated radial velocity from the model for the same epoch as the observed. The variance of the formal observational error is $\sigma^2_{RV_i}$.

The preliminary test to the optical data is always done with the inbuilt Lomb-Scargle Periodogram routine, in order to see whether a significant planetary periods from the data can be identified. After fitting, a Levenberg-Marquardt local minimization algorithm (LM: Press et al. 1992) is available to polish the model parameter space by minimizing the derived χ^2_{red} fit. In more complicated multi-planet radial velocity signals the *global minimization* Simulated annealing method (SA: Press et al. 1992) can be used to find whether there is more than one local minimum.

When fitting the RV data, there are $5n + 1$ Keplerian parameters to be fit, where n is the number of planets, the period of the planet's orbit P, the semi-amplitude of the RV signal K, the eccentricity of the orbit e, the longitude of periastron ϖ, the date of periastron passage t_p, and the additional fitting parameter is the RV data offset from the RV zero point. *Systemic Console* can also fit non-coplanar systems by allowing the inclinations and the longitudes of the ascending nodes of the planets to be $i \neq 90°$ and $\Omega \neq 0°$. Finally, this software can also provide the user with Bootstrap and Markov Chain Monte Carlo test needed for estimating the uncertainty of fitted parameters.

In case the obtained dynamical fit is consistent with a multiple planetary system, only the automatically converted Jacobi coordinates from the *Console* are taken. Those are: mean anomaly M, semi-major axis a, eccentricity e, argument of periastron ω, orbital inclination i, longitude of the ascending node Ω, and absolute planetary mass m_2.

For testing the stability of planetary systems I have used the *Mercury* N-body simulator. All dynamical simulations in the Thesis have been tested with the inbuilt *hybrid sympletic/Bulirsch–Stoer* algorithm, which computes close encounters between the planets by reducing the integra-

tion time step automatically. The starting epoch is always taken to be the first date of the observation and for which the obtained Jacobi coordinates are valid. The typical integration time is between 10^5 and 10^7 years depending on the selected system. In some exceptions the integration test have been extended even for 2 x 10^8 years (see §4). The time step used for the integrations has been set to be 8 days, however when more accurate integrations are required the time step was reduced to 0.5 days. Collisions and ejections are allowed during the simulations. The stability criteria on which one fit is considered as stable depends mostly on the architecture of the studied planetary system, but in general is as follows:

Unstable systems are considered if collisions or ejections occur during the dynamical evolution test. I define a system to be stable if none of the planets in the system are ejected or experienced a collision and the planetary semi-major axes remain within 0.2 AU from the initial semi-major axes values (for some systems the limit is 0.4 AU) at the beginning of the simulation during the maximum integration time. However, if the system survives without ejections or collisions, but the planetary semi-major axes are showing multiple scattering to a different semi-major levels, I have classified them as *chaotic*, even though they may not satisfy the technical definition of chaos. This stability criterion can give fast and accurate estimate of the dynamical behavior of the studied system, and distinguishes the stable from the chaotic and the unstable configurations.

In order to examine the statistical and dynamical properties of orbital parameter space around the best fit, I have developed a *Java* based script that is performing a detailed systematic grid search using the *Console*. Depending on the studied planetary system, two of the orbital parameters are manipulated from the script, while the remaining orbital parameters in the model are fitted until the best possible dynamical χ^2_{red}fit to the data is achieved. The result is a 2D grid of dynamical grids that reveals the statistical properties around the best possible solution.

Next step is all these orbital fit solutions to be checked for long term stability. For my research needs, I have developed a *Python* based code that runs *Mercury* multiple times on a standard PC. Thus, all the obtained 2D grids of dynamical fits are transformed into an effective stability maps. The 2D grids give important statistical information around the possible parameters space of orbital elements, while from the long-term integrations I could judge for most possible planetary configurations based on stability constrains.

CHAPTER 2

LICK G AND K GIANTS SURVEY

Based on

"Precise Radial Velocities of Giant Stars
VI. Occurrence Rate of Giant Extrasolar Planets as a Function of Mass and Metallicity"

S. Reffert[1], Christoph Bergmann[1,2], A. Quirrenbach[1], **T. Trifonov**[1], and Andreas Künstler[1,3]

subbmited to A&A

[1]ZAH-Landessternwarte, Königstuhl 12, 69117 Heidelberg, Germany
[2]University of Canterbury, Dept. of Physics and Astronomy, Christchurch 8041, New Zealand
[3]Leibniz-Institut für Astrophysik Potsdam, An der Sternwarte 16, 14482 Potsdam, Germany

2.1 Introduction

We have started our K giants program in 1999. Observations are taken using the the 0.6 m Coudé Auxiliary Telescope (CAT) in conjunction with the Hamilton High Resolution Spectrograph at Lick Observatory and the Iodine cell method (Vogt 1987; Marcy & Butler 1992; Valenti et al. 1995). Initially the focus of the program was finding stable astrometric reference stars for the Space Interferometry Mission (SIM). In order to perform high precision astrometric observations with SIM, very stable reference stars were needed. K giants had been proposed to be ideal for this purpose. Those objects are very luminous and appear bright even at large distances.

By characterizing the level of intrinsic radial velocity jitter, our goal was to identify unwanted binary stars among a large sample of K giants distant approximately at 2 k pc. The precise RV measurements obtained at Lick on the order of 3–5 m s^{-1} (see Butler et al. 1996) and the low amplitude of stellar jitter that large fraction of the K giants exhibit allow us to effectively identify not only binaries from our sample, but also to detect planetary companions. At the time when this survey started, most known extrasolar planets were discovered around main sequence stars using the Doppler technique. K giants also appeared to be very good targets for planet hunting. They are bright and have numerous deep and sharp spectral lines due to their slow rotation. However, because of their evolutionary status and the fact that it was believed that K giants are sort of RV variable (Walker et al. 1989) it was not clear whether those objects could harbor planetary

companions or not.

Not long after the start of our program the first planet orbiting a giant star was discovered around ι Dra (Frink et al. 2002). Thus, our focus shifted to monitoring precise radial velocities of K giants in order to identify more substellar companions, and to obtain the planetary occurrence statistics for these objects.

2.2 STAR SELECTION

The selection criteria for the stars is described in details by Frink et al. (2001). The initial sample was consistent with only 86 K giant selected from the Hipparcos catalog, with the strict condition to be brighter than 6-th magnitude in V and to have declinations between $-30°$ and $+68°$. Another condition for the selected stars was they to be neither variable nor binaries. In 2000 the sample was enlarged by another 96 K giants, by relaxing some of the very strict initial selection criteria (e.g. the requirements on photometric). In 2004, we added another 194 stars, this time with with slightly different selection criteria. Earlier investigations on the intrinsic stellar RV jitter in Frink et al. (2001), showed that bluer stars have in general lower levels of intrinsic scatter. Thus, we selected mostly late G and early K giants, with $B - V$ colors between 0.8 and 1.2 mag. The stars have also been chosen to be more massive than the stars from the first 2 sub-samples. By selecting more massive stars, our goal was to see whether or not more massive stars also host planets and if they do, we would be able to study the planet occurrence and properties as a function of stellar mass.

The stellar masses have been determined using a trilinear interpolation between evolutionary tracks and isochrones (Girardi et al. 2000), respectively, and metallicity as a third parameter (Künstler 2008). Because the location of evolutionary tracks and isochrones depends on the assumed metallicity, taking into account the metallicities is crucial. Most of the metallicities were derived from the equivalent widths of iron lines by Hekker & Meléndez (2007). We performed the interpolation for separate stages of the evolutionary tracks and isochrones in order to determine the probabilities for the stars to be on the red giant branch (RGB) or on the horizontal branch (HB), respectively. For each star we generated 10 000 positions within the three-dimensional space ($B - V$, M_V, [Fe/H]), using the measured color, absolute magnitude and metallicity taking Gaussian errors into account. For each of these generated positions we determined the stellar parameters from evolutionary tracks by interpolation. We estimated probabilities of a star being either on the RGB or on the HB and we simply use the mass which has the higher probability (see Reffert et al. 2014).

At some point, three stars from the sample were excluded, as they turned out to be visual binaries. The total number of stars we monitored regularly at Lick was 373 G and K giant stars.

2.3 Observations

We used the CAT between six and eight nights per month, between 1999 and 2012. The Hamilton spectra have a high resolution of approximately $R = 60\ 000$ between 5000 and 5800 Å, the wavelength range of the iodine lines which is used for the derivation of the radial velocities. The typical S/N is of the order of 80−100, reaching radial velocity precision of $\sigma_{RV} \approx 5\ \mathrm{m\,s^{-1}}$. This error is much lower that the typical stellar RV jitter in terms of velocities. The exposure needed for such S/N depends on the magnitude of the observed star. Usually, for a 3th [mag] star the exposure time is about 5 minutes and between 25−30 minutes for a 6th [mag] star.

Each star in our sample had been observed at least once per observing season, but stars which exhibit periodic or systematic RV patterns or are classified as potential planetary hosts have been observed more often. In total, we have typically around 30 observations for the stars in the initial sample, and more than 100 observations for the stars observed more often. For the stars added after 2004, we have obtained ∼ 20 observations.

2.4 Substellar Companion Statistics

As discussed in §1.3 giant stars have larger stellar jitter than MS stars, and the planetary interpretation of the RV signal can be sometimes difficult. The expected stellar jitter of our late G and early K giants is less than $\sim 20\ \mathrm{m\,s^{-1}}$, the jitter for late K giants (with $B - V$ around 1.6) can be up to $100\ \mathrm{m\,s^{-1}}$ and more. Hence, a smaller mass or longer period planets, which would have smaller RV semi-amplitudes, cannot be identified as easily as those around MS stars.

Observations with long baselines covering at least a few periods are needed to ensure that the phase and amplitude of the observed RV signal are constant over time. Also, longer observations can compensate the stellar jitter and reveal planetary companions. For these reasons we have split our planetary detections into two categories: planets and planet candidates. Planets we define as those which we consider secure detections with no doubts about the planetary nature of the Doppler signal, and planet candidates, whose existence is more doubtful. The secure planets have a clear and convincing periodic RV signal, and have been observed over several cycles. On the other hand, the planet candidates also exhibit periodic RV signals, but the ratio between RV semi-amplitude and stellar jitter is smaller than for the secure planets. The candidate planets can be non-radial pulsations and if they are indeed such, many observations over a long time baseline are needed in order to test for phase and amplitude stability of the RV signal. One way to distinguish between pulsations and spots from one side and an orbiting substellar or planetary companion from the other is the comparison of the RV signal obtained in the optical and another one from the near-IR. In the near-IR the pulsation driven stellar line distortion must be lower, and thus the near-IR RV signal must have lower amplitude (see §1.4). Thus, we have also started observing 20 K giants with periodic RVs from our science sample with the high resolution near-IR spectrograph CRIRES at VLT (see §3).

In our Lick sample, we have secure planets around 15 stars, while two of them have an additional secure planet and two have an additional candidate planet. The candidate planets in

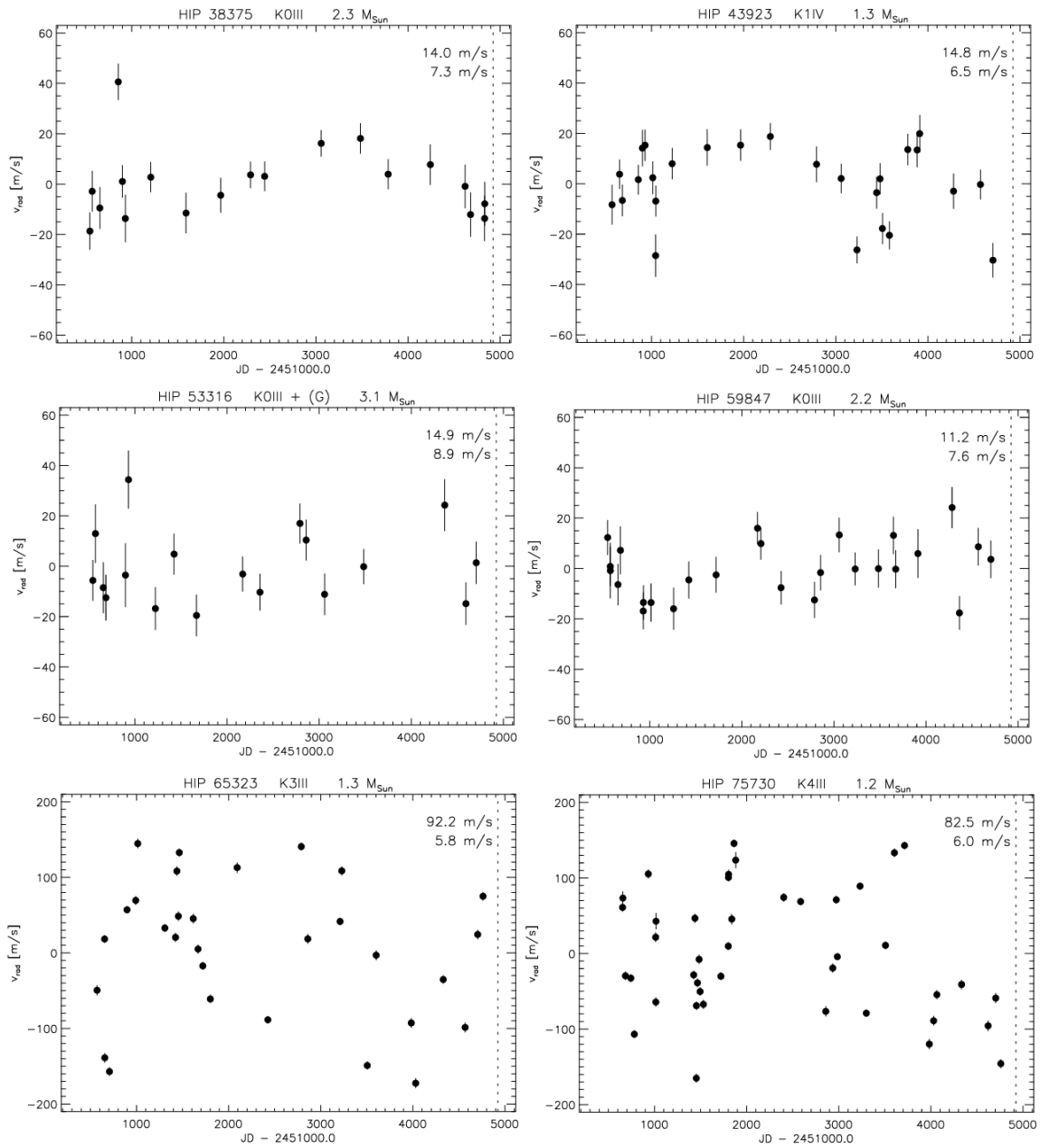

Figure 2.1: K giants without planets from the Lick survey. The top four are RV quiet early K giants. Their radial velocity jitter is on the order of 10–20 m s^{-1}. The bottom two represent a later spectral class that obviously have larger stellar jitter that is not associated with substellar companion.

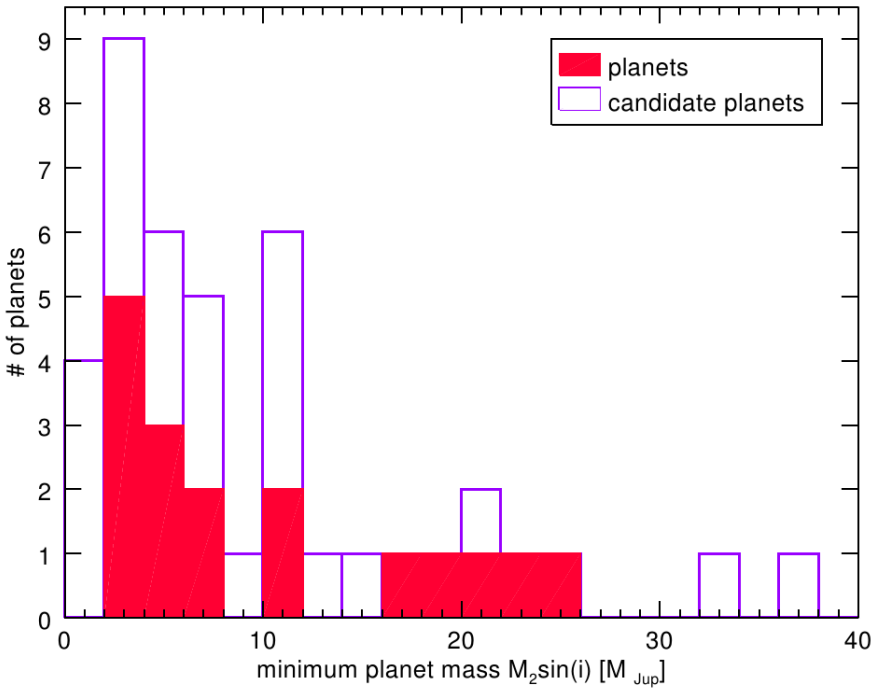

Figure 2.2: Histogram of minimum masses derived for 17 secure and 26 candidates planets in our Lick sample. Two of the 26 candidate planets have minimum masses larger than 40 $M_{\rm Jup}$ and are not shown in the plot. *Credit*: Reffert et al. (2014)

our sample are around 20 stars. Four of these have an additional candidate planet and two of these stars display a notable linear trend on top of the candidate planet RV periodicity. Such a trend could be caused by substellar object in very long orbits. In addition, two secure planets and another four candidate planets have been founded in spectroscopic binaries. Overall, we have up to 43 candidate planets orbiting around 35 extrasolar planetary systems. A histogram of minimum planet masses is shown in Fig. 2.2. The smallest minimum mass of a secure planet is 2.3 $M_{\rm Jup}$, while the smallest minimum mass of a planet candidate is 1.1 $M_{\rm Jup}$. The largest minimum mass among the secure planets is 25 $M_{\rm Jup}$, over the brown dwarf limit, while we have found candidate planets that could have masses even more massive than brown dwarfs. However, this is still rather uncertain because some have long period orbits which still did not finish a full period on out RV data.

Eight of the 15 systems with a secure planet in our Lick sample have been published already: ι Dra b (Frink et al. 2002), Pollux b (Reffert et al. 2006; Hatzes et al. 2006), ε Tau b (Sato et al. 2007), 11 Com b (Liu et al. 2008), ν Oph b and c (Quirrenbach et al. 2011; Sato et al. 2013), τ Gem b and 91 Aqr b (Mitchell et al. 2013) and η Cet b and c (Trifonov et al. 2014). These planetary systems are discussed in detail in §5, §6 and §7.

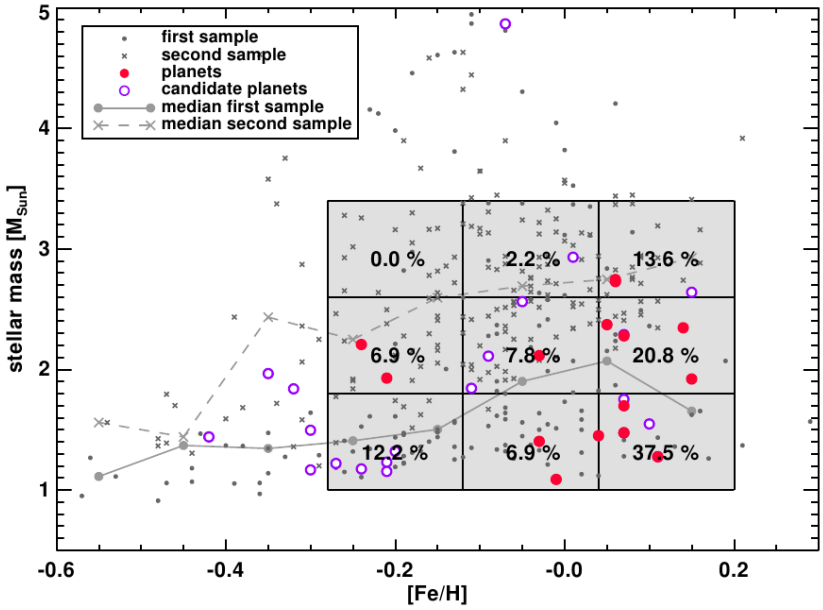

Figure 2.3: Planet occurrence rate as a function of metallicity and stellar mass in our Lick sample. The percentage numbers give the fraction of the number of stars with a planet and/or planet candidate of all stars in that bin. One can clearly see that the planet occurrence rate in our Lick sample increases strongly with stellar metallicity and decreases with stellar mass. *Credit*: Reffert et al. (2014).

2.5 LICK PLANET OCCURRENCE RATE VS. STELLAR METALLICITY

The planetary occurrence versus the stellar metallicity correlation in our K giants sample is very similar to that observed for MS stars by Fischer & Valenti (2005) and Udry & Santos (2007). However, our results do not agree with the results of Pasquini et al. (2007) and Takeda et al. (2008), who did not find any dependence of the planet occurrence rate with metallicity in their giant star samples. This consistency might come from their less-strict selection criteria for confirmed planets compared to ours. For the planet-metallicity dependence from our survey, we have used only secure planets, which is essential. The secure planets and the planetary candidates show a different distribution versus to metallicity, thus we believe that our sample of candidate planets is actually a mixture of stars with true planets and stars without any planets (or at least there is no evidence for such).

Maldonado et al. (2013) also have noted a difference in planet occurrence rate versus the stellar metallicity between low-mass and high-mass giant stars. By dividing our sample of secure and candidate planetary hosts at a stellar mass of 1.5 $M_{\odot}$ as is done in Maldonado et al. (2013), we also do not observe a strong planet-metallicity correlation for the lower mass sample, but we find a strong planet-metallicity correlation for the higher mass sample (see Fig. 2.3). The possible reason for this is that the candidate planets have been found at lower metallicity and also at lower mass and thus pollute the strong planet-metallicity correlation of the secure planets. The different findings for lower and higher mass giant stars could thus simply be a consequence

of a polluted sample of planet hosts with non-planet bearing stars. We conclude that there are strong indications for a planet-metallicity correlation among giant stars planetary hosts, which is in agreement with observed planet-metallicity dependence for MS planet hosts.

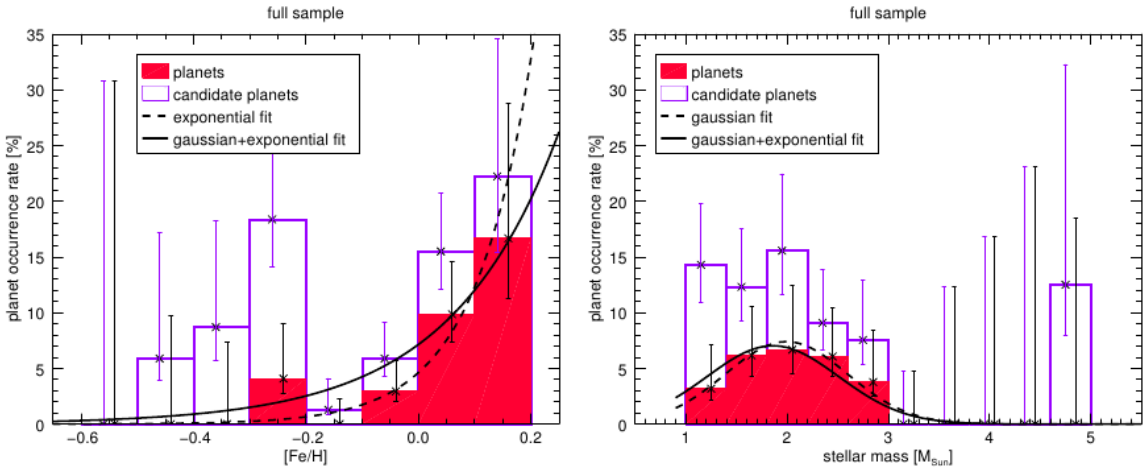

Figure 2.4: Planet metallicity correlation observed in our Lick sample, ignoring the effect of stellar mass on the planet occurrence rate. The filled histogram shows secure planets, whereas the open histogram includes candidate planets as well. Error bars are computed based on binomial statistics as explained in the text. The dashed line denotes an exponential fit to the planet occurrence rate of secure planets as a function of metallicity. The solid line in contrast shows the dependence of our fitted planet occurrence rate as a function of metallicity and stellar mass on metallicity only; a scaling factor was adjusted to compensate for the stellar mass distribution. The planet metallicity correlation is steeper if stellar mass is not accounted for. *Credit*: Reffert et al. (2014).

2.6 Lick Planet Occurrence Rate vs. Stellar Mass

Based on our statistical analysis, we have found that giant planet occurrence is clearly declining for stars with masses larger than 2.5 to 3 $M_{\odot}$. We do not find any secure planets around a stars with a mass larger than 2.7 $M_{\odot}$, although there are 113 such objects in the sample.

In contrast to most of the Doppler surveys around late-type MS stars, whose main targets are stars with masses 0.7 and 1.5 $M_{\odot}$ (Fischer & Valenti 2005; Udry & Santos 2007), in our sample we have large amount of stars with masses between 2 and 5 $M_{\odot}$. Thus, we lead the first survey that can extract any planetary occurrence statistics around more massive stars.

In our Lick K giant survey the stars with masses of about 2 $M_{\odot}$ are those with the highest planet occurrence rate and are significantly higher than those for stars of about 1 $M_{\odot}$. Similary for sub-giants Johnson et al. (2010) found that planet occurrence rate increases with mass up to masses of about 2 $M_{\odot}$.

Burkert & Ida (2007) have also reported a lack of Jovian mass planets at intermediate orbital distances for MS stars with masses between 1.2 and 1.5 $M_{\odot}$. This results are different compared

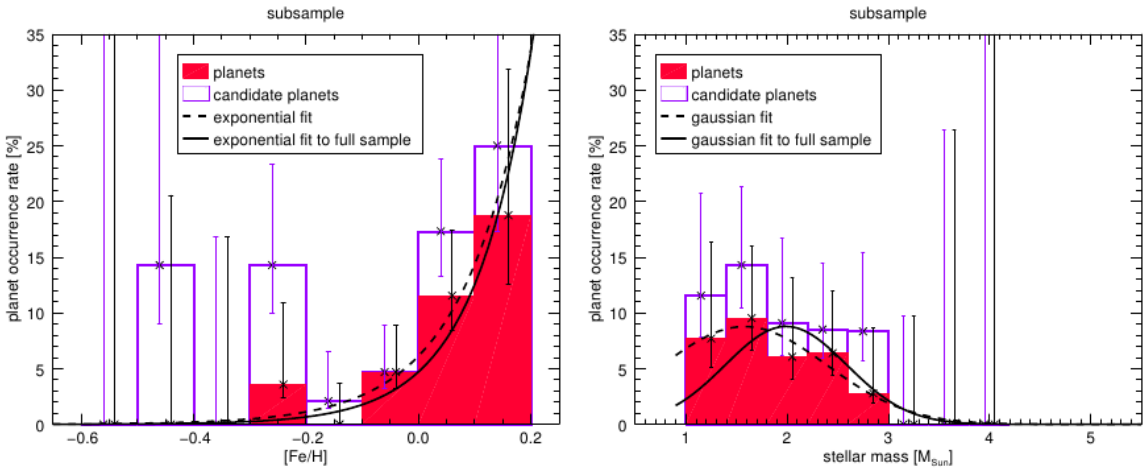

Figure 2.5: Planet occurrence rate as a function of metallicity for a subsample of the full Lick sample with uniform planet detectability, as described in the text. The dashed line denotes an exponential fit to the metallicity dependence of the planet occurrence rate of the subsample, whereas the solid line denotes the same kind of fit for the full sample. Any small differences are not significant. *Credit*: Reffert et al. (2014).

to the planets found around stars in the mass range from about 0.7−1.2 $M_{\odot}$. These differences in planet occurrence statistics at smaller masses might be an indication that the planetary formation and evolution is affected by the initial stellar mass.

To explain the observed differences in the planet properties, Burkert & Ida (2007), attributed a shorter disk depletion timescale to the stars with higher mass, compared to those around lower mass stars. By using slightly different giant planet formation models, Ida & Lin (2005) and Kennedy & Kenyon (2008b) both have predicted an increase in the giant planet formation rate with the stellar mass over a range of about 0.5 to 3.0 $M_{\odot}$. However, after a well defined maximum of the planetary occurrence in these models, the giant planet formation rate decreases strongly for higher stellar mass in both models. The results we have obtained for the planetary occurrence at higher mass agreed with the results in the mass range predicted by those two models. More massive stars will result in larger disk masses from which planets can form and thus might explain the increased planet occurrence rate with stellar mass. Hence, Neptune mass planets are found to be frequent around lower mass stars according to the observations, and to the models. However, giant planets do not form often around lower-mass stars according to Johnson et al. (2007).

The conclusion based on observations and theory is that higher disk masses increase the chance of forming a giant planets (and planets in general), so the planetary occurrence rate must correlate with stellar mass. Nevertheless, the positive correlation when assuming stellar masses of 2.5−3 $M_{\odot}$ the planetary occurrence breaks. This might be explained with the following scenario: The snow line, beyond which most giant planets are believed to form, must be located further out for stars with higher masses. This is a particular problem for the planetary formation due to smaller gas densities and Kepler velocities, which both slow down growth rates. Thus, the migration time scale (τ_{mig}) is also longer ($\tau_{mig} \propto M^{1.5}$, Kennedy & Kenyon (2008a)), while stellar disk dispersal is faster (Kennedy & Kenyon 2009). The slower growth rate, together with

the increased migration time scale and short lifetime of the protostellar disk might prevent stars with masses larger than 2.5−3 $M_{\odot}$ to form giant planets. This might be one good explanation on the observable semi-major axes of a few AU around late intermediate stars probed by our survey.

2.7 Summary and results from the Lick survey

After we have analyzed the planetary distribution over the 373 G and K giants from our Lick sample with respect to metallicity and stellar mass. In overall, during the thirteen years of observations at Lick we have found a 15 stars with secure planets and 20 stars with candidate planets. The secure companions are all giant planets with minimum masses in the range between 2.3 to 25 $M_{\rm Jup}$, which is in the brown dwarf regime.

We do not find a clear correlation between the candidate planets in our sample and the metallicity abundance of their potential host stars. We assume that some of these candidates may not be real, despite the observed RV periodicities. However, we have found a strong planet-metallicity correlation for the planets in our Lick sample that we treat as secure. Our results matches the planet-metallicity correlations from Fischer & Valenti (2005); Udry & Santos (2007) obtained for MS stars.

We have found that giant planet occurrence rate and stellar mass are strongly correlated. We estimated that the planet occurrence rate is highest for stars with mass of $M = 1.86 \pm 0.04$ $M_{\odot}$, and is decreasing very fast assuming larger masses of $M > 2.5$−3.0 $M_{\odot}$. The σ width of the Gaussian distribution has been estimated to be 0.65 ± 0.05 $M_{\odot}$, while the companion occurrence rate in the stellar mass interval from 2.7 to 5.0 $M_{\odot}$ is $< 1.6\%$ with 68.3% confidence. These results are in agreement with the planet formations models of Ida & Lin (2005) and Kennedy & Kenyon (2008a), which predict a strong decrease in the planetary rates for stellar masses above roughly 1.5 to 3 $M_{\odot}$. This dependence might be explained by a smaller growth rate, longer migration timescale and the shorter lifetime of the protostellar disk for the more massive stars compared to the less massive ones. The luck of giant planets for stars with $M > 2.5$−3 $M_{\odot}$ is most likely not connected to the stellar evolution and more likely they just do not form at least within a few AU, so they can be detected based on the time span of a Doppler program.

CHAPTER 3

RADIAL VELOCITIES IN THE NEAR INFRARED WITH CRIRES

Based on

"Precise Radial Velocities of Giant Stars

VIII. Testing the planetary hypothesis around giant stars with CRIRES"

T. Trifonov[1], S. Reffert[1], M. Zechmeister[2], A. Reiners[2] and A. Quirrenbach[1]

in preparation to A&A

[1]ZAH-Landessternwarte, Königstuhl 12, 69117 Heidelberg, Germany
[2]Institut für Astrophysik, Georg-August-Universität, Friedrich-Hund-Platz 1, 37077 Göttingen, Germany

3.1 Introduction

By December 2013, the number of confirmed substellar companions discovered with the Doppler technique has reached 431[1]. This number constitutes ~ 60% of the total number of planets discovered using all planet search methods and shows that the precise radial velocity method still remains the most powerful extrasolar planet search tool to date.

The revolutionary concept of the ultra stable Èchelle spectrographs, such as HARPS (Mayor et al. 2003) already broke the sub-m s^{-1} technological (and psychological) barrier of accuracy and potentially allows astronomers to search for Earth mass planets. The Doppler technique, however, can suffer from false positive detections due to the radial velocity variations intrinsic to each star. In addition to the short period $p-$mode pulsations, which are excited by convection and seen as stellar RV scatter, surface stellar spots or even non-radial gravitational $g-$mode pulsations can potentially cause line shape deformations that can wrongly be interpreted as velocity shift during data reduction. These intrinsic phenomena can have long periods and semi-amplitudes of several hundred m s^{-1} that can effectively mimic a planet (e.g. Hatzes & Cochran 1999).

[1]http://exoplanets.org

Detailed studies of spectral line profile bisectors have often been used to support the companion hypothesis. However, this method requires a very high resolution spectra, and the absence of spectral line variations is just a necessary condition, but not sufficient to definitively prove the existence of a substellar companion.

Searching for radial signals in the near infrared (near-IR) is another promising test that can be performed. The contrast ratio between the star's surface blackbody intensity and that of a cooler spot is much larger at optical than in the IR domain. In case of spots, the line shape deformations in the IR data must produced be with much lower amplitude. We can also expect different RV amplitudes and periods in the two domains, in case of non-radial $g-$mode pulsations, while this metod this test yields no difference in the obtained velocities in case of a planet.

For example, the young star TW Hya, which did not show any line bisector variations in the optical, led Setiawan et al. (2008) to conclude that a substellar companion was the reason for the observed RV periodicity. Later, Huélamo et al. (2008) showed that a cold spot was responsible for the RV pattern observed in the optical, which was not reproduced in the infrared.

An alternative high precision radial velocities derived from the infrared wavelength regime can be a rather critical test for planet confirmation. This test is valid mostly for active stars, for which other viable explanations for periodic radial velocities such as spots or pulsations cannot be excluded by any other means. Such a test is urgently needed for K giants, in particular, but has not been carried out yet.

Perhaps the best choice for this test is the ESO pre-dispersed CRyogenic InfraRed Echelle Spectrograph (CRIRES), mounted at the Nasmyth focus B of the 8m VLT UT1 (Kaeufl et al. 2004). CRIRES has a resolving power of $R \approx 100\,000$ when used with a 0.2" slit and covers the J, H, K, L and M near-infrared bands. Several studies have demonstrated that accurate radial velocity measurements between $10 - 35$ m s^{-1} are possible with CRIRES. Using CRIRES, Seifahrt & Käufl (2008a) reached a precision of ≈ 35 m s^{-1}, when using N_2O gas cell for calibration. Also, Huélamo et al. (2008) and Figueira et al. (2010) showed that the achieved Doppler precision can be even ≈ 10 m s^{-1}, when using telluric CO_2 lines in the $H-$band as reference spectra.

In this paper, we describe our observational program with CRIRES in detail, and reveal our precise IR velocity derivation methods. In section §3.2 we briefly introduce our philosophy behind this program. Section §3.3 describes our observational setup with CRIRES. In §3.4 we will explain the data reduction process and analysis with our CRIRES pipeline in great detail. Our methods of extracting the precise RVs will be given in §3.5 and in §3.6 we will discuss obtained errors from our pipeline. Finally §3.7 will be for our discussions and conclusions.

3.2 THE K GIANT SAMPLE

Our Doppler survey began in 1999, at Lick observatory, an was conducted with the Hamilton spectrograph, in conjunction with the Iodine cell method (Marcy & Butler 1992; Butler et al. 1996). The initial goal of our program and the star selection criteria are described in Frink et al.

(2001). Our results concerning planetary occurrence were recently published in Reffert et al. (2014). We regularly observed 373 very bright ($V \leq 6$ [mag]) and photometrically constant G and K giants, selected from the Hipparcos catalog. The objective of our program was to investigate planet occurrence and evolution as a function of stellar mass and metallicity for intermediate mass stars.

A sub-sample of 20 stars from our survey are of special interest to us. Those stars have a clear and convincing signal of one or two distinct periodic RVs, which would be consistent with one or two orbiting substellar companions. A few planets from the sub-sample have already been announced (Frink et al. 2002; Reffert et al. 2006; Quirrenbach et al. 2011; Mitchell et al. 2013; Trifonov et al. 2014) and other papers announcing the rest are under preparation. Despite the good results from our survey, in order to close the individual cases, we want to be confident that the radial velocity periodicities we observed are indeed caused by substellar companions, rather than intrinsic variations. The intrinsic hypothesis poses some initial constraints: Long-term $g-$mode pulsations are unlikely, due to the large convective layer in the giant stars. These non-radial pulsations must be located in the radiative layers, where gravity is a restoring force, while on the surface, short-period pressure mode ($p-$mode) pulsations must be prominent. Spots, on the other hand, can effectively mimic a planet, but again can be ruled out, because stars would have much larger photometric variability if spots caused the RV signal. In general, $g-$mode pulsations and spots must be associated with photometric variability with periods same as the RV period, which for our 20 stars is not supported by the Hipparcos data. Nevertheless, we cannot fully dismiss either the very unlikely spot possibility, or the more probable long-period pulsations ($g-$mode or of unknown nature). Thus, since October 2011, our sub-sample of 20 stars has been observed in the infrared with CRIRES in our final attempt to prove the companion hypothesis.

3.3 Observational setup

CRIRES is temperature stabilized at $\sim 25 \pm 0.1$ K, and has a maximum resolution of $R \approx 100\,000$ when used with a 0.2" slit ($\Delta\upsilon \approx 1.5$ km s^{-1} per pixel). Despite broad, near-IR coverage between 950 – 5200 nm (J, H, K, L and M infrared bands), as a pre-dispersed long slit spectrograph, the available wavelength coverage per single observation is much smaller than in high resolution cross-dispersed spectrographs in the optical (i.e. HARPS). Wavelength ranges can be selected by choosing which grating orders from the CRIRES standard wavelength settings should be imposed on the detector. The spectrum is imaged on the detector mosaics of four Aladdin III detectors, forming an effective 4096 x 512 pixel array (with gap of $\sim$ 280 px between the detectors). This arrangement is somehow problematic, however, because wavelength solutions must be obtained for each detector separately and with great accuracy. The standard CRIRES pipeline recipes offer such calibration, but the lack of proper calibration lamps in the near-IR restricts the achieved RV accuracy to a level far below the range necessary for detecting planetary signals.

Thus, we had two options when calibrating our spectra: to use an approach similar to the I_2 cell method by adopting N_2O or NH_3 gas cells (Seifahrt & Käufl 2008a; Bean & Seifahrt 2009) or to calibrate our spectra using the atmospheric telluric lines playing the role of always available

on-sky gas cell lines. We chose to follow the telluric method, as did Huélamo et al. (2008) and Figueira et al. (2010).

3.3.1 SPECTRAL WINDOW

Our observational window using CRIRES was selected by inspecting the Arcturus near-IR spectral atlas from Hinkle et al. (1995). We searched for dense stellar line regions that were also consistent with deep and sharp telluric lines that could be used for wavelength calibration.

We chose a wavelength setting in the $H-$band (36/1/n from the CRIRES user manual), with a reference wavelength of $\lambda = 1594.5$ nm corresponding to the wavelength at the middle of detector number three. In fact, the selected region is very close to that successfully used by Figueira et al. (2010). This setup, which is characterized by the presence of many sharp atmospheric CO_2 lines, unfortunately fall only on detector 1 and 4. Although detectors 2 and 3 yielded abundant stellar lines, we were not able to construct a wavelength solution for these spectra, and thus excluded them from our study.

3.3.2 OBSERVATIONS

The observations have been made with standard ABBA two nodding cycle, including three jitter observations per nod in order to subtract the sky background emission. The total exposure time required for each individual target to reach a S/N $\geq$ 300 at the reference wavelength has been estimated with an ESO Exposure Time Calculator[2] (ETC) to be between 18 seconds for the brightest stars and 3 minutes for the faintest stars. To achieve the highest possible precision, the spectrograph is used with the 0.2" slit, thus resulting in a resolution of $R = 100\,000$. In order to avoid RV errors related to the imperfect photo center illumination of the slit, the observations were done in NoAO mode (without Adaptive Optics) and, if applicable, nights with poor seeing conditions were requested.

Since typical K giant periods derived from optical RV data are, on average, 1–2 years long, we took at least four RV measurements per year in order to determine orbital parameters from the radial velocity curve. During the four semesters of observations, some targets were given higher priority than others, and were observed two or three more times than the lower priority targets.

3.4 CALIBRATION AND DATA REDUCTION

Dark, flat, and non-linearity corrections, as well as a combination of raw jittered frames in each nodding position were performed using the standard ESO CRIRES pipeline recipes. The final output from the CRIRES pipeline is an extracted one-dimensional co-added spectrum, but we also obtained spectra from the individual A and B nodding frames. Wavelength calibrations

[2] http://www.eso.org/observing/etc/

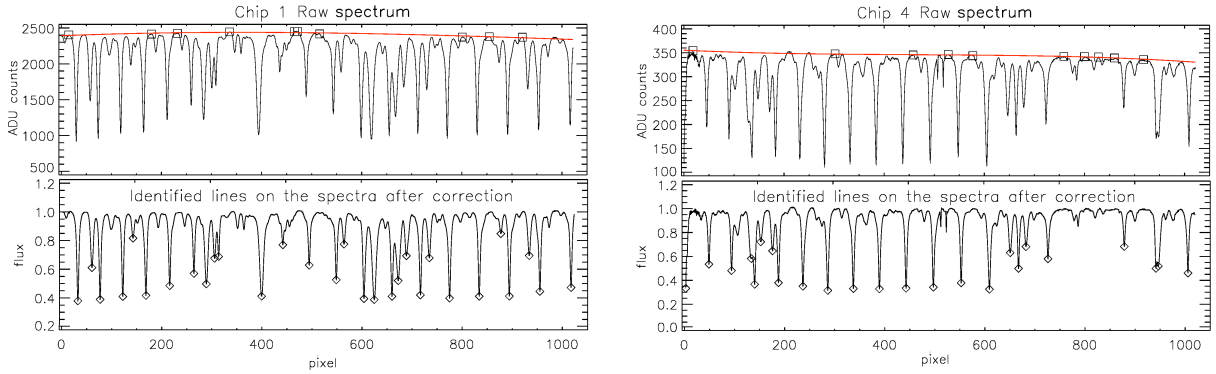

Figure 3.1: Normalization and line identification in the raw spectra taken at JD = 2455932.825 for the K giant 11 Com. Only detectors one (left) and four (right) were used for precise radial velocities, as detectors two and three suffered from lack of deep and sharp telluric lines needed for a precise wavelength solution. However, for some targets at given epochs, only one of the detectors has been used, due to significant telluric line contamination over the stellar lines. After normalization, all the significant telluric and stellar lines were identified.

based on a robust cross-correlation technique between observed spectra and a ThAr lamp lines, or from physical, ray-tracing models are also offered by the CRIRES pipeline recipes. However, the accuracy of both wavelength solutions were insufficient for obtaining precise radial velocities. We found the wavelength solution from the physical model to be more accurate and thus used it as an initial guess, on which we further calibrated each spectral frame with telluric lines.

For further data analysis, we developed a costume semi-automatic pipeline based on a sequence of Marquardt χ^2 minimization IDL algorithms. Fig. 3.1, 3.3 and 3.4 show our data reduction cascade on detector one, plus four raw spectra for our first observation of the K giant 11 Com, while our methods are explained in more detail in the text.

3.4.1 Normalization and line identification

The precise normalization of the obtained spectra is critical to the accurate derivation of radial velocities. However, this is a very difficult task regarding our CRIRES spectra, due to several complications: first, the dense CO_2 lines on detectors one and four and the numerous stellar lines on the chosen wavelength setup lead to very few spectral regions that are free of absorption lines. In that way, the continuum identification on detectors one and four is very challenging. To some degree, the same applies for detectors two and three where, despite the lack of telluric lines, the dense stellar spectra typical for late spectral class stars leaves almost no obvious continuum level. Second, if continuum points on the spectra for a given epoch are found, they may not be valid for the later observations, due to the barycentric Doppler shift, which places stellar lines in a different wavelength position on the spectra, while the telluric lines stay static. The third problem comes from the variability on the spectrum "curvature" on detectors one and four. Not always the raw spectra is nearly even after performing the flat field correction. Finally, the continuum fit must

be performed individually, for each detector's co-added and nodding positions, leading to a total of 12 continuum fits for each epoch (though only 6 were used).

Incorrect normalization might lead to unwanted velocity shifts; hence we invested time to make sure that the continuum parts of the spectra had indeed been identified correctly. To perform a proper normalization, we developed an automated algorithm that identifies areas of the raw spectrum that are free of abortion lines. However, to find the real continuum points on the raw spectra, we performed the same test on a free of noise synthetic spectra constructed from telluric and stellar lines valid for the given epoch of observations (see §3.4.2). The matching continuum points between both spectra were selected for the construction of low-order polynomial fit that represents the estimated continuum level. The raw individual spectrum was then divided by the found solution, leaving a normalized spectrum between 0 and 1.

In the next step, we identified all the significant absorption lines in the spectra with transmission below 85% from the continuum. Telluric lines are known to be nearly static with relatively constant equidistant wavelengths. Thus the automated algorithm first identifies them by comparing the founded lines in the wavelength space from the CRIRES physical model with a $C0_2$ line list from the HITRAN database (Rothman et al. 1998). The same algorithm was then applied to the remaining lines that were deemed telluric. The laboratory wavelengths of the identified stellar spectral lines were taken from the Vienna Atomic Line Database (VALD) (Kupka et al. 1999) and calculated based on the target's $T_{\rm eff}$ and $\log g$.

Not all of the identified telluric and stellar lines were used in the forward steps. The real strength of the automated line identification algorithm lies in its ability to effectively exclude lines from line populations that are either blended or in close proximity. Also, if previously identified stellar lines are found, in fact, to be a blended stellar lines doublet, they can be avoided. The selected lines depend on the stellar line shift, which is caused by the Earth's barycentric movement. For this reason, different telluric lines have been used for wavelength calibration in each epoch.

3.4.2 WAVELENGTH CALIBRATION

For a more precise velocity measurement, each detector pixel must be transformed to a wavelength with high precision. In our case, very accurate $C0_2$ reference wavelengths can be adopted directly from the HITRAN catalog and associated with the found line centers on the pixel space. This approach is very straightforward, but it might not lead to the desired 10–20 m s^{-1} precision necessary to test the planetary hypothesis from the optical. One should take into account the $C0_2$ lines variations that are dependent on the ambient climate above the observatory when the spectra is obtained. Thus, to assure precise calibration, we adopted methods for telluric spectral synthesis similar to those used in Seifahrt & Käufl (2008b); Seifahrt et al. (2010) and Lebzelter et al. (2012). These studies constructed a detailed synthetic atmospheric spectra for modeling their CRIRES observations, although their scientific goal was not explicitly an ultra-precise wavelength solution based on the telluric lines.

Fig. 3.3 illustrates the automated wavelength derivation steps used in our pipeline, while method steps are explained in the text below.

3.4.2.1 The telluric synthetic spectra

The automated algorithm uses the physical wavelength solution from the CRIRES recipes in order to roughly identify the wavelength region of each observational epoch, and for each detector. Next using the found region, we constructed a high resolution telluric transmission spectra using the LBLRTM[3] code (part of FASCODE (Clough et al. 1981, 1992)). The molecule line positions needed for the model are taken from the HITRAN database. The wavelengths from HITRAM are known to be very precise, with typical uncertainty between 5−50 m s^{-1}. For the atmospheric profile above VLT, we adopted the mid-latitude summer/winter meteorological model, as implemented in the LBLRTM. Additional input parameters for the atmosphere model included ambient atmospheric pressure and temperature at the time of observations, together with the target's zenith angle. These data were stored in the image FITS headers, which allowed access to an independent atmospheric model for each observational epoch. We were interested only in the CO_2 absorption spectra, but in order to avoid confusion resulting from any unresolved lines that might appear on science spectra, we used all the available atmospheric molecules from HITRAN and obtained the telluric mask. The resulting spectra for detectors one and four were always consistent with very deep and sharp CO_2 lines in absorption. Detector two also resulted in few CO_2 absorption lines, but their intensity declined fast, at longer wavelengths and, in general, was heavily blended with stellar lines on the science spectra. No deep telluric lines could be seen on detector three.

Many other very weak lines caused by other molecules, which could not be identified on the science spectra, but contributed by limiting the access to the total continuum level, were also present. As noted in §3.4.1, by adding properly-shifted stellar lines to atmospheric lines, one can obtain very a good solution of the continuum level. Comparing the continuum level from the science and the synthetic spectra was thus a crucial step in our study.

3.4.2.2 Line fitting

The unblended telluric lines on the science spectra are oversampled and interpolated with a spline function. Line centers are obtained by adopting a custom Marquardt least χ^2 based routine that can utilize Gaussian, Lorentzian or Pseudo-Voigt[4] fits, depending on the user's choice. The same has been done for the theoretical lines, in order to identify the line center on the wavelength space. Theoretical spectra, by default, is constructed from Voigt lines, and thus the Pseudo-Voigt fit is the best choice for fitting. Science spectra telluric lines are also better represented by Voigt fit, however, in order to avoid possible weak line contamination on the line wings, we decided to fit only near the line's full width, at half maximum (FWHM) depth. Based on many tests, we found that, at that level, the lines are best fit with the Lorentzian model, which was thus selected for telluric fitting in our study (see Fig. 3.2).

[3]LBLRTM − Line By Line Radiative Transfer Model available at http://rtweb.aer.com/

[4]Pseudo-Voigt approximation is function consisting of a weighted sum of a Gaussian and a Lorenzian fits

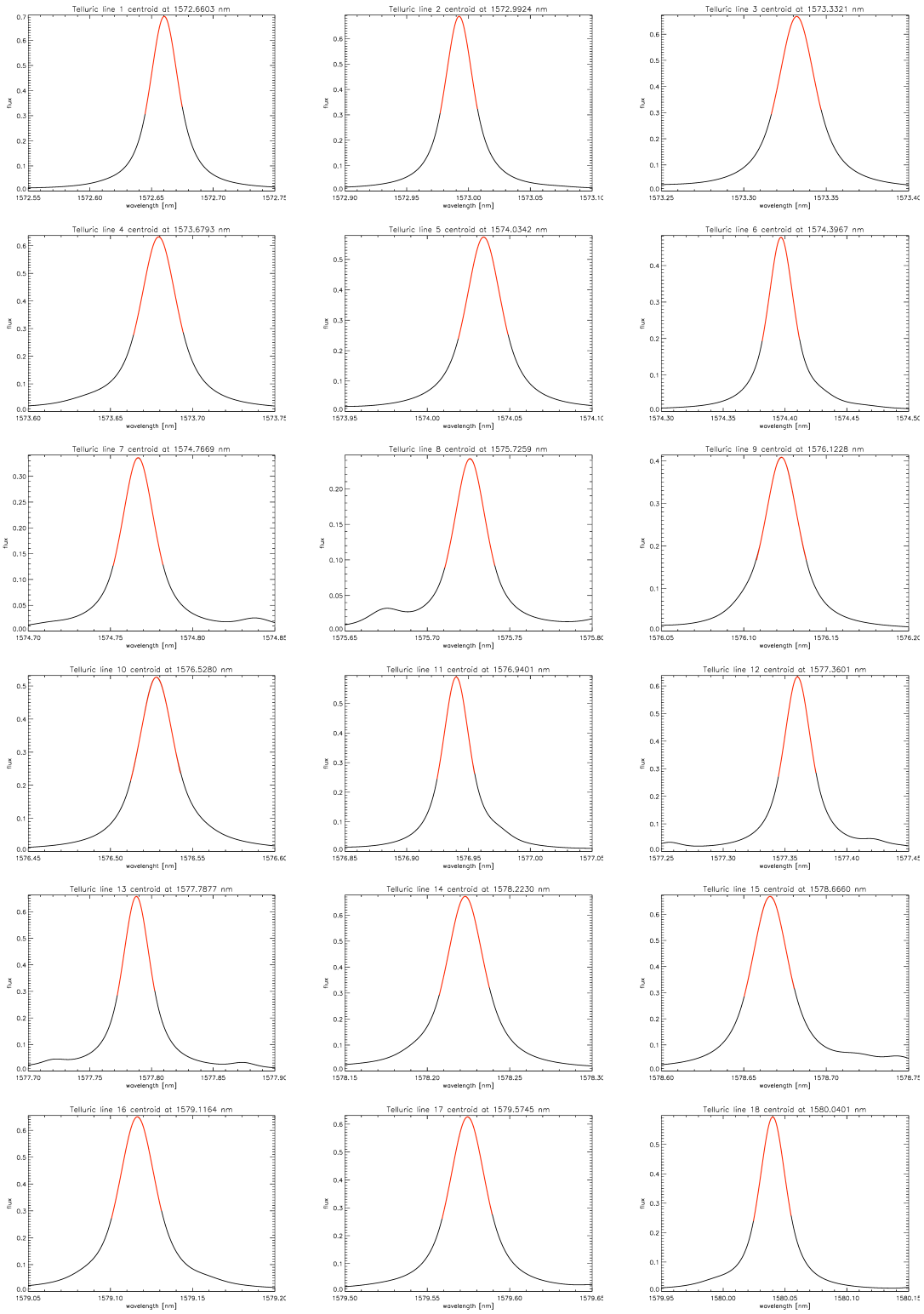

Figure 3.2: Wavelengths of the telluric line centroids were obtained by implementing a Lorentzian fit on the synthetic lines. The fits are constructed only above the FWHM of the Voigt lines, and very accurately represent the line profiles at that level. The same has been done for the telluric lines on the science spectra, albeit on an oversampled pixel space. Note that the figure shows only the telluric lines from detector one. Usually, not all of them were used for wavelength solutions.

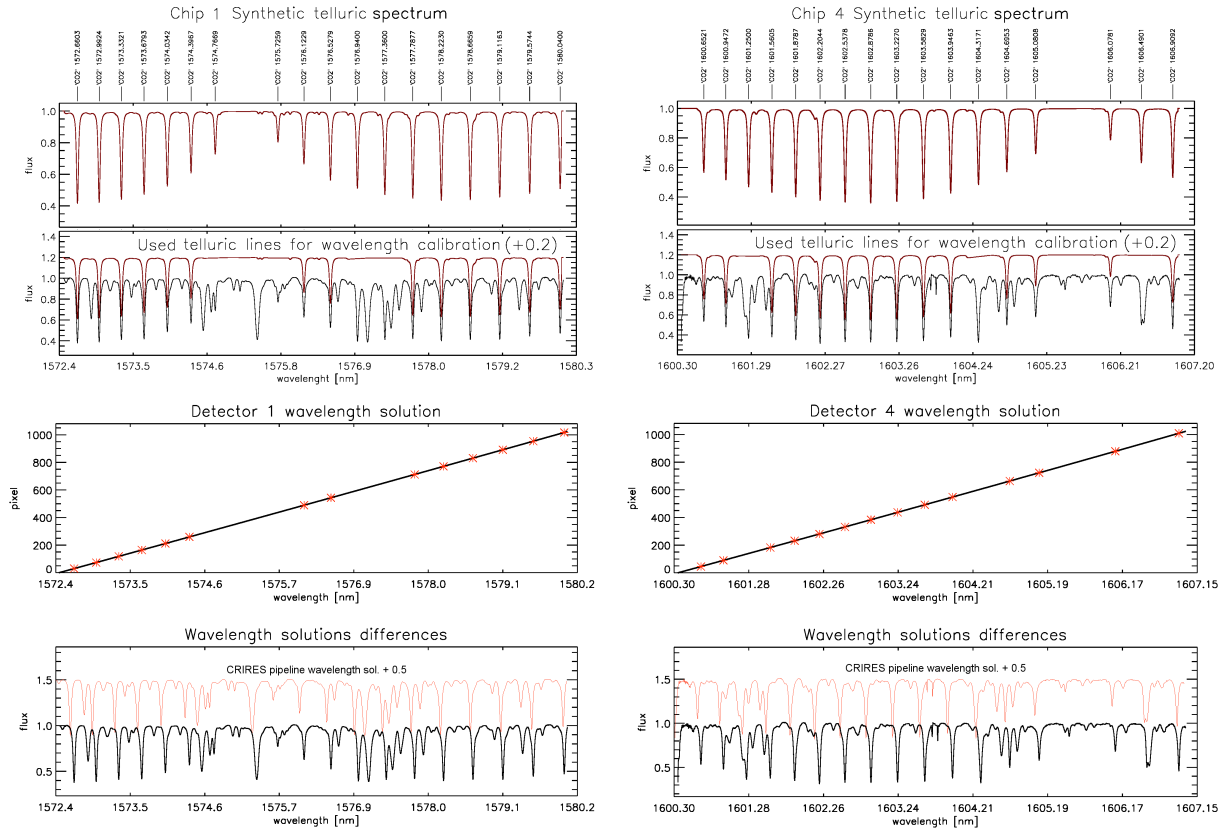

Figure 3.3: Model spectra of the telluric transmission for detectors one (left) and four (right). The synthetic spectra were created with the HITRAN molecular transition database and the LBLRTM code, and finally convolved with the CRIRES instrument profile. Non-blended telluric lines on the pixel-based science spectra are selected and fitted with the Lorentzian profile. The same is done for the synthetic spectra in their theoretical wavelength space (see Fig. 3.2). The wavelength solution is then constructed by fitting a third order polynomial between the pixel and the wavelength solutions. The lower panel shows the obvious difference between our wavelength solution (black) and the wavelength solution from the CRIRES recipes.

3.4.2.3 The wavelength solution

The wavelength solution is obtained by constructing a χ^2 based, third order polynomial fit between the precise pixel coordinates and their wavelength centers found on the synthetic spectra. The bottom panel from Fig. 3.3 shows the notable difference between the CRIRES wavelength solution dispersion and that which was constructed using the telluric model spectra. Obtained wavelength solutions tend to be more precise than those from the CRIRES pipeline and can ultimately be used for obtaining precise RVs. Our radial velocity precision, however, will always be limited to the individual telluric line accuracy from the HITRAN catalog (5–50 m s^{-1}). Hence, in order to stay within that precision level, the number of telluric lines used for wavelength calibration must be as high as possible. This standard can be hardly achieved in some cases, due to the large number of blended atmospheric and stellar lines.

3.5 OBTAINING THE RADIAL VELOCITIES

To obtain precise radial velocities, we adopted the cross-correlation method (Baranne et al. 1996). This technique, in conjunction with weighted binary mask Pepe et al. (2002), is known to produce the most accurate RVs to date (i.e. HARPS). We implemented a similar approach in our pipeline, where cross-correlation was achieved by comparing our science spectra with an adjustable line list binary mask. Our binary template is consistent with noise free continuum level values at wavelength, where we did not identified stellar lines (i.e. values of 1) and a non-continuum level for the stellar wavelength positions. Depending on the user's choice, the non-continuum line positions can be either a simple delta function with a value of zero at maximum absorption, or can adopt the stellar line depths found in the science spectra. Another option available when using the pipeline is the possibility for users to adjust mask aperture widths. This capability can be useful if one wants to take into account the stellar lines FWHM, or to select a costume width, thus making the apertures a box-like shape.

Initially, when we only had a few CRIRES observations for our targets, we obtained the CCF based on a binary mask with a weighted delta function. Despite the relatively good results, some near-IR RVs had large residuals around the Keplerian model prediction, so it became clear that we might be far from the wanted accuracy of 10−25 m s^{-1}. The main problem was that, for some epochs, one or even both detectors had only two unblended stellar lines that could be used to construct a CCF (absolute minimum for our pipeline). That result revealed a problem. If one of the two lines is slightly deformed by a nearby line, a delta function or box-like aperture mask will also lead to biased CCF, and respectively to unwanted velocity shift. We realized that either we needed more stellar lines to test, or we needed a cross-correlation with a stellar template that represented the science spectra as closely as possible.

Based on the experience of Figueira et al. (2010) in their CRIRES study, we know that line position precision as calculated by state-of-the-art stellar atmosphere models such as PHOENIX[5] is estimated to be lower than those obtained from the high S/N near-IR spectra itself. Thus, we decided not to invest time and effort on obtaining a synthetic spectra from a model, and chose to construct such from our observations, instead. We adopted two different ways of constructing the stellar mask; the steps are explained in the text below.

3.5.1 SPECTRA INTERPOLATION AND TELLURIC SUBTRACTION

Each found wavelength solution for each chip and nodding position was interpolated and re-sampled to exactly 10^5 pixel grid of regularly spaced wavelengths. Based on this oversampled grid solution, we interpolated both the science and model spectra from their original, irregularly-spaced wavelength solutions. Re-sampling on the spectra was completed by adopting an IDL routine that performs smooth spline interpolation to the regular grid with minimum information lost. The high resolution LBLRTM telluric mask was interpolated to a ∼ three times higher sampling than the original, while the science spectra had almost 100 times the number of the original 1024 pixels.

[5] http://www.hs.uni-hamburg.de/EN/For/ThA/phoenix/index.html

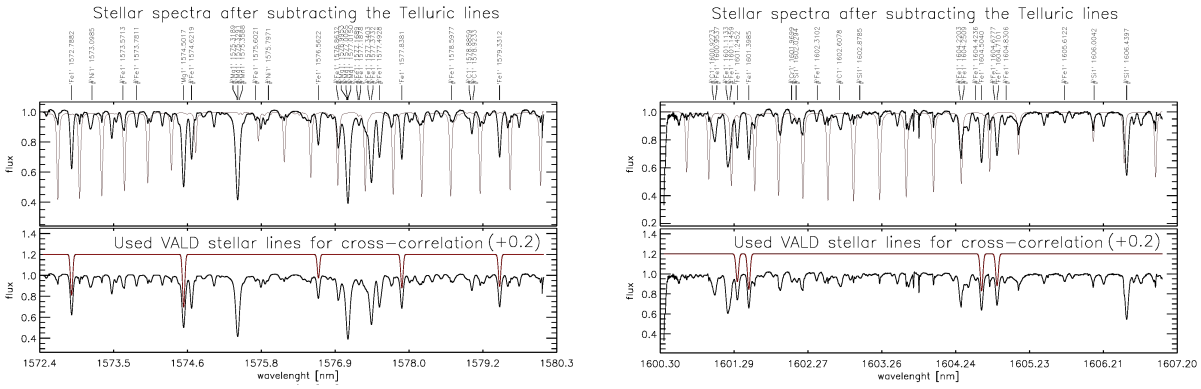

Figure 3.4: Both detector spectra are divided by the theoretical telluric spectra, leaving only the stellar lines. The telluric free spectra from all observational epochs is later shifted and combined in one very high S/N stellar line template. However, only the non-blended lines are used for obtaining the radial velocities via CCF with a synthetic stellar template.

Having both science and theoretical telluric spectra on the same wavelength space is a great advantage. In this way, the telluric lines in both spectra will match on the wavelength space and thus allow us to remove their contribution from each CRIRES spectra. Theoretical spectra, however, have deeper and narrower lines, and must therefore be smoothed with the CRIRES instrument profile (IP) in order to match the observed line widths and depths. Instead of measuring each telluric line to identify the IP, we applied a more global strategy. By using a least-χ^2 algorithm, we compared the science spectra on one hand and the convolved with a Gaussian kernel theoretical mask on the other. In this algorithm, the width of the Gaussian kernel is the only free parameter, and the final IP is found when the residuals from subtraction of both spectra are at a minimum. With this technique, the IP is obtained quickly and interdependently for each nod and detector. In our test, we assumed that the IP is a simple Gaussian, although in reality the IP is a more complicated sum of several Gaussian profiles coming from different optical parts of the spectrograph. In the future, the user of our pipeline will be provided with the option to construct the IP more precisely by using a custom number of Gaussian kernels. Despite this future improvement, we believe that this improvement might not have a large impact on obtained velocities, as the simple Gaussian IP already yields very good results.

Telluric lines may be removed from our pipeline by dividing the science spectra by the convolved synthetic one, thus leaving only the stellar lines. Fig. 3.4 (upper panel) illustrates the final output from the spectral division. The figure shows many blended and unblended stellar lines remaining on the spectra, but there are also many week stellar lines, for which we do not have information from VALD.

We believe that dividing the spectra in such a way provides us with the most accurate stellar template that can be extracted from the CRIRES spectra. This method gives much better results that simply masking the telluric lines from the spectra, for in this way, we remove the total atmospheric contribution to the science template.

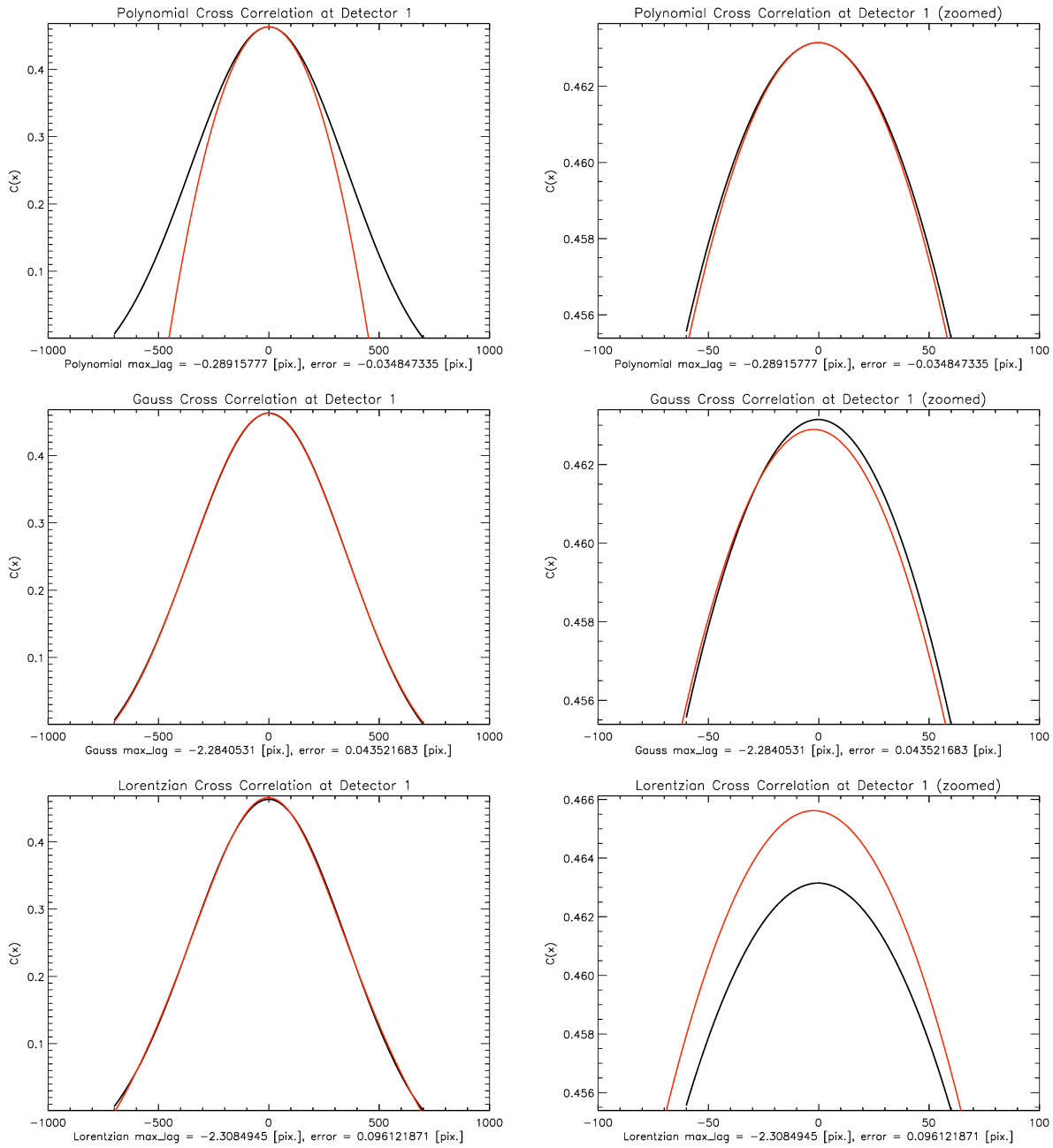

Figure 3.5: Cross-correlation function obtained from 11 Com spectra at detector one. Our pipeline allows the usage of three different fits to obtain the maximum cross-correlation function. Gaussian (middle) and Lorentzian (bottom) models represent the CCF very well, but inadequately represent the CCF peak (right panels). Thus we decided to use only the Polynomial fit (upper panel), which is constructed solely from the points around the CCF peak, to derive our RV velocities.

3.5.2 CCF WITH NOISE-FREE STELLAR MASK

To obtain accurate radial velocities, one needs not only precise wavelength solutions, but also the necessary tools to extract the Doppler shift. This step can be accomplished for CRIRES spectra by modeling the stellar lines, where one of the free parameters is the line center on the wavelength space, from which the wavelength shift can be obtained. The other method is to obtain CCF from a binary template, as discussed above. Both techniques, however, might give poor results, if the number of used spectral lines is low. Thus, we have decided to adopt a method which is a sort of combination of these two techniques. First, to be secure, we chose only single deep and sharp stellar lines and modeled these using a Gaussian profile. In fact, the modeling can be done by using a Lorentzian or a Pseudo-Voigt model, depending on the user's choice, but we found that the better fit and lack of complexity of the Gaussian profile suited it well for our study. We then obtained the lines FWHM and their individual spectral depths from the continuum level. In the next step, we shifted the identified reference stellar wavelengths by taking the target's absolute radial velocity into account[6]. Additionally, we applied a precise barycentric correction to the reference wavelengths that has an accuracy rate better than ~ 1 m s^{-1} (Roytman 2013). In this way, we took all the necessary line shifts into account, so the synthetic spectrum resulted in line positions very similar to those observed on the science spectrum.

Therefore, once we obtained the shifted line wavelengths, as well as their median FWHM and absorption depths, we constructed an artificial free-of-noise spectrum on the same oversampled wavelength space as the science one. Fig. 3.4 (lower panel) illustrates the final stellar mask for detectors one and four. As expected, due to the proper theoretical line shift, both spectra almost match, and any small differences between them can be attributed to the additional wavelength shift that is likely caused by any hypothetical companion(s). Therefore, to save PC time, the cross-correlation is performed only around the stellar lines. The maximum of the CCF can be obtained down to sub-pixel level using three χ^2 Marquardt algorithms. We were able to fit the Gaussian, Lorentzian or low-order Polynomial fits constructed only around the maximum of the CCF. Gaussian and Lorentzian fits usually represent the CCF very well, however, we found that the Polynomial model can better fit the points around the CCF maximum. For this reason, this model was selected for deriving precise velocities. Fig. 3.5 shows the CCF obtained from 11 Com spectra at detector one and the comparison between the three fitting models in our pipeline.

The same method was also applied for co-added spectra and nodding positions A and B at detectors one and four. This step resulted in 6 different radial velocities for a given epoch. Final radial velocity was obtained by calculating a weighted median of all radial velocities, where the weight was chosen to be the individual S/N value of each spectrum frame taken from the fits headers. Usually, the highest S/N ratio had the co-added spectra from detector one, and lowest belonged to one of the nodding positions at detector four. In some targets (and epochs), only detector one or four was used, due to the lack of available stellar lines for obtaining the cross-correlation.

[6]Taken from SIMBAD, http://simbad.u-strasbg.fr/simbad/ or have been estimated manually using our pipeline

3.5.3 CCF WITH MEDIAN COMBINED STELLAR MASK

As can be seen from Fig. 3.4, there are many unresolved stellar lines on detectors one and four. On top of that there are few unblended very deep stellar lines that according to the VALD line list are actually spectral doublets.These cannot be used for precise RVs in the context defined in §3.5.2, although they are containing Doppler information.

After the telluric removal on all available spectra, we decided to combine all frames in one master median template and try to cross-correlate all the epoch with this stellar mask. This has several major advantages:

1. Median combination will remove all the telluric artifacts remained on the individual frames after the division with the LBLRTM mask.

2. This will allow to use all the available spectral lines, even the unknown and unresolved doublet lines.

3. As long as we can construct wavelength solution, we can obtain RVs, even if all the singe lines are blended – something that is not possible by cross-correlating with noise free template.

4. Cross-correction between two identical functions will lead to CCF close to the maximum and thus, one can very accurately estimate the Doppler shift.

This method, requires several challenging steps. Individual spectra has different wavelength shifts and therefore needs to be shifted carefully. This is done by interpolating each spectra to the most accurate wavelength solution that we believe we have achieved (i.e. most telluric references have been used). Then we cross-correlated the spectrum with reference wavelength solution respect to the rest, and we are obtaining the relative shift in the sub-pixel space. Each spectra is then shifted exactly with the difference from the reference spectra and finally a median combination is applied. The result is high S/N stellar mask having the wavelength solution from the grid constructed with the largest number of telluric lines available for a given target.

This method becomes available only after the end of our program, when we reach 8−10 epochs for each target. For better results even larger number of individual spectra is necessary, but, nevertheless, the final output was spectacular. At the moment this technique is still in experimental level, although we achieved very good results for some targets in our sample. Also, so far detector one performs much better than detector four, where the lower S/N and the abundant and faint stellar lines seems to bias the CCF.

The resulting radial velocity for each epoch is calculated with the same cross-correlation steps and weighted median combination of individual frames RVs, as defined in §3.5.2.

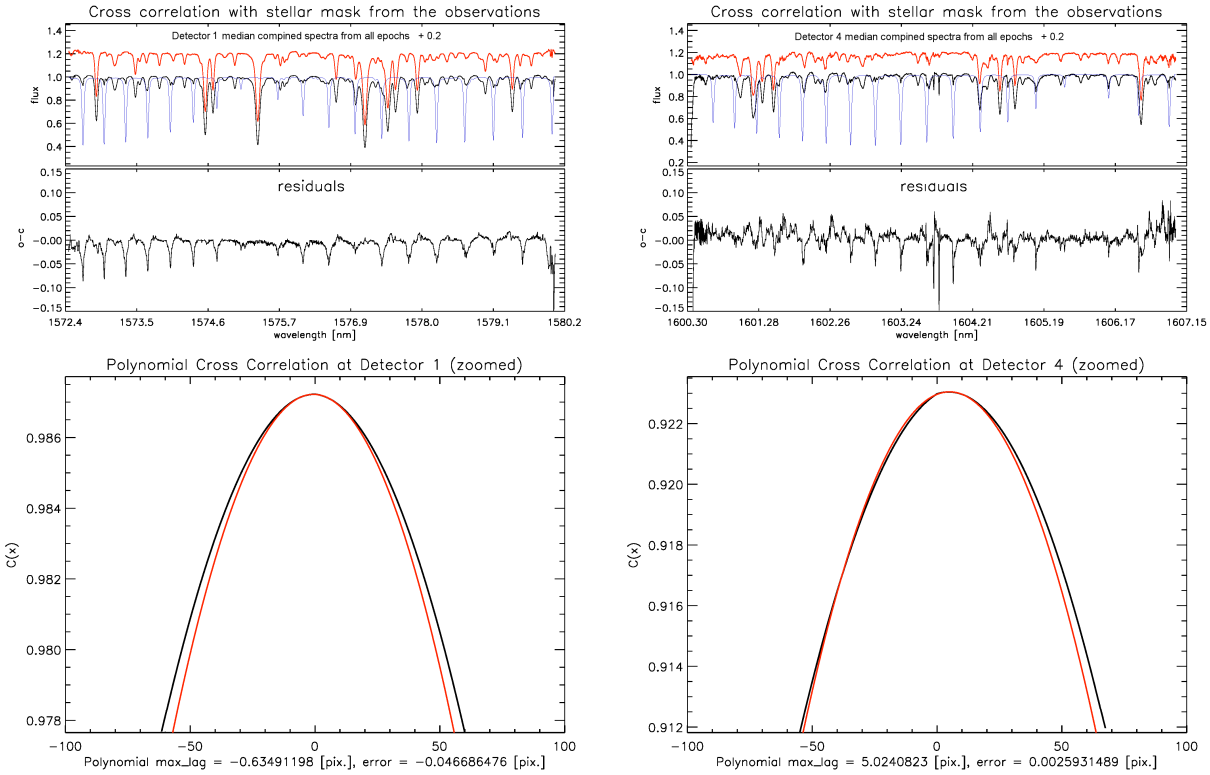

Figure 3.6: Cross-correlation function obtained from 11 Com spectra at detectors one and four using a stellar mask constructed from the observations. The mask is median combination of all available telluric free and properly shifted spectra. This method of cross-correlation gives very high CCF peak (bottom panels, zoomed CCF peaks). This is expected given the fact that we are using all stellar lines for cross-correlation. The residuals shows dispersion only around regions with removed telluric lines as such do not exist on the co-added spectra due to the median combination. This is an experimental method and so far detector one perform much better than detector four, where the lower S/N and the abundant and faint stellar lines bias the CCF.

3.6 Error estimation and RV comparison with the optical

Based on our results we estimated the formal error of our CRIRES measurements to be not more than 40 m s^{-1}. Estimation was done based on the *r.m.s.* dispersion values around the best fit model obtained from the Lick survey. This value is very likely to be over-estimated for many of our targets as can be seen on the RV plots in §4, §5, §6 and §7. This is especially valid for those targets with lower levels of stellar RV jitter from our K giant sub-sample. Nevertheless, we believe that the adopted level of uncertainties is reasonable, giving the fact that the telluric references from HITRAN can have similar velocity errors (5−50 m s^{-1}). Also, this error is adequate enough to test the expected RV optical phase and amplitude and hence, the planetary companion hypothesis. VLT data best agrees to the RV models that assumed a brown dwarf planetary masses. In these cases the RV semi-amplitude is much larger than the estimated uncertainty,

while was more challenging for planetary mass objects as their RV semi-amplitude usually was between three and five times the adopted precision. The *r.m.s.* dispersion value also depends on the star it self. Some stars had much lower level of line contamination than others, and thus for these obtaining RVs was easier.

The near-IR velocities from VLT have not been used for fitting together with the velocities from Lick. As mentioned above the CRIRES data have large uncertainty and therefore they have negligible total weight to the final fit, compared to the optical RVs. To test both data sets we only have to fit the zero offset between the relative RVs from Lick and the absolute RVs from VLT, until we reach the best consistency.

3.7 RESULTS AND DISCUSSIONS

Final CRIRES velocities are shown in Chapters §4, §5, §6 and §7. Results from only ten out of twenty targets are introduced in this thesis, and all these we believe to be a confirmed as planetary companions rather than pulsations. Radial velocities from three of targets have been already submitted or published in referee papers (Mitchell et al. 2013; Trifonov et al. 2014), while the remaining will be subject of future publications. The rest ten targets will also be published in near future with a planetary announcement or rejection of the planetary hypothesis.

The CRIRES survey as prolongation of the Lick survey has reached its goal. The obtained radial velocities are in agreement with the phase and amplitude of the optical data, and therefore are following the best Keplerian and dynamical fit models prediction. The achieved RV precision at the moment is set to uniform value of 40 $\mathrm{m\,s^{-1}}$, which might be too large than the real near-IR uncertainties for some targets. There is room for the pipeline improvement and accurate individual error estimation of each RV point is perhaps, the next step.

The automated pipeline algorithm methods used in our code tend to be complex and accurate, but in the same time standard. In this context, with small adjustment the whole set of algorithms can be effectively used for precise RV extraction from other instruments than CRIRES. This can be done for other wavelength regions, where a telluric lines are present. We can adapt the pipeline even if a gas cell was used for references, unless there is an available gas spectrum template. The opportunities are broad and even after the termination of the CRIRES program the pipeline can be used or serve as a base for future observing programs.

CHAPTER 4

THE η CET PLANETARY SYSTEM

Based on

"Precise Radial Velocities of Giant Stars
VII. Discovery and stability analysis of the planetary system around the K giant star η Cet"

T. Trifonov[1], S. Reffert[1], X. Tan[2], M. H. Lee[2], and A. Quirrenbach[1]

subbmited to A&A

[1]ZAH-Landessternwarte, Königstuhl 12, 69117 Heidelberg, Germany
[2]Department of Earth Sciences, The University of Hong Kong, Pokfulam Road, Hong Kong

4.1 INTRODUCTION

169 known multiple planet systems are present in the literature up to October 2013, and their number is constantly growing (www.exoplanet.eu). The first strong evidence for a multiple planetary system around a main-sequence star was reported by Butler et al. (1999), showing that together with the 4.6 day-period radial velocity signal of υ And (Butler et al. 1997), two more long-period, sub-stellar companions can be derived from the Doppler curve. Later, a second Jupiter mass planet was found to orbit the star 47 UMa (Fischer et al. 2002), and another one around the G star HD12661 (Fischer et al. 2003).

Interesting cases also include planets locked in mean motion resonance (MMR), like the short-period 2:1 resonance pair around GJ 876 (Marcy et al. 2001), the 3:1 MMR planetary system around HD 60532 (Desort et al. 2008; Laskar & Correia 2009), or the 3:2 MMR system around HD 45364 (Correia et al. 2009). Follow-up radial velocity observations of well known planetary pairs showed evidence that some of them are actually part of higher order multiple planetary systems. For example, two additional long-period planets are orbiting around GJ 876 (Rivera et al. 2010), and up to five planets are known to orbit 55 Cnc (Fischer et al. 2008). More recently Lovis et al. (2011) announced a very dense, but still well-separated low-mass planetary system around the solar-type star HD 10180. Tuomi (2012) claimed that the planets in this system might even amount to nine, which would make it the most compact and populated extrasolar multiple system known to date.

Now, almost two decades since the announcement of 51 Peg b (Mayor & Queloz 1995), 93 multiple planetary systems have been found using high-precision Doppler spectroscopy. Another 67 multiple planetary systems have been found with the transiting technique, the vast majority of them with the Kepler satellite. Techniques such as direct imaging (Marois et al. 2010) and micro-lensing (Gaudi et al. 2008) have also proven to be successful in the detection of multiple extrasolar planetary systems.

The different techniques for detecting extrasolar planets and the combination between them shows that planetary systems appear to be very frequent in all kinds of stable configurations. Planetary systems are found to orbit around stars with different ages and spectral classes, including binaries (Lee et al. 2009) and even pulsars (Wolszczan & Frail 1992). Nevertheless, not many multiple planetary systems have been found around evolved giant stars so far. The multiple planetary systems appear to be a very small fraction of the planet occurrence statistics around evolved giants, which are dominated by the single planetary systems. Up to date there is only one multiple planetary system candidate known around an evolved star (HD 102272, Niedzielski et al. 2009a), and two multiple systems consistent with brown dwarf mass companions around BD +20 2457 (Niedzielski et al. 2009b) and ν Oph (Quirrenbach et al. 2011; Sato et al. 2012).

In this paper we report the detection of two Jovian planets orbiting the K giant η Cet based on precise radial velocities. We also carry out an extensive stability analysis to demonstrate that the system is stable and to further constrain its parameters.

The outline of the paper is as follows. In §4.2 we introduce the stellar parameters for η Cet and we describe our observations taken at Lick observatory and at the VLT. Section §4.3 describes the derivation of the spectroscopic orbital parameters. In §4.4 we explain our dynamical stability calculations, and in §4.5 we discuss the possible origin of the η Cet system and the population of planets around giants. Finally, we provide a summary in Section §4.6.

4.2 OBSERVATIONS AND STELLAR CHARACTERISTICS

4.2.1 THE K GIANT STAR η CET

η Cet (= HIP 5364, HD 6805, HR 334) is a bright (V = 3.46 mag), red giant clump star ($B - V$ = 1.16). It is located at a distance of 37.99 ± 0.02 pc (van Leeuwen 2007) and flagged in the Hipparcos catalog as photometrically constant.

Luck & Challener (1995) propose $T_{\rm eff}$ = 4425 ± 100 K, derived from photometry, and $\log g$ = 2.65 ± 0.25 [cm · s^{-2}] estimated from the ionization balance between Fe I and Fe II lines in the spectra. Luck & Challener (1995) give [Fe/H] = 0.16 ± 0.05, and a mass of M = 1.3 ± 0.2 $M_{\odot}$. A more recent study of η Cet by Berio et al. (2011) derives the stellar parameters as $T_{\rm eff}$ = 4356 ± 55 K, luminosity L = 74.0 ± 3.7 $L_{\odot}$, and the estimated radius as R = 15.10 ± 0.10 $R_{\odot}$. Berio et al. (2011) roughly estimate the mass of η Cet to be M = 1.0−1.4 $M_{\odot}$ by comparing its position in the HertzsprungRussell (HR) diagram with evolutionary tracks of solar metallicity.

Using a Lick template spectrum without iodine absorption cell lines Hekker & Meléndez (2007) estimated η Cet to be metal rich with [Fe/H] = 0.07 ± 0.1. Based on this metallicity and the observed position in the HR diagram, a trilinear interpolation in the evolutionary tracks and isochrones (Girardi et al. 2000) yields $T_{\rm eff}$ = 4529 ± 19 K, $\log g$ = 2.36 ± 0.05 [cm · s^{-2}], L = 77.1 ± 1.1 $L_\odot$ and R = 14.3 ± 0.2 $R_\odot$ (Reffert et al. 2014).

We determined the probability of η Cet to be on the red giant branch (RGB) or on the horizontal branch (HB) by generating 10 000 positions with (B − V, M_V, [Fe/H]) consistent with the error bars on these quantities, and derived the stellar parameters via a comparison with interpolated evolutionary tracks. Our method for deriving stellar parameters for all G and K giant stars monitored at Lick Observatory, including η Cet, is described in more detail in Reffert et al. (2014).

Our results show that η Cet has a 70% probability to be on the RGB with a resulting mass of M = 1.7 ± 0.1 $M_\odot$. In case η Cet is on the HB the mass would be M = 1.6 ± 0.2 $M_\odot$. Here we simply use the mass with the highest probability. All stellar parameters are summarized in Table 4.1.

Table 4.1: Stellar properties of η Cet.

Parameter	η Cet	reference
Spectral type	K1III	Gray et al. (2006)
	K2III CNO.5	Luck & Challener (1995)
m_v [mag]	3.46	van Leeuwen (2007)
$B-V$	1.161 ± 0.005	van Leeuwen (2007)
Distance [pc]	37.99 ± 0.02	van Leeuwen (2007)
π [mas]	26.32 ± 0.14	van Leeuwen (2007)
Mass [$M_\odot$]	1.7 ± 0.1	Reffert et al. (2014)
	1.3 ± 0.2	Luck & Challener (1995)
	1.2 ± 0.2	Berio et al. (2011)
Luminosity [$L_\odot$]	77.1 ± 1.1	Reffert et al. (2014)
	74.0 ± 3.7	Berio et al. (2011)
Radius [$R_\odot$]	14.3 ± 0.2	Reffert et al. (2014)
	15.1 ± 0.1	Berio et al. (2011)
$T_{\rm eff}$[K]	4528 ± 19	Reffert et al. (2014)
	4563 ± 82	Prugniel et al. (2011)
	4425 ± 100	Luck & Challener (1995)
	4356 ± 55	Berio et al. (2011)
$\log g$[cm · s^{-2}]	2.36 ± 0.05	Reffert et al. (2014)
	2.61 ± 0.21	Prugniel et al. (2011)
	2.65 ± 0.25	Luck & Challener (1995)
[Fe/H]	0.07 ± 0.1	Hekker & Meléndez (2007)
	0.12 ± 0.08	Prugniel et al. (2011)
	0.16 ± 0.05	Luck & Challener (1995)
RV$_{absolute}$ [km s^{-1}]	11.845	this paper

4.2.2 LICK DATA SET

Doppler measurements for η Cet have been obtained since July 2000 as part of our precise ($5 - 8\ \mathrm{m\,s^{-1}}$) Doppler survey of 373 very bright ($V \leq 6$ mag) G and K giants. The program started in June 1999 using the 0.6 m Coudé Auxiliary Telescope (CAT) with the Hamilton Échelle Spectrograph at Lick Observatory. The original goal of the program was to study the intrinsic radial velocity variability in K giants, and to demonstrate that the small levels of stellar jitter make these stars a good choice for astrometric reference objects for the Space Interferometry Mission (SIM) (Frink et al. 2001). However, the low amplitude of the intrinsic jitter of the selected K giants, together with the precise and regular observations, makes this survey sensitive to variations in the radial velocity that might be caused by extrasolar planets.

All observations at Lick Observatory have been taken with the iodine cell placed in the light path at the entrance of the spectrograph. This technique provides us with many narrow and very well defined iodine spectral lines, which are used as references, and it is known to yield precise Doppler shifts down to $3\ \mathrm{m\,s^{-1}}$ or even better for dwarf stars (Butler et al. 1996). The iodine method shall not be discussed in this paper; instead we refer to Marcy & Butler (1992); Valenti et al. (1995) and Butler et al. (1996), where more details about the technique and the data reduction can be found.

The wavelength coverage of the Hamilton spectra extends from 3755 to 9590 Å, with a resolution of $R \approx 60\,000$ in the wavelength range from 5000 to 5800 Å, where most of the iodine lines can be found and where the radial velocities are measured. The typical exposure time with the 0.6 m CAT is 450 seconds, which results in a signal-to-noise ratio of about 100, reaching a radial velocity precision of better than $5\ \mathrm{m\,s^{-1}}$. The individual radial velocities are listed in Table 4.2, together with Julian dates and their formal errors.

4.2.3 CRIRES DATA SET

Eight additional Doppler measurements for η Cet were taken between October 2011 and July 2013 with the pre-dispersed CRyogenic InfraRed Echelle Spectrograph (CRIRES) mounted at VLT UT1 (Antu), (Kaeufl et al. 2004). CRIRES has a resolving power of $R \approx 100\,000$ when used with a 0.2" slit, covering a narrow wavelength region in the J, H, K, L or M infrared bands (960 – 5200 nm). Several studies had demonstrated that accurate radial velocity measurements between 10 and 35 $\mathrm{m\,s^{-1}}$ are possible with CRIRES. Seifahrt & Käufl (2008a) reached a precision of $\approx 35\ \mathrm{m\,s^{-1}}$ when using reference spectra of a N_2O gas cell, and Bean & Seifahrt (2009) even reached $\approx 10\ \mathrm{m\,s^{-1}}$ with an ammonia (NH_3) gas-cell. Huélamo et al. (2008) and Figueira et al. (2010) show that the achieved Doppler precision can be better than $\approx 25\ \mathrm{m\,s^{-1}}$ when using telluric absorption lines in the H band as reference spectra.

Motivated by these results, our strategy with CRIRES is to test the optical Doppler data with that from the near-IR regime, for those objects in our G and K giants sample that clearly exhibit periodicity consistent with one or more substellar companion(s). If the periodic Doppler signal was indeed due to a planet, we would expect the near-IR radial velocities to follow the best fit model derived from the optical spectra.

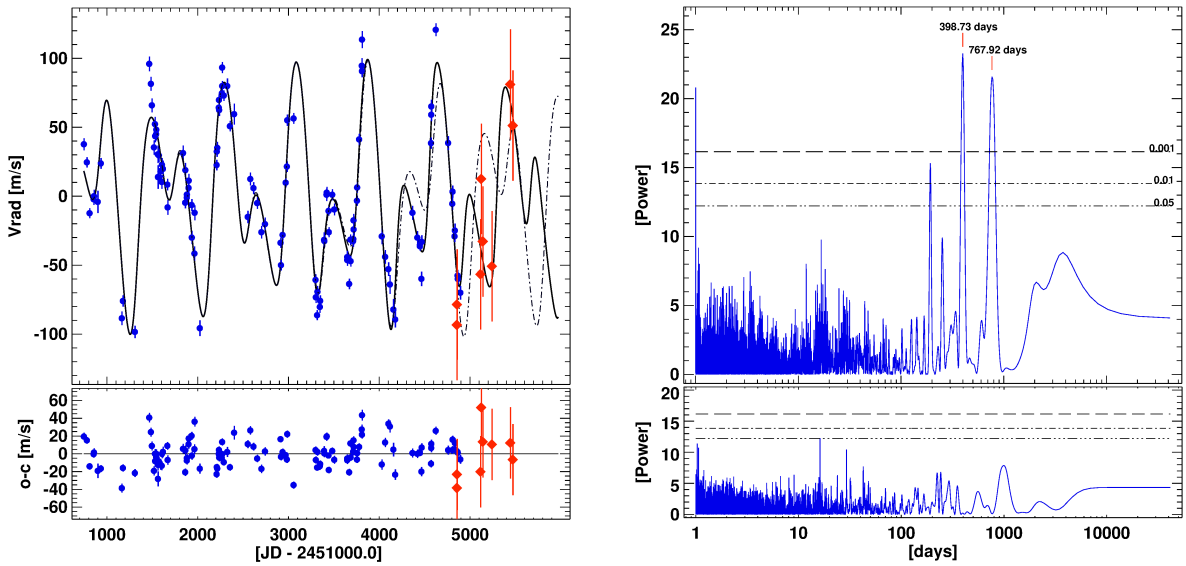

Figure 4.1: *Top left panel*: Radial velocities measured at Lick Observatory (*blue circles*), along with error bars, covering about 11 years from July 2000 to October 2011. Two best fits are over-plotted to the data: double-Keplerian fit (*dot dashed*) and the best dynamical edge-on coplanar fit (*solid line*). The two fits are not consistent in later epochs due to the gravitational interactions considered in the dynamical model. Despite the large estimated errors, the data from CRIRES (*red diamonds*) seem to follow the best fit prediction from the dynamical fit. *Bottom left panel*: No systematics are visible in the residuals. The remaining radial velocity scatter has a standard deviation of 15.9 $\mathrm{m\,s^{-1}}$, most likely caused by rapid solar–like p – mode oscillations.
Top right panel: The periodogram of the measured radial velocities shows two highly significant peaks around 399 and 768 days, while the Kepler fit to the data reveals a best fit at periods around 406.9 and 750.5 days. *Bottom right panel*: No significant peak is left in the periodogram of the residuals after the two periods from the Keplerian fit have been removed.

If the radial velocity variations in the optical and in the near-IR are not consistent, the reason may be either large stellar spots (Huélamo et al. 2008; Bean et al. 2010) or non-radial pulsations that will result in a different velocity amplitude at visible and infrared wavelengths (Percy et al. 2001). When stellar spots mimic a planetary signal, the contrast between the flux coming from the stellar photosphere and the flux coming from the cooler spot is larger at optical wavelengths and thus, has a higher RV amplitude with respect to the near-IR.

However, in our case, the stellar spot hypothesis is already excluded by the Hipparcos observations. If the RV signal is indeed caused by large spots, they must lead to photometric variations that should be detected by the Hipparcos satellite. However, our K giant sample is flagged as photometrically quiet. Thus, we are using CRIRES to rule out the possibility of non-radial pulsations, which in principle may have large amplitudes and low frequencies, and may be wrongly interpreted as substellar companions (Mitchell et al. 2013).

For our observation with CRIRES we decided to adopt an observational setup similar to that

Table 4.2: Measured velocities for η Cet and the derived errors

JD	RV [m s^{-1}]	σ_{RV} [m s^{-1}]	JD	RV [m s^{-1}]	σ_{RV} [m s^{-1}]	JD	RV [m s^{-1}]	σ_{RV} [m s^{-1}]
2451745.994	37.8	4.3	2453231.961	64.3	4.0	2454711.893	−32.4	4.1
2451778.895	24.7	3.7	2453233.909	69.9	3.9	2454713.873	−31.0	4.2
2451808.867	−12.2	3.6	2453235.960	62.6	4.2	2454715.882	−17.4	4.6
2451853.766	−2.1	4.1	2453265.899	74.7	3.8	2454716.875	−24.0	4.1
2451856.801	0.1	4.6	2453268.919	93.4	4.0	2454753.885	−3.2	3.6
2451898.637	−4.0	8.0	2453269.810	80.0	3.5	2454755.850	6.4	3.8
2451932.609	23.9	3.9	2453286.828	73.1	3.8	2454777.733	41.3	4.1
2452163.861	−89.3	4.9	2453324.713	80.0	5.5	2454806.796	94.7	5.5
2452175.851	−75.7	4.0	2453354.654	50.9	3.8	2454808.770	90.8	4.3
2452307.598	−98.1	4.5	2453400.642	59.6	7.5	2454809.763	113.7	6.1
2452465.989	96.1	5.3	2453550.983	−14.9	4.4	2455026.973	−30.0	5.7
2452483.985	81.6	5.0	2453578.964	12.6	4.6	2455063.965	−43.9	5.0
2452494.987	66.0	5.0	2453613.923	6.0	4.2	2455099.996	−52.8	4.9
2452517.936	35.5	5.2	2453654.771	−4.9	4.1	2455116.856	−63.9	6.8
2452528.910	52.4	5.2	2453701.724	−26.0	4.6	2455154.739	−82.1	7.6
2452530.910	43.7	4.5	2453740.745	−20.1	4.7	2455174.788	−89.3	5.8
2452541.904	45.1	4.5	2453911.993	−33.7	3.6	2455364.972	−11.9	5.0
2452543.883	48.3	5.0	2453917.013	−49.9	3.9	2455419.012	−29.9	4.7
2452559.914	30.5	6.4	2453934.974	−28.0	3.9	2455446.847	−35.4	3.6
2452561.795	14.0	8.4	2453968.925	9.9	3.2	2455446.856	−36.2	3.1
2452571.791	29.7	5.0	2453981.851	21.6	3.8	2455463.833	−59.8	5.2
2452589.810	18.3	5.7	2453985.899	55.2	4.0	2455466.842	−33.0	4.8
2452603.782	10.4	4.9	2454055.755	56.8	3.9	2455569.653	40.0	4.1
2452605.724	22.9	4.8	2454297.975	−60.6	4.1	2455571.713	59.6	4.6
2452616.772	19.9	5.9	2454300.974	−73.2	4.0	2455572.671	65.6	4.8
2452665.604	8.5	4.2	2454314.939	−86.2	3.6	2455621.621	121.2	4.6
2452668.611	−8.0	5.3	2454318.981	−69.2	4.2	2455757.974	39.1	5.0
2452837.972	31.3	5.4	2454344.859	−80.2	4.3	2455803.919	−5.4	4.3
2452861.963	−4.6	4.1	2454348.917	−75.8	4.0	2455806.936	3.4	4.3
2452863.985	19.0	5.2	2454391.887	−31.6	5.4	2455828.781	−30.0	4.2
2452879.918	−0.9	4.2	2454394.775	−32.4	4.2	2455831.849	−24.8	5.1
2452880.947	1.3	5.0	2454418.777	1.2	4.5	⋆2455853.844	−93.0	40.0
2452898.911	6.1	4.7	2454420.763	2.7	4.2	⋆2455854.616	−78.3	40.0
2452900.928	11.4	4.8	2454440.653	−10.6	3.4	2455861.842	−57.5	4.2
2452932.839	−6.3	4.3	2454443.651	−26.0	3.6	2455864.796	−59.9	4.4
2452934.804	−29.9	4.6	2454481.638	1.2	3.9	2455892.745	−69.9	4.9
2452963.753	−41.5	5.2	2454503.651	−9.5	4.3	⋆2456113.863	−56.3	40.0
2452965.809	−11.9	5.4	2454645.984	−44.1	4.5	⋆2456121.811	12.8	40.0
2453022.630	−95.6	5.6	2454646.968	−46.2	4.2	⋆2456139.747	−32.5	40.0
2453208.010	22.7	3.8	2454668.009	−63.5	3.7	⋆2456239.563	−50.5	40.0
2453209.978	32.5	3.7	2454681.904	−31.4	3.8	⋆2456239.563	81.4	40.0
2453214.961	35.2	4.2	2454683.970	−47.0	3.8	⋆2456239.563	51.5	40.0

⋆ - CRIRES data
absolute RV_{CRIRES} = 11.845 km s^{-1}

successfully used by Figueira et al. (2010). We chose a wavelength setting in the H band (36/1/n), with a reference wavelength of λ = 1594.5 nm. This particular region was selected by inspecting the Arcturus near-IR spectral atlas from Hinkle et al. (1995), and looking for a good number of stellar as well as telluric lines. The selected spectral region is characterized by the presence of many deep and sharp atmospheric CO_2 lines, taking the role of always available on-sky gas cell. In order to achieve the highest possible precision the spectrograph is used with a resolution of R = 100 000. In order to avoid RV errors related to non-uniform illumination of the slit, the observations were done in NoAO mode (without Adaptive Optics), and nights with poor seeing

conditions were requested.

Values for the central wavelengths of the telluric CO_2 lines were obtained from the HITRAN database (Rothman et al. 1998), allowing us to construct an accurate wavelength solution for each detector frame. The wavelengths of the identified stellar spectral lines were taken from the Vienna Atomic Line Database (VALD) (Kupka et al. 1999), based on the target's $T_{\rm eff}$ and $\log g$.

Dark, flat, and non-linearity corrections and the combination of the raw jittered frames in each nodding position are performed using the standard ESO CRIRES pipeline recipes. Later, the precise RV is obtained from a cross-correlation (Baranne et al. 1996) of the science spectra and the synthetic telluric and stellar mask; this is obtained for each frame and nodding position individually. We estimate the formal error of our CRIRES measurements to be of the order of $\sim$40 m s^{-1}, based on the *r.m.s.* dispersion values around the best fits for all good targets of our CRIRES sample. This error is likely to be over-estimated in particular for the η Cet data set.

The full procedure of radial velocity extraction based on the cross-correlation method will be described in more detail in a follow-up paper (Trifonov et al. 2014).

The CRIRES observations of η Cet were taken with an exposure time of 3 seconds, resulting in a S/N of $\approx$ 300. Our measured CRIRES radial velocities for η Cet are shown together with the data from Lick Observatory in Fig. 4.1, while the measured values are given in Table 4.2.

4.3 Orbital fit

Our measurements for η Cet, together with the formal errors and the best Keplerian and dynamical edge-on coplanar fits to the data, are shown in Fig 4.1. We have used the *Systemic Console* package (Meschiari et al. 2009) for fitting.

A preliminary test for periodicities with a Lomb-Scargle periodogram shows two highly significant peaks around 399 and 768 days, suggesting two sub-stellar companions around η Cet (see Fig. 4.1).

The sum of two Keplerian orbits provides a reasonable explanation of the η Cet radial velocity data (see Fig. 4.1). However, the relatively close planetary orbits and their derived minimum masses raise the question whether this planetary system suffers from sufficient gravitational perturbations between the bodies which might be detected in the observed data. For this reason we decided to use Newtonian dynamical fits, applying the Gragg-Bulirsch-Stoer integration method (B-SM: Press et al. 1992), built into *Systemic*. In this case gravitational perturbations that occur between the planets are taken into account in the model.

We use the simulated annealing method (SA: Press et al. 1992) to find whether there is more than one $\chi^2_{\rm red}$ local minimum in the data. When the global minimum is found, the derived Jacobi orbital elements from the dynamical fit are: the masses of the planets $m_{b,c}$, the periods $P_{b,c}$, eccentricities $e_{b,c}$, longitudes of periastron $\varpi_{b,c}$, and the mean anomaly $M_{b,c}$ (b always denotes the inner planet and c the outer planet). To explore the statistical and dynamical properties of the fits around the best fit, we adopt the systematic grid search techniques coupled with dynamical fitting. This technique is fully described for the HD 82943 two-planet system (Tan et al. 2013).

Table 4.3: η Cet system best fits (Jacobi coordinates).

Orb. Param.	η Cet b	η Cet c
Best Keplerian		
P [days]	403.5 ± 1.50	751.9 ± 3.8
m [$M_{\rm Jup}$]	2.55 ± 0.13	3.32 ± 0.18
e	0.13 ± 0.05	0.1 ± 0.06
M [deg]	193.5 ± 24.6	240.5 ± 34.8
ϖ [deg]	250.6 ± 20.5	67.54 ± 5.2
K_1 [m s^{-1}]	49.7	52.4
a [AU]	1.27	1.93
r.m.s. [m s^{-1}]	15.9	
RV$_{\rm offset}$ [m s^{-1}]	−0.77	
$\chi^2_{\rm red}$	13.67 (1.17 with jitter)	

Orb. Param.	η Cet b	η Cet c
Best coplanar edge-on		
P [days]	407.5 ± 2.67	739.9 ± 4.8
m [$M_{\rm Jup}$]	2.55 ± 0.16	3.26 ± 0.17
e	0.12 ± 0.05	0.08 ± 0.04
M [deg]	208.2 ± 13.7	227.8 ± 19.6
ϖ [deg]	245.4 ± 9.5	68.2 ± 22.3
K_1 [m s^{-1}]	49.4	51.6
a [AU]	1.28	1.91
r.m.s. [m s^{-1}]	15.19	
RV$_{\rm offset}$ [m s^{-1}]	0.0	
$\chi^2_{\rm red}$	11.39 (1.001 with jitter)	
Best coplanar inclined		
P [days]	396.8 ± 0.1	767.1 ± 0.27
m [$M_{\rm Jup}$]	3.85 ± 0.03	5.52 ± 0.02
e	0.24 ± 0.05	0.1 ± 0.01
M [deg]	163.3 ± 0.1	78.8 ± 0.05
ϖ [deg]	292.2 ± 0.1	221.3 ± 0.1
i [deg]	35.5	35.5
K_1 [m s^{-1}]	44.8	50.2
a [AU]	1.26	1.96
r.m.s. [m s^{-1}]	14.56	
RV$_{\rm offset}$ [m s^{-1}]	−3.28	
$\chi^2_{\rm red}$	10.89 (0.925 with jitter)	
Best mutually inclined		
P [days]	404.4 ± 2.7	748.2 ± 6.8
m [$M_{\rm Jup}$]	5.5 ± 1.08	7.74 ± 1.45
e	0.06 ± 0.06	0.05 ± 0.07
M [deg]	168.4 ± 28.1	145.3 ± 31.1
ϖ [deg]	283.7 ± 23.3	138.8 ± 70.2
i [deg]	151.7 ± 24.9	155.0 ± 34.6
$\Delta\Omega$ [deg]	345.4 ± 46.4	
K_1 [m s^{-1}]	50.2	52.1
a [AU]	1.28	1.93
r.m.s. [m s^{-1}]	14.61	
RV$_{\rm offset}$ [m s^{-1}]	−1.89	
$\chi^2_{\rm red}$	10.90 (0.95 with jitter)	

Orb. Param.	η Cet b	η Cet c
2:1 MMR coplanar edge-on		
P [days]	407.5 ± 2.67	744.5 ± 3.71
m [$M_{\rm Jup}$]	2.54 ± 0.16	3.28 ± 0.19
e	0.155 ± 0.05	0.025 ± 0.05
M [deg]	211.1 ± 45.33	268.0 ± 21.33
ϖ [deg]	244.7 ± 31.64	32.5 ± 32.72
K_1 [m s^{-1}]	49.6	51.7
a [AU]	1.28	1.92
r.m.s. [m s^{-1}]	15.28	
RV$_{\rm offset}$ [m s^{-1}]	−0.08	
$\chi^2_{\rm red}$	11.65 (1.013 with jitter)	
2:1 MMR coplanar inclined		
P [days]	407.3 ± 2.1	744.3 ± 4.1
m [$M_{\rm Jup}$]	2.46 ± 0.12	3.16 ± 0.2
e	0.17 ± 0.05	0.02 ± 0.03
M [deg]	208.9 ± 16.1	262.7 ± 41.2
ϖ [deg]	247.2 ± 13.5	36.67 ± 41.1
i [deg]	81.9	81.9
K_1 [m s^{-1}]	49.8	51.6
a [AU]	1.28	1.92
r.m.s. [m s^{-1}]	15.2	
RV$_{\rm offset}$ [m s^{-1}]	−0.58	
$\chi^2_{\rm red}$	11.84 (1.04 with jitter)	
2:1 MMR mutually inclined		
P [days]	407.8 ± 2.9	742.2 ± 4.5
m [$M_{\rm Jup}$]	2.45 ± 0.12	3.14 ± 0.17
e	0.13 ± 0.05	0.06 ± 0.04
M [deg]	209.0 ± 15.4	247.2 ± 54.5
ϖ [deg]	246.8 ± 12.7	51.1 ± 52.2
i [deg]	88.0	92.0
$\Delta\Omega$ [deg]	0.0	
K_1 [m s^{-1}]	47.7	49.5
a [AU]	1.29	1.92
r.m.s. [m s^{-1}]	15.4	
RV$_{\rm offset}$ [m s^{-1}]	−0.46	
$\chi^2_{\rm red}$	11.84 (1.03 with jitter)	

It is important to note that a good fit means that the $\chi^2_{\rm red}$ solution is close to one. In our case the best edge-on coplanar fit has $\chi^2_{\rm red}$ = 11.39 (see §4.3.1) for 118 radial velocity data points, meaning that the data is scattered around the fit, and indeed this can be seen in Fig. 4.1. The reason for that is additional radial velocity stellar jitter of the order of ∼15 m s^{-1} that is not taken

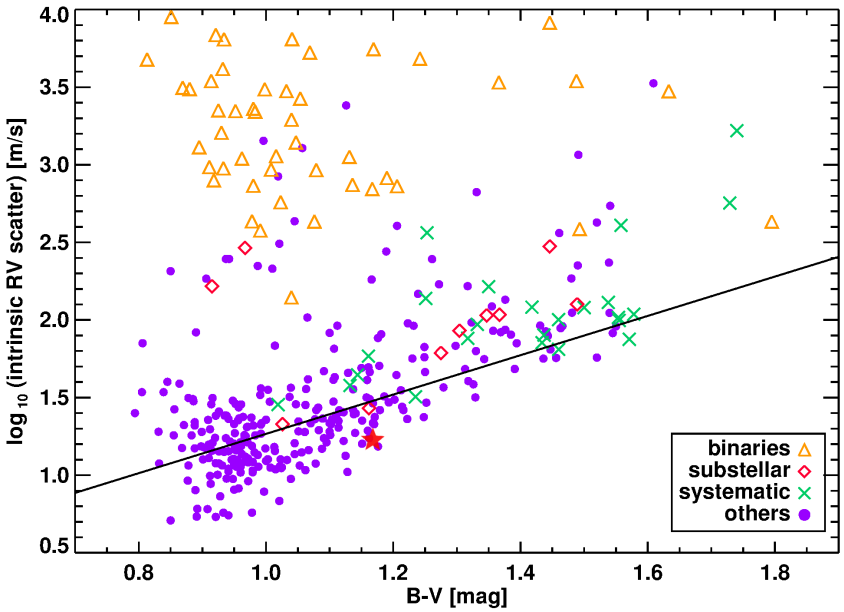

Figure 4.2: Intrinsic RV scatter observed in our sample of 373 K giants versus $B-V$ color. A clear trend is visible in the sense that redder stars with no companions (*circles*) have larger intrinsic RV variations. A number of stars lie above the almost linear relation between color and the logarithm of the scatter. These stars have clearly periodic RVs harboring a sub-stellar or stellar companions. Stars with non-periodic, but still systematic radial velocities are indicated with green crosses. The RV scatter of ~15 m s^{-1}, for η Cet (*red star*) derived as the r.m.s. around the orbital fit, is lower than the 25 m s^{-1} derived from the linear trend at the star's color index.

into account in the weights of each data point.

This jitter value has been determined directly as the r.m.s. of the residual deviation around the model. In fact, this value is close to the bottom envelope of the points in Fig. 4.2 for η Cet's color index ($B-V$ = 1.16), which is likely the minimum jitter for η Cet. Based on the long period of our study and the large sample of stars with similar physical characteristics, we found that the intrinsic stellar jitter is clearly correlated with the color index $B-V$ of the stars and, and its value for η Cet is typical for other K2 III giants in our Lick sample (see Fig. 4.2). For η Cet we have estimated an expected jitter value of 25 m s^{-1} (see Fig. 4.2), which is larger than the amount of jitter estimated from the r.m.s. of the fit. It is also known that late G giants (Frandsen et al. 2002; De Ridder et al. 2006) and K giants (Barban et al. 2004) exhibit rapid solar-like p-mode oscillations, much more rapid than the typical time sampling of our observations, and appearing as scatter in our data.

Re-assessing the $\chi^2_{\rm red}$ by quadratically adding the stellar jitter to the formal observational errors (3–5 m s^{-1}) for each radial velocity data point will scale down $\chi^2_{\rm red}$ of the best fit close to unity. For our edge-on coplanar case $\chi^2_{\rm red}$ = 11.39 is scaled down to $\chi^2_{\rm red}$ = 1.001. In this paper we provide both: the non-scaled $\chi^2_{\rm red}$ value together with the derived stellar jitter, as well as the $\chi^2_{\rm red}$ value where the average stellar jitter derived above has been taken into account.

Error estimation of the derived orbital parameters has been performed using two independent methods available as part of the *Console*: bootstrap synthetic data refitting and MCMC statistics, running multiple MCMC chains in parallel with an adaptive step length. Both estimators gave similar formal errors for the orbital parameters. However, the MCMC statistics has been proven to provide better estimates of planetary orbit uncertainties than the more robust bootstrap algorithm (i.e. Ford (2005), Meschiari & Laughlin, in preparation). Therefore, we will use only the MCMC results in this paper.

The eight near-IR Doppler points from CRIRES are overplotted in Fig. 4.1, but have not been used for fitting. The reason to not consider the CRIRES data are their large uncertainties and the negligible total weight to the fit, compared to the Lick data. Another complication is the radial velocity offset between the two datasets, which introduces an extra parameter in the χ^2 fitting procedure. Nevertheless, the CRIRES data points are in good agreement with the Newtonian fit predictions based on the optical data (see Fig. 4.1), providing strong evidence for the two planet hypothesis.

4.3.1 FORMALLY BEST EDGE-ON COPLANAR FIT

Assuming an edge-on, co-planar planetary system ($i_{b,c} = 90°$), the global minimum has $\chi^2_{\rm red} = 11.39$ (1.001 with jitter), constituting a significant improvement from the best two-Keplerian fit with $\chi^2_{\rm red} = 13.67$ (1.17 with jitter). This $\chi^2_{\rm red}$ improvement indicates that the strong interaction between the two planetary companions is visible in the radial velocity signal even on short timescales. The derived planetary masses are $m_b \sin i_b = 2.5\ M_{\rm Jup}$ and $m_c \sin i_c = 3.3\ M_{\rm Jup}$, with periods of $P_b = 407.5$ days and $P_c = 739.9$ days. The eccentricities are moderate ($e_b = 0.12$ and $e_c = 0.08$), and the longitudes of periastron suggest an anti-aligned configuration with $\varpi_b = 245.1°$ and $\varpi_c = 68.2°$ i.e. $\varpi_b - \varpi_c \approx 180°$. Orbital parameters for both planets, together with their formal uncertainties, are summarized in Table 4.3.

Dynamical simulations, however, indicate that this fit is stable only for $\lesssim 17\,000$ yrs. After the start of the integrations, the planetary semi-major axes evolution shows a very high perturbation rate with a constant amplitude. Although the initially derived periods do not suggest any low order MMR, the average planetary periods appear to be in a ratio of 2:1 during the first 17 000 years of orbital evolution, before the system becomes chaotic and eventually ejects the outer companion. This indicates that within the orbital parameter errors, the system might be in a long term stable 2:1 MMR. Such stable edge-on cases are discussed in §4.4.2 and §4.4.3. Evolution of the planetary semi-major axes for this best fit configuration are illustrated in Fig. 4.3.

4.3.2 FORMALLY BEST INCLINED FITS

We also tested whether our best dynamical fit will improve significantly by allowing the inclinations with respect to the observer's line of sight (LOS), and the longitudes of the ascending nodes of the planets to be $i_{b,c} \neq 90°$ and $\Delta\Omega_{b,c} = \Omega_b - \Omega_c \neq 0$, respectively.

The impact of the LOS inclinations on the fits mainly manifests itself through the derived

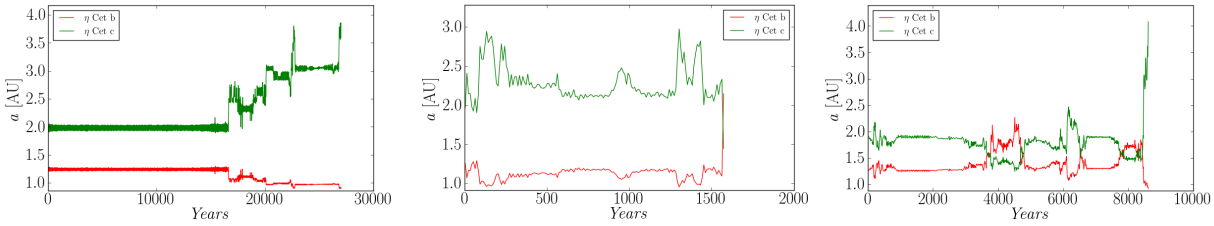

Figure 4.3: Semi-major axes evolution of the best dynamical fits. Left: The edge-on coplanar fit remains stable in a 2:1 MMR only for 17 000 years, when the system starts to show chaotic behavior and eventually ejects the outer planet. The best inclined coplanar (middle) and mutually inclined (right) fits fail to preserve stability even on very short timescales.

planetary masses. The mass function is given by

$$\frac{(m_p \sin\ i)^3}{(M_\star + m_p)^2} = \frac{P}{2\pi G} K_\star^3 \sqrt{(1-e^2)^3} \tag{4.1}$$

where m_p is the planetary mass, $M_\star$ the stellar mass and G is the universal gravitational constant, while the other parameters come from the orbital model: Period (P), eccentricity (e) and radial velocity amplitude ($K_\star$). It is easy to see that if we take $\sin\ i \neq 1$ ($i \neq 90°$), the mass of the planet must rise to satisfy the right side of the equation. However, we note that this general expression is valid only for the simple case of one planet orbiting a star. Hierarchical two-planet systems and the dependence of the minimum planetary mass on the inclination are better described in Jacobian coordinates. For more details, we refer to the formalism given in Lee & Peale (2002).

We have separated the inclined fits in two different sets, depending on whether the planets are strictly in a coplanar configuration (yet inclined with respect to the LOS), or if an additional mutual inclination angle between the planetary orbits is allowed (i.e. $i_b - i_c \neq 0°$ and Ω_b - $\Omega_c \neq 0°$).

For the inclined co-planar test we set $i_b = i_c$, but $\sin i_{b,c} \leq 1$, and we fixed the longitudes of ascending nodes to $\Omega_b = \Omega_c = 0°$. In the second test the inclinations of both planets are fitted as independent parameters, allowing mutually inclined orbits. However, i_b and i_c are restricted to not exceed the $\sin i_{b,c} = 0.42$ ($i_{b,c} = 90° \pm 65°$) limit, where the planetary masses will become very large. Also as discussed in Laughlin et al. (2002) and in Bean & Seifahrt (2009), the mutual inclination ($\Phi_{b,c}$) of two orbits depends not only on the inclinations i_b and i_c, but also on the longitudes of the ascending nodes Ω_b and Ω_c:

$$\cos\ \Phi_{b,c} = \cos\ i_b\ \cos\ i_c + \sin\ i_b\ \sin\ i_c\ \cos\ (\Omega_b - \Omega_c). \tag{4.2}$$

The longitudes of the ascending node, Ω_b and Ω_c, are not restricted and thus can vary in the range from 0 to 2π. The broad range of $i_{b,c}$ and $\Omega_{b,c}$ might lead to very large mutual inclinations, but in general $\Phi_{b,c}$ was restricted to 50°, although this limit has never been reached by the fitting algorithm.

For the coplanar inclined case, the minimum appears to be $\chi^2_{\rm red} = 10.89$, while adding the

same stellar jitter as above to the data used for the coplanar fit gives $\chi^2_{\rm red} = 0.925$. Both planets have orbits with relatively large inclinations with respect to the LOS ($i_{b,c} = 35.5°$). The planetary masses are: $m_b = 3.85\ M_{\rm Jup}$ and $m_c = 5.52\ M_{\rm Jup}$, and the planetary periods are closer to the 2:1 ratio: $P_b = 396.8$ days and $P_c = 767.1$ days.

The derived mutually inclined best fit has $\chi^2_{\rm red} = 10.90$, ($\chi^2_{\rm red} = 0.95$). This fit also has a high planetary inclinations and thus, the planetary masses are quite more massive: $m_b = 5.50\ M_{\rm Jup}$ and $m_c = 7.74\ M_{\rm Jup}$, while the periods are $P_b = 404.4$ days and $P_c = 748.2$ days. Orbital parameters and the associated errors for the inclined fits are summarized in Table 4.3. An F-test shows that the probability that the three additional fitting parameters significantly improve the model is $\sim 90\%$.

Dynamical simulations based on the inclined fits show that these solutions cannot even preserve stability on very short time scales. The large planetary masses in those cases and the higher interaction rate make these systems much more fragile than the edge-on coplanar system. The best inclined co-planar fit appears to be very unstable and leads to planetary collision in less than 1600 years. The best mutually inclined fit is chaotic from the very beginning of the integrations. During the simulations the planets exchange their positions in the system until the outer planet is ejected after $\sim$ 9000 years. The semi-major axes evolution for those systems is illustrated in Fig. 4.3.

4.4 STABILITY TESTS

4.4.1 NUMERICAL SETUP

For testing the stability of the η Cet planetary system we used the *Mercury* N-body simulator (Chambers 1999), and the *SyMBA* integrator (Duncan et al. 1998). Both packages have been designed to calculate the orbital evolution of objects moving in the gravitational field of a much more massive central body, as in the case of extrasolar planetary systems. We used *Mercury* as our primary program, and *SyMBA* to double check the obtained results. All dynamical simulations were run using the hybrid sympletic/Bulirsch-Stoer algorithm, which is able to compute close encounters between the planets if such occur during the orbital evolution. The orbital parameters for the integrations are taken directly from high density $\chi^2_{\rm red}$ grids (see §4.4.2, §4.4.3, §4.4.4 and §4.4.5) ($\sim$ 120 000 fits). Our goal is to check the permitted stability regions for the η Cet planetary system, and to constrain the orbital parameters by requiring stability.

The orbital parameter input for the integrations are in *astrocentric* format: mean anomaly M, semi-major axis a, eccentricity e, argument of periastron ω, orbital inclination i, longitude of the ascending node Ω, and absolute planetary mass derived from fit (dependent on the LOS inclination). The argument of periastron is $\omega = \varpi$ - Ω, and in cases of an edge-on or co-planar configuration Ω is undefined and thus $\omega = \varpi$. From the orbital period P and assuming $m_{b,c} \sin\ i_{b.c} \ll M_\star$, the semi-major axes $a_{b,c}$ are calculated from the general form for the two-body problem:

$$a_{b,c} = \left(\frac{GM_\star P_{b,c}^2}{4\pi^2} \right)^{1/3} \tag{4.3}$$

Another input parameter is the *Hill radius*, which indicates the maximum distance from the body that constitutes a close encounter. A Hill radius approximation is calculated from:

$$r_{b,c} \approx a_{b,c}(1 - e_{b,c}) \left(\frac{m_{b,c}}{3M_\star} \right)^{1/3} \tag{4.4}$$

All simulations were started from JD = 2451745.994, the epoch when the first RV observation of η Cet was taken, and then integrated for 10^5 years. This timescale is chosen carefully to minimize CPU resources, while still allowing a detailed study of the system's evolution and stability. In case a test system survives this period, we test whether the system remains stable over a longer period of time by extending the integration time to 10^8 years for the edge-on coplanar fits (§4.4.2), and to $2\text{x}10^6$ years in the case of inclined configurations (§4.4.3 and §4.4.4). On the other hand, the simulations are interrupted in case of collisions between the bodies involved in the test, or ejection of one of the planets. The typical time step we use for each dynamical integration is equal to 8 days, while the output interval from the integrations is set to one year. We define as ejection if one of the planet's semi-major axes exceeds 5 AU during the integration time.

In some cases none of the planets is ejected from the system and no planet-planet or planet-star collisions have occurred, but due to close encounters, their eccentricities become very large and the semi-major axes show single or multiple times planetary scattering to a different semi-major axis within the 5 AU limit. Those kind of systems show unpredictable behavior, and in our study we have classified them as *chaotic*, even though they may not satisfy the technical definition of chaos.

We define a system to be stable if the planetary semi-major axes remain within 0.2 AU from the semi-major axes values at the beginning of the simulation during the maximum integration time. This stability criterion provides us with a very fast and accurate estimate of the dynamical behavior of the system, and clearly distinguishes the stable from the chaotic and the unstable configurations. In this paper we will not discuss the scattering (chaotic) configurations, but rather we will focus on those configurations which we qualify as stable.

4.4.2 Two planet edge-on coplanar system

The instability of the best fits motivated us to start a high density $\chi^2_{\rm red}$ grid search, in order to understand the possible sets of orbital configurations for the η Cet planetary system. For constructing these grids we have used only scaled $\chi^2_{\rm red}$ fits with stellar jitter quadratically added, so that $\chi^2_{\rm red}$ is close to unity. Later, we test each individual set for stability, transforming those

grids to effective stability maps.

In the edge-on coplanar two dimensional grid we vary the eccentricities of the planets from $e_{b,c} = 0.001$ (in order to have access to $\varpi_{b,c}$) to 0.251 with steps of 0.005 (50x50 dynamical fits), while the remaining orbital parameters in the model ($m_{b,c} \sin\ i_{b,c}$, $P_{b,c}$, $M_{b,c}$, $\varpi_{b,c}$ and the RV offset) are fitted until the best possible solution to the data is achieved. The resulting $\chi^2_{\rm red}$ grid is smoothed with bilinear interpolation between each grid pixel, and 1, 2 and 3σ confidence levels (based on $\Delta\chi^2_{\rm red}$ from minimum) are shown (see Fig. 4.4). The grid itself shows that very reasonable $\chi^2_{\rm red}$ fits can be found in a broad range of eccentricities, with a tendency towards lower $\chi^2_{\rm red}$ values in higher and moderate eccentricities, and slightly worse for the near-circular orbits. However, our dynamical test of the edge-on coplanar grid illustrated in Fig. 4.4 shows that the vast majority of those fits are unstable. The exceptions are a few isolated stable and chaotic cases, a large stable region at lower eccentricities and a narrow stable island with moderate e_b, located about 1 σ away from the global minimum.

It is not surprising that the planetary system has better chances to survive with near circular orbits. In these configurations, the bodies might interact gravitationally, but at any epoch they will be distant enough to not exhibit close encounters. By direct long-term N-body integrations, we conclude that the individual fits in the low eccentricities region are stable for at least 10^8 years and none of them is involved in low order MMR. Instead the average period ratio of the stable fits in this region is between 1.8 for the very circular fits and 1.88 at the border of the stable region. This range of ratios is far away from the 2:1 MMR, but could be close to a high order MMR like 9:5, 11:6, 13:7 or even 15:8. However, we did not study these possible high order resonances, and we assume that if not in 2:1 MMR, then the planetary system is likely dominated by secular interactions.

The right column of Fig. 4.5 shows the dynamical evolution of the most circular fit from Fig. 4.4 with $\chi^2_{\rm red} = 14.1$, ($\chi^2_{\rm red} = 1.22$), $m_b \sin i_b = 2.4\ M_{\rm Jup}$, $m_c \sin i_c = 3.2\ M_{\rm Jup}$, $a_b = 1.28$ AU, $a_c = 1.94$ AU. We started simulations with $e_{b,c} = 0.001$, and the gravitational interactions forced the eccentricities to oscillate very rapidly between 0.00 and 0.06 for η Cet b, and between 0.00 to 0.03 for η Cet c. The arguments of periastron ω_b and ω_c circulate between 0 and 360°, but the secular resonant angle $\Delta\omega_{b,c} = \omega_c - \omega_b$, while circulating, seems to spend more time around 180° (anti-aligned). Within the stable near-circular region, the gravitational perturbations between the planets have lower amplitudes in the case of the most circular orbits compared to other stable fits with higher initial eccentricities (and smaller $\chi^2_{\rm red}$).

The middle column of Fig. 4.5 illustrates the best $\chi^2_{\rm red}$ fit within the low-eccentricity stable region with $\chi^2_{\rm red} = 13.03$ ($\chi^2_{\rm red} = 1.13$) and initial orbital parameters of $m_b \sin i_b = 2.4\ M_{\rm Jup}$, $m_c \sin i_c = 3.2\ M_{\rm Jup}$, $a_b = 1.28$ AU, $a_c = 1.93$ AU, $e_b = 0.06$, and $e_c = 0.001$. The mean value of $\Delta\omega_{b,c}$ is again around 180°, while the amplitude is $\approx \pm\ 90°$. Immediately after the start of the integrations e_c has increased from close to 0.00 to 0.07, and oscillates in this range during the dynamical test, while e_b oscillates from 0.05 to 0.11. In particular, the maximum value for e_b is very interesting because, as can be seen from Fig. 4.4, starting integrations with $0.08 < e_b < 0.11$ in the initial epoch yields unstable solutions. The numerical stability of the system appears to be strongly dependent on the initial conditions that are passed to the integrator. For different epochs the gravitational perturbations in the system would yield different orbital parameters than

derived from the fit, and starting the integrations from an epoch forward or backward in time where e_b or e_c are larger than the $e_{b,c} = 0.08$ limit might be perfectly stable.

We investigated the orbital evolution of a large number of fits in the low eccentricities region and we did not find any aligned system configuration. Instead, all systems studied with near circular configurations seem to settle in a secular resonance where $\Delta\omega_{b,c} \approx 180°$ shortly after the start of the integrations, and exhibit a semi-chaotic behavior. This is expected as the system's secular resonance angle $\Delta\omega_{b,c}$ will circulate or librate, depending on the initial $\Delta\omega_{b,c}$ and eccentricity values at the beginning of the stability test (e.g. Laughlin et al. 2002; Lee & Peale 2003). The fits in the near circular island always favor $\Delta\omega_{b,c} \approx 180°$, and thus the system spends more time during the orbital evolution in this anti-aligned configuration.

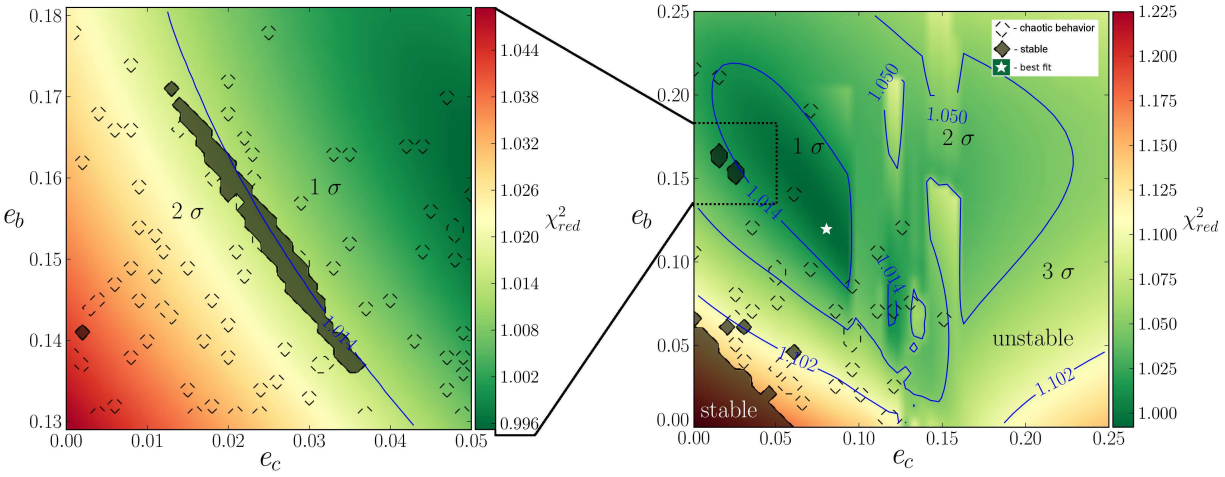

Figure 4.4: Right: Edge-on coplanar $\chi^2_{\rm red}$ grid with jitter included. The eccentricities of both planets are varied in the range from 0.001 to 0.251 with steps of 0.005, while the other orbital parameters and the zero-point offset were fitted until the $\chi^2_{\rm red}$ minimum is achieved. The solid black contours indicate the stable fits, while the dashed contours indicate fits where the system survives the dynamical tests, but with *chaotic* scattering behavior. While the best dynamical fit is unstable (*white star*), we found two stability islands where long-term (10^8 yrs) stability is achieved. With a moderate e_b, at the 1σ border (blue contours), a stable 2:1 MMR region exists, and at lower eccentricities a broad stability region can be seen at more than 3σ from the best fit, without showing any signs of a low order MMR. Left: Higher resolution zoom of the stable 2:1 resonant region.

4.4.2.1 Narrow 2:1 MMR region

The low-eccentricity island is located further away from the best co-planar fit than the 3σ confidence level, so we can neither consider it with great confidence nor reject the possibility that the η Cet system is perfectly stable in a near circular configuration. Thus, we focus our search for stable configurations on regions closer to the best fit. In the edge-on coplanar (e_b, e_c) grid (Fig. 4.4), we have spotted a few fits at the 1σ border that passed the preliminary 10^5 years stability test. The additional long-term stability test proves that three out of four fits are stable for 10^8 years.

To reveal such a set of stable orbital parameters, we create another high density (e_b, e_c) grid around these stable fits. We started with $0.131 \geq e_b \geq 0.181$ and $0.001 \geq e_c \geq 0.051$ with steps of 0.001 (50x50 fits). The significant increment of the resolution in this (e_b, e_c) plane reveals a narrow stable island, where the vast majority of the fits have similar dynamical evolution and are stable for at least 10^8 years (see left panel of Fig. 4.4).

4.4.2.2 STABLE NEAR-CIRCULAR CONFIGURATION

The derived initial planetary periods for those fits are very close to those from the grid's best fit (§4.3.1) and initially do not suggest any low-order MMR. However, the mean planetary periods during the orbital evolution show that the system might be efficiently trapped in a 2:1 MMR. This result requires close examination of the lowest order eccentricity-type resonant angles:

$$\theta_b = \lambda_b - 2\lambda_c + \varpi_b, \quad \theta_c = \lambda_b - 2\lambda_c + \varpi_c \tag{4.5}$$

where $\lambda_{b,c} = M_{b,c} + \varpi_{b,c}$ is the mean longitude of the inner and outer planet, respectively. The resonant angles θ_b and θ_c librate around ~0° and ~180°, respectively, for the whole island, leaving no doubt about the anti-aligned resonance nature of the system. θ_b and θ_c librate in the whole stable region with very large amplitudes of nearly ±180°, so that the system appears to be very close to circulating (close to the separatrix), but in an anti-aligned planetary configuration, where the secular resonance angle $\Delta\omega = \theta_b - \theta_c = \omega_b - \omega_c$ librates around 180°. A similar behavior was observed during the first 17 000 years of orbital evolution of the best edge-on coplanar fit from §4.3.1. These results suggest that systems in the (e_b, e_c) region around the best edge-on fit are close to 2:1 MMR, but also appear to be very fragile, and only certain orbital parameter combinations may lead to stability.

Fig. 4.5 (left column) illustrates the orbital evolution of the system with the best stable fit from the resonant island; the initial orbital parameters can be found in Table 4.3. The eccentricities rapidly change with the same phase, reaching moderate levels of $e_b = 0.15 \ldots 0.25$ and $e_c = 0.0 \ldots 0.08$, while the planetary semi-major axes oscillate in opposite phase, between $a_b = 1.21 \ldots 1.29$ AU and $a_c = 1.92 \ldots 2.06$ AU. During the dynamical test over 10^8 years $\Delta\omega_{b,c}$ librates around 180° with amplitude of $\approx \pm 15°$, while the ω_b and ω_c are circulating in an anti-aligned configuration.

4.4.3 COPLANAR INCLINED SYSTEM

In order to create coplanar inclined grids we have used the same technique as in the edge-on coplanar grids, with additional constraints $i_b = i_c$ and $i_{b,c} \neq 90°$. We kept $\Omega_{b,c} = 0°$ as described in §4.3.2, so that we get an explicitly coplanar system. A set of grids concentrated only on the 2:1 MMR stable island are shown in Fig. 4.6 (left panel), and larger grids for the low eccentricities region are shown in the right panel of Fig. 4.6, respectively. For reference,we placed the two grids from Fig. 4.4 with $\sin i = 1$ on the top of Fig. 4.6. This coplanar inclined test shows how

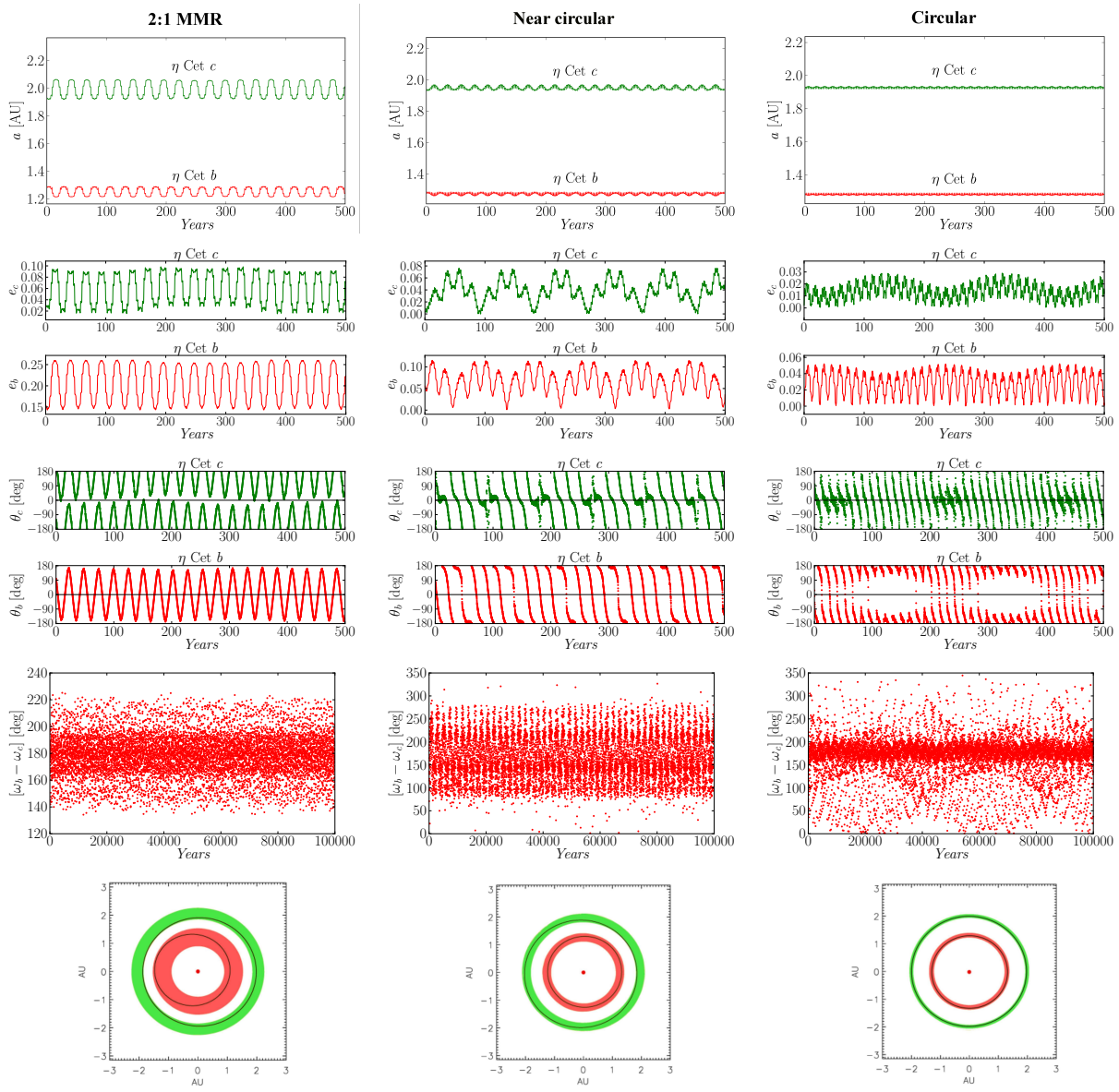

Figure 4.5: Evolution of the orbital parameters for three different fits, stable for at least 10^8 years. the best 2:1 MMR fit (left panels), the best stable fit from the low-eccentricity region (middle panels), and the fit with the most circular orbits (right panels). In the 2:1 MMR fit the gravitational perturbation between the planets is much higher than in the other two cases. It is easy to see that eccentricities for given epochs can be much larger than their values at the initial epoch of the integration. For convenience the evolution of the semi-major axes, eccentricities, the resonant angles (third row) and the $\Delta\omega_{b,c}$ are given for 500 and 10^5 years, respectively. The bottom row gives the orbital precession region, the sum of orbits for each integration output.

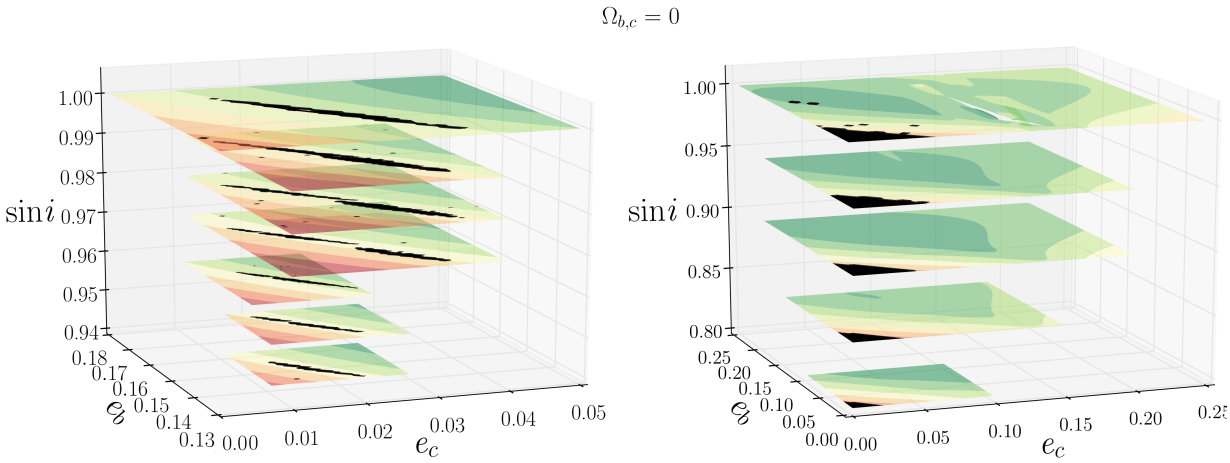

Figure 4.6: Coplanar inclined grids illustrate the stability dependence on $m_{b,c} \sin i_{b,c}$. Color maps are the same as in Fig. 4.4 with the difference that for clarity only the stable regions are shown (filled with black color). The top layer shows the grids from Fig. 4.4, where $\sin i_{b,c} = 1$ ($i_{b,c} = 90°$). Decreasing the inclination leads to smaller near-circular and 2:1 MMR stability regions. The resonant region shrinks and moves in the (e_b, e_c) plane, and it completely vanishes when $\sin i \leq 0.93$. The stable island at low eccentricities vanishes at $\sin i \leq 0.75$, when even the most circular ($e_{b,c} = 0.001$) fit is unstable.

the stable islands behave if we increase the planetary masses via the LOS inclination. We have limited the grids with $\sin i \neq 1$ in Fig. 4.6 to a smaller region in the (e_b, e_c) plane than the grids from Fig. 4.4 in order to use CPU time efficiently, focusing on the potentially stable (e_b, e_c) space and avoiding highly unstable fit regions.

The smaller grid area however is compensated with greater resolution, as those grids have between 3 600 and 10 000 fits. For simplicity we do not show the chaotic configurations, but illustrate only the stable fits that survived the maximum evolution span of 10^5 years (dark areas) for this test in Fig. 4.6. Studying the near circular stable region, we have decreased $\sin i$ with a step size of 0.05 in the range from 1 to 0.80. The five stability maps of Fig. 4.6 (right panel) clearly show the tendency that the near circular stable region becomes smaller when the planetary mass increases with decreasing $\sin i$. The stable island near circular orbits preserves stability down to $\sin i \approx 0.75$ ($i \sim 49$ deg), when even the most circular fit ($e_{b,c} = 0.001$) becomes unstable.

The 2:1 MMR region strongly evolves and also decreases in size while decreasing $\sin i$. When $\sin i \approx 0.94$ ($i \approx 70°$), the 2:1 MMR region is smallest and completely vanishes when $\sin i \leq 0.93$. We find that the maximum stable area appears for the case $\sin i = 1$, and thus, there is a high probability that the η Cet system is observed nearly edge-on and involved in an anti-aligned 2:1 MMR. The repeated tests with *SyMBA* for $2\text{x}10^6$ years, show consistency with the *Mercury* results, although the stability regions were somewhat smaller. This is due to the longer simulations which eliminate the long term unstable fits. Integrating for 10^8 years may leave only the true stable central regions, however, such a long term dynamical test over the grids require much longer CPU time that we had for this study.

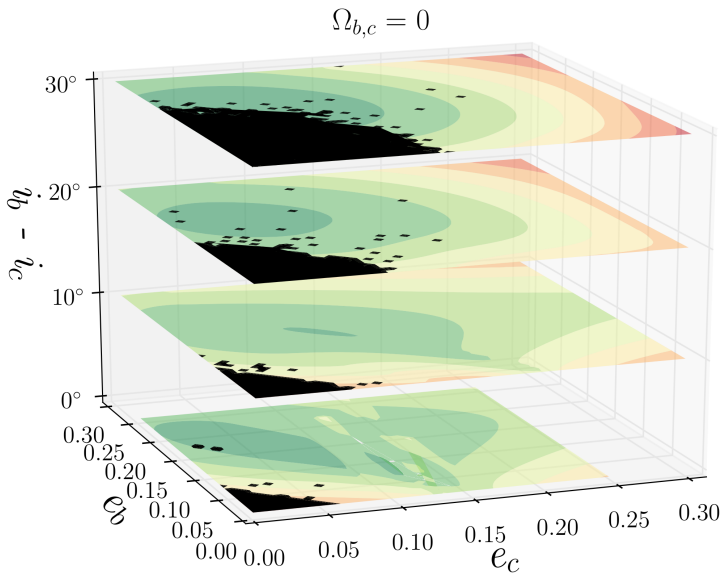

Figure 4.7: Mutually inclined grids where $\Omega_{b,c} = 0$, and the mutual inclination comes only from $\Delta i_{b,c} = i_b - i_c$. The low eccentricities stable island increases its size by assuming larger mutual inclinations, eventually creating an overlap with the 1σ confidence level from the grid's best fit (dark green contours).

4.4.4 Mutually inclined system

Constraining the mutual inclination only from the RV data is very challenging, even for well-known and extensively studied extrasolar planetary systems, and requires a large set of highly precise RV and excellent astrometric data (see Bean & Seifahrt 2009). For η Cet, the number of radial velocity measurements is relatively small, so that we cannot derive any constraints on the mutual inclination from the RV. We tried to derive additional constraints on the inclinations and/or the ascending nodes of the system from the Hipparcos Intermediate Astrometric Data, as is done in Reffert et al. (2006) for other systems. We found that all but the smallest inclinations (down to about 5 °) are consistent with the Hipparcos, so no further meaningful constraints could be derived.

We have shown in §4.4.2 and §4.4.3 already that, most likely, we observe the η Cet planetary system nearly edge-on, as we find a maximum of stable fits at $\sin i = 1$, in line with the Hipparcos constraint. Assuming smaller inclinations, the size of the stability region in the (e_b, e_c) plane decreases. Having constrained the system's inclination only by stability criteria, it would be interesting to see whether the stability will sufficiently increase if we allow mutual inclination between the orbits to occur in our fits, or whether the system will become more unstable compared to the coplanar fits. Also, as we have shown in §4.3.2, by adding three additional fitting parameters we get significantly better fits (although very unstable), and it is important to see if we can find any stable solutions or even stable islands for highly inclined non-coplanar configurations.

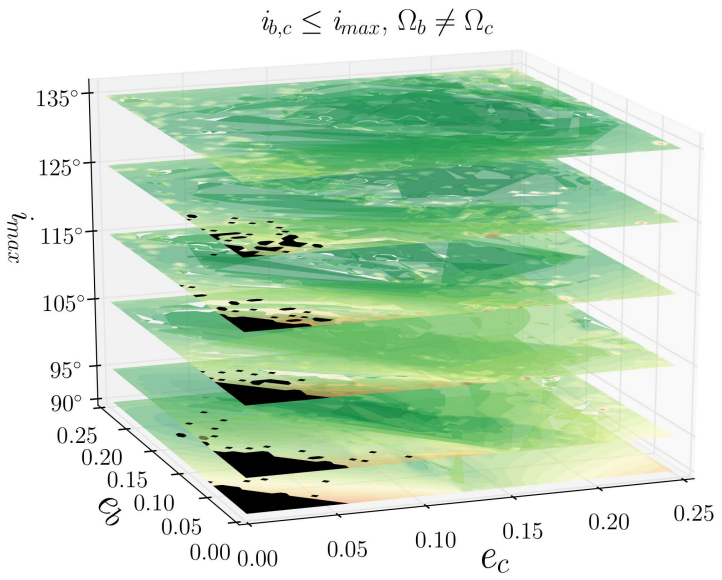

Figure 4.8: Grids with mutual inclination dependent on $\Delta\Omega_{b,c}$ and $i_{b,c} \leq i_{\max}$. During the fitting the mutual inclinations from the grids are very small, on the order of $\sim 3°$. The stability area has a maximum at $i_{\max} = 95°$, slightly larger than the coplanar grid at 90°. The stability decreases at larger $i_{\max}$ due to the larger planetary masses and the stronger perturbations. There is no stable solution at $i_{\max} = 135°$.

In order to study the dynamics of the η Cet system for mutually inclined orbits we investigate the stability with the following three different strategies:

1) We fix the $\Delta i_{b,c}$ to be constant, and we assume $\Omega_{b,c} = 0°$, so the mutual inclination depends only on $i_{b,c}$. We define $\Delta i_{b,c} = i_b$-i_c, where for the 2:1 MMR region the $i_b = 89.5°$, 89°, 88.5° and $i_c = 90.5°$, 91°, 91.5°. We found that the size of the 2:1 MMR stable region decreases very fast with mutual inclination, and after $\Delta i_{b,c} > 2°$ the 2:1 MMR island completely vanishes. For the global (e_b, e_c) grid we define $i_b = 85°$, 80°, 75° and $i_c = 95°$, 100°, 105°. The results from this test are illustrated in Fig. 4.7. From the grid we found that the low eccentricities stable region shows a trend of expanding its size with the mutual inclination for $\Delta i_{b,c} = 10°$ and 20°. When $\Delta i_{b,c} = 30°$ the stable area expands and we find many stable fits for moderate e_c within the 1σ confidence region from the $\Delta i_{b,c} = 30°$ grid. This test shows that in case of large mutual inclination there is a high probability for the system to have near circular orbits, or moderate e_c.

2) We again rely on the (e_b, e_c) grids, where additional free parameters in the fits are $i_{b,c}$ and $\Omega_{b,c}$. However, in the fitting we restricted the minimum inclination to be $i_{b,c} = 90°$ and the $\sin i_{\max}$ factor comes only from inclination angles above this limit. In this test we study only the global (e_b, e_c) plane, without examining the 2:1 MMR region separately. Initially, for the first grid we set $\sin i_{\max} = 0.707$ ($i_{\max} = 135°$), while $\Omega_{b,c}$ is unconstrained and can vary across the full range from 0 to 2π. Later we constructed grids by decreasing the maximum allowed inclination to $\sin i_{\max}$ = 0.819, 0.906, 0.966 and at last 0.996 ($i_{\max} = 125°$, 115°, 105°, and 95°, respectively), thereby decreasing the upper limit on the planetary masses and mutual inclination angle $\Delta i_{b,c}$. In all grids we allow $i_b \neq i_c$ and $\Omega_b \neq \Omega_c$ as we discussed in §4.3.2. We find that when increasing $i_{\max}$, the grid's χ^2_{red} values became better, and the planetary $i_{b,c}$ are usually close to $i_{\max}$. The obtained

$\Delta\Omega_{b,c}$ is also very small, favoring small mutual inclinations in this test. When $i_{\max} = 95°$ the average mutual inclination over the grid is 0.22° making the grid nearly coplanar. In this case the planetary masses are only $\sim 0.5\%$ higher than their minimum, which has a negligible effect on the stability. However, the very small orbital misalignment in those systems seems to have a positive influence on system stability, and we find slightly more stable fits compared to the edge-on coplanar case discussed in §4.4.2 (see Fig. 4.8).

At larger $i_{\max}$ the $\chi^2_{\rm red}$ distribution in general has lower values, but the size of the stability region is decreasing. This is probably due to the increased planetary masses and the stronger gravitational perturbations in the dynamical simulations. There is not even one stable solution at $i_{\max} = 135°$, but we have to note that there are many *chaotic* fits that survived the 10^5 yr test, which are not shown in Fig. 4.8.

3) Because of the resulting small mutual inclination in the second test, we decided to decouple the planetary orbits and to test for larger mutual inclinations by allowing $\Delta\Omega_{b,c} \neq 0$, in contrast to the first test where $\Delta\Omega_{b,c} = 0$. We constructed a grid of best fits for fixed $i_{b,c}$ (i_b, i_c grid). The planetary inclination $i_{b,c}$ is increased from 90° to 140° with steps of 1°, while rest of the orbital parameters are free in the fitting. This test attempts to check for stability for almost all the possible mutual inclinations in the system. Fig. 4.9 illustrates the stability output in the (i_b, i_c) plane. The $\chi^2_{\rm red}$ solutions in this grid have lower values when $i_b \approx i_c$ (close to coplanar configuration), and have a clear trend of better fits when the LOS inclination is large. However, we could not find any stable configuration near the coplanar diagonal of best fits from $i_{b,c} = 90°$ to 140°. There are many chaotic survivals and few stable islands at higher mutual inclinations, more than 3σ away from the grid minimum.

We are aware of the fact that, when including the $i_{b,c}$ and $\Omega_{b,c}$ in the fitting model, the parameter space becomes extremely large, and perhaps many more smaller and possibly stable minima might exist, but we have not been able to identify any in this study.

4.4.5 Impact of stellar mass on the stability analysis

Finally, we have tested how the change of stellar mass will influence the stability in (e_b, e_c) space. We generate coplanar edge-on $\chi^2_{\rm red}$ grids by assuming different stellar masses, using the values in Table. 4.1. We take the same (e_b, e_c) grid area and resolution as those discussed in §4.4.2 (Fig. 4.4), and we started our grid search with 1 $M_\odot$ and 1.4 $M_\odot$, which are the lower and upper stellar mass limits for η Cet proposed by Berio et al. (2011), respectively. Next we assume 1.3 $M_\odot$ from Luck & Challener (1995), then 1.84 $M_\odot$, which is the upper limit from Reffert et al. (2014), and we already have the 1.7 $M_\odot$ grid from §4.4.2 . The maximum integration time applied to the stability test for these grids is 10^5 years.

Stability results are shown in Fig. 4.10, which clearly shows a trend of higher stability with larger stellar mass. Our starting mass of 1 $M_\odot$ leads almost to the disappearance of the low eccentricities stable island, and only few stable solutions can be seen for very circular orbits. Increasing the stellar mass to 1.3 $M_\odot$, 1.4 $M_\odot$ and 1.7 $M_\odot$ reveals larger stable areas at low eccentricities. Finally, in the 1.84 $M_\odot$ grid we see the largest low eccentricities stable island in

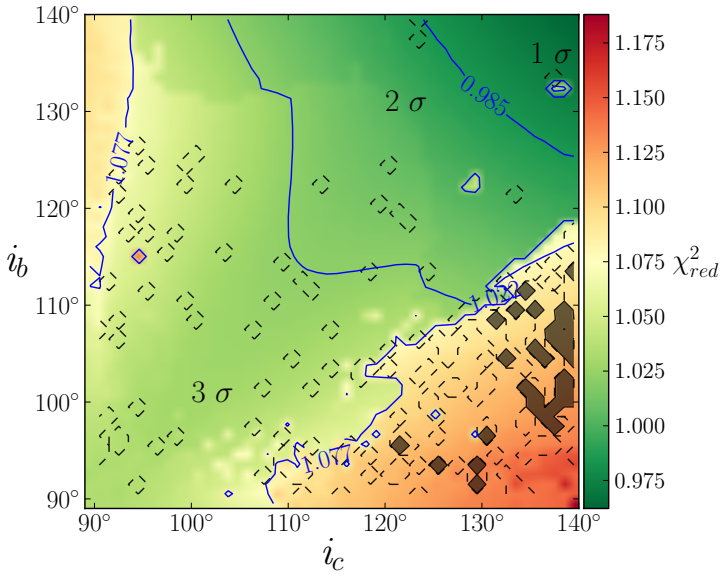

Figure 4.9: Except for the inclinations the remaining orbital parameters are free to vary for the (i_b, i_c) grid (50x50 fits). The $\chi^2_{\rm red}$ solutions suggest a higher LOS inclination and close to coplanar configurations. There are no obvious stable solutions near the coplanar diagonal of best fits from $i_{b,c}$ = 90° to 140°). Instead, there are many chaotic survivals and few stable islands at higher mutual inclinations, more than 3 σ away from the grid minimum.

our test.

Similarly, the 2:1 MMR region evolves and decreases in size with decreasing η Cet mass. No resonant island is seen at 1 $M_\odot$. However, the 2:1 MMR region has a larger area at 1.7 $M_\odot$ than in the 1.84 $M_\odot$ grid.

This effect comes from the fact that starting the fitting process with lower stellar mass will also scale down the whole planetary system. The derived orbital angles and the periods from the dynamical fitting will remain almost the same in the (e_b, e_c) grids when fitting from 1 $M_\odot$ to 1.84 $M_\odot$. However, as can be seen from equations (1), (3) and (4), the planetary masses, semi-major axes $a_{b,c}$ and the Hill radii $r_{b,c}$ are dependent on the stellar mass. By scaling down the planetary masses, we would expect the gravitational interactions between the planets to be less destructive, and we would thus expect more stable fits when adopting a lower mass for the primary. This is exactly the opposite of what can be seen in Fig. 4.10. It turns out that the dynamical simulations are much more sensitive to $\Delta a_{b,c} = a_c - a_b$ than to the planetary mass ratio. From equations (4) and (5) it can be seen that $r_{b,c}$ will slightly decrease when assuming a lower stellar mass, although not as fast as the $a_{b,c}$ will decrease. $\Delta a_{b,c}$ for the 1 $M_\odot$ grid is on average $\approx$ 0.54 AU, and for the 1.84 $M_\odot$ grid $\approx$ 0.65 AU. The more similar planetary semi-major axes in lower stellar mass systems leads to more close encounters during the orbital evolution, and thus, to a higher ejection rate, especially for fits with higher $e_{b,c}$. On the other hand, the $\Delta a_{b,c}$ for the grid with maximum mass for η Cet (1.84 $M_\odot$) is enough to keep the two planets well separated, and the stability region in lower eccentricities increases.

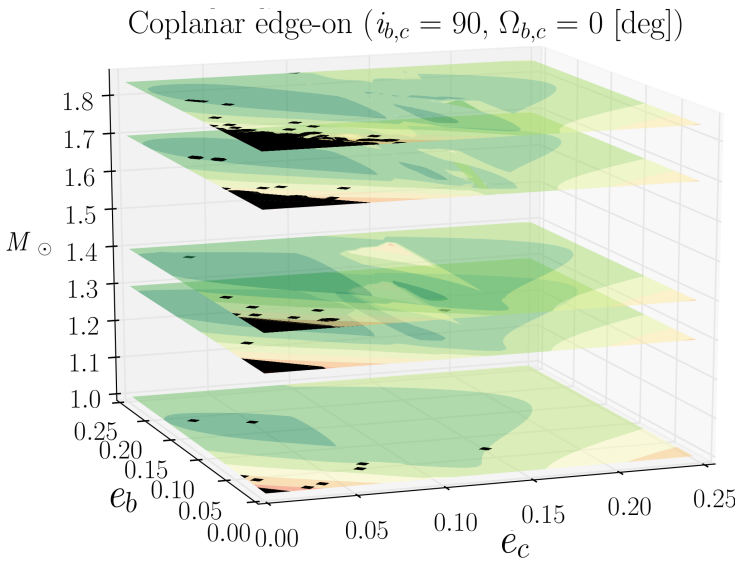

Figure 4.10: Stability maps with different initial masses for η Cet. A clear stability trend can be seen in the (e_b, e_c) grids in the sense that increasing the stellar mass up to the maximum of 1.84 $M_\odot$ the size of the stable region increases as well.

4.5 Discussion

4.5.1 Giant stars planetary population

With the detection of the first extrasolar planet around a giant star ι Dra b (the first planet announced from our Lick sample – Frink et al. (2002)) the search for planets around evolved intermediate mass stars has increased very rapidly. Several extrasolar planet search groups are working in this field, to provide important statistics when it comes to planet occurrence rate as a function of stellar mass, evolutionary status, and metallicity (Frink et al. 2001; Sato et al. 2003; Hatzes et al. 2006; Niedzielski et al. 2007; Döllinger et al. 2009b; Mitchell et al. 2013& etc.). Up to date there are 56 known planets around 53 giants stars in the literature and all of them are in wide orbits.

Except for the η Cet discovery, there are only three multiple planetary systems known orbiting giant stars, and all of them show evidence of two massive substellar companions. Niedzielski et al. (2009a,b) reported planetary systems around the K giants HD 102272 and BD +20 2457. While the radial velocity measurements of HD 102272 are best modeled with a double Keplerian, an initial stability test based on the published orbital parameters shows very fast collision between the planets. This appears to be due to the very eccentric orbit of the outer planet which leads to close encounters, making the system unstable. The case of BD +20 2457 is even more dramatic. The best fit solution suggests one brown dwarf and a very massive planet just at the brown dwarf mass border, with minimum masses of $m_1 \sin i_1 \approx 21.4\ M_{\rm Jup}$ and $m_2 \sin i_2 \approx 12.5\ M_{\rm Jup}$, respectively (1 is the inner and 2 outer planet). This system has very close orbital periods of $P_1 = 379.63 \pm 2$ days and $P_2 = 622 \pm 10$ days for such a massive pair, and the gravitational

interactions are extremely destructive. We have tested several orbital parameter sets within the derived parameter errors and, without making any comprehensive stability analysis, so far we could not find any stable configuration for BD +20 2457. However, we have to caution that the formal best fit for η Cet was also unstable, and only after an extensive stability analysis we have found long term stable regions. In this context we do not exclude the possibility that HD 102272 and BD +20 2457 do indeed harbor multiple planetary systems, but more efforts must be undertaken to prove the stability, perhaps including highly mutually inclined configurations, or even better constraints on the stellar masses.

Of particular interest is also the system around the K giant ν Oph (Quirrenbach et al. 2011; Sato et al. 2012), which is consistent with two brown dwarfs with masses $m_1 \sin i_1 \approx 22.3\ M_{\rm Jup}$, $m_2 \sin i_2 \approx 24.5\ M_{\rm Jup}$. The two brown dwarfs exhibit a clear 6:1 MMR, with periods of $P_1 = 529.9 \pm 0.1$ days and $P_2 = 3184 \pm 7$ days.

Although ν Oph and potentially BD +20 2457 are not planetary systems, they may present important evidence for brown dwarf formation in a circumstellar disk. Such objects may form because in general the more massive stars should have more massive disks from which protoplanetary objects can gain enough mass to become brown dwarfs. It might be possible for the 6:1 resonance configuration of ν Oph to have formed via migration capture in a proto-planetary disk around a young intermediate-mass progenitor, and the brown dwarf occurrence may be rather high (Quirrenbach et al. 2011).

Therefore, if we exclude those two brown dwarf systems and the HD 102272 system which suffers from stability issues, the η Cet plane

4.5.2 THE UNIQUE η CET'S ORBITAL CONFIGURATION

The stable solutions from the 2:1 MMR region in the edge-on coplanar and inclined tests raise some important questions about the possible formation and evolution of the η Cet planetary system. The $\theta_b \approx 0^\circ$ and $\theta_c \approx 180^\circ$ 2:1 MMR configuration is similar to that of the 2:1 resonance between the Jovian satellites Io and Europa, but the Io-Europa configuration is not supposed to exist for relatively large eccentricities (see Beaugé et al. 2003; Lee 2004). The average e_b (~ 0.2) and e_c (~ 0.05) for η Cet are much larger than the e_b,e_c boundary where the $\theta_b \approx 0^\circ$ and $\theta_c \approx 180^\circ$ configuration exists. An aligned configuration with both θ_b and θ_c librating about 0° is expected for mass ratio $m_b/m_c \approx 0.77$ and the eccentricities in the 2:1 MMR region.

One possible stabilizing mechanism for the η Cet system might be the large libration amplitudes of both θ_b and θ_c, which are almost circulating. We have made some preliminary attempts and failed to find a small libration amplitude counterpart. More work is needed to understand the stability of this 2:1 MMR configuration, as well as its origin if η Cet is indeed in this configuration.

We cannot fully exclude that the true system configuration of η Cet corresponds to some of the single isolated stable fits that we see in the stability maps, and neither can we exclude one of the numerous fits stable for 10^8 years which show a scattering chaotic behavior. A non-resonant system in near circular orbits is also possible.

4.6 Summary

We have reported the discovery of a planetary system around the K giant star η Cet. This discovery is the result of a long-term survey, which aims to discover planetary companions around 373 intermediate-mass G and K giant stars, and which started back in 1999 at Lick Observatory. We present 118 high precision optical radial velocities based on the observations with the Hamilton spectrograph at Lick Observatory and eight near-infrared data points from the ESO CRIRES spectrograph, all together covering more than a decade.

We have fitted a dynamical model to the optical data, which ensures that any possible gravitational interactions between the planets are taken into account in the fitting process. We show that the dynamical model represents a significant $\chi^2_{\rm red}$ improvement over the double Keplerian fit.

In an attempt to characterize the most likely planetary configuration, we performed an extensive stability analysis of the η Cet system. We have made a large variety of high resolution co-planar and inclined dynamical $\chi^2_{\rm red}$ grids, which we have used as an input for our numerical analysis. Thus, we transformed those grids into detailed stability maps. In total, we have carried out more than 200 000 dynamical integrations with typical time spans of 10^5 and $2\text{x}10^6$ years, and we extended the test to 10^8 years when studying the edge-on coplanar case.

For the edge-on coplanar grid we used a set of best fits for fixed e_b and e_c. We find that the η Cet system can be stable for at least 10^8 years, locked in a 2:1 MMR in a region with moderate e_b, that lies about 1σ away from the best co-planar fit. A much larger non-resonant stable region exists with nearly circular orbits, although it is located more than 3σ away from the best fit and is thus less likely. In the 2:1 MMR region all fits are in an anti-aligned planetary configuration and very close to the separatrix. The low-order eccentricity type resonant angles θ_b and θ_c librate around 0° and 180° respectively, but with very large amplitudes of $\approx \pm 180^\circ$. A similar near separatrix behavior can be seen in the stable fits with near circular orbits, where the secular resonance angle $\Delta\omega_{b,c}$ circulates, but during most of the simulation the planetary configuration is anti-aligned ($\Delta\omega_{b,c} \approx 180^\circ$).

We provide a detailed set of (e_b, e_c) coplanar inclined stability maps, showing that the η Cet system is very likely observed in a near edge-on configuration ($i_{b,c} \approx 90^\circ$). The size of the stable region is largest when the system is assumed to have $i_{b,c} = 90^\circ$, and when we increase the planetary mass via $\sin i_{b,c}$, the size of the two stability regions in the (e_b, e_c) plane becomes smaller. The 2:1 MMR stable island totally disappears when $i_{b,c} \approx 70^\circ$, while the near circular stable island survives until the LOS inclination becomes $i_{b,c} \sim 49^\circ$. Going below the last inclination limit, all the fits in the (e_b, e_c) plane become unstable.

We also present results from a grid based on mutually inclined configurations, although we point out that they need not be exhaustive. This is due to the large amount of computational time needed when the parameter space is expanded. Another way of constraining the mutual inclination would be a very extensive and precise radial velocity and astrometric data set, which is so far not available for η Cet.

The most important conclusion from the inclined dynamical test is that the planets cannot be more massive than a factor of $\sim$1.4 heavier than their suggested minimum masses. Larger

inclinations, and thus larger planetary masses, lead to instability in all cases. This excludes the possibility of two brown dwarfs purely based on stability considerations, and strongly favors a planetary system.

We have also tested how the uncertainty of the stellar mass will affect the dynamical stability of the system. Decreasing the stellar mass leads to a smaller size of the stable region in the (e_b, e_c) grids, and thus we conclude that the stellar mass value from Reffert et al. (2014) is indeed a very reasonable estimate.

The η Cet system is only the fourth known multiple substellar system around a G or K giant star, and is the only one for which the truly planetary nature and the long-term stability have been demonstrated. The η Cet system presents an important milestone for understanding planetary formation and evolution as a function of stellar mass, metallicity and age.

CHAPTER 5

PLANETS AND PLANETARY SYSTEMS

Finding extrasolar planets around giants is an important task. Compare to the MS stars, this type of stars in most cases are products of more massive intermediate mass stars progenitors. Young intermediate mass stars, however, are not good targets for a Doppler study due to the lack of deep and sharp stellar lines in their spectra, which are necessary for precise RV extraction. Hence, by studying the planetary occurrence around giant stars, one can make a solid conclusions on the planet formation rate around stars with higher masses. As it was shown in §1.3, this task is not trivial, even if one uses a high precision spectroscopy data such as that obtained with the Hamilton spectrograph at Lick (see §2). Spots are still expected to produce radial velocity variations that can fake a Doppler curve caused by a planet. Also, $g-$mode non-radial pulsations (or pulsations of unknown nature) can make the picture even more complicated.

In this Chapter are introduced few planetary systems found in our K giant sample, which have passed the near-IR and the stability test criteria. Subsection §5.1 gives details about the Jovan planet around the K giant 91 Aqr. Based on our Lick and VLT data sets, this planet was announced by Mitchell et al. (2013), together with a brown dwarf companion around τ Gem (§6.1). In this work are given slightly different orbital solution and estimated uncertainties for 91 Aqr b. Also, an improved near-IR radial velocities for 91 Aqr from CRIRES are presented. In §5.2 are shown our Lick and CRIRES data for ϵ Tau, which confirms the massive planet announced by Sato et al. (2007). The rest of the planetary companions in this chapter are members of multiple planetary systems, where additional dynamical stability test has been performed.

The first planetary system ever discovered around giant star – ι Dra (Frink et al. 2002) is discussed in §5.3. This system is well studied and is known to have an additional RV linear trend possibly caused by another distant companion. For a first time the ι Dra radial velocity signal is tested for signs of gravitational perturbations between ι Dra b and the hypothetical companion ι Dra c. Based on the dynamical fits, For this system are performed deep and conclusive stability analysis, characterizing the ι Dra c's orbit and mass. This test with a great confidence proves the existents of a second planetary object around ι Dra.

In §5.4 is announced a planetary system around the K giant HR 5678. From the Lick RV signal can be easily identified a Jovan planet orbiting at 1.4 AU. In addition, the best dynamical fit has significantly better $\chi^2_{\rm red}$ value, if the system is multiple suggesting that another massive planet orbiting at 6 AU. The multiple system is long-term-stable and has passed the near-IR radial velocity test, which confirms at least the periodicity caused from the inner planet.

In §5.5 is discussed the interesting multiple planetary system around the red giant star 7 CMa. The dynamical fit of system is consistent with two planets orbiting near to 4:3 MMR. Although, 7 CMa's best fit is unstable (as it was the case for η Cet system in §4), there are many stable fits in a close orbital phase space to those from the best fit. The CRIRES radial velocities are consistent with the Lick data, inclining in favor of a real planetary system around 7 CMa, instead of pulsations.

Due to the large number of data points from the Lick data set, as well as the additional VLT data set for the aforementioned stars, the individual radial velocities and their estimated errors will not be given in this thesis. Instead, they will be provided if requested. When results for some targets have already been published, a reference to the publication will be given.

The observational techniques used for the Lick and the VLT data sets are explained in detail in §2, and §3.

5.1 HIP 114855 (91 *Aqr*)

91 Aqr (= HR 8841, HD 219449, HIP 114855) is a Horizontal Branch (HB) star of stellar class K0III, with an effective temperature of $T_{\rm eff}$ = 4665 ± 18 K and is slightly less metal rich than the Sun ([Fe/H] = −0.03). The mass of 91 Aqr is M = 1.4 ± 0.13 $M_\odot$ and the age is estimated to be 3.56 ± 0.63 G yr. The physical characteristics of 91 Aqr are given in Table 5.2, taken from Reffert et al. (2014). It has been speculated in the literature that 91 Aqr is actually part of triple star system (Eggleton & Tokovinin 2008). More recently, Roell et al. (2012) suggested that 91 Aqr is physically connected with a faint close binary system (91 Aqr B and C), separated ∼ 2400 AU from the primary.

A planetary companion around 91 Aqr (hereafter 91 Aqr instead of 91 Aqr A) was announced in AAS conference meeting by Mitchell et al. (2003). Ten years later the companion was confirmed by Mitchell et al. (2013), using the total set of the Lick radial velocities, together with the near-IR radial velocities obtained at VLT (see §3). Mitchell et al. (2013), has excluded the rotational modulation as one possible explanation for the RV signal of 91 Aqr. Rotating surface spots are not good explanation for the seen RV of 91 Aqr, as they must occupy around 50 % of the stellar surface in order to create significant asymmetries in the stellar absorption lines. Such a large stellar inhomogeneous would imply to photometric signatures enough to be detected by the Hipparcos satellite. Instead, 91 Aqr is flagged as photometrically stable, within the 0.02 magnitudes limit of Hipparcos. Also, given the estimated radius of 11.0 $R_\odot$ and RV period of 181 days for 91 Aqr, Mitchell et al. (2003) derived a rotational velocity of 3.0 km s^{-1}, which even in the order of the errors is less than the observed rotational velocity of 3.9 km s^{-1} (Tokovinin & Smekhov 2002). Thus, the spot driven RVs was dismissed. The CRIRES data in this study was

also consistent with the best Keplerian prediction.

In this sub-chapter are introduced new orbital parameters for 91 Aqr b, which in fact are not much different than those from Mitchell et al. (2003). The orbital error estimation here, however, tend to be more precise. Multiple MCMC chains have been run with the *Systemic Console* in order to obtain the uncertainties. In this thesis a new and improved set of the VLT data is introduced. All the available near-IR data points confirm the planetary hypothesis for the RV signal of 91 Aqr.

5.1.1 Observations

91 Aqr is one the most observed targets in our Lick study. Since 1999, until the termination of our program in the end of 2011, we obtained a total of 174 optical Doppler observations. Typical exposure time for 91 Aqr at Lick was 12 min, leading to S/N around 120−150. The Lick mean radial velocity precision is $\sigma_{Lick} \sim 5$ m s^{-1}, which is very adequate RV error for our study, giving the fact that the estimated stellar jitter is on the order of 20 m s^{-1}.

VLT data were taken for 8 epochs between 2011 and 2013. The exposure time at UT1 (VLT) telescope needed for S/N > 300 was only 5 seconds per nod and per jitter frame. For each epoch we had obtained two nods with three jitter frames per nod, leading to total exposure of 30 seconds The typical RV uncertainties from CRIRES are $\sigma_{VLT} \sim 40$ m s^{-1}.

Table 5.1: Stellar properties of 91 Aqr

Spectral type	K0III
Age [G yr]	3.56 ± 0.63
Mass [$M_\odot$]	1.40 ± 0.13
Luminosity [$L_\odot$]	51.5 ± 1.1
Radius [$R_\odot$]	11.01 ± 0.14
$T_{\rm eff}$[K]	4665 ± 18
log g[cm · s^{-2}]	2.52 ± 0.05
[Fe/H]	−0.03 ± 0.1
RV$_{absolute}$ [km s^{-1}]	−25.89

Table 5.2: 91 Aqr best fit orbital parameters

Orb. Param.	91 *Aqr* b
P [days]	181.36 ± 0.12
m sin$i$ [$M_{\rm Jup}$]	3.19 ± 0.08
e	0.026 ± 0.017
M [deg]	172.1 ± 71.1
ϖ [deg]	176.7 ± 71.8
$K_\star$ [m s^{-1}]	91.65
a [AU]	0.70
$r.m.s.$ [m s^{-1}]	19.0
$\chi^2_{\rm red}$	14.05

valid for JD = 2451744.976

5.1.2 Orbital fit

Periodogram of the optical radial velocity data for 91 Aqr, shows one significant peak at 181.4 days. The constructed Keplerian fit model to the data is consistent with the obtained value from the Lomb-Scargle periodogram, resulting in one planetary companion with period of 181.36 ± 0.12 days and mass of $m_b \sin i = 3.19\ M_{\rm Jup}$. Eccentricity of the planet is very low, almost circular ($e_b = 0.026$). The fit has $\chi^2_{\rm red}$ value of 14.05, which is caused by the additional intrinsic RV jitter typical for stars with spectral class K0III. The estimated $r.m.s.$ of the data is 19.0 m s^{-1}. The rest

of the obtained orbital elements are available in Table 5.2. The orbital elements and their errors introduced in this chapter are slightly different from those published by Mitchell et al. (2013). Perhaps, this is due to the different tools used for constructing the fit and estimating the orbital elements errors. In this work the orbital uncertainties are based on large set of MCMC chains, obtained with the *Console* package.

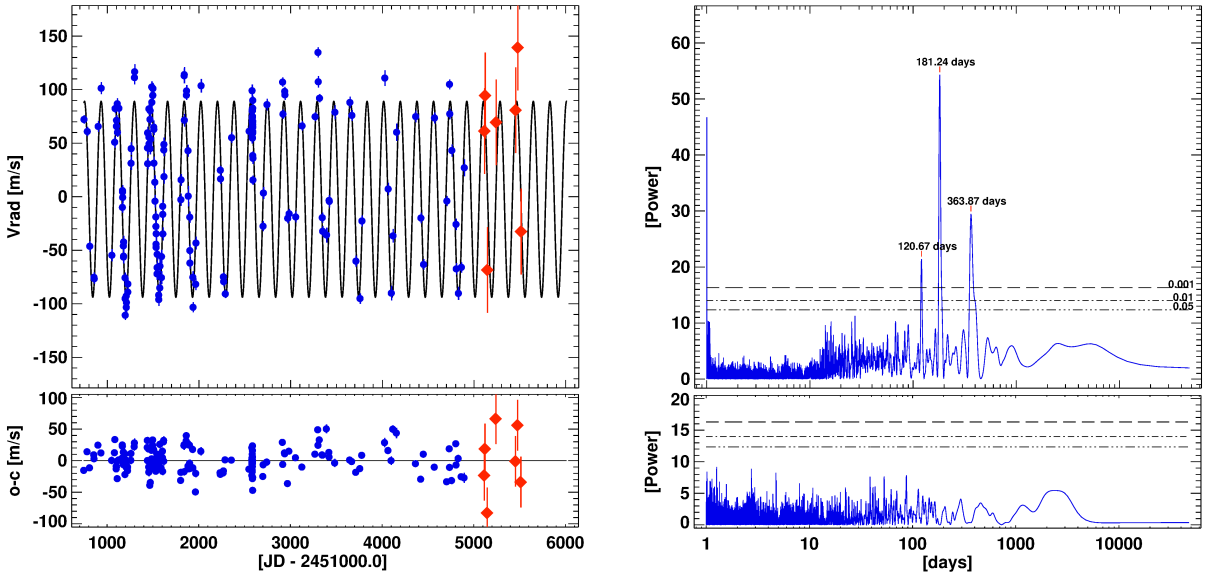

Figure 5.1: Radial velocity plot for 91 Aqr . *Top left panel*: Lick RV data (*blue*) and CRIRES data (*red*) show good agreement. The best Keplerian model to the data is constructed only using the Lick data, while VLT data is only overploted. *Bottom left panel*: Residual RV data after subtraction of best fit shows *r.m.s.* = 19 m s^{-1}. *Top right panel*: Periodogram of the radial velocity data for τ Gem, shows a significant peak at 181.24 days, matching the period from the Keplerian orbital fit (P = 181.36 days). *Bottom right panel*: Periodogram for the residual data after subtraction of the orbital fit. There is no significant peak present.

5.1.3 THE CRIRES TEST

The CRIRES data introduced in Mitchell et al. (2013) had only four RV points. After the paper was submitted for publication, three additional observations have been obtained at VLT. All of them are consistent with the best Keplerian fit, by following the phase and amplitude of the Lick data, whiting the stellar jitter and observational errors (see Fig. 5.1). The first CRIRES observation at JD = 2455854.611 is not shown on the Fig. 5.1 plot. After the re−reduction of all available near-IR data from CRIRES, the spectra from this epoch was not consistent with the fit. The reason for this difference is so far not know.

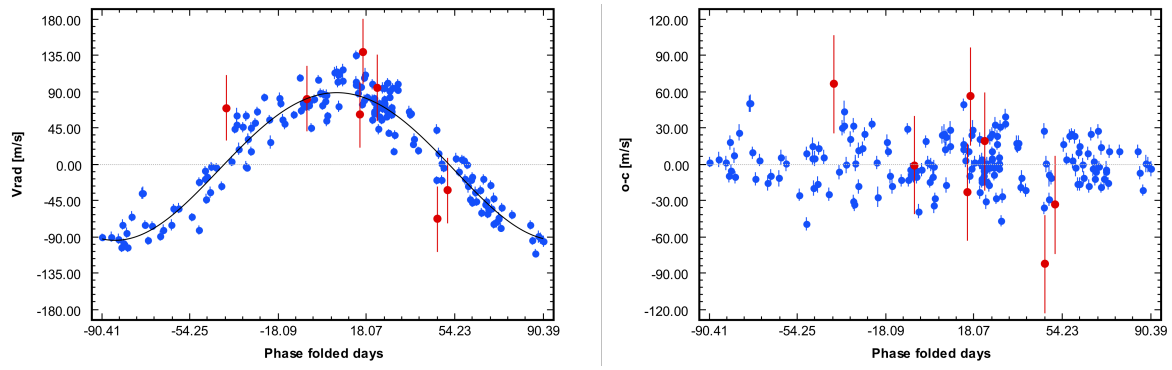

Figure 5.2: *Left*: the phase folded plot for 91 Aqr, shows more clearly the periodicity of the Doppler signal. *Right*: The residuals from the plot.

5.1.4 Discussion

The evidences of 91 Aqr being part of a triple stellar system make the planetary system around this star an interesting case. However, we assume only the minimum mass of the 91 Aqr b. Constraining the inclination and thus, the real mass of the planet is subject on future study. Precise astrometric data from future projects like the Gaia satellite can give more information about the 91 Aqr architecture. At least we can conclude that the pulsation and the spot theory about the radial velocity periodicity have been rejected, in favor of the planetary companion around 91 Aqr.

5.2 HIP 20889 (ϵ *Tau*)

ϵ Tau (= HD 28305, HR 1409, HIP 20889) is a Horizontal Branch (HB) star of stellar class K0III, with effective temperature of $T_{\rm eff}$ = 4860 ± 18 K and apparent magnitude in V = 3.53 [mag]. It has near solar metallicity of [Fe/H] = 0.05 and is estimated to be member of the intermediate mass star population with M = 2.4 ± 0.15 $M_{\odot}$. More physical characteristics of ϵ Tau are given in Table 5.3.

A planetary companion around ϵ Tau was announced by Sato et al. (2007). As ϵ Tau is a star member of the Hyades open cluster, when announced this planet was the first discovered in an open cluster. The precise RV observations for ϵ Tau have stared in late 2003 using the HIDES Spectrograph (Izumiura 1999), at OAO[1] and have finished in the mid 2006, collecting total of 20 data points. Based on these data and by adopting a stellar mass of M = 2.7 $M_{\odot}$ Sato et al. (2007) announced a planetary object with minimum mass of m_b sin$i$ = 7.6 ± 0.2 $M_{\rm Jup}$, eccentricity of e_b = 0.15 ± 0.02 and an orbital period of P_b = 594.9 ± 5.3 days. Sato et al. (2007), showed that ϵ Tau do not exhibit any significant emission in the Ca II H lines, and thus excluded the possibility the RV periodicity seen from the OAO observations to be caused by stellar activity.

Our group had observed ϵ Tau from 2004 till 2013 with both, Hamilton spectrograph at Lick

[1]OAO – Okayama Astrophysical Observatory, National Astronomical Observatory of Japan

and in the near-IR with CRIRES spectrograph at VLT. Our data set is the largest precise radial velocity set for this star. In this sub-chapter new and improved orbital parameters for ϵ Tau b, are introduced based on the data set from Sato et al. (2007) and our own observations taken at Lick. This star has passed the near-IR test, which confirms the planetary hypothesis for the RV signal of ϵ Tau.

5.2.1 OBSERVATIONS

In addition to the 20 observational epochs from OAO, ϵ Tau has been observed 63 times from Lick observatory and 8 times from VLT, part of our G and K giant planets search program. Typical exposure time for ϵ Tau at Lick was 450 sec, leading to S/N around 120−150. The Lick mean radial velocity precision is $\sigma_{Lick} \sim 5$ m s^{-1}, while the RV error from OAO is estimated to be $\sigma_{OAO} \sim 6$ m s^{-1}. These uncertainties are lower than the typical stellar RV scatter for K0III giants.

VLT data is taken for 8 epochs between 2011 and 2013. The exposure time at UT1 (VLT) telescope needed the co-added spectra to reach S/N > 300. was set to only 3 sec per jitter frame. For each epoch we had obtained two nods with three jitter frames per nod, leading to total exposure of 18 seconds The typical RV uncertainties from CRIRES are $\sigma_{VLT} \sim 40$ m s^{-1}. More details for the observational setup and RV derivation methods are explained in §3.

Table 5.3: Stellar properties of ϵ Tau

Spectral type	K0III
Age [G yr]	1.13 ± 0.4
Mass [$M_\odot$]	2.37 ± 0.15
Luminosity [$L_\odot$]	85.3 ± 2.7
Radius [$R_\odot$]	13.05 ± 0.23
$T_{\rm eff}$[K]	4860 ± 18
log g[cm · s^{-2}]	2.59 ± 0.03
[Fe/H]	0.05 ± 0.1
RV$_{absolute}$ [km s^{-1}]	38.26

Table 5.4: ϵ Tau best fit orbital parameters

Orb. Param.	ϵ Tau b
P [days]	583.8 ± 1.5
m sin$i$ [$M_{\rm Jup}$]	6.87 ± 0.14
e	0.10 ± 0.02
M [deg]	272.9 ± 13.8
ϖ [deg]	106.1 ± 13.6
$K_\star$ [m s^{-1}]	93.62
a [AU]	1.83
$r.m.s.$ [m s^{-1}]	10.8
$\chi^2_{\rm red}$	3.57

valid for JD = 2453354.731

5.2.2 ORBITAL FIT

Lomb-Scargle periodogram of the combined optical RV data for ϵ Tau shows one significant peak at 582.4 days. The constructed Keplerian fit model to the optical data is consistent with the obtained value from the periodogram, resulting in one planetary companion with period of $P_b = 583.8 \pm 1.5$ days and mass of $m_b \sin i = 6.87 \pm 0.14$ $M_{\rm Jup}$. The planetary eccentricity is $e_b = 0.1 \pm 0.02$. The Keplerian fit has $\chi^2_{\rm red}$ value of 3.57, with $r.m.s.$ of the data around the model of 10.84 m s^{-1}, which more likely is caused by the additional intrinsic RV jitter typical for stars with spectral class K0III. The rest of the obtained orbital elements and their MCMC derived 1σ errors are available in Table 5.4.

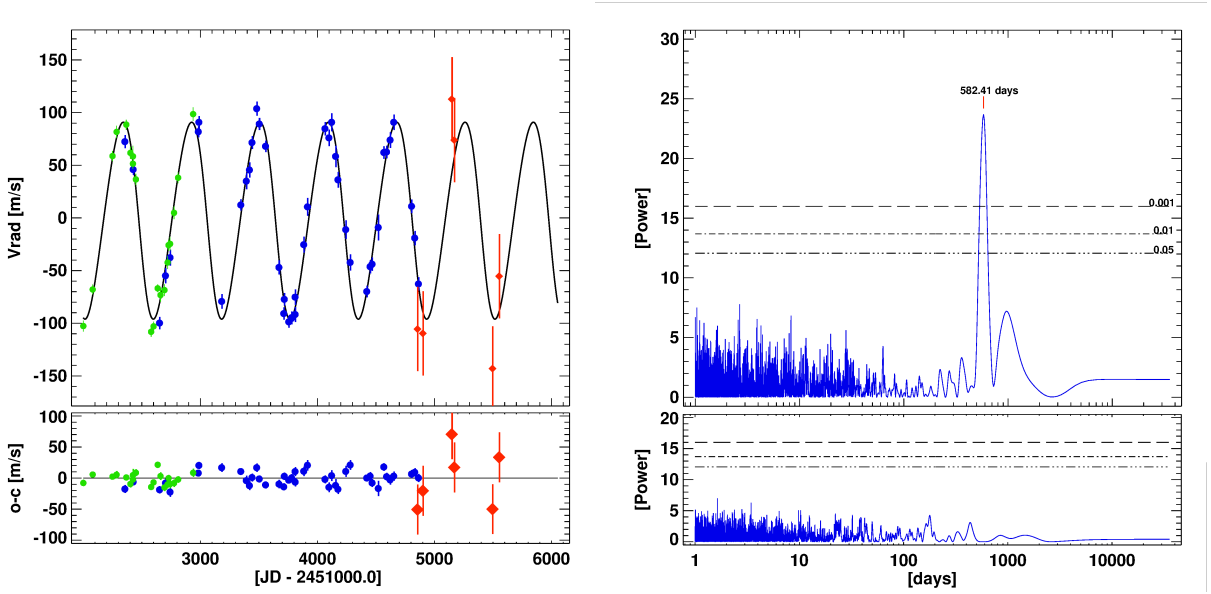

Figure 5.3: Radial velocity plot for ϵ Tau. *Top left panel*: The OAO RV data (*green*), Lick RV data (*blue*) and CRIRES data (*red*) show good agreement. The best Keplerian model to the data is constructed using the Lick and OAO data, while VLT data is only overploted. *Bottom left panel*: Residual RV data after subtraction of best fit shows *r.m.s.* = 10.8 m s^{-1}. *Top right panel*: Periodogram of the radial velocity data for ϵ Tau, shows a significant peak at 582.41 days, matching the period from the Keplerian orbital fit (P = 583.8 days). *Bottom right panel*: Periodogram for the residual data after subtraction of the orbital fit. There is no significant peak present.

5.2.3 The CRIRES test

Six out of eight near-IR have been used to test the optical data RV phase and amplitude. As discussed in §3, due to the barycentric movement of the Earth the stellar spectral lines can exhibit blue or red shifted velocities of $\sim \pm$ 30 km s^{-1}. In certain epochs this line shift might lead to unwanted overlap of the useful spectra with the nearly constant telluric absorption lines from the Earth's atmosphere. In this cases the spectra cannot be used for precise velocity derivation. Such was the case for the spectra obtained at JD = 2456244.649 and 2456288.568. The stellar lines were contaminated by atmospheric telluric lines and it was impossible to obtain useful RV information. The two spectra in question had very large dispersion from the Keplerian fit and thus, were excluded. The rest six data points seem to follow the phase and amplitude prediction from the Keplerian model to the optical data (see Fig. 5.3).

5.2.4 Discussion

The evidences of ϵ Tau harboring planet and being part of star cluster is an interesting case. However, as in the case of 91 Aqr we can estimate only the minimum mass of the ϵ Tau b. Future high precision astrometry surveys might obtain the line of site inclination and thus, we

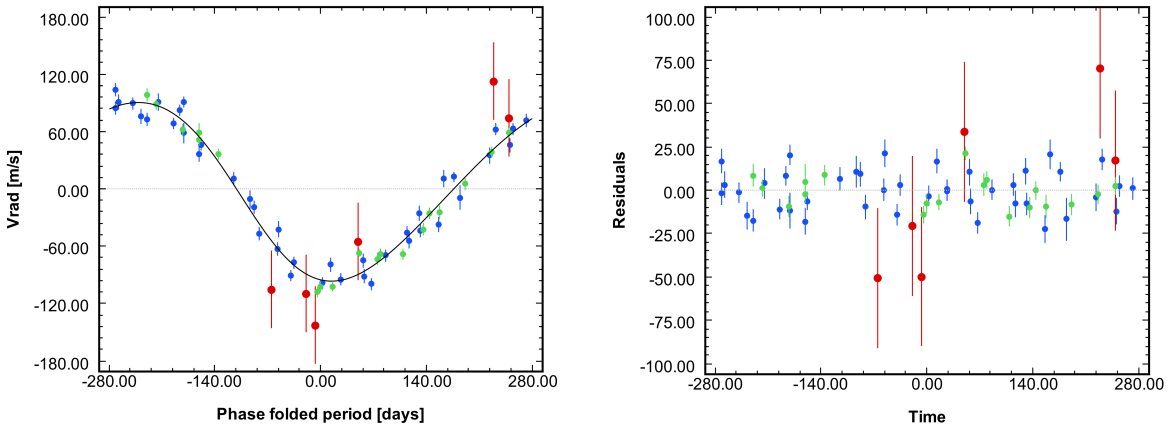

Figure 5.4: *Left*: the phase folded plot for ϵ Tau, shows more clearly the RV periodicity of the Doppler signal. *Right*: The residuals from the plot.

can derive the real mass of the planet. So far we conclude that the pulsation and the spot theory are dismissed, and the planetary hypothesis for ϵ Tau b have been confirmed.

5.3 HIP 75458 (ι *Dra*)

ι Dra (= HIP 75458, HD 137759, HR 5744) is a well-known K giant hosting a sub-stellar companion. In fact, ι Dra is the first star from our Lick sample founded to have a planetary companion, and the first planetary system around giant star announced in the literature (Frink et al. 2002). According to Reffert et al. (2014), ι Dra is a Horizontal Branch (HB) star of spectral class K2III, with mass of $M = 1.28 \pm 0.20\ M_{\odot}$ and $T_{\rm eff} = 4577 \pm 20$ K. It is more metal abundant than the Sun ([Fe/H] = 0.11 ± 0.1) and ~ 12 times more luminance than the Sun. More stellar properties are listed in Table 5.5.

The star and it's companion are well studied during the past decade. When discovered by in 2002 by Frink et al. (2002) the RV signal of ι Dra was consistent with only one well defined period of one very eccentric ($e_b = 0.7$) and massive sub-stellar companion. In 2002 the estimated mass for ι Dra was $M = 1.05\ M_{\odot}$ (from Allende Prieto & Lambert 1999). Using this mass, Frink et al. (2002) give a minimum mass of ι Dra b $m_b \sin i = 8.9\ M_{\rm Jup}$ orbiting with a period of $P_b = 536$ days.

ι Dra was studied again in Zechmeister et al. (2008), using the follow-up Lick data from our program and two additional data sets with shorter time basis from the Alfred-Jensch 2 m telescope at TLS and the 2.7 m telescope at the McDonald Observatory. Zechmeister et al. (2008) showed more clearly the RV period and determined the ι Dra b orbit and it's parameter uncertainties. In 2008, the ι Dra stellar mass used to derive the orbital fit was 1.4 $M_{\odot}$, giving a period of $P_b = 511 \pm 0.15$, eccentricity $e_b = 0.726 \pm 0.006$, and minimum planetary mass of $m_b \sin i = 10.3\ M_{\rm Jup}$. Also, Zechmeister et al. (2008) showed that ι Dra exhibits low amplitude, $p-$mode solar-like oscillations with frequencies ~ 3 to 4 days (34.7–46.3 μ Hz) that can be seen

as scatter noise around the best fit Keplerian model. Kane et al. (2010) presented a new revised fit of the further extended Lick RV data and performed a photometric analysis of the stellar variability. Kane et al. (2010) studied the potential transit probability of ι Dra b, and concluded that due to the eccentric orbit of planet, and the inflated status of ι Dra star, the probability of transiting for ι Dra b, if it has nearly Jupiter size is $\sim$ 17%. This estimation of transiting is larger than probability for hot Jupiter with circular orbit to transit a K giant ($\sim$ 4.7%). However, it is worth to note that the transit signal of a Jupiter-sized planet around a K giant star will be comparable with that of an Earth sized planet crossing the disk of solar sized star, and will lead to negligible transiting gap in the photometry (Assef et al. 2009). Thus, the current base ground transiting surveys are unable to detect transiting Jupiter-sized planets around giant stars, although this can be potentially achieved with future space based telescopes such as *Kepler*.

Due to the high eccentricity of the ι Dra b orbit, there are no doubts about the Keplerian nature on the RV signal. Thus, the planet is qualified as confirmed, and no additional near-IR test has been performed for this star.

5.3.1 Orbital fit

A Lomb-Scargle periodogram test to the Lick data shows few significant peaks, but the most prominent is at 511.82 days (see Fig. 5.5). This value agrees with the orbital period for ι Dra b from the most recent study of this system (Kane et al. 2010). The other significant peaks seen on the periodogram, cannot be correlated with the fitted model and are most probability an alias to the 511.82 days peak.

Fitting to the data is done using the *Systemic Console* package (Meschiari et al. 2009). The model selected to obtain the orbital parameters was the Gragg-Bulirsch-Stoer (GBS) method (B-SM: Press et al. 1992) built into the *Systemic* software. Thus, using GBS, any gravitational perturbations between the planets are taken into account in the model. Only Jacobi orbital elements are obtained from the dynamical fit. Assuming stellar mass from Reffert et al. (2014) to be 1.3 $M_{\odot}$, the dynamical fit is consistent with two sub-stellar companions and it has a $\chi^2_{\rm red}$ value of 9.046. This $\chi^2_{\rm red}$ value is slightly better than the double Keplerian fit with the same stellar mass ($\chi^2_{\rm red}$ = 9.05), where no gravitational interactions are considered. As expected the inner planet has similar orbital configuration to the given in Frink et al. (2002); Zechmeister et al. (2008) and Kane et al. (2010), although the different stellar mass adopted in this thesis gives a slightly lower planetary mass compared to that from Kane et al. (2010). The residuals to the dynamical fit, shown in Fig. 5.5 , have a *r.m.s.* value of 13.04 m s^{-1}, which is less than *r.m.s.* value of 15.05 m s^{-1} from Kane et al. (2010). The second companion has mass within the planetary regime (m_c = 7.87 $M_{\rm Jup}$) and an orbital period of P_c = 6303.9 days. Both planets are very eccentric (e_b = 0.71, e_c = 0.63), with arguments of periastron $\omega_{c,b}$ in nearly anti-aligned configuration ($\Delta\omega \sim 180°$). This orbital alignment and planetary eccentricities might imply to very close encounters and thus, to potential stability issues (see §5.3.3). All the planetary orbital elements and their uncertainties estimated via MCMC approach are given in Table 5.6.

Table 5.5: Stellar properties of ι *Dra*

Spectral type	K2III
Age [G yr]	6.72 ± 2.54
Mass [$M_\odot$]	1.28 ± 0.20
Luminosity [$L_\odot$]	58.8 ± 0.8
Radius [$R_\odot$]	12.22 ± 0.13
$T_{\rm eff}$[K]	4577 ± 20
$\log g$[cm · s^{-2}]	2.40 ± 0.07
[Fe/H]	0.11 ± 0.1
RV$_{absolute}$ [km s^{-1}]	−10.71*

$\star$ taken from SIMBAD

Table 5.6: ι *Dra* best fit orbital parameters

Orb. Param.	ι Dra b	ι Dra c
P [days]	511.0 ± 0.05	6309.9 ± 1416.6
$m \sin i$ [$M_{\rm Jup}$]	10.23 ± 0.06	7.87 ± 2.9
e	0.71 ± 0.003	0.63 ± 0.14
M [deg]	128.7 ± 0.15	23.0 ± 12.6
ϖ [deg]	90.0 ± 0.5	284.6 ± 9.6
$K_\star$ [m s^{-1}]	310.2	92.9
a [AU]	1.37	7.32
$r.m.s.$ [m s^{-1}]	13.04	
$\chi^2_{\rm red}$	9.046	

valid for JD = 2451685.854

To constrain the most possible orbital parameters for the outer planet ι Dra c, a systematic 2D grid of edge-on coplanar ($i_{c,b} = 90°$, $\Delta\Omega = 0°$) best dynamical fits, was created. The fixed orbital parameters in the grid were the ι Dra c's eccentricity e_c and period P_c (converted to semi-major axis a_c on the grid). All obtained fits (total of 2600 fits), are tested for stability, similarly to that for the η Cet system (see §4).

5.3.2 NUMERICAL SETUP FOR THE ι DRA SYSTEM

For testing the stability of the ι Dra planetary system was used the *Mercury* N-body simulator (Chambers 1999). The simulations were run using the hybrid sympletic/Bulirsch-Stoer algorithm, which is able to compute close encounters between the planets, if such occur during the orbital evolution. The orbital parameter input for the integrations are taken directly from the *Console* output in *astrocentric* format as it is explained in §1.4.2 and §4.4.1. The starting epoch for the simulations is always JD = 2451685.854, which is the epoch when the first RV observation of ι Dra was taken. The initial integration time span is set for 10^5 years, with time step of 8 days, but in case of stability the test is repeated for 10^7 years, and the time step is decreased to 0.5 days. The fit is classified as stable, if during the integration the companions show constant semi-major axes (i.e. a_b and a_c do not exceed their starting semi-major axis by ± 0.5 AU during the simulations). As it was defined earlier for the η Cet planetary system, the system will be classified to have a *chaotic behavior*, if during the simulations none of the companions was ejected or no collisions were occurred, but the semi-major axes scatter chaotically multiple times and are exceeding the 0.5 AU limit.

5.3.3 STABILITY RESULTS - CONSTRAINING THE OUTER COMPANION

The best possible dynamical fit turned out to be unstable. This result was not unexpected given the large planetary eccentricities and the orbital configuration in general. Close planetary approaches destroyed the system in only ∼ 200 years, by ejecting the inner planet.

It is also true that the outer companion ι Dra c cannot be well identified from the current

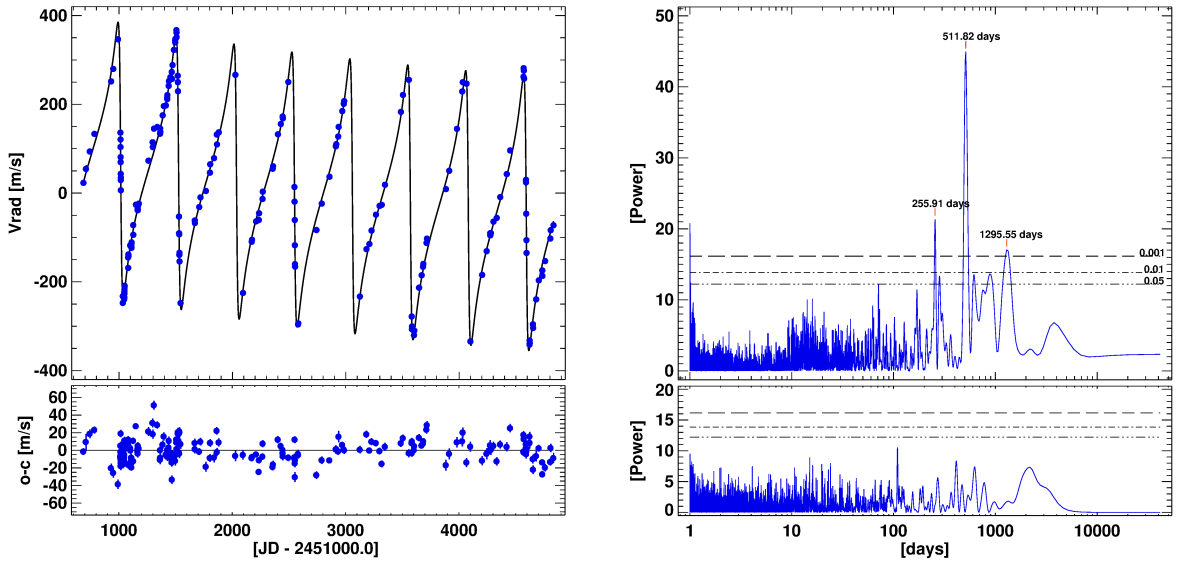

Figure 5.5: *Top left panel*: Dynamical fit to the Lick data for ι Dra. *Bottom left panel*: No short term periodicity can be seen from the RV residuals.
Top right panel: Periodogram of the radial velocity data shows a significant peak at 511 days, matching the period of the inner eccentric companion obtained from the dynamical fit. Few other peaks can be seen, but based on this sample no further significant periods can be found. *Bottom right panel*: There is no significant peak after subtraction of the orbital fit.

data. The created 2D grid shows nearly indistinguishable $\chi^2_{\rm red}$ solutions in the (e_c,a_c) space. Nevertheless, the detailed stability test over the $\chi^2_{\rm red}$ fits from the grid reveals the most probable set e_c and a_c based on stability constant.

Fig. 5.6 shows the stable fit configurations for ι Dra c. They are all located between 7 and 11 AU, where there are many stable fits with $e_c = 0.3$. Increasing the planetary eccentricity on the grid, the permitted semi-major axis region shrinks and only few fits are stable above $e_c = 0.5$. Maximum stable fits can be seen between $a_c = 9$ and 10 AU and $e_c = 0.3$ and 0.5. Lower e_c might lead to more stable solutions, but such are not considered for test due to the badness of the dynamical fit at these eccentricities. The grid has been constructed only around the best possible dynamical fit and thus, other possible stable configurations are not studied, although they might exist.

Almost all stable fits are consistent with a planetary mass object. Few exceptions are the stable fits at 11 AU, where the obtained planetary mass lies a little over the 13 $M_{\rm Jup}$ mass limit (see Fig. 5.6 *right*) and ι Dra c is considered as brown dwarf object[2]

In Fig. 5.7, two stable fits from this study are shown. The *left* side of Fig. 5.7, represent the orbital evolution of the best stable fit from Fig. 5.6. This stable fit has $\chi^2_{\rm red} = 9.079$ and Jacobi coordinates of: $e_c = 0.54$, $a_c = 8.00$ AU, $\omega_c = 294.03°$ and mass of $m_c = 8.55\ M_{\rm Jup}$.

[2]Currently, the International Astronomical Union considers an object with a mass above the limiting mass for thermonuclear fusion of deuterium (13 Jupiter masses for objects of solar metallicity)

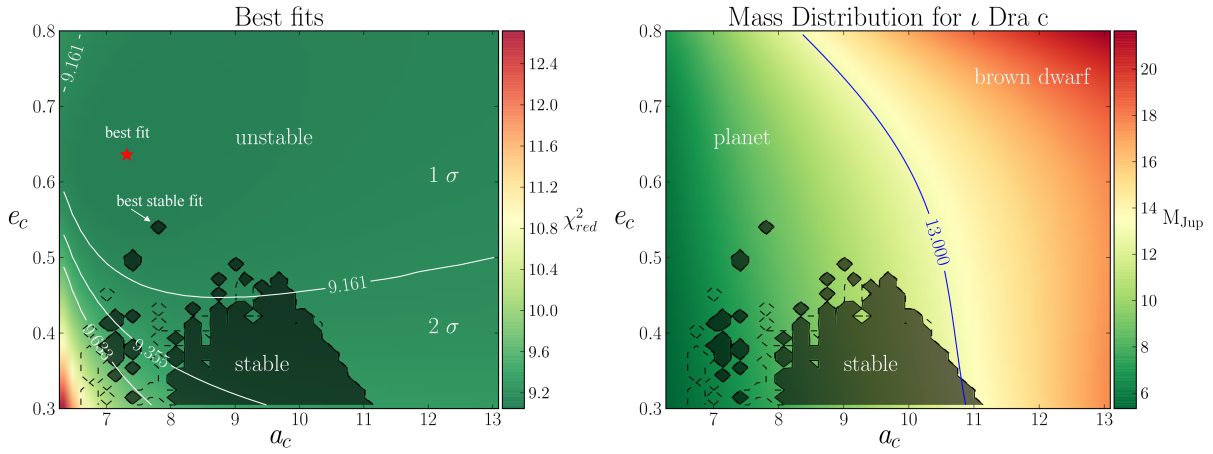

Figure 5.6: Stability maps for the ι Dra planetary system over a 2D grid of dynamical best fits solutions, where the fixed parameters are the outer companion's eccentricity e_c and semi-major axis a_c. *Left*: The second companion of the ι Dra planetary system cannot be well defined on the current data set. Large set of initially different orbital configurations for ι Dra c leads to similar $\chi^2_{\rm red}$ values. However, applying a stability test can effectively constrain the possible eccentricity, period and mass for the ι Dra c. *Right*: Stability is most likely possible if the second companion is a planetary object with moderate eccentricity.

The orbital parameters for the inner planet are initially very well constrained and do not differ significantly from the best possible fit. The semi-major axes orbital evolution shows that this planetary configuration is stable for 10^7 years (only 10^5 years are shown on Fig. 5.6), without exhibiting any large oscillations around the starting a_b and a_c values. As can be seen, the outer planet semi-major axis a_c is a bit more "unstable" and shows small pattern variations every 10^4 years, but the planet remains in stable orbit. The planetary eccentricities are very dynamic during the simulations and dramatically changing every $\sim 10^4$ years. The eccentricity libration amplitudes are vary large leading e_c to librate between 0.52 and 0.64, while the inner planet has e_b always in off-phase libration with values between 0.54 and 0.72. Despite the clear pattern in the orbital evolution, the lowest order eccentricity-type resonant angles θ_b, θ_c circulate (then $\Delta\omega$ is also circulating) and thus, there is no evidence (so far) of resonance behavior in this system configuration.

Fig. 5.7 *right*, represents the orbital evolution of randomly selected fit with moderate e_c stable island from Fig. 5.6. The fit is selected to be in the middle of the stable island and has $\chi^2_{\rm red}$ = 9.334 and Jacobi coordinates of: e_c = 0.32, a_c = 9.425 AU, ω_c = 315.67° and mass of m_c = 9.83 $M_{\rm Jup}$. The orbital parameters for the inner planet are similar to those from the best fit given in Table 5.6. The semi-major axes orbital evolution for both planets is more stable, perhaps, due to the larger orbital separation compared to the fit shown in Fig. 5.6 *left*. The planetary eccentricities have very large libration amplitudes, but in general the period of libration is also very long ($\sim$ 1.2*10^5 years). The eccentricity e_c for the outer planet is periodically oscillating between 0.2 and 0.5, while the inner planet has always large and off-phase amplitudes to e_c, between e_b = 0.35 and 0.75. The libration of the secular resonance angle $\Delta\omega$ around 180° for this fit is intriguing. The amplitude is large (± 60° around 180°), but in obvious anti-aligned

configuration. So far, a possible high order resonances for this and other fits stable fits are not studied, but is the orbital evolution behavior of the fit from Fig. 5.7 *right* deserve to be studied in future. Detailed investigations on this system might prove the existence of high-order and anti-aligned resonance, which includes a very large planetary eccentricities. If such configuration indeed exists, it might lead to important conclusions about the planetary evolution around giant stars.

5.3.4 Summary and Discussion

ι Dra is well studied system, but in this work for a first time are given the possible orbital parameters of the hypothetical outer companion. According to the stability test, the outer companion must have a planetary mass. The assemble of best stable fits inclines to the conclusion that the mass of the second planet is between 6 and 13 $M_{\rm Jup}$ and in few cases a bit more than brown dwarf limit of 13 $M_{\rm Jup}$. All stable fits are assuming a_c between 7 and 11 AU, and e_c not higher than ~ 0.55.

However, larger orbital period P_c and more massive outer companion for ι Dra c cannot be excluded. All best fits are based on relatively small possible region of a_c, around the best achieved dynamical fit. Other regions are not considered due to the increased badness of the $\chi^2_{\rm red}$ fits assuming larger P_c and lower e_c than 0.3. Fig. 5.6 grid, reveals the region around the global $\chi^2_{\rm red}$ minimum, and my goal was to study this particular region. The test can be considered as successful as a result of the large amount of *good* $\chi^2_{\rm red}$ dynamical fits that can preserve stability in broad region of orbital parameters. The best stable fit from Fig. 5.6, at first look do not suggest any possible secular resonance between the planets. The fit from the inner part of the stable island shows interesting secular behavior, and deserves to be studied in details in future work.

One possibility, which was not discussed here is the assumption that the second companion can be very massive and highly inclined. This configuration can lead to Kozai effects and thus, explain the very large eccentricity of ι Dra b. It is not clear how ι Dra b has settled in to this high eccentricity orbit, but Kozai effects, caused by an external massive companion at larger distance is one possible option. The other, perhaps, more probable scenario is gravitational instabilities in the early epochs of the ι Dra system. Events such as collisions and ejections can destroy the system's equilibrium, and might pump the eccentricities of the remaining planets to the observed values. It is possible in the past the ι Dra system has been a host of more planets in near circular orbits, but only two planets have survived in our days (at least we have no evidence for even more distant objects than ι Dra c).

Speculations over the ι Dra system are useful, however, only future observations of this system can reveal important information about the extremely complex orbital configuration. Future observations can finally close the case and confirm the existence of the second planet, which most likely is causing the ι Dra's linear trend seen on the Lick data.

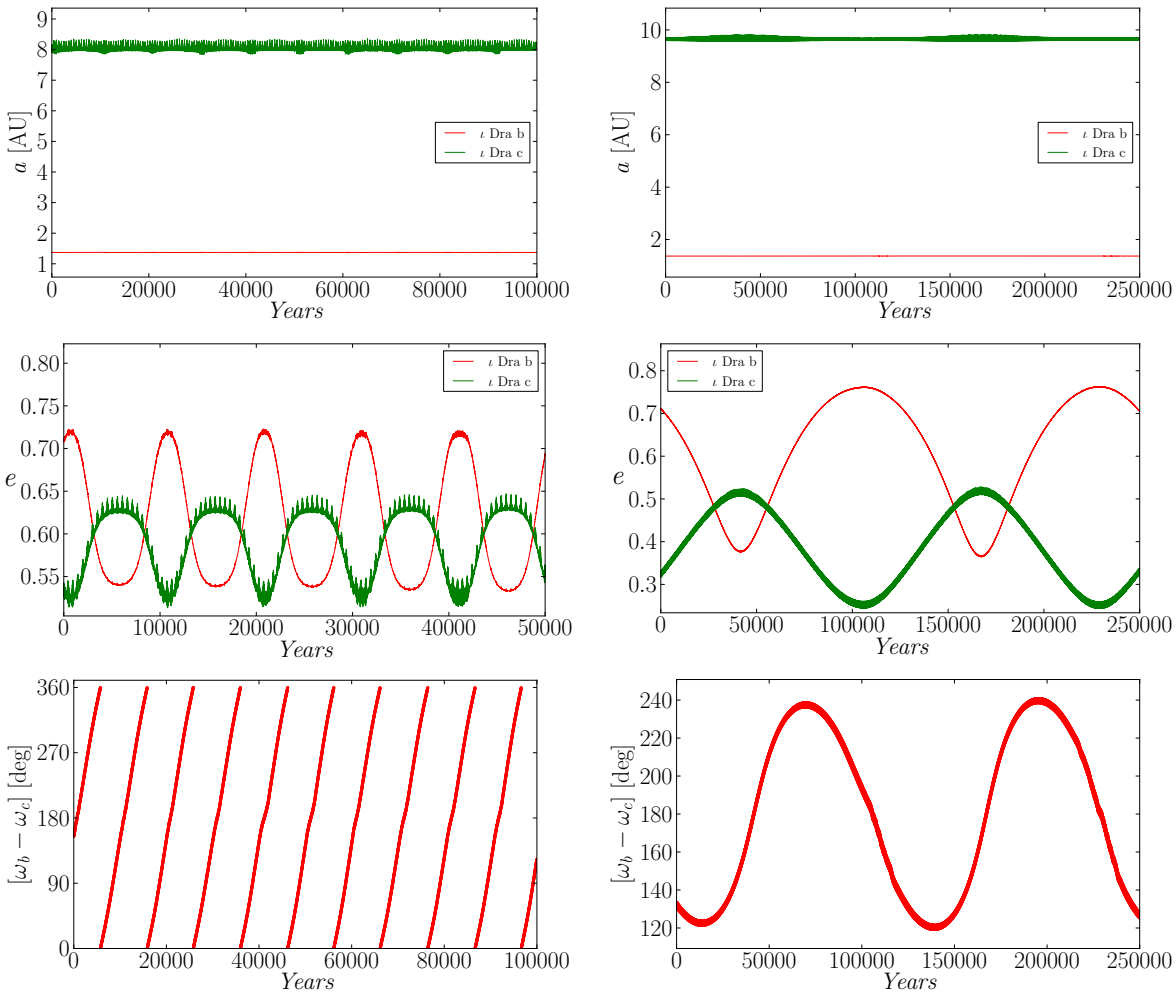

Figure 5.7: The best long-term stable dynamical fit ($\chi^2_{\rm red}$ = 9.079) configuration for ι Dra b and ι Dra c is shown on the *left* section. The outer planet ι Dra c, exhibits small Jacobian semi-major axis variations, while the well constrained inner companion ι Dra b has rather constant orbital evolution. Then system remains long-term stable despite the relatively large planetary eccentricities and their large off-phase libration amplitudes. $\Delta\omega$ (*left bottom*) is circulating between 0 and 2π.
Right section shows the evolution of random stable fit chosen near the center of the stable region on the Fig. 5.6 grid. The larger planetary separation and the lower e_c = 0.32, make the orbital evolution much different that those from the best stable fit. The planetary eccentricities librate with larger amplitudes and with longer periods compared to the best stable fit. The libration of the secular resonance angle $\Delta\omega$, however, is clearly librating around 180° with large amplitudes of ± 60°. This configuration might be locked in secular anti-aligned resonance, which is stabilizing the system.

5.4 HIP 74732 (HR 5678) PLANETARY SYSTEM

HR 5678 (= HD 135534, HIP 74732) is an K giant star of spectral type K2III in the constellation Libra. The apparent magnitude in V is 5.52 [mag]. The metallicity of HR 5678 is [Fe/H] = 0.07 ± 0.1, while the mass has been estimated to be M = 1.47 ± 0.21 $M_{\odot}$. Effective temperature is $T_{\rm eff}$ = 4219 ± 19 K and the surface gravity is $\log g$ = 1.78 ± 0.06 [cm · s^{-2}]. Additional information about the physical characteristics can be found in *SIMBAD*[3], while Table 5.7 summarizes stellar parameters for HR 5678 taken from Reffert et al. (2014).

5.4.1 OBSERVATIONS

In total we obtained 110 optical observations for HR 5678 using the Hamilton spectrograph at Lick observatory. This star was observed regularly between 2000 and 2011, when our observational program was terminated. Additional 7 near-IR radial velocities are taken with the CRIRES spectrograph from 2011 till 2013, in order to test the Doppler signal from the optical. We have performed six jitter images in 2 nodding positions for each observational epoch with VLT (see §3). The typical exposure time needed to achieve S/N ∼ 100 at Lick was between 25 and 30 min, while at the much larger UT1 (VLT) telescope aperture the individual jitter exposures were set to 10 seconds, in order the final co-added spectra to have S/N > 300. The typical RV uncertainties from the Hamilton spectrograph have σ_{Lick} ∼ 5 m s^{-1}, lower than the typical intrinsic stellar jitter of HR 5678 estimated to be 31 m s^{-1} (as the *r.m.s.* over the best fit). The estimated RVs uncertainties from CRIRES are σ_{VLT} ∼ 40 m s^{-1}.

Table 5.7: Stellar properties of HR 5678

Spectral type	K2III
Age [G yr]	3.73 ± 1.44
Mass [$M_{\odot}$]	1.47 ± 0.21
Luminosity [$L_{\odot}$]	200.1 ± 16.0
Radius [$R_{\odot}$]	26.52 ± 1.08
$T_{\rm eff}$[K]	4219 ± 19
$\log g$[cm · s^{-2}]	1.78 ± 0.06
[Fe/H]	0.07 ± 0.1
RV$_{absolute}$ [km s^{-1}]	−9.63

Table 5.8: HR 5678 best fit orbital parameters

Orb. Param.	HR 5678 b	HR 5678 c
P [days]	500.2 ± 1.7	4355.3 ± 1841.24
$m \sin i$ [$M_{\rm Jup}$]	5.20 ± 0.23	3.94 ± 2.12
e	0.07 ± 0.04	0.22 ± 0.12
M [deg]	314.3 ± 59.0	7.1 ± 106.2
ϖ [deg]	286.6 ± 60.3	160.4 ± 80.7
$K_{\star}$ [m s^{-1}]	102.0	38.3
a [AU]	1.41	5.98
r.m.s. [m s^{-1}]	31.0	
$\chi^2_{\rm red}$	38.96	

valid for JD = 2451653.873

5.4.2 ORBITAL FIT

The Lomb-Scargle periodogram test to the Lick data shows only one significant peak at 500.3 days (see Fig. 5.8). Fitting to the data is as usual done using the *Systemic Console* package. The model

[3] http://simbad.u-strasbg.fr/simbad/

selected to obtain the orbital parameters was the Gragg-Bulirsch-Stoer (GBS) method, built into the *Systemic* software, which allows gravitational perturbations between planetary companions to be considered in the final fit model. The HR 5678's best fit $\chi^2_{\rm red}$ value is 38.96 consistent with two planetary companions having masses of m_b = 5.2 $M_{\rm Jup}$ and m_c = 3.9 $M_{\rm Jup}$, distant at a_b = 1.41 AU and a_c = 5.98 AU. The inner companion has low eccentricity of e_b = 0.07, while the outer is more eccentric with e_c = 0.22. The badness of the fit with $\chi^2_{\rm red}$ much above 1 is coming from the additional stellar jitter. The estimated *r.m.s.* from the fit is $\sim$ 31 m s^{-1}, which is close to the jitter value expected for K2III giants from our sample. The jitter is most likely caused by a $p-$mode short term stellar oscillations consistent with periods in the order of few days. These oscillations are much more frequent that the typical time span for our observations, and therefore they appear as additional RV noise in out data.

The VLT data from CRIRES almost agrees with the obtained RV prediction from the dynamical fit, but not as good as for most of the companions described in this work.

All the planetary orbital elements and their uncertainties estimated via MCMC approach are given in Table 5.8.

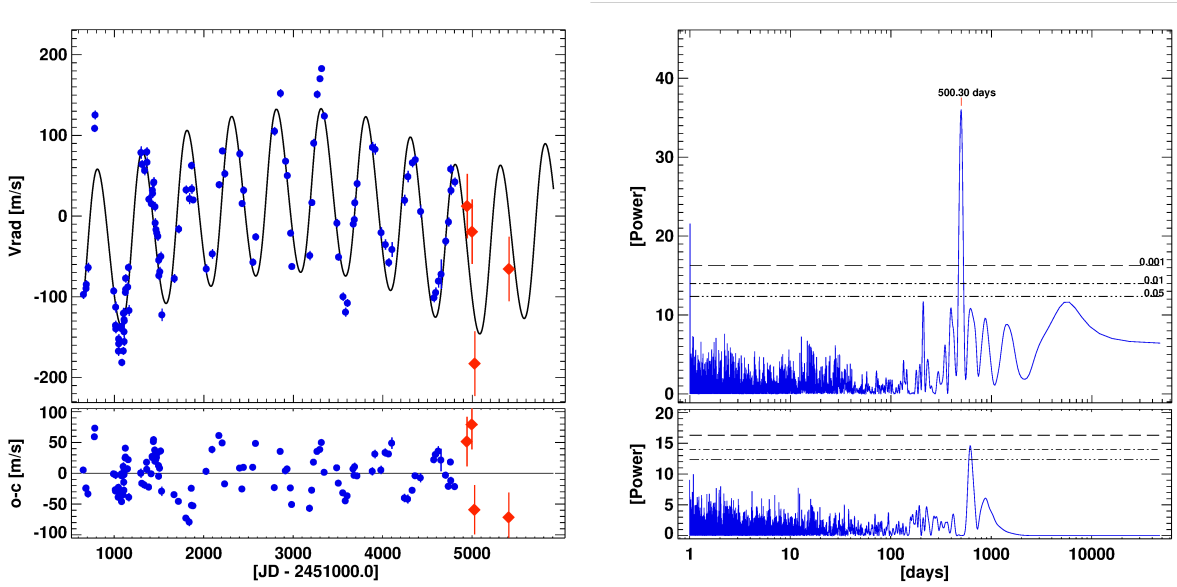

Figure 5.8: Radial velocity plot for HR 5678 . *Top left panel*: Lick RV data (*blue*) and CRIRES data (*red*) show good agreement. The best Keplerian model to the data is constructed by using the Lick data, while VLT data is only overploted. *Bottom left panel*: Residual RV data after subtraction of best fit shows *r.m.s.* = 32.3 m s^{-1}. *Top right panel*: Periodogram of the radial velocity data for HR 5678, shows a significant peak at 500.3 days, matching the period from the Keplerian orbital fit (P = 500.26 days). *Bottom right panel*: Periodogram for the residual data after subtraction of the orbital fit. There is no significant peak present.

5.4.3 Stability analysis of the best dynamical fit

To test the dynamical stability on the best possible edge-on coplanar configuration for HR 5678, The *Mercury* code was used again, by adopting the Jacobi best fits coordinates as input. Despite the fact that the planetary orbits are well separated according to the fit, the simulations were run using the hybrid sympletic/Bulirsch-Stoer algorithm, which is standard for this work. Therefore, if unlikely close encounters occur, they can be computed more precise with an adaptive time step. The integration time span was set for 10^7 years, with initial time step of 8 days. Stability is excepted, if the none of the planetary companions being ejected, collided with the star or the other companion. Also, the planetary semi-major axes a_b and a_c, must be nearly constant during the integration and do not exceeds their starting semi-major axis values by ± 0.5 AU. The starting epoch used for the simulation was epoch, when the first RV observation of HR 5678 was taken JD = 2451653.873, and for which the input Jacobi coordinates are valid.

As expected, the large planetary separation and relatively low eccentricities, preserve the system stable. Fig. 5.9 shows the eccentricity and semi-major orbital evolution for HR 5678 b and c. For clearness, the plot shows only the first 10^5 years of the integrations. Both planets are bounded to very stable orbits with nearly constant semi-major axes. The planetary eccentricities, however, are not constant. They oscillate with period ~ 8*10^4 years leading e_b to librate between 0.05 and 0.27, while the outer planet eccentricity e_c libtrate with smaller amplitude between 0.07 and 0.23, but always in off-phase to e_b.

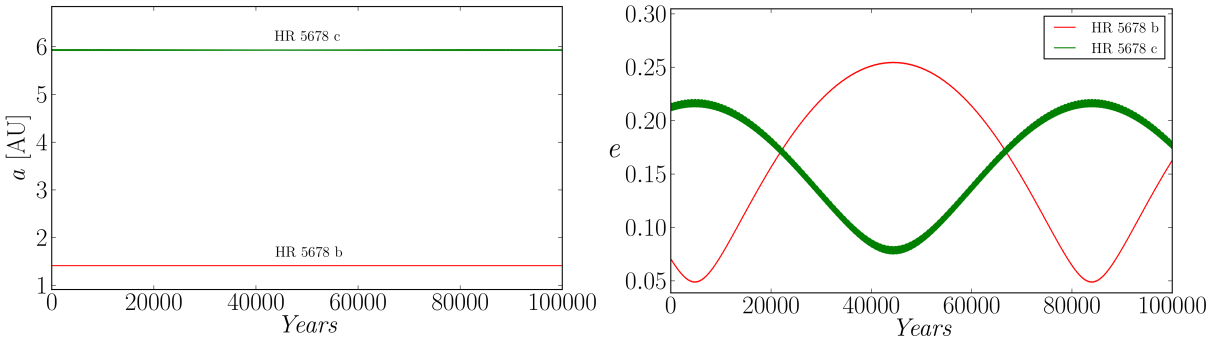

Figure 5.9: Stable orbital evolution of the planetary pair around HR 5678 shown for 10^5 years. While the planetary semi-major axes are constant, the planetary eccentricities have large long-term off-phase amplitude. The HR 5678 system remains long-term stable due to the large planetary separation. The best fit solution, however, cannot constrain well the orbital parameters of the outer planet, and studied orbital evolution might be only one of the many possible stable configurations if indeed the second companion exist.

5.4.4 Summary and Discussion

The proposed best fit is stable, but no conclusive stability analysis has been made for this system. Mostly because of the $\chi^2_{\rm red}$ fit badness and the large uncertainties for the outer planet. As in the ι Dra case, very reasonable fits can be obtained, if the second planet is actually more distant and

more massive respectively. All the test fits with such configurations are found to have moderate eccentricities. The dynamical test shows that they are all stable (not shown in this work). Longer observations are required for this star in order to prove the existence of not only the secondary companion, but also on the inner one. Based on the CRIRES results and the stability tests we have enough arguments in favor of two planetary system, but perhaps, other planetary diagnostics methods like the line bisector analysis can be performed.

5.5 HIP 31592 (7 *CMa*) PLANETARY SYSTEM

7 CMa (= HD 47205, HR 2429, HIP 31592) is an orange giant star in the constellation Canis Major. Hipparcos observations show that 7 CMa is photometrically stable with an apparent visual magnitude of $V = 3.95$ [mag]. The chemical abundance of 7 CMa is [Fe/H] = 0.21 ± 0.1 and the estimated mass is $M = 1.37 \pm 0.18\ M_{\odot}$. The star's effective temperature is $T_{\rm eff} = 4758 \pm 100$ K and the surface temperature is $\log g = 3.17 \pm 0.12$ [cm · s^{-2}]. Table 5.9 summarizes the physical parameters of 7 CMa taken from Reffert et al. (2014).

7 CMa has one confirmed planet known to date. The planetary system around 7 CMa was the first reported discovery from the Pan-Pacific Planet Search survey at the 3.9 m Anglo-Australian Telescope (AAO). Based on 21 RVs taken between 2009 and 2011 at the AAO, and by adopting a stellar mass for 7 CMa of $M = 1.52\ M_{\odot}$, Wittenmyer et al. (2011) announced an evidence of a massive planet ($m_b \sin i = 2.6\ M_{\rm Jup}$), with period of $P_b = 763 \pm 17$ days, and eccentricity $e_b = 0.14 \pm 0.06$. Wittenmyer et al. (2011) have already excluded the possibility the RV variations to be associated with stellar activity or circulation of stellar spots. First, Wittenmyer et al. (2011) analyzed the Hipparcos photometry, and they did not find any significant photometric variations that can be correlated with the hypothetical planetary signal. Also, the star's rotational velocity has been estimated to be much shorter that the seen RV period of $P_b = 763$ days. Second, in that study have been performed a line shape analysis of few strong and unblended spectral lines that have not been contaminated with the iodine calibration spectra. The bisector velocity spans from this test are founded to be inconsistent with the RVs variations, and hence, Wittenmyer et al. (2011) have concluded that 7 CMa has a planetary companion.

In this sub-chapter are introduced our results covering more than 13 years of precise RV observations for 7 CMa. Based on our data set we have found that this system is likely to host not one, but two planetary companions with period ratios very close to 4:3 MMR.

5.5.1 OBSERVATIONS

We observed 7 CMa regularly since 2000. In addition to the 65 precise RVs taken at Lick we have obtained another 21 ultra precise RV at the ESO La Silla 3.6m telescope in conjunction with HARPS[4]. This star was also observed at VLT with ESO CRIRES spectrograph between 2011 and 2013. The CRIRES observational goal and setup is explaned in more details in §3.

[4]HARPS - High Accuracy Radial velocity Planet Searcher spectrograph at ESO La Silla

The typical exposure time needed to achieve S/N ~ 100 at Lick, when the sky was photometric was 600 sec, while at the much larger UT1 (VLT) telescope aperture the six individual jitter exposures were set to only 5 seconds Thus, the combined jitter frames had always S/N > 300. The typical RV uncertainties from the Hamilton spectrograph have $\sigma_{Lick} = 3-5$ m s^{-1}, lower than the seen *r.m.s.* = 9 m s^{-1} of the 7 CMa data around the best fit. The estimated RVs uncertainties from CRIRES are $\sigma_{VLT} \sim 40$ m s^{-1}, while the individual HARPS radial velocities are estimated to be very precise with $\sigma_{HARPS} \sim 0.3-0.5$ m s^{-1}.

Table 5.9: Stellar properties of 7 *CMa*

Spectral type	K1III
Age [G yr]	5.22 ± 2.84
Mass [$M_\odot$]	1.37 ± 0.18
Luminosity [$L_\odot$]	12.0 ± 0.6
Radius [$R_\odot$]	16.48 ± 1.48
$T_{\rm eff}$[K]	4758 ± 100
log g[cm · s^{-2}]	3.17 ± 0.12
[Fe/H]	0.21 ± 0.1
RV$_{absolute}$ [km s^{-1}]	2.27

Table 5.10: 7 *CMa* best fit orbital parameters

Orb. Param.	7 CMa b	7 CMa c
P [days]	754.8 ± 6.5	928.3 ± 32.6
m sin i [$M_{\rm Jup}$]	1.89 ± 0.08	0.95 ± 0.11
e	0.1 ± 0.01	0.061 ± 0.01
M [deg]	290.0 ± 22.9	285.2 ± 48.1
ϖ [deg]	54.6 ± 23.7	220.5 ± 50.2
$K_\star$ [m s^{-1}]	34.32	16.2
a [AU]	1.80	2.06
r.m.s. [m s^{-1}]	9.07	
$\chi^2_{\rm red}$	3.437	

valid for JD = 2451808.021

5.5.2 Orbital fit

The Lomb-Scargle periodogram test to the combined optical data shows only one significant peak at 729.43 days, corresponding to the period of the inner planet (see Fig. 5.10). Subtracting only the first planet period from the data, lead to one significant peak at ~ 996 days, which can be seen on the Lomb-Scargle periodogram of the residuals. This period is near to the period of the outer planet derived from the best dynamical fit (see text below).

Fitting to the data is done using the *Systemic Console* package. The standard model selected for dynamical fitting was the Gragg-Bulirsch-Stoer (GBS) method built into the *Systemic* software. With GBS any gravitational perturbations between the 7 CMa's companions are taken into account into the model. The dynamical fitting must give better $\chi^2_{\rm red}$ value than simple multiple Keplerian model if the companions exhibit gravitational perturbations. Assuming stellar mass to be 1.37 $M_\odot$, the dynamical model on the Lick data has $\chi^2_{\rm red}$ value of 3.44, while simple Keplerian has slightly worse $\chi^2_{\rm red} = 3.51$. A fit based on all available data from the optical wavelength has been also constructed (i.e. Lick, HARPS and AAO). The combined optical RVs has a very good dynamical fit value of $\chi^2_{\rm red} = 3.00$, while the Keplerian fit in this case has $\chi^2_{\rm red} = 3.10$. In this work, however, only the Lick data is considered for dynamical fitting and all other are just overploted by adjusting only their RV offset. Table 5.10 summarizes the best dynamical fit obtained only from the Lick data.

The Jacobi orbital elements obtained from the dynamical fit are consistent with two planetary

companions having minimum masses of m_b = 1.89 ± 0.08 $M_{\rm Jup}$, m_c = 0.95 ± 0.11 $M_{\rm Jup}$). Both companions have relatively low eccentricities of e_b = 0.1 and e_c = 0.06. The periods from the best fit given in Table 5.10 shows that the planets must be very close. The inner one has P_b = 754.8 ± 6.5 days, and the outer has P_c = 928.3 ± 32.6 days, leading to a_b = 1.80 AU and a_c = 2.06 AU respectively.

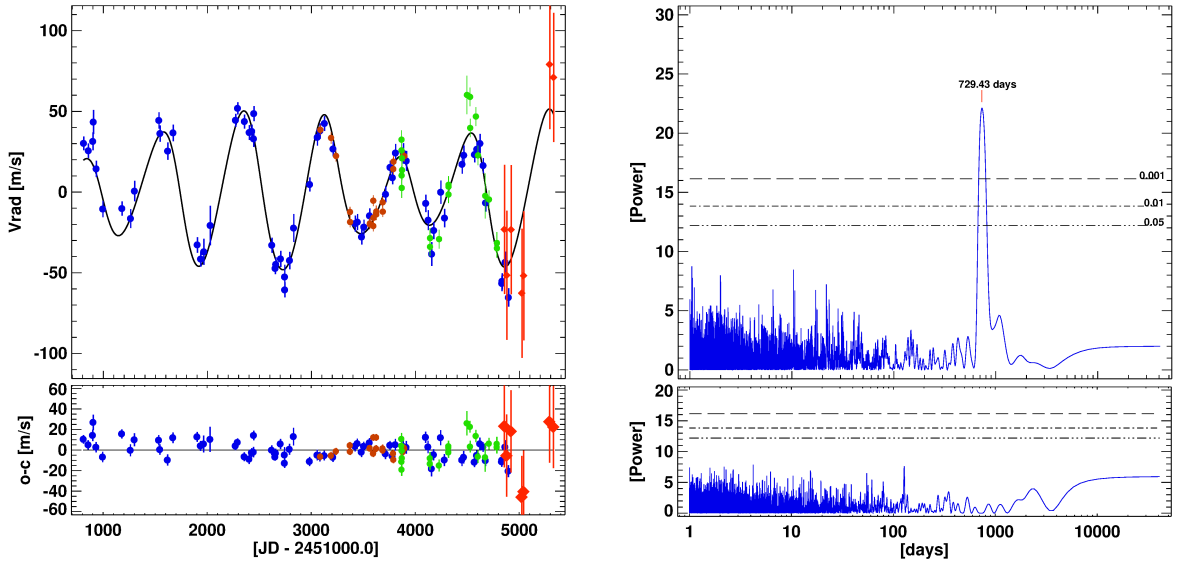

Figure 5.10: *Top left panel*: Dynamical fit to the combined AAO (green), Lick (blue) and HARPS data (dark red) for 7 CMa. Red diamonds are the overploted near-IR velocities from VLT, which are in good agreement with the optical data. *Bottom left panel*: No additional periodicity can be seen from the RV residuals.
Top right panel: Periodogram of the radial velocity data shows very significant peak at 729.43 days, corresponding to the period of the inner planet. *Bottom right panel*: There is no significant peak after subtraction of the the best orbital fit. However, if only the inner planet is subtracted, then a very significant peak at ~ 996 days can be seen on the Lomb-Scargle periodogram plot of the residuals (not shown here), corresponding to the period of the outer planet.

As is discussed in §5.5.5, this close configuration is unstable. However, there are many nearly indistinguishable in terms of $\chi^2_{\rm red}$ value fits around the best one that are long-term stable and are clearly close to the 4:3 period ratio, suggesting a resonant behavior for this planetary system. In order to constrain the permitted orbital parameters, a systematic 2D grid of edge-on coplanar ($i_{c,b} = 90°$, $\Delta\Omega = 0°$) best dynamical fits, was obtained. The fixed grid orbital parameters are the 7 CMa's orbital periods P_b and P_c respectively. All the obtained fits (total of 2600 fits) are tested for stability, similarly to what has been done for the η Cet and ι Dra planetary systems (see §4 and §5.3).

5.5.3 The CRIRES test

Fig. 5.10 shows that the VLT velocities from the CRIRES spectrograph are in fair agreement with the obtained dynamical fit. Nevertheless, only seven out of nine CRIRES data points have been used for the near-IR test. In general, this target had very difficult spectra for precise RVs derivation. Almost all epochs contained spectra heavily contaminated by atmospheric telluric lines. Thus, neither there are unblended telluric lines necessary for precise wavelength calibration, nor there are sharp stellar lines with symmetric profiles needed to obtain the precise velocities. This makes the RV derivation very challenging and for some epochs impossible. Two epochs at JD = 2456244.653 and JD = 2456406.497 have been deselected exactly because of this reason.

For this star was used a different RV derivation approach. After the wavelength solution in each spectral frame is constructed, the spectra is divided by a theoretical telluric spectra, leaving only the stellar lines on the spectra. This has been done for all the epochs, and the tellturic free spectra is later combined in one median very high S/N ratio stellar mask. The wavelength solution for this mask is adopted from the first observation of 7 CMa. After that both telluric free spectra are cross-correlated, and the difference between gives the near-IR radial velocity. This method in principle must give better results than the cross-correlating method with a synthetic spectra containing only few spectral line, as it is done successfully on all other targets in this work, but is still experimental and has it's limitations (see §3 for more details). It has to be noted that using the standard method of cross-correlating with synthetic spectra for this star gives also good results, however, only half of the RV points can be effectively used.

The residuals from CRIRES are large, but the same apply for the optical data. The HARPS data for example has only $\sigma_{HARPS} \sim 0.3{-}0.5$ m s^{-1}, but the *r.m.s.* around the best fit is comparable with the those from Lick and AAO. The estimated residuals to the optical data from all the fits has *r.m.s.* ~ 9 m s^{-1}. This value is even lower than expected for K1III giants from our sample.

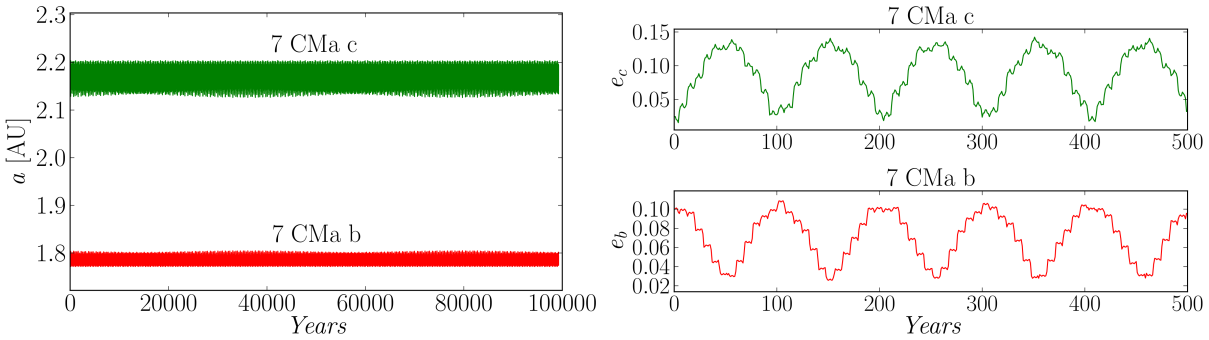

Figure 5.11: Stable orbital evolution for planetary pair around 7 CMa shown for 10^5 years Gravitational interactions are very strong due to the planetary proximity and the planetary mass ration of $m_c/m_b = 0.5$. From the plot can be seen the relatively large semi-major axis libration amplitude. Eccentricities also librate periodically, but the system remains long-term stable.

5.5.4 NUMERICAL SETUP FOR THE 7 CMA PLANETARY SYSTEM

The best dynamical fit from Table 5.10 has been tested with the *Mercury* N-body simulator. Testing first the best dynamical fit for stability is a standard procedure, and it has been done for all the planetary systems discussed in this work.

Later, the set of best inclined fits from the 2D grid was tested for 10^5 years. The starting epoch used for all the simulations was JD = 2451808.021, for which the Jacobi coordinates, are valid and it was an epoch when the first RV observation of 7 CMa was obtained at Lick.

The simulations have been started using the hybrid sympletic/Bulirsch-Stoer algorithm, implemented in the *Mercury* package. The integration time span for the best fit was set for 10^7 years, and with integration time step of 0.5 days. For the grid test the step size has been increased to 8 days and the integration time was decreased to 10^5 years. Stability is excepted, none of the companions is ejected of collide with the star or the other companion. System is classified as stable also if during the integration the companions show constant semi-major axes $a_{c,b}$ during the integration and do not exceed their starting semi-major axis by ± 0.5 AU during the integration time. The system is classified to have a *chaotic behavior*, if none of the companions was ejected or no collisions were occurred during the simulations, but the semi-major axes a_b and a_c scatter chaotically multiple times in different orbital levels by exceeding the ± 0.5 AU border.

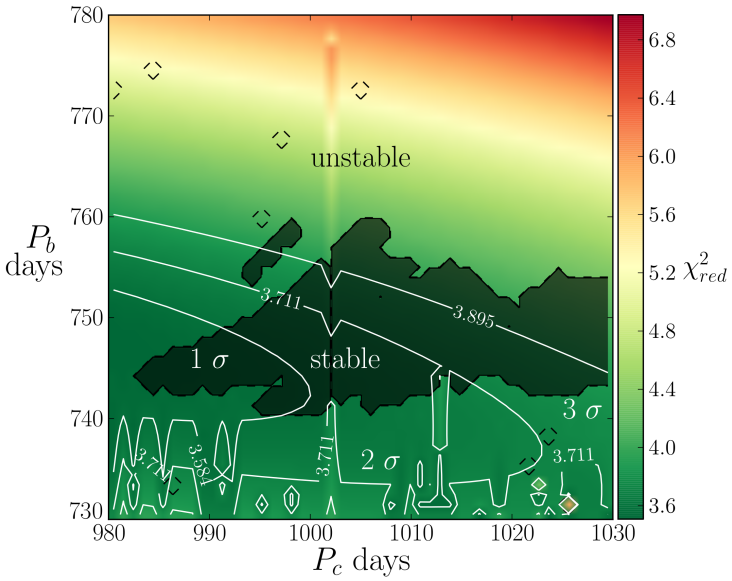

Figure 5.12: Stability map over 2D grid of best dynamical fits for 7 CMa, where the fixed parameters are the planetary periods P_b and P_c. White lines show the 68.3%, 95.5% and the 99.7% $\chi^2_{\rm red}$ confidence levels. The system is stable in very large region of best fits having near 4:3 period ratio (black contour), and only few exhibit a chaotic behavior (dashed contour).

5.5.5 Results from the Stability analysis for 7 CMa

The best dynamical fit to the Lick data was unstable. This result was not unexpected given the close planetary periods and their masses. Close planetary approaches destroyed the system in only ~ 11k years, by ejecting the other planet out of the system.

The stability test over the 2D grid with different planetary periods, however, was very successful. Around 20 % of the fits turned out to be stable for at least 10^5 years. All this fits had period ratios very close to the 4:3. Particularly, from Fig. 5.12 we can see that the stability limiting factor is the period of the inner planet, which cannot be larger than $P_b \sim 760$ days. Most of the stable solutions (darker contour on the Fig. 5.12 grid) are between $P_b = 740$ and 750 days, while the period of the outer can be between $P_c = 990$ and 1030 days. Although, by placing the outer planet further it is expected the system to become more stable, the whole stability region on Fig. 5.12 is somehow unexpected. Most of the fits are almost indistinguishable from the best fit by eye and just slightly worse than the best fit $\chi^2_{\rm red} = 3.44$ value. This leads to the conclusion that indeed we might observe two interacting planets locked in 4:3 MMR around a giant star.

Fig. 5.11 shows the eccentricity and the semi-major orbital evolution for the best stable fit from Fig. 5.12. Eccentricities are dynamic and are changing in off-phase fashion every ~ 100 years. The inner planet eccentricity varies between $e_b = 0.03$ and 0.10, while the other varies between $e_c = 0.03$ and 0.13. In this configuration the semi-major axes a_b and a_c are well separated and librate around their initial values of $a_b = 1.78$ and $a_c = 2.15$ AU. Conclusive study to clearly identify the 4:3 MMR for this system has not been performed. This will be subject of future study, as this is more complex configuration than the, for example, the 2:1 MMR case in η Cet system.

5.5.6 Discussion

Seven out of nine near-IR points are consistent with the dynamical fit constructed from the optical data. Together with the lack of photometric variations, the line shape analysis made by Wittenmyer et al. (2011) and the stability analysis are very convincing argument in favor of the sub-stellar nature of the RV signal of 7 CMa. This system is very interesting because of its relatively massive planets in close orbits. Moreover, if they are indeed in 4:3 mean-motion resonance, this will be the third planetary system in our G and K giant sample that is locked in MMR (see §4 and §6.3)

The planetary system around 7 CMa reminds on the 4:3 MMR pair around the sub-giant star HD 200964 (Johnson et al. 2011). This means that such high order resonance configurations might be common around giants and sub-giants.

Nevertheless the good stability results, we leave some space for discussion about the real nature of the RV signal of 7 CMa. The RV curve very suspiciously reminds to a *beating* phenomenon exited by two oscillations with nearly equal periods. This might be indeed a sign for non-radial $g-$mode pulsations with long periods. As discussed in §1.3.2, so far there are no evidences supporting this theory, so the only possible explanation of the RV periodicity of 7 CMa is two interacting planetary companions, likely locked in mean-motion resonance.

CHAPTER 6

THE BROWN DWARFS

During the past decade it has become clear that brown dwarf objects are common stellar companions. Until then brown dwarfs were thought to form from gravitational collapse inside the molecular cloud, in the same way as stars. Although, this is likely to be one possible formation mechanism, the results from recent planet search surveys, incline scholars to conclude that brown dwarf can also be formed in a massive debris disc, like gas giant planets.

In this Chapter, are introduced three brown systems found around K giants from the Lick sample. First, in §6.1 is shown the τ Gem system, with a slightly different orbital solution for τ Gem b than was given Mitchell et al. (2013), where this brown dwarf was announced. Second, §6.2 reveals the well-known brown dwarf around the 11 Com, which we had observed from Lick and VLT. An update to this system's orbital solution is given, based on the RV data from Liu et al. (2008) and our own optical and near-IR data sets.

Few times in this work has been mentioned the spectacular brown dwarf multiple system around ν Oph. In §6.3 are introduced the dynamical stability results for this system. The two brown dwarfs seem to be locked in 6:1 high order MMR, and they have stable orbits for a large set of coplanar and mutually inclined alignments. It might be possible for the 6:1 resonance configuration of ν Oph to have formed via migration capture in a proto-planetary disk around a young intermediate-mass progenitor.

All brown dwarfs introduced here have passed the near-IR test from CRIRES successfully, showing excellent agreement between the optical and the near-IR data.

Due to the large number of data points from the Lick data set, as well as the additional VLT data set for the aforementioned stars, the individual radial velocities and their estimated errors will not be given in this thesis. Instead, they will be provided if requested. When results for some targets have already been published, a reference to the publication will be given.

The observational techniques used for the Lick and the VLT data sets are explained in detail in §2, and §3.

6.1 HIP 34693 (τ *Gem*)

τ Gem (= HD 54719, HR 2697,HIP 34693) is a HB star of spectral class K2III, with an effective temperature of $T_{\rm eff}$ = 4388 ± 25 K and apparent visual magnitude of V = 4.42. This star has a higher metallicity than Solar ([Fe/H] = 0.14). τ Gem is an intermediate mass star M = 2.34 ± 0.3 $M_{\odot}$, and, thus, evolved to the giant phase relatively quickly (1.22 ± 0.76 G yr). Using the parallax technique, van Leeuwen (2007) estimated the distance from τ Gem to Earth to be roughly 98 parsecs (321 light-years). Other physical parameters of τ Gem are given in Table 6.1.

This star is a known brown dwarf host. Its companion was announced in Mitchell et al. (2013), together with a planetary companion around 91 Aqr (see §5.1). The discovery was made using the Doppler technique and was part of our efforts of searching planetary companions around giant stars at Lick and VLT. Mitchell et al. (2013), has denied that rotational modulation could be one possible explanation for the RV signal of τ Gem. Rotating surface spots do not sufficiently explain the seen RV of this star, as they must occupy around 50% of the stellar surface, in order to distort the stellar line profiles significantly enough to mimic a sub-stellar companion. Large stellar inhomogeneity would imply photometric signatures strong enough to be detected by the Hipparcos satellite, but such signatures forτ Gem have not been reported. Also, given its estimated radius of R = 26.7 $R_{\odot}$ and RV period of P = 306 days, Mitchell et al. (2003) derived a rotational velocity of 4.4 km s^{-1}. This velocity is much higher than the derived rotational velocity of < 1 km s^{-1} for τ Gem (de Medeiros & Mayor 1999).

The CRIRES data presented in Mitchell et al. (2013) is consistent with the best Keplerian prediction. Here, in this work are presented improved near-IR radial velocities for τ Gem and slightly different orbital parameters for τ Gem and slightly different orbital parameters for τ Gem b. The orbital errors are estimated with the *Systemic Console*, by running Multiple MCMC chains in parallel, and therefore tend to be more precise.

6.1.1 OBSERVATIONS

We have made 95 RV measurements for τ Gem, usingthe CAT telescope, in conjunction with the Hamilton spectrograph, at Lick observatory. The resulting radial velocities are given in Mitchell et al. (2013). This star was observed regularly between 2000 and 2011, when our observational program finished. An additional 7 near-IR radial velocities were taken with the CRIRES, between 2011 and 2013, following the observational and data reduction strategy defined in §3.

The typical exposure time needed to achieve S/N ~ 100 at Lick was between 900 and 1200 sec, while at the much larger UT1 (VLT) telescope aperture for the individual jitter exposures was set to 5 seconds, in order for the combined near-IR spectra to reach S/N > 300. The typical RV uncertainties from the Hamilton spectrograph have σ_{Lick} = 3−5 m s^{-1}. These values are much lower than the intrinsic stellar jitter for τ Gem. The estimated RV uncertainties from CRIRES are σ_{VLT} ~ 40 m s^{-1}.

6.1.2 Orbital fit

The Lomb-Scargle periodogram test, when applied to the Lick data, showed one significant peak at 305 days. The Keplerian model to the τ Gem data is consistent with the value obtained from the Periodogram, suggesting a brown dwarf companion ($m_b \sin i = 20.32 \pm 0.19\ M_{\rm Jup}$) with orbital an period $P_b = 305.45$ days. The orbital elements that are introduced in this chapter were obtained independently from those published by Mitchell et al. (2013), but, as expected, they are very similar. MCMC routine from the *Systemic Console* has been used in order to derive the orbital errors. Running multiple MCMC chains in parallel is known to be a more precise method for deriving planetary uncertainties (i.e. Ford (2005)). Only the Lick data is used for the Keplerian fitting, resulting in a $\chi^2_{\rm red}$ value of 19.79 – much larger than the ideal value of 1. As can be seen from Fig. 6.1 the data are indeed scattered around the fit, due to the additional RV jitter intrinsic to the star. The data residuals from the best Keplerian fit have a *r.m.s.* = 21.21 $\rm m\,s^{-1}$. This value is typical (or even low) for stars with spectral class K2III. The rest of the obtained orbital elements are summarized in Table 6.2.

Table 6.1: Stellar properties of τ *Gem*

Spectral type	K2III
Age [G yr]	1.22 ± 0.76
Mass [$M_\odot$]	2.34 ± 0.3
Luminosity [$L_\odot$]	238.4 ± 11.4
Radius [$R_\odot$]	26.76 ± 0.71
$T_{\rm eff}$[K]	4388 ± 25
$\log g$[cm · $\rm s^{-2}$]	1.96 ± 0.07
[Fe/H]	0.14 ± 0.1
$\rm RV_{\mathit{absolute}}$ [$\rm km\,s^{-1}$]	22.02

Table 6.2: τ *Gem* best fit orbital parameters

Orb. Param.	τ *Gem* b	
P [days]	305.45	± 0.12
$m \sin i$ [$M_{\rm Jup}$]	20.32	± 0.19
e	0.03	± 0.01
M [deg]	77.3	± 17.3
ϖ [deg]	137.4	± 17.1
$K_\star$ [$\rm m\,s^{-1}$]	352.2	
a [AU]	1.175	
r.m.s. [$\rm m\,s^{-1}$]	21.21	
$\chi^2_{\rm red}$	19.79	

valid for JD = 2451809.039

6.1.3 The CRIRES test and brief Discussion

The CRIRES data introduced in Mitchell et al. (2013) is already consistent with the best Keplerian fit. After that paper was submitted for publication, additional improvements to the RV derivation pipeline have been made. The new obtained RVs have *r.m.s.* comparable to those of the optical, which was a significant improvement. In fact, τ Gem is one of the best examples of near-IR and optical RVs consistency from our sample. Fig. 6.2 illustrates the optical phase and amplitude on the VLT and Lick RV data. Therefore, τ Gem is once again confirmed to host at least one brown dwarf planetary object.

The exceptionally circular orbit for τ Gem b merits further study. It will be exciting if in future can be constrain the real mass on the hypothetical brown dwarf. Precise astrometric signatures on the movements of τ Gem from the Gaia satellite are expected to reveal more information about the architecture of this planetary system.

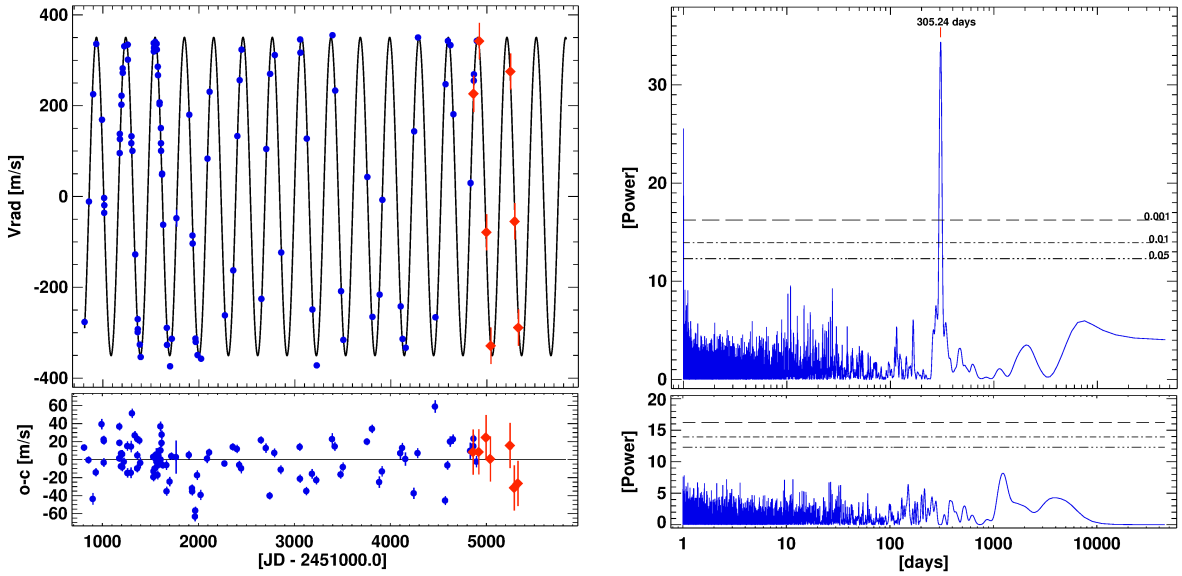

Figure 6.1: Radial velocity plot for τ Gem. *Top left panel*: Lick RV data (*blue*) and CRIRES data (*red*) show very good agreement. The best Keplerian data model is constructed only using the Lick data. *Bottom left panel*: Residual RV data after subtraction of best fit shows *r.m.s.* = 30.3 m s^{-1}, which is most likely the jitter value for τ Gem. *Top right panel*: Periodogram of the radial velocity data for τ Gem, shows a significant peak at 305.5 days, exactly matching the duration period from the Keplerian orbital fit. *Bottom right panel*: Periodogram for the residual data after subtraction of the orbital fit. No significant peak is present.

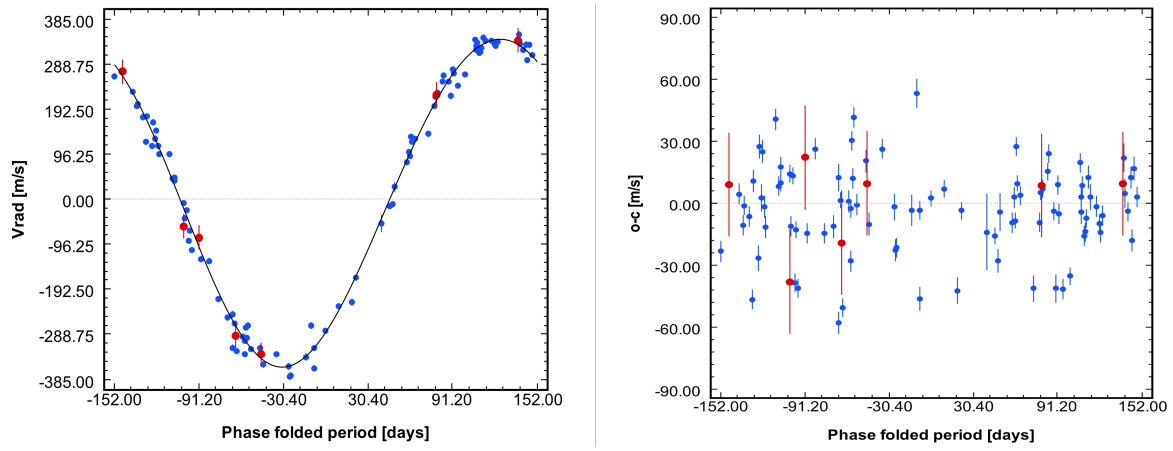

Figure 6.2: *Left*: the phase folded plot for τ Gem, clearly shows the RV periodicity of the Doppler signal. *Right*: The residuals from the plot.

6.2 HIP 60202 (11 *Com*)

11 Com (= HD 107383, HR 4697, HIP 60202) is a late orange G8III giant star in the constellation Coma Berenices. At 290 light years away (~ 112 pc), it's apparent magnitude in V is 4.72 [mag]. 11 Com is a metal-poor star with [Fe/H] = −0.24 ± 0.1, with mass of $M = 2.21 \pm 0.31\ M_{\odot}$. Its effective temperature is $T_{\rm eff} = 4829 \pm 28$ K and the surface gravity is $\log g = 2.43 \pm 0.07$ [cm · s^{-2}]. Stellar parameters from Reffert et al. (2014) are summarized in Table 6.3.

In *SIMBAD*[1] 11 Com is given as double-star system. Little is known about its faint ($V = 12.9$ mag) companion BD +18 2592B. Since 2008, the primary 11 Com has been known to harbor a sub-stellar companion. A brown dwarf object with a minimum mass of $m \sin i = 19.4 \pm 1.5\ M_{\rm Jup}$, eccentricity of $e_b = 0.231 \pm 0.005$, and an orbital period of $P_b = 326.03 \pm 0.32$ days was first announced by Liu et al. (2008). That paper was a joint effort from two planet-search programs between China and Japan. 25 precise radial velocities were taken at OAO (Japan) between 2003 and 2007, and, in order to confirm the star's variations a separate set of 18 RVs were obtained at Xinglong observatory (China), between 2005 and 2007. Liu et al. (2008), by showing that there is no significant emission in the Ca II lines, thus excluded the possibility that the RV periodicity seen from the Xinglong and OAO data was caused by stellar activity.

6.2.1 Observations

The precise RV observations for 11 Com began at Lick, in late 2004 and were completed in the late 2011. We obtained a total of 89 RV measurements for 11 Com with a typical RV precession from the Hamilton spectrograph of around $\sigma_{Lick} = 3$–5 m s^{-1}. An additional 8 near-IR radial velocities have been taken with the CRIRES between 2011 and 2013, following the observational and data reduction strategy defined in §3. The typical CRIRES uncertainties are larger than those derived from the Hamilton ($\sigma_{VLT} \sim 40$ m s^{-1}). The exposure time needed to achieve S/N ~ 100 at Lick ranged from 900 to 1200 sec, while, at the much larger UT1 (VLT) telescope aperture, the jitter exposures necessary for co-added spectra from CRIRES to reach S/N > 300 were only 5 seconds

6.2.2 Orbital fit

One significant peak at 320 days can be seen on the Lomb-Scargle periodogram. All the available optical radial velocities from OAO, Xinglong and Lick were used to construct the Periodogram and the best Keplerian fit. When applying the Keplerian model to the 11 Com optical data, the model is consistent with a companion with an orbital period of $P_b = 323.1 \pm 0.50$ days, which is very close to the obtained value from the Lomb-Scargle periodogram. The large RV amplitude of $K_\star = 300.43$ m s^{-1}, suggests a massive companion with $m_b \sin i = 16.69 \pm 0.33\ M_{\rm Jup}$. The orbital elements that are introduced in this work tend to be a recent update to the orbital configuration given in Liu et al. (2008). Table 6.4 gives the new orbital elements for 11 Com b and their

[1] http://simbad.u-strasbg.fr

orbital uncertainties, as estimated with the *Console's* MCMC package. The Keplerian fit to the combined data has a $\chi^2_{\rm red}$ value of 9.39. The poorness of the fit comes from the additional RV jitter intrinsic to the star, which is caused by short period $p-$mode stellar oscillations. The estimated *r.m.s.* of the data is 30.30 m s^{-1}, which is larger when compared to the stars from our Lick sample from spectral class G8III.

Table 6.3: Stellar properties of 11 *Com*

Spectral type	G8III
Age [G yr]	1.19 ± 0.44
Mass [$M_\odot$]	2.21 ± 0.31
Luminosity [$L_\odot$]	112.0 ± 4.6
Radius [$R_\odot$]	15.14 ± 0.36
$T_{\rm eff}$[K]	4829 ± 28
log g[cm · s^{-2}]	2.43 ± 0.07
[Fe/H]	−0.24 ± 0.1
RV$_{absolute}$ [km s^{-1}]	43.060

Table 6.4: Updated best fit for 11 *Com*

Orb. Param.	11 Com b	
P [days]	323.09	± 0.50
m sin$i$ [$M_{\rm Jup}$]	16.69	± 0.33
e	0.243	± 0.013
M [deg]	144.24	± 4.37
ϖ [deg]	92.78	± 4.31
$K_\star$ [m s^{-1}]	300.43	
a [AU]	1.201	
r.m.s. [m s^{-1}]	30.3	
$\chi^2_{\rm red}$	9.39	

valid for JD = 2453002.279

6.2.3 THE CRIRES TEST AND BRIEF DISCUSSION

As can be seen from Fig. 6.3 and Fig. 6.4, the near-IR VLT data are in very good agreement with the best Keplerian fit. The obtained near-IR RVs have *r.m.s.* comparable to those from the optical, which is essentially the case for all brown dwarf companions introduced in this thesis. However, for fitting have been used only six out of eight data points. As discussed in §3, not all of the epoch can be used for precise velocity derivation. Due to the Earth's barycentric movement the stellar spectral lines can have shifts ∼ ± 30 km s^{-1}, which might lead to unwanted overlap of the useful spectra with the nearly static atmospheric absorption lines. The spectra from epochs JD = 2455934.78 and 2456024.59, did not contain useful stellar lines for precise RVs. Instead, the stellar lines were contaminated by atmospheric telluric lines, and thus making it impossible to obtain useful RV information. The two spectra in question had very large dispersion from the Keplerian fit and were therefore excluded.

The near-IR test and the observed Keplerian eccentricity are two very strong arguments in favor of the planetary hypothesis for 11 Com b. Overall, our use of four different instruments that measured precise radial velocities within a span of more than 10 years produced conclusive planetary confirmation. Therefore, although we know only the minimum mass, the substellar nature of 11 Com b is clear.

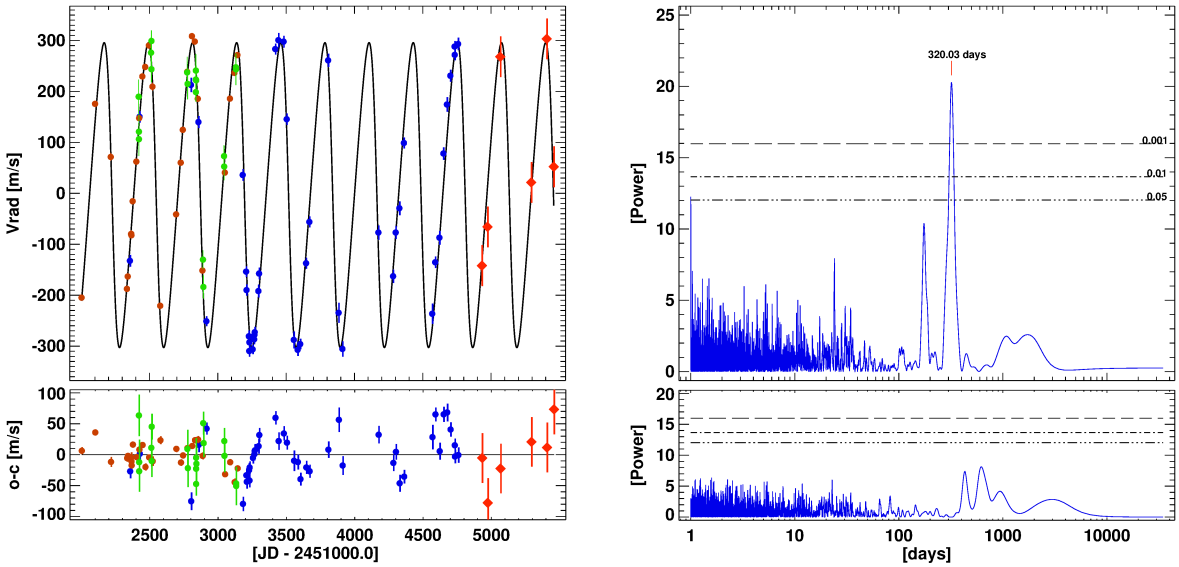

Figure 6.3: *Top left panel*: Radial velocities of 11 Com observed at OAO (*red circles*), Xinglong (*green*), Lick (*blue*) and VLT (*red diamonds*). The Lick and CRIRES data obtained in this study, agreed strongly with the original data from Liu et al. (2008). Keplerian orbit is constructed using only optical data, while only the RV offset is fitted for the near-IR data. *Bottom left panel*: the residuals show jitter much larger than the observational error from the optical. *Top right panel*: The Lomb-Scargle periodogram peak (320 days) is consistent with that obtained from the Keplerian model (323 days). Another alias peak can be seen at 174 days, but cannot be correlated with a planet on the fit. *Bottom right panel*: No additional peak can be seen in the periodogram residuals.

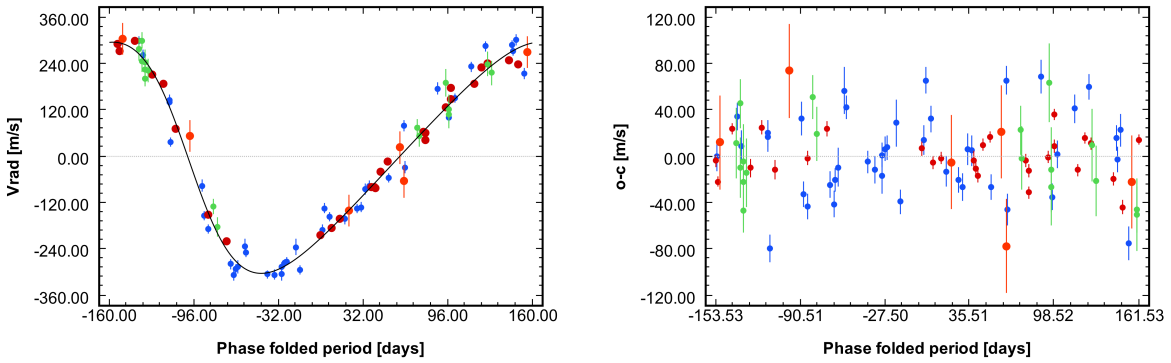

Figure 6.4: *Left*: the phase folded plot for 11 Com, shows clearly the RV's eccentric signature. CRIRES data points (orange) are very consistent with the RV optical phase and amplitude and follow the best Keplerian fit. *Right*: The residuals from the plot.

6.3 HIP 88048 (ν *Oph*)

ν Oph (= HD 163917, HR 6698, HIP 88048) is a bright (V = 3.31), giant G9III star, with near solar metallicity ([Fe/H] = 0.06 ± 0.1) and an effective temperature $T_{\rm eff}$ = 4886 ± 42 K. Due to its large mass ($M_{\odot}$ = 2.73 ± 0.15), ν Oph have evolved fast, having an estimated age of only 0.65 ± 0.17 G yr. More stellar parameters from Reffert et al. (2014) are given in Table. 6.5.

ν Oph is one of the most unique stars in our sample. Mitchell et al. (2003) announced the discovery of a brown dwarf companion around this star with $m_b \sin i$ = 22.2 ± 0.1 $M_{\rm Jup}$, based on the initial data from our survey. However, follow-up observations at Lick showed that a single Keplerian fit cannot explain the data satisfactorily. By the time we finished our observations at Lick, the full optical data set clearly revealed the presence of a second sub-stellar companion with a minimum mass slightly larger than $m_c \sin i$ = 24 $M_{\rm Jup}$. This system was announced in Quirrenbach et al. (2011), and, a year later, the system was independently discovered and confirmed by Sato et al. (2012). In this thesis, are introduced the extended optical observations for ν Oph up to November 2011. In addition, between 2011 and 2013, a total of 10 near-IR absolute RV's were taken with the CRIRES spectrograph at VLT.

6.3.1 OBSERVATIONS

In total, we obtained 150 optical observations for ν Oph using the CAT telescope in conjunction with the Hamilton spectrograph at Lick observatory. This star was observed regularly between 2000 and 2011, when our observational program Lick finished. An additional 10 near-IR radial velocities were taken with the CRIRES spectrograph from 2011 to 2013, in order to test the Doppler signal against the optical. The typical exposure time needed to achieve S/N ~ 100 at Lick was 300 sec, while at the much larger UT1 (VLT) telescope aperture, the six individual jitter exposures were set to only 3 sec, so the combined jitter frames always had S/N > 300 at reference wavelength. The typical RV uncertainties from the Hamilton spectrograph are lower than the typical intrinsic stellar jitter of ν Oph (9 m s^{-1}), at σ_{Lick} = 3−5 m s^{-1}. The adopted RVs uncertainties from CRIRES are σ_{VLT} ~ 40 m s^{-1}.

6.3.2 ORBITAL FIT

The Lomb-Scargle periodogram test to the Lick data shows only one significant peak at at 533.81 days (see Fig. 6.5). Few other alias peaks can be identified but none of them are consistent with the orbital fit model. A peak shown in the *upper right* on Fig. 6.5 at 3096.11 days, most likely corresponds to the period of the second companion derived from the fitting (see the text below).

Data fitting was accomplished using the *Systemic Console* package. The Gragg-Bulirsch-Stoer (GBS) method, one of the dynamic engines built into the Systemic software, was selected to obtain orbital parameters. Using GBS, any gravitational perturbations between the ν Oph's companions are taken into account. In general, the dynamical fitting must give better $\chi^2_{\rm red}$ value than a simple multiple Keplerian model, if the companions exhibit gravitational perturbations.

Table 6.5: Stellar properties of ν *Oph*

Spectral type	G9III
Age [G yr]	0.65 ± 0.17
Mass [$M_\odot$]	2.73 ± 0.15
Luminosity [$L_\odot$]	109.3 ± 3.1
Radius [$R_\odot$]	14.62 ± 0.32
$T_{\rm eff}$[K]	4886 ± 42
$\log g$[cm · s^{-2}]	2.56 ± 0.04
[Fe/H]	0.06 ± 0.1
RV$_{absolute}$ [km s^{-1}]	12.950

Table 6.6: ν *Oph* best fit orbital parameters

Orb. Param.	ν Oph b	ν Oph c
P [days]	530.1 ± 0.13	3186.3 ± 6.76
$m \sin i$ [$M_{\rm Jup}$]	22.20 ± 0.1	24.42 ± 0.18
e	0.126 ± 0.004	0.189 ± 0.007
M [deg]	236.6 ± 1.62	222.2 ± 2.1
ϖ [deg]	9.00 ± 1.57	9.27 ± 2.2
$K_\star$ [m s^{-1}]	289.6	176.9
a [AU]	1.79	5.92
r.m.s. [m s^{-1}]	9.07	
$\chi^2_{\rm red}$	2.78	

valid for JD = 2451853.595

Assuming stellar mass to be 2.7 $M_\odot$, the dynamical fit has a very good $\chi^2_{\rm red}$ value of 2.78, while the Keplerian has a slightly worse $\chi^2_{\rm red}$ value of 2.80. The badness of the fit ~ 2 units above 1, arises from the additional $p-$mode short term stellar oscillations. The estimated *r.m.s.* from the fit is ~ 9 m s^{-1}. This value is expected for G9III giants from our sample and is, in fact, much lower than the jitter of the vast majority of K type giants (see Fig. 4.2).

The Jacobi orbital elements obtained from the dynamical fit are consistent with two sub-stellar companions having minimum masses in the brown dwarf regime (m_b = 22.2 $M_{\rm Jup}$ and m_c = 24.4 $M_{\rm Jup}$). Both companions have intermediate eccentricities (e_b = 0.13, e_c = 0.19), with arguments of periastron $\omega_{c,b}$ in aligned configuration ($\Delta\omega$ ~ 0°), The conclusion from the best fit is that the companions orbital periods are very close to ratio of 6:1 (P_b = 530 days, P_c = 3184 days).

The VLT data from the near-IR wavelength region agrees almost perfectly with the obtained RV prediction from the dynamical fit. One point, however, is not shown on Fig. 6.5, due to its significant inconsistency with the fit (more than -400 m s^{-1}). Close investigation from the near-IR spectra taken at JD = 2456496.673 shows that the necessary S/N of ~ 300 have not been reached, and thus, leads to large RV derivation error. Nine out of ten near-IR points consistent with the fit, together with the Keplerian nature of the obtained orbital elements are very convincing argument in favor of the sub-stellar nature of the RV signal of ν Oph. All the planetary orbital elements and their uncertainties estimated via MCMC approach are given in Table 6.6.

Even after the good near-IR and stability results for ν Oph, one could not be sure, if the system is really coplanar, neither what is it's line of sight inclination. To constrain the most possible orbital parameters for the companions of ν Oph, and to try to give an upper limit on their inclinations and masses, A systematic 2D grid of best dynamical fits was created, where the fixed orbital parameters are the companions inclinations i_b and i_c. $\Delta\Omega$ is left fixed at 0°, so the mutual inclination comes only from the difference between i_c and i_b ($\Delta\, i = i_c$ - i_b). All the obtained set of fits (~ 2600 fits), are after that tested for stability, making this $\chi^2_{\rm red}$ grit an effective stability map, similarly to those made for the η Cet system (see §4).

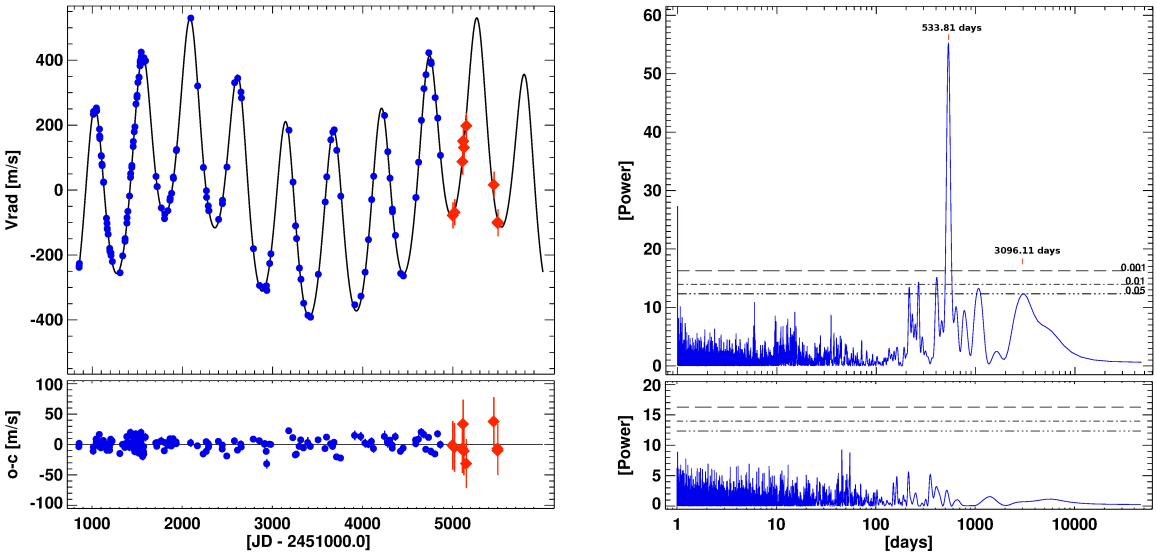

Figure 6.5: *Top left panel*: Dynamical fit to the Lick data for ν Oph. *Bottom left panel*: No additional periodicity can be seen from the RV residuals.
Top right panel: Periodogram of the radial velocity data shows very significant peak at 533.81 days, and few other that are not matching with the periods from the dynamical fit. The 3096.11 days peak is close to the second companion's period from the dynamical fit (P_c = 3186.3 days). *Bottom right panel*: There is no significant peak after subtraction of the orbital fit.

6.3.3 NUMERICAL SETUP FOR THE ν OPH PLANETARY SYSTEM

To test the dynamical stability of the ν Oph's best dynamical fit, the obtained Jacobi orbital elements are passed to the *Mercury* N-body simulator as input. Testing fist the best dynamical fit for stability is a standard procedure in this work and it has been done for all the planetary systems discussed in this thesis.

Later, the set of best inclined dynamical fits from the 2D grid are integrated for 10^5 years. The starting epoch used for all the simulations – JD = 2451853.595, which was the epoch when the first RV observation of ν Oph was obtained at Lick and for which the input Jacobi elements are valid.

The simulations were performed using the hybrid sympletic/Bulirsch-Stoer algorithm, implemented in the *Mercury* package. The integration time span for the best fit was set for 10^7 years, with integration time step of 0.5 days, in order to obtain more precisely the orbital evolution. For the grid test the step size have been increased to 8 days so less CPU time was used. In fact, even larger time step should perform accurate results, given the well separated planetary orbits, but these time steps are standards for the stability test in this work and thereby, are left unchanged. Stability is excepted, if none of the companions are ejected of have collided with the star or between each other. System is classified as stable also if during the integration the companions show constant semi-major axes (i.e. do not exceeds their starting semi-major axis by ± 0.5 AU during the simulations). As it was defined earlier for the η Cet planetary system, the system will be classified to have a *chaotic behavior* if none of the companions were ejected or

collided during the simulations, but the semi-major axes a_b and a_c scattered chaotically multiple times in different orbital levels, by exceeding the ± 0.5 AU border.

6.3.4 Results from the stability analysis for the ν Oph system

Without any surprise, the stability showed that the best fit is stable for 10^7 years. Fig. 6.6 shows the eccentricity and the semi-major orbital evolution for 10^5 years. The planetary companion ν Oph b varying it's eccentricity between $e_b = 0.12$ and 0.14, due to the gravitational interactions with the outer companion ν Oph c. The eccentricity of ν Oph c is much larger, but the oscillating amplitude is somehow lower than the inner. The semi-major axes for both are constant, and even for much longer integration period are not expected to change in this orbital set.

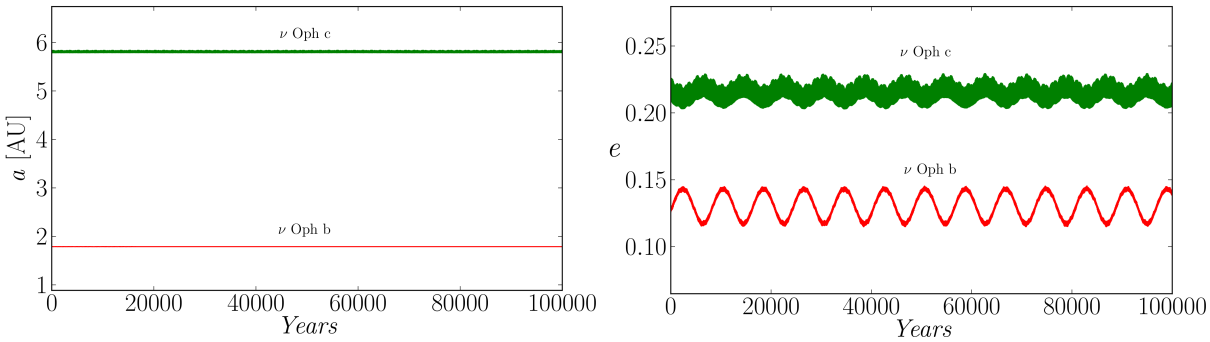

Figure 6.6: The best dynamical fit of ν Oph system is long-term stable. *Left*: the Jacobi semi-major axis of both ν Oph b and c is constant, and during the orbital evolution are consistent with mean orbital periods involved in 6:1 MMR. *Right*: eccentricities are moderate and exhibit relatively small libration amplitudes.

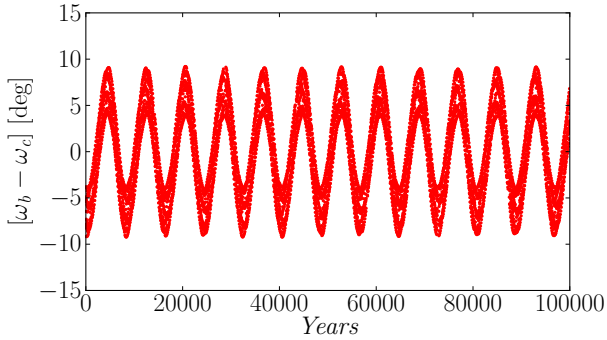

Figure 6.7: Evolution of the secular resonance angle $\Delta\omega$ of the ν Oph system's best fit. $\Delta\omega = \omega_b$ - ω_c is librating around 0°. This aligned configuration is expected giving the fact that the mean planetary period ratio is in 6:1. The resonant nature of the ν Oph system is obvious.

As it was assumed in the beginning, the system indeed shows a resonant behavior. The mean periods are in stable 6:1 MMR, while the secular resonance angle $\Delta\omega = \theta_b$ - $\theta_c = \omega_b$ - ω_c is librating strictly around 0°. Fig. 6.7 illustrates the evolution of $\Delta\omega$. The libration amplitude is ± 9°, keeping both resonant angles $\theta_b \approx 0°$ and $\theta_c \approx 0°$. This is typical resonant behavior and is expected to occur during a smooth migration capture in earlier epoch of the system.

The final test performed was to test the 2D grid of best inclined fits. Each fit from the inclined grid was tested for stability using the criteria and the setup defined above, but for only 10^5 years. Fig. 6.8 introduce the final stability results over the 2D $\chi^2_{\rm red}$ surface. The system turn out to be stable in broad range of inclined coplanar and mutually inclined configurations. The maximum inclination for a stable coplanar configuration is at $i_{c,b} \sim 155°$. Assuming higher inclinations, and thus higher drown dwarf masses, the system becomes unstable. Very high mutual inclinations are also not feasible, limiting the mutual inclination border at $\sim 45{-}50°$. On Fig. 6.8 is also shown a grid map where instead of the $\chi^2_{\rm red}$ surface is introduced the companion's mass ratio from the obtained fits. Bold black lines notate the border between the brown dwarf and low mass star masses ($m_{c,b} > 80\ M_{\rm Jup}$). The stability is impossible if ν Oph b is a low mass star, but stable mutual inclined solutions can be found if ν Oph c turns out to be a low mass star.

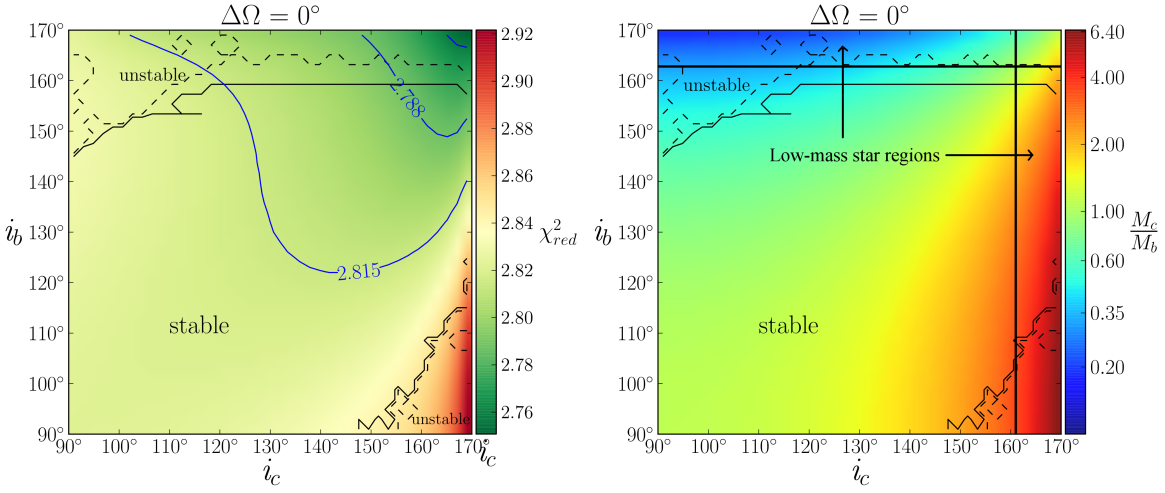

Figure 6.8: Stability map over 2D grid of best dynamical fits for the ν Oph system, where the fixed parameters are the planetary inclinations i_b and i_c. $\Delta\Omega$ is fixed to be 0°, thus, the mutual inclination comes only from the difference between i_c and i_b ($\Delta\, i = i_c - i_b$). *Left*: The system is stable in broad range of coplanar and mutual inclinations. The maximum stable coplanar configuration is at $i_{c,b} \sim 160°$. Assuming higher inclinations, and thus higher planetary masses, the system becomes unstable. *Right*: is shown a grid map where is introduced the companion's mass ratio from the obtained fits. Bold black lines notate the border between the brown dwarf and low mass star masses. The stability is impossible if ν Oph b is a low mass star, while stable mutual inclined solutions exist if ν Oph c is a low mass star.

6.3.5 DISCUSSION

The brown dwarf companions around ν Oph found in our Lick sample are indeed rising some questions. So far it is not very clear whether a brown dwarf mass objects can form in a proto-planetary disk just like the planets, but the ν Oph configuration would incline to this possibility. There indisputable evidences that both objects are in 6:1 MMR, which means that they must settle in this orbits by migration. At least this possibility is the most accepted theory for the founded planetary pairs in mean motion resonance. The ν Oph K giant it self is also quite massive. Perhaps, the formation of such massive "planets" depends on the more massive protoplanetary disk, which the young ν Oph most probably had in the past.

CHAPTER 7

PLANETS IN CLOSE BINARY SYSTEMS

Astronomers already have discovered planets orbiting stars in binary systems. This might not be very surprising, having in mind that at least 50 % of the stars in our galaxy are physically coupled with one or more stars. Even in our Lick study we have founded planets orbiting around a star member of this population (see 91 Aqr §5.1 and 11 Com §6.2). More complicated cases are planets in circumbinary orbits (i.e. planet orbiting around the common mass center of two very close stars instead of one (Welsh et al. 2012; Orosz et al. 2012)). Stars in close binary systems where one of the stars is a planetary host, are also know to the astronomers. There are many challenges in terms of explaining the formation of planets around close gravitationally interacting stars, and it is also very challenging to provide arguments supporting the long-term stability of such a system.

One member of such a complicated configuration is the well known γ Cephei system. The primary is a orange sub-giant star of class K1III-IV, while the secondary is relatively small star orbiting in slightly eccentric orbit with semi-major axis of only 25 to 30 A.U. from the primary star, making this system a binary with period of P < 50 years. The planetary system around γ Cephei A was discovered by Hatzes et al. (2003), using a precise radial velocity measurements from the McDonald Observatory. In fact γ Cephei Ab would have been the first true extrasolar planet discovered, as it was spotted first by Campbell et al. (1988). Later Walker et al. (1992) also observed the RV signal from γ Cephei Ab, but dismissed the planetary hypothesis because they detected weak variations in the Ca II emission line index with the same period as the planet.

In the Lick data we have found two binary systems that like in the case of γ Cephei system show signature of a planet orbiting the primary. In fact, the Lick examples are even more complicated due to the closer proximity of the binary. The HR 2877 (see §7.1) is consistent with luminous K giant with about two Solar masses, which have a close (a = 13.5 AU) and very eccentric stellar companion (e = 0.73 !), with mass half of the Solar. In addition, the K giant RV signal is showing signs of massive planetary companion orbiting at 1.1 AU. The other very interesting example is the 39 Cyg system (see §7.2) , which has a RV signal remarkably similar

to γ Cephei system, when observed by Campbell et al. (1988); Walker et al. (1992) and Hatzes et al. (2003). However, the secondary – a very low mass star, has been estimated to have very circular orbit with semi-major axis of only 7.5 AU. This makes 39 Cyg the most compact close binary system with planet around one of the stars that is know so far.

Despite that, in order to be fully accepted, both systems have been tested with with CRIRES. Later, the planetary long-term stability has been tested, based on the obtained orbits from the dynamical fit model. Both tests, the near-IR and the stability, gave positive results. The CRIRES radial velocities well fit to the predicted phase and amplitude from the dynamical model constructed based on the optical data, and for both systems long-term stable orbital configurations have been obtained.

Due to the large number of data points from the Lick data set, as well as the additional VLT data set for the aforementioned stars, the individual radial velocities and their estimated errors will not be given in this thesis. Instead, they will be provided if requested. When results for some targets have already been published, a reference to the publication will be given.

The observational techniques used for the Lick and the VLT data sets are explained in detail in §2, and §3.

7.1 HIP 36616 (HR 2877)

HR 2877 (= HD 59686, HIP 36616) is a bright (V = 5.45 mag) horizontal branch (HB) giant star in the constellation Gemini. The effective temperature of HR 2877 is estimated to be $T_{\rm eff}$ = 4658 ± 24 K and the derived metal abundance is [Fe/H] = 0.15 ± 0.1. This is inflated star with a radius of R = 13.17 ± 0.34 $R_{\odot}$, and it is almost twice more massive than Sun (M = 1.92 ± 0.21 $M_{\odot}$). Physical parameters for HR 2877 are given in Table 7.1.

In November 2003, a planet orbiting HR 2877 was announced by Mitchell et al. (2003). In this study was used the initial set of our Lick data, which clearly reveals a RV periodicity, associated with a massive planetary companion. The planet has been estimated to have minimum mass of $m_b \sin i$ = 5.25 $M_{\rm Jup}$, with very circular orbit and with a period of P_b = 303 days. The follow-up observations on HR 2877 from Lick implied that actually this system is much more complex than it was thought. Soon after the announcement by Mitchell et al. (2003), it has become clear that another massive companion is in orbit around HR 2877.

Now, almost 14 years after the first Lick observation, it is rather clear that a short period and very eccentric sub-stellar object is also accompanying HR 2877, and thus, challenging the system's stability and the possible formation scenarios.

7.1.1 OBSERVATIONS

In total we obtained 88 optical observations at Lick in the period from 1999 to the end of 2011. Additional 8 near-IR radial velocities were taken with the CRIRES spectrograph from 2011 to 2013 in order to test the near-IR Doppler signal against the optical. The typical exposure time

needed to achieve S/N of ∼ 100 at Lick was 30 min, while at the much larger VLT telescope aperture the jitter exposures had only 15 sec. in order the combined spectra to have S/N of ∼ 300 at the reference wavelength at detector three (see §3). The typical RV uncertainties from the Hamilton spectrograph are much lower (σ_{Lick} ∼ 5 m s^{-1}), with respect to the intrinsic stellar jitter of HR 2877 (∼ 20 m s^{-1}) and the RV uncertainties from CRIRES (σ_{VLT} ∼ 40 m s^{-1}).

7.1.2 Orbital fit

A Lomb-Scargle periodogram test to the Lick data cannot identify any significant peak due to the complex RV curve of HR 2877 (see Fig. 7.1). Dynamical fitting to the optical data reveals more information about the structure of the HR 2877's non-trivial configuration. The model chosen for fitting is again the Gragg-Bulirsch-Stoer (GBS) (B-SM: Press et al. 1992), implemented to the the *Systemic Console* package (Meschiari et al. 2009). Thus, the gravitational perturbations between the companions are taken into account. Only Jacobi orbital elements are obtained from the dynamical fit. Assuming the stellar mass of HR 2877 to be 1.92 $M_{\odot}$ (Reffert et al. 2014), the dynamical fit has a $\chi^2_{\rm red}$ value of 11.902. The obtained orbital parameters are consistent with one very eccentric (e_c = 0.728) low mass stellar companion with Period of 11621.9 days, which considered with the assumed mass of HR 2877, will give a Jacobi semi-major axis of 13.55 AU. The inner planetary companion has similar orbital constrains as have been given in the work of Mitchell et al. (2003), although the derived mass in this work is larger ($m_b \sin i$ = 6.95 M_{jup}). The residuals of the Lick data to the dynamical fit, shown in Fig. 7.1, has a *r.m.s.* value of 19.8 m s^{-1}, typical for other K2III giant in our sample. Similar *r.m.s.* value has also the near-IR data as can be seen from the RV plot in Fig. 7.1. The near-IR VLT data points are in close agreement with the best Keplerian fit and thus confirm the companion(s) for HR 2877. Orbital parameters for HR 2877 b and HR 2877 c (hereafter HR 2877 c instead of HR 2877 B) and their MCMC derived errors are given in Table 7.2.

Table 7.1: Stellar properties of HR 2877

Spectral type	K2III
Age [G yr]	1.73 ± 0.47
Mass [$M_{\odot}$]	1.92 ± 0.21
Luminosity [$L_{\odot}$]	73.3 ± 3.3
Radius [$R_{\odot}$]	13.17 ± 0.34
$T_{\rm eff}$[K]	4658 ± 24
log g[cm · s^{-2}]	2.49 ± 0.05
[Fe/H]	0.15 ± 0.1
RV$_{absolute}$ [km s^{-1}]	−34.42

Table 7.2: HR 2877 best fit orbital parameters

Orb. Param.	HR 2877 b	HR 2877 c
P [days]	299.2 ± 0.3	11621.9 ± 118.08
$m \sin i$ [$M_{\rm Jup}$]	6.95 ± 0.17	554.83 ± 0.8
e	0.06 ± 0.02	0.728 ± 0.002
M [deg]	292.2 ± 41.3	258.5 ± 1.1
ϖ [deg]	128.8 ± 41.5	149.4 ± 0.2
$K_{\star}$ [m s^{-1}]	136.9	4722.9
a [AU]	1.09	13.55
r.m.s. [m s^{-1}]	19.8	
$\chi^2_{\rm red}$	11.902	

valid for JD = 2451482.024

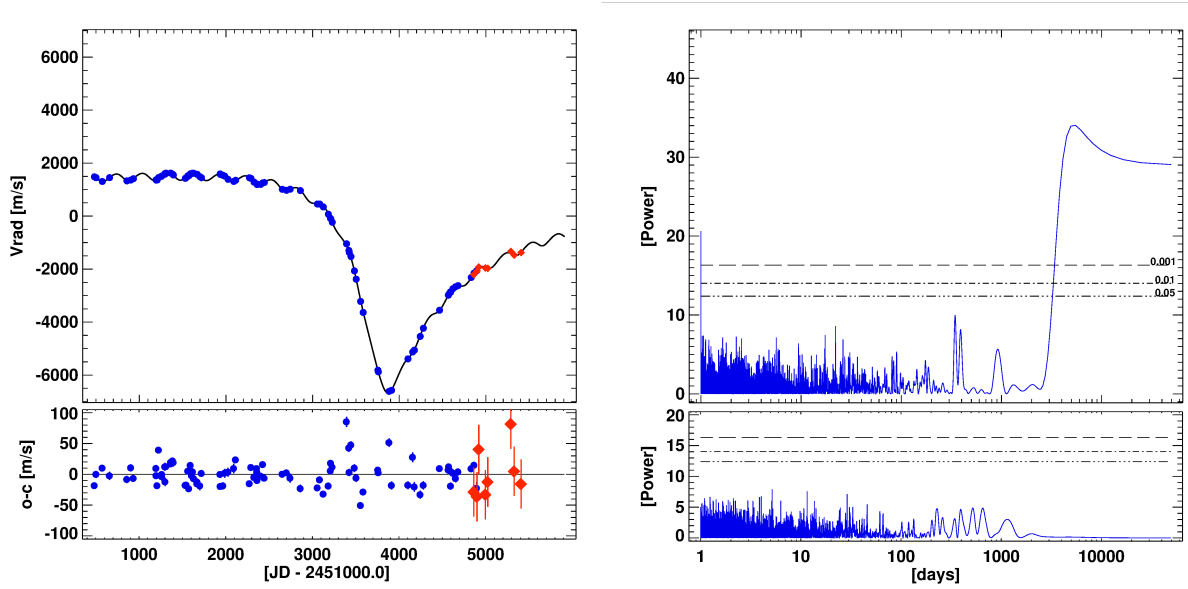

Figure 7.1: Radial velocity plot for HR 2877. *Top left panel*: Lick RV data (*blue*) and CRIRES data (*red*) show excellent agreement. The best dynamical model to the data is constructed only using the Lick data, while VLT data is only overploted by adjusting the RV_{CRIRES} offset. *Bottom left panel*: Residual RV data after subtraction of best fit shows *r.m.s.* = 19.8 m s^{-1}. *Top right panel*: Periodogram of the radial velocity data for HR 2877, fails to find any significant, due to the non-trivial signal from the radial velocity curve for HR 2877. *Bottom right panel*: Periodogram for the residual data after subtraction of the orbital fit. There are no significant peaks presented.

7.1.3 STABILITY ANALYSIS OF THE BEST DYNAMICAL FIT

The best two companion fit was found very hardly by the *Console*. Usually the *Console* was falling into a local $\chi^2_{\rm red}$ minimum of best fits that were consistent with up to three companions. Two of these had stellar nature with average eccentricities and one had a planetary mass close to the one derived in Table 7.2. Those fits had rather good explanation of the data, but they had on average $\chi^2_{\rm red} \sim 42$, and were extremely unstable. After a deep search for two companion fit, much better Newtonian fit ($\chi^2_{\rm red} = 11.902$) was founded and it was consistent with two companions of HR 2788. This fit was a great improvement and for a first time the system was classified as potentially stable. However, the dynamical fit gives to the second companion mass and eccentricity that at first look can put into question this configuration and it's stability (see Table 7.2 for orbital parameters).

To test the dynamical stability on this extreme configuration, again the *Mercury* code was used, by passing the Jacobi best fits coordinates as input. The simulations were run using the hybrid sympletic/Bulirsch-Stoer algorithm, so close encounters with adaptive time step can be computed if such occur. The integration time span was set for 10^7 years, and small time step of 0.5 days was used for this system. Stability is excepted, if the inner planetary companion survives the dynamical test without being ejected, collides with one of the stars or shows constant semi-major axis during the integration (i.e. do not exceed its starting semi-major axis by ± 0.5 AU

during the simulations). The starting epoch used for the simulations was epoch, when the first RV observation of HR 2877 was taken (JD = 2451482.024).

It was a great success, when the results from the N-body analysis showed that the system is indeed stable for at least 10^7 years. Fig. 7.2 shows the eccentricity and semi-major orbital evolution for HR 2877 b and c. For clearness, the plot shows only the first 500 years of the integrations. The smaller binary companion disturbs the planetary eccentricity with each periastron passage, but the planet seems to have a stable orbit. Small fluctuations can be seen on the HR 2877 c semi-major axis and eccentricity as well.

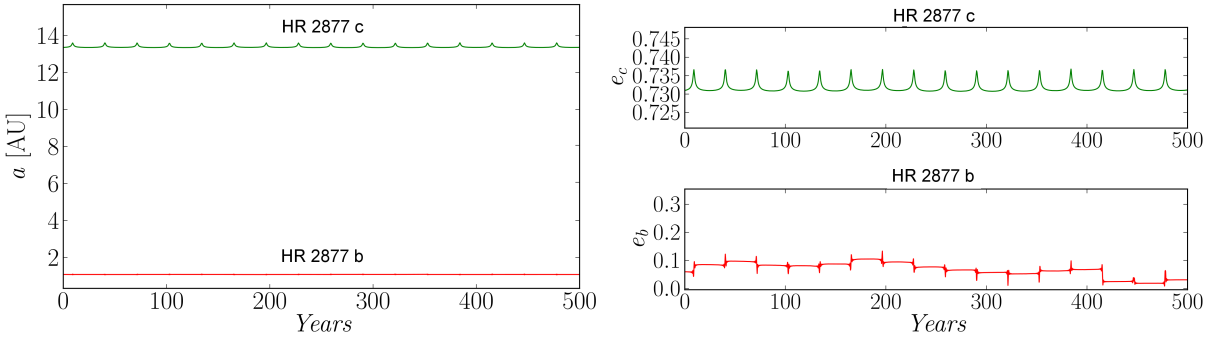

Figure 7.2: Stable orbital evolution of the HR 2877 binary. The planet HR 2877 b orbits around the primary star, while the primary and the second low mass star HR 2877 c are orbiting around their common mass center. Every passage of the low mass star near the primary disturbs the planetary orbit, but the dynamical calculations show that the planet is in a stable orbit for at least 10^7 years.

7.1.4 Discussion

The inner companion around the primary of the HR 2877 binary is placed in very fragile orbit. Attempts to constrain the permitted orbital alignments has been made, but in major of these tests have failed. Any slightly different binary and/or planetary configuration were leading to instability. Possible mutual inclinations assumed by the dynamical fitting routine in general gave a bit better $\chi^2_{\rm red}$, but were also unstable.

It will be surprising, if we indeed reach the real configuration of HR 2788, only by analyzing the RVs from Lick and VLT. However, it turns out that only very near to the best fit we can obtain a "quasi" stable configuration. Longer dynamical simulations are not obtained, because we have presumed that the rate of mass loss for the primary must be taken also into account in such a fragile system. Up to now we do not have a proper tool to manipulate the rate of the mass loss durng the integrations, but this test is planed in future. For sure more efforts can be done in order to understand this system. It is worth this system to be tested with different initial primary mass as it was done for η Cet (see §4).

7.2 HIP 100587 (39 *Cyg*)

39 Cyg (= HD 194317, HR 7806, HIP 100587) is a bright (V = 4.436) red giant star in the constellation Cygnus, distant at ~ 260 light years away from Earth (van Leeuwen 2007). Spectral type of 39 Cyg is K3III, and according to Reffert et al. (2014) is has 80% probability to be on the RGB, with mass of $M = 1.45 \pm 0.18\ M_{\odot}$. The estimated effective temperature is $T_{\rm eff} = 4225 \pm 20$ K. The metallicity of 39 Cyg is nearly solar with [Fe/H] = 0.04 ± 0.1. More stellar characteristics taken from Reffert et al. (2014) are given in Table 7.3.

7.2.1 OBSERVATIONS

In total we have obtained 65 Lick optical radial velocities in the period between 2000 and 2011. Additional 7 near-IR radial velocities were taken at the VLT with the CRIRES spectrograph from 2011 to 2013. The typical Lick exposure time used to reach a S/N of ~ 100 was between 900 and 1200 sec. At the VLT the individual jitter exposures were only 3 seconds−, much shorter due to the huge collecting power of the UT1 8 m telescope. The typical RV uncertainties from the Hamilton spectrograph are $\sigma_{Lick} \sim 5\ {\rm m\,s^{-1}}$, and the typical RV uncertainties from CRIRES have $\sigma_{VLT} \sim 40\ {\rm m\,s^{-1}}$.

7.2.2 ORBITAL FIT

When applied a Lomb-Scargle periodogram test to the optical data from Lick, one can distinguish only the RV periodicity from the low stellar mass binary companion at 5835.49 days (see Table 7.4 and Fig. 7.3). Fitting the data is done by adopting the Gragg-Bulirsch-Stoer method, implemented in the *Systemic Console* software. Double Keplerian fit, which does not take into account the gravitational interaction between the companions, has also been performed. Using the stellar mass from Reffert et al. (2014) $M = 1.4\ M_{\odot}$, the Keplerian and the GBS Jacobi coordinates are sightly different, but both give a very adequate representation to the Lick data. The dynamical fit has a $\chi^2_{\rm red}$ value of 16.31, and is consistent with two companions, one of them with stellar nature ($m_c \sin i = 158.6\ M_{\rm Jup}$). This $\chi^2_{\rm red}$ value has slightly better value than that from the double Keplerian fit with the same stellar mass ($\chi^2_{\rm red} = 16.37$). Thus, in Table 7.4 are introduced only the Jacobi coordinates from the dynamical fit. The inner companion has a mass within the planetary regime ($m_c = 4.24\ M_{\rm Jup}$) and an orbital period of $P_c = 651.2$ days. This period and stellar mass lead to semi-major axis of 1.65 AU − placing this giant planet at the orbit of Mars. Both companions have low eccentricity of $e_b = 0.14$ and $e_c = 0.03$, which makes their orbits well separated in any epoch. Therefore, while the primary and its planetary companion on one side, and the secondary from other, are orbiting in near circular orbits respect to their common mass center, no close approaches between the secondary and the planetary companion can occur. The residuals shown in Fig. 7.3 have a *r.m.s.* value of 17.9 ${\rm m\,s^{-1}}$, which is actually low respect to other K3III giants from our sample. All the planetary orbital elements and their uncertainties estimated via MCMC approach are given in Table 7.4.

One could not be sure, whether the system is really coplanar and what is it's line of sight inclination. To constrain the most possible orbital parameters for this very complex system, and to try to give an upper limit on the companions inclinations and their masses, a systematic 2D grid of best dynamical fits was created. The fixed orbital parameters in the grid are the companions inclinations i_b and i_c. $\Delta\Omega$ is left fixed to be 0°, so the mutual inclination comes only from the difference between i_c and i_b ($\Delta i = i_c$ - i_b).

Table 7.3: Stellar properties of 39 *Cyg*

Spectral type	K3III
Age [G yr]	4.97 ± 2.97
Mass [$M_\odot$]	1.45 ± 0.18
Luminosity [$L_\odot$]	159.3 ± 5.4
Radius [$R_\odot$]	23.60 ± 0.46
$T_{\rm eff}$[K]	4225 ± 20
$\log g$[cm · s^{-2}]	1.86 ± 0.07
[Fe/H]	0.04 ± 0.1
RV$_{absolute}$ [km s^{-1}]	-13.98

Table 7.4: 39 *Cyg* best fit orbital parameters

Orb. Param.	39 Cyg b	39 Cyg c
P [days]	651.2 ± 2.8	5998.8 ± 112.9
$m \sin i$ [$M_{\rm Jup}$]	4.24 ± 0.19	158.6 ± 4.07
e	0.14 ± 0.06	0.03 ± 0.004
M [deg]	143.5 ± 28.9	306.6 ± 4.7
ϖ [deg]	167.0 ± 33.2	104.6 ± 6.4
$K_\star$ [m s^{-1}]	80.3	1415.8
a [AU]	1.65	7.49
r.m.s. [m s^{-1}]	17.9	
$\chi^2_{\rm red}$	16.31	

valid for JD = 2451743.855

7.2.3 The CRIRES test

Fig. 7.3 shows the overploted VLT radial velocities. With CRIRES, 39 Cyg was observed only seven times. This star was one of the most difficult stars for data reduction in our sample observed with CRIRES Due to the lack of almost any well defined single stellar lines, the data reduction was done with a median stellar mask created from the observations is self (see §3.5.3). The CCF maximum for detector one using a median mask gives very fair results. Only the first point has relatively large dispersion from the best dynamical model and all other show consistency with the *r.m.s.* residual level from the Lick data. This star and 7 CMa (see §5.5) show the potential of the cross-correlation method using a combined stellar mask, for stars with almost none available stellar lines for cross-correlation with synthetic noise free stellar spectrum.

7.2.4 Numerical setup for the 39 Cyg system

To test the dynamical stability of the 39 Cyg configuration, The Jacobi best fits coordinates have been passed as an input to the *Mercury* N-body simulator, as has been done for all the planetary systems discussed in this thesis. The simulations were run using the hybrid sympletic/Bulirsch-Stoer algorithm, so close encounters with adaptive time step can be computed if such occur. The integration time span for the best fit was set for 10^7 years and time step of 8 days. Stability is excepted, if the inner planetary companion survives the test and shows constant semi-major axis during the integration (i.e. do not exceeds its starting semi-major axis by ± 0.5 AU during the simulations).

The assemble of best inclined fits from the 2D grid have been tested only for 10^5 years, with the same criteria as above (also how it is done for HR 2877 in §7.1). The starting epoch used for all the simulations was the epoch, when the first RV observation of 39 Cyg was taken (JD = 2451743.855).

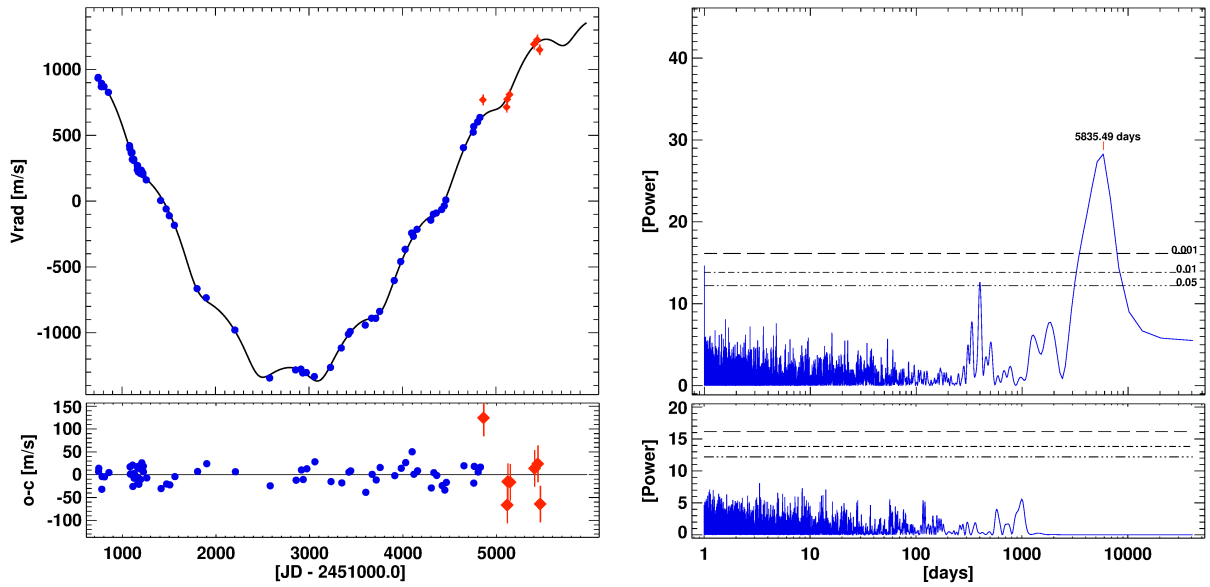

Figure 7.3: Radial velocity plot for 39 Cyg. *Top left panel*: Lick RV data (*blue*) and CRIRES data (*red*) show fair agreement. If we do not consider the first observation, which has poor agreement with the model, the rest of CRIRES data has similar residuals, as those from the Lick data. The best model to the data is constructed using only the Lick data, while VLT data is overploted by adjusting the RV_{CRIRES} offset. *Bottom left panel*: Residual RV data after subtraction of best fit shows *r.m.s.* = 18 m s^{-1}. *Top right panel*: Periodogram of the radial velocity data for 39 Cyg, shows a significant peak at 5835.49 days, near the period of the stellar companion (P_c = 5998.8 days). *Bottom right panel*: Periodogram for the residual data after subtraction of the orbital fit. There is no significant peak presented.

7.2.5 RESULTS FROM THE STABILITY ANALYSIS FOR 39 CYG

As expected, the stability test over the best fit was successful. The fit is stable for 10^7 years, despite the large mass ratio between the low mass star and the giant planet. Also, the low eccentricity orbits for both companions kept their orbits well separated, preventing any closer encounters, which may destroy the system. Fig. 7.4 shows the eccentricity and the semi-major orbital evolution for 10^5 years. The planetary companion 39 Cyg b is slightly disturbed varying it's eccentricity between e_b = 0.12 and 0.14, while the low mass star 39 Cyg c (hereafter 39 Cyg c instead of 39 Cyg B) has much lower eccentricity amplitude oscillating around $e_c \sim 0.04$. The semi-major axes for both are constant and even for much longer integration period are not expected to change in this orbital set. Many different dynamical tests for this binary/planetary system were performed, sometimes with fits over 3σ away from the best fit (not shown in this

thesis), and all have appeared to be stable for at least 10^5 years (which was maximum test time span).

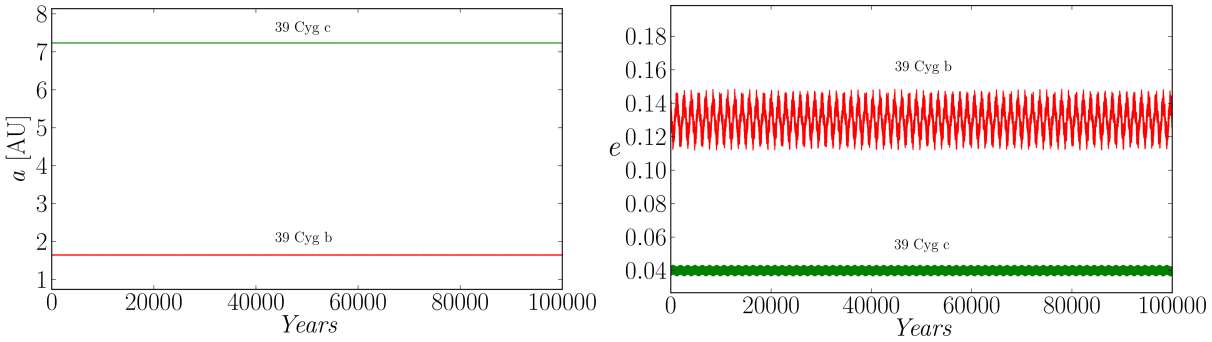

Figure 7.4: The best dynamical fit for 39 Cyg system is long-term stable. *Left*: the semi-major axes evolution shows constant behavior, nevertheless the stellar mass nature of the outer companion 39 Cyg c (hereafter 39 Cyg c instead of 39 Cyg B). *Right*: the eccentricity of 39 Cyg b is fluctuating between 0.12 and 0.14, while at amplitude of 39 Cyg c's eccentricity is much smaller and the star remains in near circular orbit. This best fit solution still might be only one of the many possible stable configurations as the period of the 39 Cyg c is not well constrained.

The final test was performed on the 2D grid of best inclined fits. Each fit from the inclined grid was tested for stability using the criteria and the setup defined above, but for only 10^5 years. Fig. 7.5 introduces the final stability results over the 2D $\chi^2_{\rm red}$ surface. The system is stable in all possible coplanar (limited to $i_{c,b} = 165°$) inclinations, increasing the companion masses to a brown dwarf mass for the inner and to a star having a mass of $\sim 0.6\ M_\odot$ for the outer respectively.

In fits with large mutual inclinations and large mass ratios (see Fig. 7.5 *right*) the system also preserves stability. However, when $\Delta i = |60°|$ the system is unstable. On Fig. 7.5 is shown a grid map where is introduced the companion's mass ratio from the obtained fits. Above $i_b = 161°$, 39 Cyg b should have a brown dwarf mass (i.e. $m_b > 13\ M_{\rm Jup}$). There are many stable solutions above this limit. The best dynamical fit on the grid map (and for this data) is as well above the brown dwarf limit and is stable. This set of orbital elements has mutual inclination of $\Delta i \sim |25°|$, and planetary mass ratio of $M_c/M_B \sim 10$, which excludes the planetary hypothesis for 39 Cyg.

7.2.6 Discussion

The inner companion around the primary of the 39 Cyg binary has a very stable orbit. Almost none of the obtained dynamical fit was able to prevent the long-term stability of the 39 Cyg system. Attempts to constrain the permitted orbital parameters and the possible orbital alignments, were done by using a inclined grid test. However, no conclusions can be made, when almost all of the the proposed configurations are stable. Perhaps, more attention can be given to the best possible fit from the i_b,i_c grid. This fit excludes the planetary companion assumption in favor of a brown dwarf object orbiting together with 0.25 $M_\odot$ K dwarf star. The difference between the best edge-on coplanar (i.e. $i_{b,c} = 90°$) dynamical fit and the best mutual inclined is insignificant to

make firm conclusions about the real architecture of this system. There are not enough evidences in favor of any inclined configuration, besides the fact that the vast majority of them are stable.

The 39 Cyg system reminds for the γ Cephei Ab planet found to orbit around the more massive star from the γ Cephei close binary Hatzes et al. (2003). The main difference between the two systems that 39 Cyg is much more compact. The semi-major axis of the low mass star in the 39 Cyg system is only 7.5 AU, which makes it the most compact close binary system with a planet around the primary that is know so far.

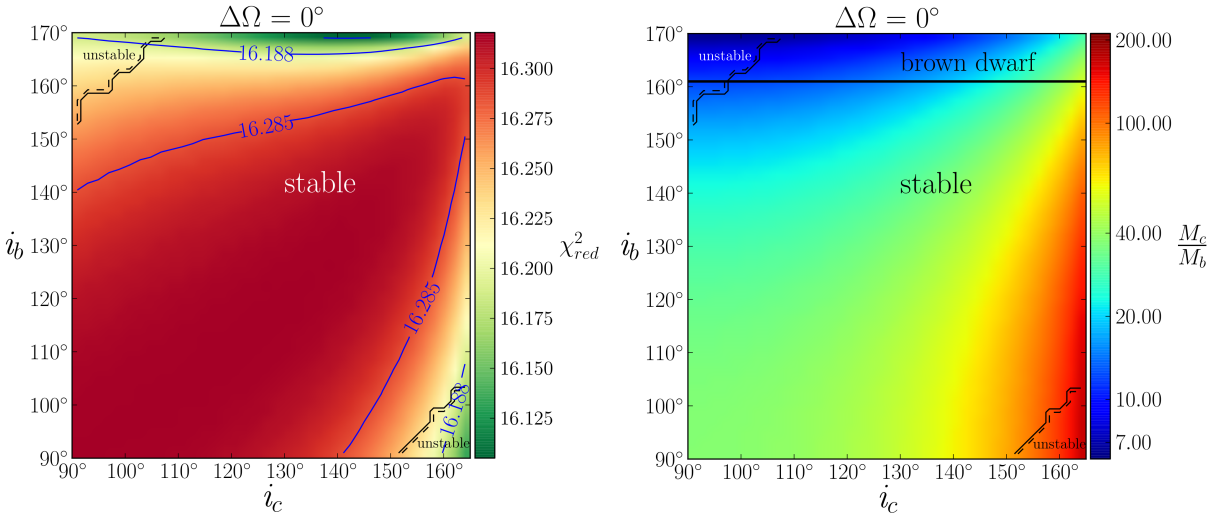

Figure 7.5: Stability map over 2D grid of best dynamical fits for the 39 Cyg system, where the fixed parameters are the planetary inclinations i_b and i_c. $\Delta\Omega$ is fixed to be 0°, thus, the mutual inclination comes only from the difference between i_c and i_b ($\Delta i = i_c$ - i_b). *Left*: The system is practically stable in all possible coplanar inclinations, increasing the companion masses. In very large mutual inclinations (Δi = 65° ~ 80°), however, the system is unstable. *Right*: is shown a grid map, where the companion's mass ratio from the obtained fits is introduced. Above i_b= 161° 39 Cyg b has a brown dwarf mass. There are a many stable solutions above this limit. In fact, the best stable dynamical fit requires brown dwarf mass for 39 Cyg b with mutual inclination with 39 Cyg c of $\Delta i \approx 25°$, and planetary mass ratio of $M_c/M_B \sim 10$.

SUMMARY AND FUTURE WORK

My Doctoral research deals with the detection and characterization of extrasolar planets around evolved intermediate stars such as G and K giants using a precise Doppler spectroscopy. I have used observations from the Hamilton spectrograph at Lick Observatory that date back from 1999 until the end of the observing program in 2012. Giants, however, can exhibit intrinsic to the star long-period RV variations that can effectively mimic a planet. Such can be large surface spots or even non-radial $g-$mode pulsations (e.g. Hatzes & Cochran 1999). Line shape analysis in the sense to measure lines bisectors can be effective tool to distinguish line distortion related RV variations from a planetary signal, but the relatively lower spectral resolution of Hamilton (R = 60 000) and the Iodine line contamination makes this task very difficult. Nevertheless, the Hipparcos photometry data does not support the spot related variations as our targets are photometrically quiet, we cannot fully discharge neither the spot nor the pulsation hypothesis.

Thus, I have applied two other quantitative tests that can finally close the case for our planetary candidates:

1. I have developed a data reduction pipeline for the ESO near infrared spectrograph CRIRES (R = 100 000) on which our group has been awarded with observing time in the last four semesters. I have obtained a precise Doppler velocities from the near-IR, and I searched for consistency with the Lick optical data. Intrinsic stellar RV variations will lead to differences in RV phase and amplitude between the optical and near-IR, while, in case of planet, both data sets are expected to be consistent.
2. For the stars that RV signature consistent with more than one sub-stellar companion (and consistent optical and near-IR velocities), the possible gravitational interactions might be significant enough to be spotted on the RV curve. In order to take to account the gravitational perturbations, I have performed a dynamical fitting model to all multiple planets system candidates and have constructed a detailed $\chi^2_{\rm red}$ grids. Each orbital solution later is tested for long-term stability using the *Mercury* N-body simulator, transforming the $\chi^2_{\rm red}$ grids to stability maps. Passing this test can mean a clear planetary conformation.

Both methods turn out to be very successful. The obtained near-IR velocity precision is in the order of 30−40 m s^{-1}, enough to confirm the RV phase and amplitude, and thus, the planetary

nature on most of our planet host candidates. The dynamical fitting for multiple companions shows better $\chi^2_{\rm red}$ values than the multiple Keplerian model. This is signature that indeed interacting planets are responsible for the Doppler shift. The obtained long term stability test shows that some systems have stable best fit orbital solution, while the rest have broad and confident long term-stable regions in orbital parameter space within 1 or 2 σ from the best fit.

In this thesis I introduced our observational strategy with both: the Hamilton spectrograph at Lick observatory, and at VLT using CRIRES. I have explained in details our CRIRES pipeline algorithms for precise RV derivation and I introduced the stability methodology used for the dynamical tests of multiple planetary systems from our sample. Combined results were shown in Chapters §4, §5, §6 and §7. In total in this thesis I have introduced 11 planetary systems around giant stars, consistent with two planetary systems in close binary stellar system, five planetary pairs most of which exhibit a mean-motion and secular resonant behavior and four single planetary systems, from which 2 are found to be actually a brown dwarfs.

For the future, I wish to expand my expertise and apply it to recent and new observations of planetary systems to explain their dynamical structure, origin and evolution.

The increased number of multiple planetary systems announced in the literature, raises the natural question: "Are all those systems indeed dynamically stable?". Although, well separated planets are likely to be in a stable configuration, close period and near resonant pairs must be studied in details. I have found cases in the literature, where the published orbital elements are not consistent with stable planetary systems. Instead, the proposed system falls a part in timescales of few thousand years or even less.

During my PhD research I have analyzed a fair number of candidate multiple systems from our Lick sample. I have learned that the obtained best fit consistent with two planets with near periods is very often dynamically unstable. This is mostly due to the finite data sample, the instrument and data reduction related systematic, and RV stellar jitter that does not allow us to reveal the true orbital configuration. I have developed an algorithm that apply a dense $\chi^2_{\rm red}$ grid search by vary the orbital parameters within their estimated errors. Each dynamical fit from the result grid is later automatically tested for long-term stability using the *Mercury* N-body simulator. The final output almost always reveals at least one very confident region of orbital space parameters that can be stable on Gyr time scale. Usually those regions are involved in mean motion or secular resonances, which are not obvious from the best fit. Subsequently, based on my experience, the question can be asked: "Do all unstable planetary systems from the literature have a stable island within 3σ from their best fit, or some systems are unlikely to exist?"

As a postdoc, I wish to apply my knowledge to newly announced and well known extrasolar planetary systems. I plan to analyze the dynamical stability of a selected sample of planetary systems, which have not yet been studied in details.

In case a test planetary system is indeed stable I can better obtain the orbital parameters driven by stability diagnostics. Broad stability analysis in multiple systems can also put an upper limit on system's orbital inclination, something that cannot be done with the Doppler technique it self. Knowing the maximum possible planetary mass ($m_p \sin i$), where the system remains stable,

can effectively distinguish the planetary from the possible brown dwarf mass population.

In other hand, if a proposed system cannot preserve stability, even when tested for non-coplanar orbits or different stellar mass, the same must be put in to question. False-positive detections can bias planetary statistics and thereby bias any correlation between theory and observations. Such doubtful planets can have a large impact on the planet formation and system evolution scenarios, and thus, must be discharged.

After publishing the results from this research in refereed journals, I plan to develop a web-based page, where the output from the dynamical simulations for each system can be publicly available and used as reference.

Our days, the new technological achievements in computer software and hardware open whole new horizons for multi-planet systems dynamical studies. Besides the fact that modern PC technology can offer up to 8 and more fast CPU's, the real novelty is the revolution of the GPU (Graphics Processing Unit) technology. GPU graphic cards consist of thousands of smaller more efficient cores designed for parallel performance. Serial portions of the code run on the CPU, while parallel portions run on the GPU can simulate simultaneously hundreds or even thousands of different orbital configurations.

For my research needs I have developed a *Python* based code that runs *Mercury* multiple times on a standard multi-core PC. The code is very adequate and in principle can be run on multi-CPU clusters without any problems. However, the possibility to develop a PC based machine with super-computer performance is very attractive.

I plan to develop a software based on CUDA 5 (nVidia tech.) GPU implementation rather than the computers CPU's. Such a workstation will be inexpensive, reliable, and the most important flexible. I would like to use it for several tasks, each of them can be treated as a separate project:

1. Multiple MCMC chains for orbital parameter error estimation.
2. Deep and conclusive stability analysis of multiple exoplanetary systems.
3. Simulations from early planetary formation to the RGB phase.

Currently, the planetary occurrence statistics shows a large fraction of planets with moderate and high eccentricities. This observation phenomena, however, in some way contradicts with the Type I migration scenario. The planets must circularize their orbits by accumulating dust and gas during this stage of evolution. Gravitational instabilities at some point of the system's evolution or even Kozai effects caused by an external massive disturber can be a good explanation for the observed planetary distribution. However, more independent efforts can be done to explain the observed planetary distribution with theory. For example, detailed N-body simulations starting with different initial configurations and taking into account the stellar evolution might show when gravitational instabilities among the planets are most likely to occur, and in which conditions a system can preserve equilibrium.

Given the above, I plan to study the early planetary formation by following the most recent planet formation theories. I am planning to start very large numbers of dynamical simulations

($\sim 10^7$), with different initial conditions. My goals are two: first, to study the formation of massive planets, function of the stellar mass, metallicity, and the mass of the protoplanetary disk. Second, based on those simulations I would like to see what fraction of the systems will exhibit gravitational instabilities for the time span of few Gyrs. In addition to that, I am also interested to study the following cases:

First, during my research in Heidelberg, I have investigated the dynamical stability of several short period binaries, where there was indisputable evidence of a planet orbiting the primary. The dynamical picture of those systems shows that the planets can survive in long term stable orbits. However, the formation history is unknown. It is interesting to see how such systems can be formed using extended, dynamical test.

Second, all the planets found around giants have well separated orbits with semi-major axes larger than 0.6 AU. I plan to simulate multiple planetary systems around intermediate mass stars having at least one massive hot Jupiter. As reaching the RGB phase, the star undergoes some mass loss, thus its gravitational pull becomes weaker. Close planets might either slowly migrate outwards, be swallowed, or by moving outwards instabilities might take place and eventually destroy the system. This might explain the observational results around giant stars (i.e. mostly single massive planets with moderate eccentricities and well separated from their parent stars)

ACKNOWLEDGEMENTS

The results introduced in this thesis could not have been performed without the enormous personal and professional help from many people I have worked with during my PhD studies.

First, I would like to sincerely thank my advisor, Andreas Quirrenbach, for giving me the opportunity to develop myself during the past three years. I appreciate all his patience and understanding, and I am really thankful for being such a great guide.

I have no words to express my deepest respect and gratitude to Sabine Reffert. Without her support and constant help during my studies none of the written in this thesis would ever be done. She has helped me through extremely difficult times over the course of my research.

I thank to my former bachelor and master advisor, Petko Nedialkov, for his great attitude to me and all opportunities he give me. I also thank to Evgeny Ovcharov for his supervision during my master degree and for all practical astronomy lessons, which I have learned from him.

I would specially like to thank to my LSW colleagues. I thank Julian Stürmer for the many useful discussions we had, and to Otmar Stahl for his always fast and expert help on my working PC. Also I would really thank to Ingo Stilz for the *Python* lessons I got from him. I am grateful to Lutz Geuer, for helping me with many practical advices. At last but not least, I had the pleasure to meet Gabriele Cologna in LSW and I am glad that he was around these three years.

I want to thank Dario and Veselina for being the best neighbors and colleagues. With them I had a great time in Eppelheim and in IMPRS in general. Without their support everything from professional aspects to the social life in Germany would be very hard.

I am thankful for meeting my wife Anna without whose love, support and understanding I would probably have never completed this doctoral thesis.

Finally, I would like to extend my deepest acknowledgments to my mother Tania for buying my first astronomy encyclopedia more than twenty years ago. I was just a little boy, who barely reads, but this book fires the spark for knowledge in science and astronomy in me.

BIBLIOGRAPHY

Allende Prieto, C. & Lambert, D. L. 1999, A&A, 352, 555

Assef, R. J., Gaudi, B. S., & Stanek, K. Z. 2009, ApJ, 701, 1616

Baranne, A., Queloz, D., Mayor, M., et al. 1996, A&AS, 119, 373

Barban, C., De Ridder, J., Mazumdar, A., et al. 2004, in ESA Special Publication, Vol. 559, SOHO 14 Helio- and Asteroseismology: Towards a Golden Future, ed. D. Danesy, 113

Bean, J. L. & Seifahrt, A. 2009, A&A, 496, 249

Bean, J. L., Seifahrt, A., Hartman, H., et al. 2010, ApJ, 711, L19

Beaugé, C., Ferraz-Mello, S., & Michtchenko, T. A. 2003, ApJ, 593, 1124

Bedding, T. R., Mosser, B., Huber, D., et al. 2011, Nature, 471, 608

Berio, P., Merle, T., Thévenin, F., et al. 2011, A&A, 535, A59

Burkert, A. & Ida, S. 2007, ApJ, 660, 845

Butler, R. P., Marcy, G. W., Fischer, D. A., et al. 1999, ApJ, 526, 916

Butler, R. P., Marcy, G. W., Williams, E., Hauser, H., & Shirts, P. 1997, ApJ, 474, L115

Butler, R. P., Marcy, G. W., Williams, E., et al. 1996, PASP, 108, 500

Campbell, B., Walker, G. A. H., & Yang, S. 1988, ApJ, 331, 902

Carroll, B. W. & Ostlie, D. A. 2006, An introduction to modern astrophysics and cosmology

Chambers, J. E. 1999, MNRAS, 304, 793

Clough, S. A., Iacono, M. J., & Moncet, J.-L. 1992, J. Geophys. Res., 97, 15761

Clough, S. A., Kneizys, F. X., Rothman, L. S., & Gallery, W. O. 1981, in Society of Photo-Optical Instrumentation Engineers (SPIE) Conference Series, Vol. 277, Atmospheric transmission, 152–166

Correia, A. C. M., Udry, S., Mayor, M., et al. 2009, A&A, 496, 521

de Medeiros, J. R. & Mayor, M. 1999, A&AS, 139, 433

de Medeiros, J. R., Setiawan, J., Hatzes, A. P., et al. 2009, A&A, 504, 617

De Ridder, J., Barban, C., Carrier, F., et al. 2006, A&A, 448, 689

Desort, M., Lagrange, A.-M., Galland, F., et al. 2008, 491, 883

Döllinger, M. P., Hatzes, A. P., Pasquini, L., Guenther, E. W., & Hartmann, M. 2009a, A&A, 505, 1311

Döllinger, M. P., Hatzes, A. P., Pasquini, L., et al. 2009b, A&A, 499, 935
Döllinger, M. P., Hatzes, A. P., Pasquini, L., et al. 2007, A&A, 472, 649
Duncan, M. J., Levison, H. F., & Lee, M. H. 1998, AJ, 116, 2067
Eggleton, P. P. & Tokovinin, A. A. 2008, MNRAS, 389, 869
Figueira, P., Pepe, F., Melo, C. H. F., et al. 2010, A&A, 511, A55
Fischer, D. A., Marcy, G. W., Butler, R. P., Laughlin, G., & Vogt, S. S. 2002, ApJ, 564, 1028
Fischer, D. A., Marcy, G. W., Butler, R. P., et al. 2003, ApJ, 586, 1394
Fischer, D. A., Marcy, G. W., Butler, R. P., et al. 2008, ApJ, 675, 790
Fischer, D. A. & Valenti, J. 2005, ApJ, 622, 1102
Ford, E. B. 2005, AJ, 129, 1706
Frandsen, S., Carrier, F., Aerts, C., et al. 2002, A&A, 394, L5
Frink, S., Mitchell, D. S., Quirrenbach, A., et al. 2002, ApJ, 576, 478
Frink, S., Quirrenbach, A., Fischer, D., Röser, S., & Schilbach, E. 2001, PASP, 113, 173
Gaudi, B. S., Bennett, D. P., Udalski, A., et al. 2008, Science, 319, 927
Gettel, S., Wolszczan, A., Niedzielski, A., et al. 2012a, ApJ, 756, 53
Gettel, S., Wolszczan, A., Niedzielski, A., et al. 2012b, ApJ, 745, 28
Girardi, L., Bressan, A., Bertelli, G., & Chiosi, C. 2000, A&AS, 141, 371
Gladman, B. 1993, Icarus, 106, 247
Gray, D. F. 1982, ApJ, 255, 200
Gray, R. O., Corbally, C. J., Garrison, R. F., et al. 2006, AJ, 132, 161
Han, I., Lee, B. C., Kim, K. M., et al. 2010, A&A, 509, A24
Hatzes, A. P. & Cochran, W. D. 1999, MNRAS, 304, 109
Hatzes, A. P., Cochran, W. D., Endl, M., et al. 2006, A&A, 457, 335
Hatzes, A. P., Cochran, W. D., Endl, M., et al. 2003, ApJ, 599, 1383
Hatzes, A. P., Guenther, E. W., Endl, M., et al. 2005, A&A, 437, 743
Hekker, S. 2007, PhD thesis, Leiden Observatory, Leiden University, P.O. Box 9513, 2300 RA Leiden, The Netherlands
Hekker, S. & Meléndez, J. 2007, A&A, 475, 1003
Hinkle, K., Wallace, L., & Livingston, W. 1995, PASP, 107, 1042
Huélamo, N., Figueira, P., Bonfils, X., et al. 2008, A&A, 489, L9
Ida, S. & Lin, D. N. C. 2005, ApJ, 626, 1045
Izumiura, H. 1999, Publications of the Yunnan Observatory, 77
Johnson, J. A., Aller, K. M., Howard, A. W., & Crepp, J. R. 2010, PASP, 122, 905
Johnson, J. A., Butler, R. P., Marcy, G. W., et al. 2007, ApJ, 670, 833
Johnson, J. A., Payne, M., Howard, A. W., et al. 2011, AJ
Jones, M. I., Jenkins, J. S., Rojo, P., Melo, C. H. F., & Bluhm, P. 2013, A&A, 556, A78
Kaeufl, H.-U., Ballester, P., Biereichel, P., et al. 2004, in Society of Photo-Optical Instrumentation Engineers (SPIE) Conference Series, Vol. 5492, Society of Photo-Optical Instrumentation Engineers (SPIE) Conference Series, ed. A. F. M. Moorwood & M. Iye, 1218–1227
Kane, S. R., Reffert, S., Henry, G. W., et al. 2010, ApJ, 720, 1644
Kennedy, G. M. & Kenyon, S. J. 2008a, ApJ, 682, 1264
Kennedy, G. M. & Kenyon, S. J. 2008b, ApJ, 673, 502
Kennedy, G. M. & Kenyon, S. J. 2009, ApJ, 695, 1210

Kessler-Silacci, J., Augereau, J.-C., Dullemond, C. P., et al. 2006, ApJ, 639, 275
Kupka, F., Piskunov, N., Ryabchikova, T. A., Stempels, H. C., & Weiss, W. W. 1999, A&AS, 138, 119
Laskar, J. & Correia, A. C. M. 2009, A&A, 496, L5
Laughlin, G., Chambers, J., & Fischer, D. 2002, ApJ, 579, 455
Lebzelter, T., Seifahrt, A., Uttenthaler, S., et al. 2012, A&A, 539, A109
Lee, B.-C., Han, I., & Park, M.-G. 2013, A&A, 549, A2
Lee, B.-C., Han, I., Park, M.-G., Mkrtichian, D. E., & Kim, K.-M. 2012a, A&A, 546, A5
Lee, B.-C., Mkrtichian, D. E., Han, I., Park, M.-G., & Kim, K.-M. 2012b, A&A, 548, A118
Lee, J. W., Kim, S.-L., Kim, C.-H., et al. 2009, AJ, 137, 3181
Lee, M. H. 2004, ApJ, 611, 517
Lee, M. H. & Peale, S. J. 2002, ApJ, 567, 596
Lee, M. H. & Peale, S. J. 2003, ApJ, 592, 1201
Liu, Y.-J., Sato, B., Zhao, G., & Ando, H. 2009, Research in Astronomy and Astrophysics, 9, 1
Liu, Y.-J., Sato, B., Zhao, G., et al. 2008, ApJ, 672, 553
Lovis, C. & Mayor, M. 2007, A&A, 472, 657
Lovis, C., Ségransan, D., Mayor, M., et al. 2011, A&A, 528, A112
Luck, R. E. & Challener, S. L. 1995, AJ, 110, 2968
Maldonado, J., Villaver, E., & Eiroa, C. 2013, A&A, 554, A84
Marcy, G. W. & Butler, R. P. 1992, PASP, 104, 270
Marcy, G. W., Butler, R. P., Fischer, D., et al. 2001, ApJ, 556, 296
Marois, C., Zuckerman, B., Konopacky, Q. M., Macintosh, B., & Barman, T. 2010, Nature, 468, 1080
Mayor, M., Pepe, F., Queloz, D., et al. 2003, The Messenger, 114, 20
Mayor, M. & Queloz, D. 1995, Nature, 378, 355
Meschiari, S., Wolf, A. S., Rivera, E., et al. 2009, PASP, 121, 1016
Mitchell, D. S., Frink, S., Quirrenbach, A., et al. 2003, in Bulletin of the American Astronomical Society, Vol. 35, American Astronomical Society Meeting Abstracts, 1234
Mitchell, D. S., Reffert, S., Trifonov, T., Quirrenbach, A., & Fischer, D. A. 2013, 555, A87
Montmerle, T., Augereau, J.-C., Chaussidon, M., et al. 2006, Earth Moon and Planets, 98, 39
Mordasini, C., Alibert, Y., & Benz, W. 2009, A&A, 501, 1139
Mordasini, C., Alibert, Y., Benz, W., Klahr, H., & Henning, T. 2012, A&A, 541, A97
Murray, C. D. & Dermott, S. F. 1999, Solar system dynamics
Nakamoto, T. & Nakagawa, Y. 1994, ApJ, 421, 640
Niedzielski, A., Goździewski, K., Wolszczan, A., et al. 2009a, ApJ, 693, 276
Niedzielski, A., Konacki, M., Wolszczan, A., et al. 2007, ApJ, 669, 1354
Niedzielski, A., Nowak, G., Adamów, M., & Wolszczan, A. 2009b, ApJ, 707, 768
Nowak, G., Niedzielski, A., Wolszczan, A., Adamów, M., & Maciejewski, G. 2013, ApJ, 770, 53
Omiya, M., Izumiura, H., Han, I., et al. 2009, PASJ, 61, 825
Orosz, J. A., Welsh, W. F., Carter, J. A., et al. 2012, Science, 337, 1511
Pasquini, L., Döllinger, M. P., Weiss, A., et al. 2007, A&A, 473, 979
Pepe, F., Mayor, M., Galland, F., et al. 2002, A&A, 388, 632

Percy, J. R., Wilson, J. B., & Henry, G. W. 2001, PASP, 113, 983
Press, W. H., Teukolsky, S. A., Vetterling, W. T., & Flannery, B. P. 1992, Numerical recipes in FORTRAN. The art of scientific computing
Prugniel, P., Vauglin, I., & Koleva, M. 2011, A&A, 531, A165
Quirrenbach, A. 2006, in Saas-Fee Advanced Course 31: Extrasolar planets, ed. D. Queloz, S. Udry, M. Mayor, W. Benz, P. Cassen, T. Guillot, & A. Quirrenbach, 1–242
Quirrenbach, A., Amado, P., Seifert, W., et al. 2013, in American Astronomical Society Meeting Abstracts, Vol. 221, American Astronomical Society Meeting Abstracts, 149.05
Quirrenbach, A., Reffert, S., & Bergmann, C. 2011, in American Institute of Physics Conference Series, Vol. 1331, American Institute of Physics Conference Series, ed. S. Schuh, H. Drechsel, & U. Heber, 102–109
Reffert, S., Christoph Bergmann, C., Quirrenbach, A., et al. 2014, A&A, submitted
Reffert, S., Quirrenbach, A., Mitchell, D. S., et al. 2006, ApJ, 652, 661
Rivera, E. J., Laughlin, G., Butler, R. P., et al. 2010, ApJ, 719, 890
Roell, T., Neuhäuser, R., Seifahrt, A., & Mugrauer, M. 2012, A&A, 542, A92
Rothman, L. S., Rinsland, C. P., Goldman, A., et al. 1998, J. Quant. Spec. Radiat. Transf., 60, 665
Sato, B., Ando, H., Kambe, E., et al. 2003, ApJ, 597, L157
Sato, B., Izumiura, H., Toyota, E., et al. 2008a, PASJ, 60, 539
Sato, B., Izumiura, H., Toyota, E., et al. 2007, ApJ, 661, 527
Sato, B., Omiya, M., Harakawa, H., et al. 2012, PASJ, 64, 135
Sato, B., Omiya, M., Harakawa, H., et al. 2013, ArXiv e-prints
Sato, B., Omiya, M., Liu, Y., et al. 2010, PASJ, 62, 1063
Sato, B., Toyota, E., Omiya, M., et al. 2008b, PASJ, 60, 1317
Seifahrt, A. & Käufl, H. U. 2008a, A&A, 491, 929
Seifahrt, A. & Käufl, H. U. 2008b, A&A, 491, 929
Seifahrt, A., Käufl, H. U., Zängl, G., et al. 2010, A&A, 524, A11
Setiawan, J., Hatzes, A. P., von der Lühe, O., et al. 2003, A&A, 398, L19
Setiawan, J., Henning, T., Launhardt, R., et al. 2008, Nature, 451, 38
Setiawan, J., Rodmann, J., da Silva, L., et al. 2005, A&A, 437, L31
Takeda, Y., Sato, B., & Murata, D. 2008, PASJ, 60, 781
Tan, X., Payne, M. J., Lee, M. H., et al. 2013, ArXiv e-prints
Tokovinin, A. A. & Smekhov, M. G. 2002, A&A, 382, 118
Toner, C. G. & Gray, D. F. 1988, ApJ, 334, 1008
Trifonov, T., Reffert, S., Tan, X., Lee, M. H., & Quirrenbach, A. 2014, A&A, submitted
Tuomi, M. 2012, A&A, 543, A52
Udry, S. & Santos, N. C. 2007, ARA&A, 45, 397
Valenti, J. A., Butler, R. P., & Marcy, G. W. 1995, PASP, 107, 966
van Leeuwen, F. 2007, A&A, 474, 653
Vogt, S. S. 1987, PASP, 99, 1214
Vogt, S. S., Butler, R. P., Rivera, E. J., et al. 2010, ApJ, 723, 954
Vogt, S. S. & Keane, M. J. 1993, in Bulletin of the American Astronomical Society, Vol. 25, American Astronomical Society Meeting Abstracts, 1305

Walker, G. A. H., Bohlender, D. A., Walker, A. R., et al. 1992, ApJ, 396, L91
Walker, G. A. H., Yang, S., Campbell, B., & Irwin, A. W. 1989, ApJ, 343, L21
Wambsganss, J. 2011, Nature, 473, 289
Wang, L., Sato, B., Zhao, G., et al. 2012, Research in Astronomy and Astrophysics, 12, 84
Welsh, W. F., Orosz, J. A., Carter, J. A., et al. 2012, Nature, 481, 475
Wittenmyer, R. A., Endl, M., Wang, L., et al. 2011, ApJ, 743, 184
Wolszczan, A. & Frail, D. A. 1992, Nature, 355, 145
Woolfson, M. M. 1993, QJRAS, 34, 1
Youdin, A. N. & Shu, F. H. 2002, ApJ, 580, 494
Zechmeister, M., Reffert, S., Hatzes, A. P., Endl, M., & Quirrenbach, A. 2008, A&A, 491, 531